Process Kinetics of Transient Liquid Phase Sintering in a Binary-Isomorphous Alloy System

by

Dennis Michael Ryan Turriff

A thesis
presented to the University of Waterloo
in fulfillment of the
thesis requirements for the degree of
Doctor of Philosophy
In
Mechanical Engineering

Waterloo, Ontario, Canada, 2007

Author's Declaration

I hereby declare that I am the sole author of this thesis. This is a true copy of the thesis, including any required final revisions, as accepted by my examiners.

I understand that my thesis may be made electronically available to the public.

Abstract

The problem of inadequate measurement techniques for quantifying the isothermal solidification process during transient liquid phase sintering (TLPS) in binary isomorphous systems such as Ni-Cu, and the resulting uncertainty regarding the solidification mechanism and its sensitivity to important process parameters, has been investigated. A unique combination of differential scanning calorimetry (DSC), neutron diffraction (ND), and metallographic techniques has enabled the quantitative characterization of important TLPS stages (i.e., solid-state sintering, melting and dissolution, isothermal solidification, and homogenization) as well as verifying the re-melt behaviour of post-sintered specimens and measuring variable melting point (VMP) properties. This has resulted in the advancement of the fundamental understanding of liquid formation and its removal mechanism during isothermal, or diffusional, solidification. The Ni-Cu system was chosen for experimentation due to its commercial relevance as a braze filler material and also because it is an ideal model system (due to its isomorphous character) that is not well understood on a quantitative or phenomenological basis. Samples consisted of elemental Ni and Cu powder mixtures of varying particle size and composition.

In DSC experiments, the progress of isothermal solidification was determined by measuring the enthalpy of melting and solidification after isothermal hold periods of varying length and comparing these to the measured enthalpy of pure Cu. The low melting enthalpies measured for all Ni/Cu mixtures heated just past the Cu melting point (1090°C) indicate that solid-state sintering and interdiffusion during heat-up significantly suppress initial liquid formation and densification from the wetting liquid. For samples heated well past the Cu melting point (1140°C), Ni dissolution causes increased initial liquid fractions and densification. It was found that significantly more time was required for complete liquid removal at 1140°C vs. 1090°C. This is attributed to the observed increase in initial liquid fractions formed at higher processing temperatures due to the dissolution of Ni. This effectively counteracts the increased diffusivities at these temperatures, and thus more time is required to completely remove the increased liquid content. TLP mixtures sintered at 1140°C using three different particle sizes revealed that fine base metal Ni particles cause high degrees of solid-state interdiffusion during heat-up, small initial liquid fractions, and accelerated liquid

removal rates due to high surface area/volume ratios. A diffusion-based analytical model was developed to account for these effects (i.e., particle size, temperature, solid-state sintering, and dissolution). Comparison with experimental DSC results reveals that this model can accurately predict liquid removal given accurate diffusivities. Metallographic analysis of post-sintered DSC specimens via SEM and EDS indicates that isothermal liquid solidification leaves behind Ni-rich cores surrounded by Cu-rich matrix regions having compositions given by the Ni-Cu phase diagram solidus (C_S) at a selected isothermal processing temperature (T_P).

ND experiments were used to investigate the melting event and interdiffusion *during* the isothermal hold segment by analyzing the evolution of the {200} FCC peaks of Ni and Cu. ND patterns were collected *in situ* at 1 minute intervals during prolonged sintering cycles for larger powder specimens. The Cu melting event was characterized by an abrupt decrease in Cu peak intensity at 1085°C as well as a shift towards higher 2θ angles corresponding to lower Cu contents. This shifted residual peak (hereafter referred to as the C_S peak) originates from regions of the specimen having compositions near solidus at T_P. Immediately following the melting event, the evolution of ND patterns shows that these C_S peaks grow rapidly, indicating the isothermal growth of a Cu-rich phase. These *in situ* findings confirmed the metallographic and DSC data and indicated that isothermal solidification of the liquid phase proceeds via the growth of a solute-rich solid solution layer surrounding the Ni particles. This occurs by the transient progression of the solid/liquid interface at compositions given by the liquidus and solidus (C_S/C_L). During sintering, diffraction intensities gradually increased at intermediate 2θ angles between previous Ni and Cu peaks. ND patterns gradually evolved from initially having a broad double-peak profile to a sharper single-peak profile due to increased Ni-Cu interdiffusion. The 2θ position and width of the post-sintered peaks indicated very homogeneous sintered alloys. Metallographic analysis of post-sintered specimens having undergone prolonged sintering and homogenization revealed extensive Kirkendall pore formation from unequal diffusivities ($D_{Cu} > D_{Ni}$).

In this study, the unique combination of diffusion-based modelling as well as DSC, ND, and supporting metallographic analysis has enabled the identification of characteristic sintering behaviour, important process parameters, and processing windows for TLPS in Ni-Cu systems. Quantitative and *in situ* information of this nature is absent in the previous TLPS literature.

Acknowledgements

I thank my supervisor, Dr. Stephen Corbin, for my introduction to research and the opportunity to work together on this project. I appreciate the support and freedom he has given me to pursue various academic and research interests as well as the timely guidance and insight provided when it was needed. Without his influence and mentorship, I would likely not have pursued this path to the extent that I have. Thank you for sparking the curious researcher in me.

I thank the numerous co-workers and friends who have supported me throughout my time here. I would like to particularly acknowledge certain people for their support and friendship over the years, namely: Aarati Vigneswaran, Alex Bardelcik, Caroline Amyot, Gregory Bourne, Roydyn Clayton, Ryan Clemmer, Mike Kuntz, Jeff McIsaac, Valentina Ngai, Saleh Tabandeh, Mark Whitney. I have shared memorable experiences, and learned so much from all of you. You have all contributed to make this a fruitful and enjoyable journey. Alex and Valentina, I am so glad to have met you during my studies. Thank you for your friendship and everything else that is much too long for these pages to rightly describe.

Many thanks must also go to Lachlan Cranswick, Mike Watson, and the Canadian Neutron Beam Centre (CNBC, Chalk River, Ontario, Canada) for their support and important technical contributions, which enabled novel neutron diffraction studies. This work has also been gratefully supported by funding from Materials and Manufacturing Ontario (MMO), an Ontario Centre of Excellence (OCE), and the Natural Sciences and Engineering Research Council of Canada (NSERC). Additional financial support from the University of Waterloo is gratefully appreciated**.**

For my parents, who have raised me to be who I am today and have made this possible. For my sister who will always be so close to me.

And for Valentina, who has been with me almost every step of the way.

"Fear paralyzes; curiosity empowers. Be more interested than afraid."

- **Patricia Alexander**

Table of Contents

List of Tables

List of Figures

1. Introduction

Sintering is a heat treatment used in powder metallurgy (PM) processes. Mixtures of pre-alloyed or elemental powder particles are heated to elevated temperatures for varying durations (hereafter referred to as a sintering temperature cycle). This process is conventionally used to form near net-shape parts, where powders can be contained in various dies during the sintering treatment. Contacting particles join and gradually reduce the inter-particle pore volume between them to form a dense part [1]. Sintering can occur at temperatures below the solidus of the powders used (i.e., solid-state sintering), whereas liquid phase sintering (LPS) occurs above the solidus in the presence of a liquid phase. The presence of the liquid in LPS techniques enhances mass transport rates and densification (vs. solid-state sintering) by exerting a capillary pull to re-arrange and consolidate powder particles within the mixture [2,3]. Due to these productivity and cost advantages, German [2] estimates that 70% of sintered products are processed in the presence of a liquid phase. Savitskii [4] suggests that as much as 90% of bulk material sintering employs a variant of liquid phase techniques. In conventional LPS techniques the liquid is persistent and must be re-solidified athermally, or frozen, by cooling below the solidus. The resulting cast microstructure can then form segregated, non-equilibrium intermediate phases, which can be detrimental to the material's mechanical properties [5]. The persistent nature of the liquid in conventional LPS necessitates low liquid volume fractions to ensure good shape retention in sintered parts.

1.1. TLP Sintering Background

Transient liquid phase (TLP) sintering, which is a variant of LPS, depends on the formation of a liquid phase that is transient in nature. In contrast to other LPS techniques, TLP sinterable powder mixtures form partial liquids that are removed during the sintering cycle by diffusional solidification. Parts are formed from powder mixtures consisting of a low melting point additive powder, which is relatively rich in a melting point depressant (considered as constituent A), and a higher melting point base metal powder (considered as constituent B). An A-rich liquid phase is formed by heating to an isothermal processing temperature (T_P)

below the melting point of the base metal powder (T_B), yet above that of the additive phase (T_A) [2,3]. During an isothermal hold at a processing temperature above T_A, the melting point depressant (i.e., the solute, A) is removed from the liquid phase through extensive diffusion into the base metal (i.e., the solvent, B). This causes a progressive removal of the liquid isothermally at T_P. Solidification in this manner avoids the formation of non-equilibrium phases and the cast microstructure otherwise formed by freezing. This process is termed 'isothermal solidification', but is sometimes also referred to as diffusional homogenization or diffusional solidification [2]. TLPS is complete once the liquid has been completely removed at T_P. When followed by an appropriate homogenization treatment, a uniform microstructure can be obtained, which consists of a solid-solution having a composition C_O [2, 3].

TLPS is a novel PM technique typically used for forming bulk materials consisting of ceramics, various metals, and metal matrix-ceramic composites. For example, TLP sintering of Fe-C powders with yttria-stabilized zirconia (YSZ), SiC, or Al_2O_3 particles can be used to form ceramic reinforced steel-matrix composites having near-net shape [6]. Other important examples of well known TLPS applications include dental amalgams made using pre-alloyed Ag-Hg powder and bronze bearings made from Cu and Sn powders [2]. Self-lubricating Cu-Sn bearings can be manufactured by TLP sintering elemental Cu and Sn powder mixtures [7]. In dental amalgams, Ag-based alloy powders can be mixed with liquid mercury to produce a slurry, which is compressed into a dental cavity. Solidification of the liquid occurs in minutes by diffusion processes [2]. Recent health concerns regarding the Hg content of amalgams [8] have spurred the development of modified TLPS systems for preventing Hg release through alloy additions such as In and Pd [9].

Unlike conventional liquid phase sintering processes, the re-melt temperature of post-processed TLP sintered material is increased due to *in situ* alloying of the mixture constituents [10,11]. This variable melting point (VMP) characteristic differentiates TLPS from other sintering techniques and can be very useful for certain applications. In particular, the potential exists to use TLPS mixtures for the development of liquid-rich powder systems to be used as VMP filler metals in soldering [12,13,14] and brazing [15,16] applications. Figure 1-1 illustrates how an A-B powder mixture, when used as a filler metal to join two substrate surfaces, will evolve through different points during a typical TLPS temperature cycle. Above the melting point of A, the initial mixture will form an A-rich liquid that will spread through

the B powders and substrate surfaces. This liquid will isothermally solidify over time at T_P. After a sufficient hold, a more homogeneous solid solution is formed having a uniform compositon near the bulk (C_O), which will exhibit a measurable melting point shift upon reheating. Such applications of TLPS require large liquid fractions for flow and densification, where shape retention is not a concern. VMP solders and brazes are attractive for use in applications where stepwise joining of complex multi-joint assemblies is desired (e.g., printed circuit boards and heat exchangers), where alloyed bonds can inhibit the re-melting and thermal fatigue of adjacent joints. VMP bonds can also be tailored to join/repair assemblies while in service. These would melt and isothermally solidify at a given service temperature.

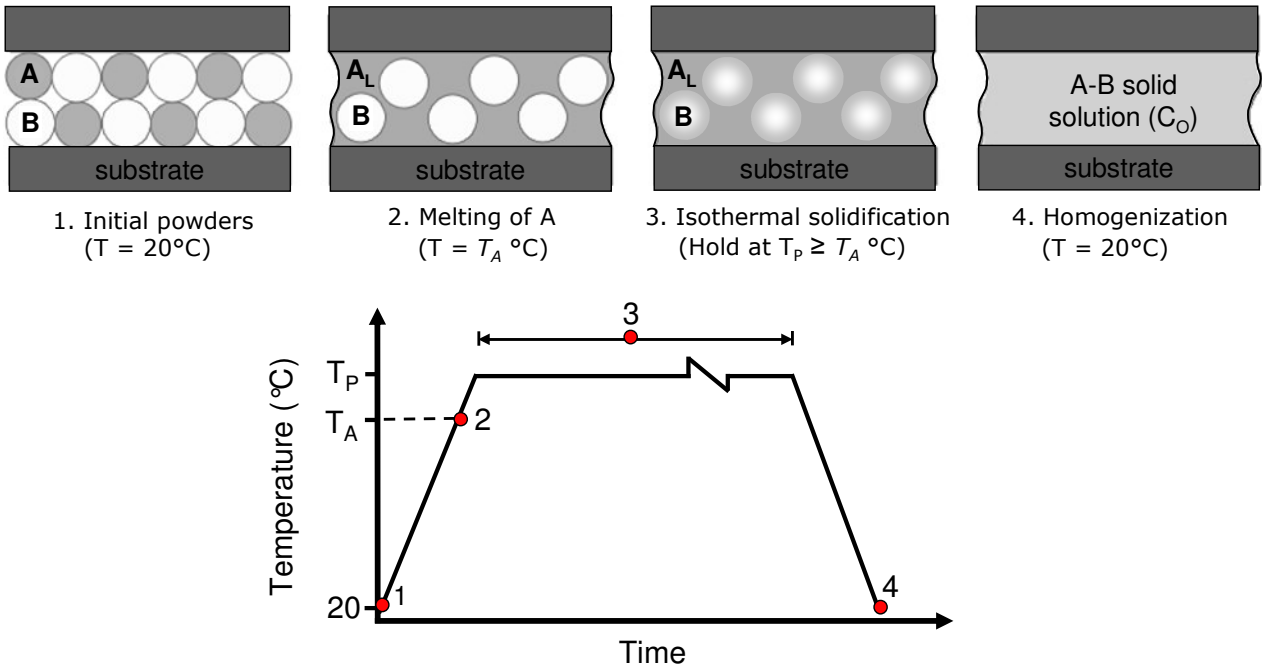

Figure 1-1: A-B TLPS powder mixtures used as a filler metal to join substrate surfaces.

As a result of the above-mentioned characteristics (i.e., isothermal solidification and VMP characteristic), TLP processing has received considerable interest in recent years for a wide range of joining applications including lead-free soldering in the microelectronics industry [11, 12, 13, 14, 17, 18, 19, 20] and high temperature brazing using traditional and wide gap transient liquid phase bonding (TLPB) [21, 22, 23, 24]. Traditional TLPB [21, 22] differs from TLPS since thin foil interlayers typically serve as the additive phase and the planar substrate material to be joined constitutes the base metal. Wide gap TLPB [23, 24] is similar to TLPS since additive powders are used to fill large clearances.

In summary, when TLPS technology is applied to braze/solder pastes it can offer a number of advantages including; 1) a reduction in the process temperature required to form a dense joint by melting elemental vs. pre-alloyed powders; 2) solidification at the process temperature by diffusional (or isothermal) solidification, 3) variable melting point behaviour allowing stepwise joining; 4) the use of less expensive elemental powders, and 5) increased microstructural homogeneity by avoiding the formation of non-equilibrium phases and a cast structure that would normally form due to solidification upon cooling However, TLPS can require relatively long solidification times and is highly sensitive to process parameters.

1.2. Problem

Despite its importance as an advanced PM technique for bulk materials, a fundamental understanding of the metallurgical processes taking place in TLPS (i.e., solid-state interdiffusion during heat-up, melting and base metal dissolution, densification, and isothermal solidification) and the variables controlling them, is incomplete [4,25,26]. Furthermore, the use of TLPS for joining applications is fairly new and the relatively large liquid fractions required and long durations emphasize the need for a better understanding of these processes in order to develop effective VMP brazes and.efficient processing conditions.

The kinetics of TLPS processes are determined by the interaction of the base and additive powders during the sintering cycle before and after the liquid has formed. The base-additive interaction kinetics are most importantly determined by the alloy system chosen, but have also been widely found to be very sensitive to important process parameters such as heating rate, green density, powder size, additive content, and processing temperature [2,3,5,10,11,13,15,25,26]. The importance of the amount and duration that the transient liquid is widely acknowledged [2,11,26,27]. Successful completion of TLPS requires that the volume of liquid formed and its duration cause the desired degree of densification, which depends critically on the amount of liquid formed and its duration [2,25,37]. In addition, the solidification kinetics of the liquid phase must be rapid enough to make TLPS a commercially viable materials joining alternative. Unfortunately, a majority of TLPS studies consist of dilatometric and *ex situ* metallographic analyses, where quantification of the liquid amount present within PM specimens is difficult. As such, melting and isothermal solidification

kinetics in TLPS are not well understood [25]. However, liquid formation and duration are important characteristics determing the viability of TLPS processes (i.e., density and duration).

Corbin and McIsaac [11], as well as others [10,13] have studied TLPS solder pastes using differential scanning calorimetry (DSC) and have developed a technique to quantify the rate of liquid removal in the Pb-Sn and Sn-Bi eutectic systems. This work led to the development of a simple diffusion-based analytical model [25] for isothermal solidification kinetics of binary-eutectic TLPS solder pastes, which shows good agreement with experimental DSC results for the Pb-Sn system [11,28]. However, the model does not account for solid-state interdiffusion between the base and additive powders during the heat-up stage since the eutectic systems studied did not exhibit significant degrees of interdiffusion prior to melting. Also, base metal powder dissolution is not accounted for since modelling is limited to cases where the processing temperature is held at the eutectic temperature. Therefore, isothermal solidification kinetics predictions using this model are not applicable for alloy systems where: 1) solid-state interdiffusion is significant during the heat-up stage (i.e., in systems exhibiting high mutual solubilities) [2,11]; and 2) when dissolution occurs for cases where T_P exceeds T_A [25]. The effects of these processes on the initial liquid fraction formed as well as their impact on the rate of isothermal solidification are not well understood. This is particularly true for binary isomorphous systems (such as Ni-Cu) [5,11], which have unlimited solubility.

1.3. Objectives

The proposed research is a study in the process kinetics of TLPS in a liquid-rich isomorphous system that may be suitable for filler metal applications in high-temperature brazing. As such, selection of the Ni-Cu alloy system will be justified in detail in Section 3.1. Experimental and analytical methods will be used to develop a more complete fundamental understanding of TLPS processes, while focusing on the isothermal solidification stage. The influence of A-B solid-state interdiffusion during heat-up and base metal dissolution on the liquid formed will be investigated. Specific objectives are:

1. Develop and characterize an experimental sample preparation technique for fluxless Ni-Cu powder systems that exhibit TLPS characteristics (i.e., melt formation, isothermal solidification, and variable melting point behaviour).

2. Develop an experimental DSC technique to quantify the amount of liquid formed and the rate of its removal. This approach can provide quantitative evidence of isothermal solidification of a transient liquid by comparing the measured amount of liquid initially formed to the amount frozen upon solidification after an interrupted isothermal hold. In previous TLPS solder work [10, 11, 13, 28] the DSC technique was used to simply determine a normalized fraction of the initial liquid remaining after various isothermal hold times at T_P. Since solid-state interdiffusion was not significant in the eutectic systems studied, it was assumed that the initial liquid fraction was given by the amount of additive powder used [10, 11, 13, 28]. In isomorphous systems however, where solid-state effects are expected to be significant, modifications will have to be made in order to determine the actual amount of liquid initially formed as well as the fraction remaining at various hold times (vs. normalized liquid fractions).

3. Identify, and study the effects of key process parameters on the TLPS process (i.e., sample preparation techniques, T_P, and powder particle size). Varying T_P above T_A will allow the investigation of dissolution phenomena. T_P is expected to affect many inter-related variables (i.e., diffusivity, solid/liquid solubilities, particle size) and the resultant effect on liquid formation and removal should be complex.

4. Investigation of *in situ* neutron powder diffraction techniques to study interdiffusion during TLPS. Although very useful, DSC does not provide direct *in situ* information regarding A-B interdiffusion *during* the initial heating segment prior to melting or *during* the isothermal segment at T_P. Instead, DSC provides valuable phase transition information at melting and solidification events near T_A. Valuable insight regarding A-B interdiffusion during these stages – particularly the isothermal solidification of the liquid - can be gained by analyzing the evolution of neutron diffraction patterns collected *in situ* during the process.

5. Modification and refinement of a diffusion-based analytical model [25] (initially developed for low-temperature TLPS solders) to verify its applicability to higher temperature isomorphous systems. Modifications will include the addition of solid-state sintering predictions as well as dissolution for sintering cases where $T_P > T_A$. The applicability of this modelling approach will be analyzed for isomorphous systems.

2. Literature Review and Research Justification

2.1. Sintering Background and Basic Theory

Materials are often formed into a desired shape by deformation at high temperatures or by melting and casting processes. Powder metallurgy (PM) processing of particulate materials offers alternate processing routes since powders conveniently exhibit fluid-like characteristics. As such, various PM shaping processes can be used to form complex shapes, such as die compaction, slip casting, tape casting, extrusion, injection molding, isostatic pressing and rolling [2]. When heated to sufficient temperatures, sintering occurs as particles bond to one another and increase the strength of the particulate arrangement [29]. This can significantly facilitate the manufacturing of near-net shape parts. For example, ceramic materials can not be formed via traditional deformation or melt casting techniques due to their brittle nature and very high melting points. As a result, ceramics are commonly formed into useful shapes by various sintering process variants [30].

Sinter-bonding typically occurs above homologous temperatures of approximately 0.5-0.75T_m (i.e., between half and three quarters of a given material's melting point). However, a wide range of sintering techniques and temperatures can be used depending on the materials selected and desired properties, which will be further differentiated in Section 2.2. For illustrative purposes, single-phase solid-state sintering will be discussed here.

Various particle sizes and shapes can also be used, where smaller, irregularly-shaped particles have relatively higher surface area/volume ratios and higher total surface energies. Figure 2-1 shows a scanning electron micrograph illustrating typical sinter bonds formed at the contact points of spherical particles, called a neck. Sintering proceeds via the growth of these neck regions as well as other accompanying morphological changes.

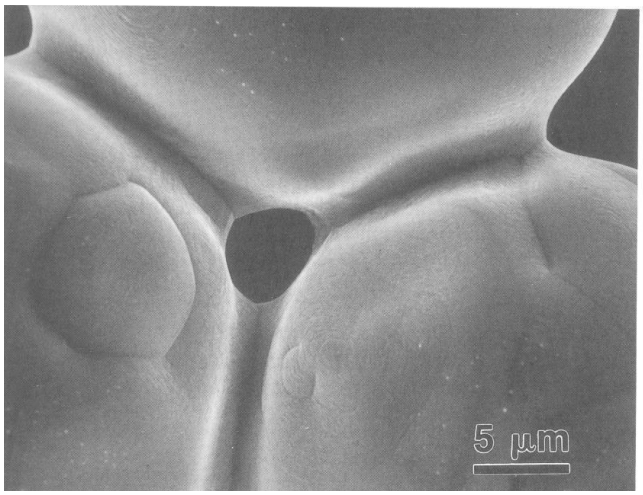

Figure 2-1: SEM image of solid-state sinter bonds formed between three contacting spherical particles [2].

Interatomic bonds first form at the initial contact points and gradually generate cohesive necks that will grow in the *x*-dimension (Figure 2-2) by various mass-transport mechanisms that occur at the atomic scale. There are five transport mechanisms to consider: surface diffusion, grain boundary diffusion, lattice/volume diffusion, evaporation-condensation, and viscous flow. For many metals and ceramics, solid-state forms of diffusion are dominant (i.e., lattice, surface, and grain boundary diffusion). If we consider the micrograph in Figure 2-1, the neck can form and grow by atoms diffusing from the volume of each contacting particle to the neck region (i.e., lattice/volume diffusion through the particle crystal lattice shown in Figure 2-2). Grain boundaries, which are visible on the particle surfaces in Figure 2-1, and the particle surfaces themselves also provide mass transport paths that are less obstructed for atoms diffusing to the neck area. Other mechanisms, such as vapour evaporation-condensation processes or plastic deformation and flow with pressure-assisted techniques may also contribute to bonding. Many of these mass transport mechanisms can act simultaneously for most materials, but some are more dominant at certain temperatures of the sintering cycle. For sintering to occur, these mass transport mechanisms must be activated by an energy source to provide atomic mobility, typically in the form of heat via a sintering furnace.

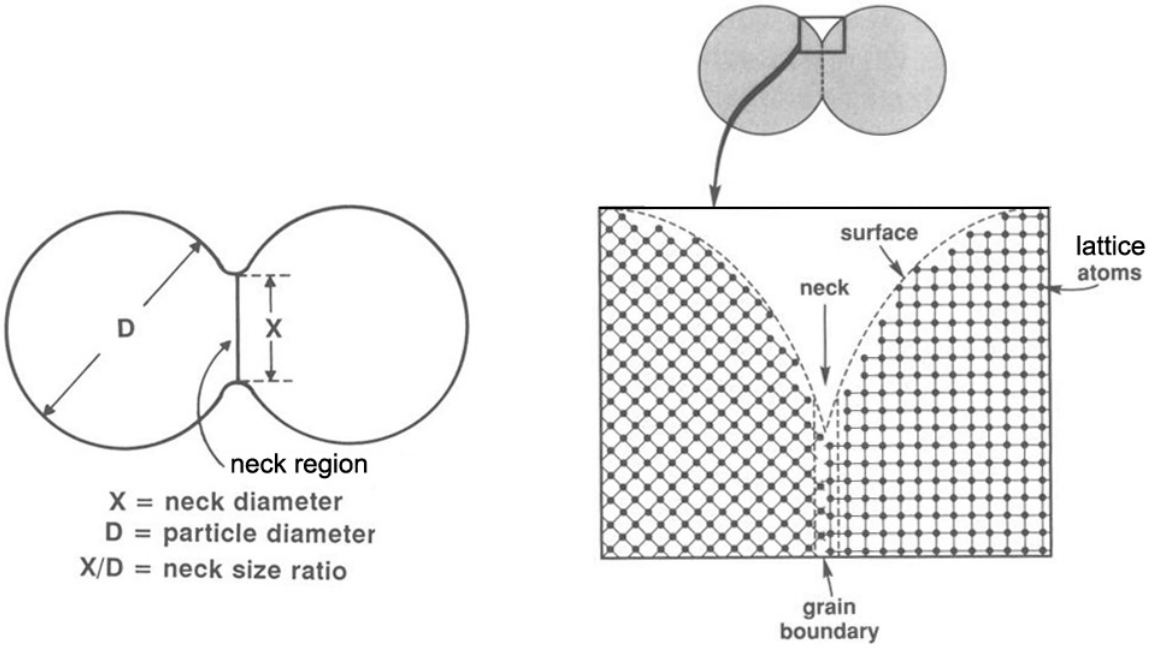

Figure 2-2: Definition of neck region, neck size, and illustration of a new grain boundary formed due to crystal misalignment at the neck (adapted from [2]).

Figure 2-3 illustrates a simple energy state diagram for the initial pre-sintered (1) and final post-sintered powder system conditions (2). The energy required to activate the mass transport systems mentioned above imposes a barrier, or activation energy requirement, which must be satisfied for sintering to occur. Once activated, the driving force for sintering is a reduction of the total free energy of a powder system (ΔG_T), which consists of the volume (ΔG_v), grain boundary (ΔG_b), and free surface energy (ΔG_s) reductions [2].

$$\Delta G_T = \Delta G_v + \Delta G_b + \Delta G_s \qquad \textbf{(2-1)}$$

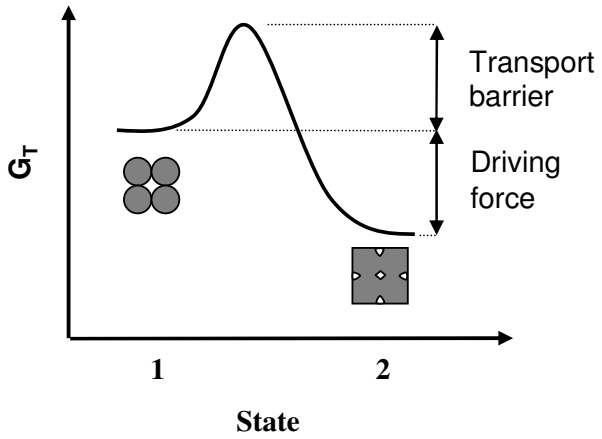

Figure 2-3: Energy reductions during sintering

Since powder materials have such high total particulate surface areas in comparison to fully dense materials, a relatively high proportion of the total free energy is associated with the internal powder surfaces. In the absence of phase transformations with sintering of non-interacting powders, ΔG_v is negligible. Grain growth during the sintering cycle can generate ΔG_b contributions; however these are relatively small in comparison to the energy of the free particle surfaces [2]. Thus, the principal driving force for sintering is the reduction of free surface energy. As such, sintering proceeds by the growth of the neck region and the concomitant reduction of inter-particle pore size, which results in a reduction of the total particulate surface area. This reduction of surface energy serves as the macroscopic driving force for solid-state sintering and directs mass flow to the neck regions - causing densification [2]. When fine powder particles are used, the total internal surface area is high and provides a greater sintering driving force. Conversely, the same mass or volume of large particles will have a lower internal surface area and generate a lower driving force for sintering.

The resultant changes in pore structure and neck growth during sintering tend to increase the density of the starting powder mixture as well as significantly improve other sintered properties such as strength, ductility, conductivity, and corrosion resistance [2]. From a simply geometrical perspective, the basic sintering process can be divided into three classic stages of morphological evolution [2]. Figure 2-4 presents an illustration of these basic stages and the corresponding densification process, where the starting condition is an array of loose powders in point contact. During the initial stage (referred to as neck growth), these contacts form visible necks that grow in size. This results in a large surface area reduction but a small degree of densification since pores are still quite large and interconnected (i.e., open porosity). During the intermediate stage, pore rounding becomes evident as the particles are more difficult to differentiate. Densification and surface area reductions are significant in this stage as a much more closed-pore structure develops. The final stage is characterized by the closure of near-spherical pores, where final densification is minimal and relatively slow. There are many variants to the basic process depicted, but these three stages provide a good general description for the morphological evolution during sintering.

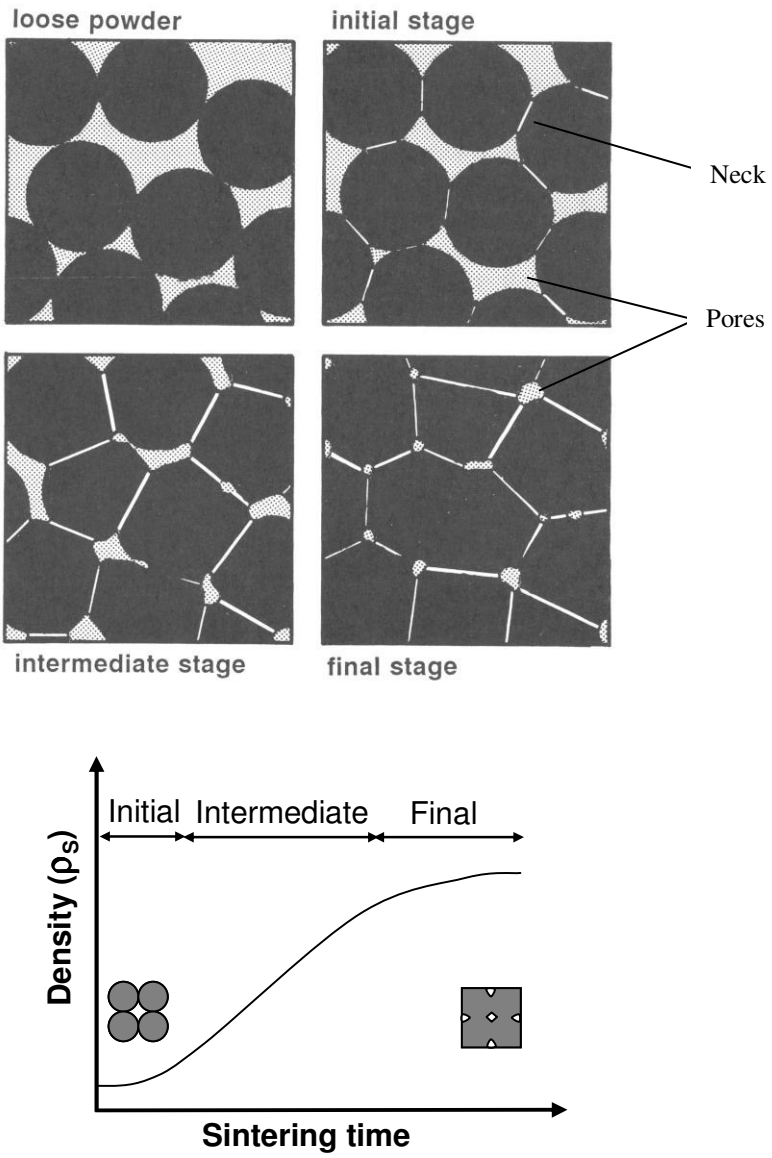

Figure 2-4: Illustration of geometrical changes and densification process during classic sintering stages [adapted from 2].

As stated above, sintering is driven by the reduction of the surface energy (γ) of a powder system. This surface energy gives rise to what can be considered as a sintering stress (σ), which arises from the energy difference between high- and low-curvature surfaces. The stress associated with a curved surface having a radius of curvature *r* is given by [2]:

$$\sigma \propto \frac{\gamma}{r} \qquad \textbf{(2-2)}$$

Smaller powders or areas having greater degrees of curvature will generally have a higher sintering stress. During sintering at high temperatures, this effective stress directs mass transport in paths/directions that contribute to particle bonding and neck growth (i.e., initially high curvature regions). This ultimately decreases the overall surface curvature of the system and causes densification by moving the particle towards each other. This sintering stress can be considered to be equivalent to the stress required to cold-press the initial powder mixture to its post-sintered density.

The activation of mass transport mechanisms is required to respond to this inherent stress in powder materials. Heat externally applied during the sintering cycle provides the thermal activation energy for atomic mobility that is required for sintering to occur. Hence two factors are important for sintering: surface stresses/energy and atomic mobility. Atomic mobility during diffusion processes for example, is dependent on diffusing atoms having sufficient energy to break bonds from their current site and migrate to a new site. Diffusion coefficients (D), which are a measure of the rate at which atoms can diffuse or migrate, are strongly temperature dependent and vary according to Arrhenius-type temperature relation [31]

$$D \propto e^{\frac{-Q}{RT}} \tag{2-3}$$

$$\text{or, } D = D_O e^{\frac{-Q}{RT}} \tag{2-4}$$

Where, Q is the activation energy for a given diffusion mechanism, R is the gas constant, T is the absolute temperature, and D_O is a pre-exponential factor, which is a material dependent constant. Therefore diffusion rates, and thus sintering rates, can increase exponentially with temperature. The Arrhenius relation in Equation (2-4) is used to model lattice, grain boundary, and surface diffusion rates [32].

The densification process during the intermediate stage of solid-state sintering can be modelled by Equation (2-5), where the rate of densification depends on many variables as described above [2]:

$$\frac{d\rho_S}{dt} = \frac{K\gamma_{SV}\Omega D}{Td^3} \tag{2-5}$$

Where D is the diffusivity of migrating atoms, Ω is the atom volume, γ_{SV} is the solid particle surface energy, K is a collection of geometric terms (typically ~5), T is absolute

temperature, and d is the average particle size. This simplified model assumes spherical, mono-sized particles. In practice, particle size distributions and non-spherical shapes must sometimes be considered. In fact, much of the difficulty in modelling sintering processes arises from the complex geometry that real particulate materials present [2]. Another limitation arises from the difficulty of obtaining reliable model parameters. For example, only one diffusivity value (typically lattice diffusivity) is used in most models, yet more than one transport mechanism may be active during sintering. The contribution of grain boundary diffusion is difficult to determine due to the lack of sufficient diffusivity data and the changing grain size during the process. Additionally, the above model does not apply to more complex liquid phase sintering processes since it does not consider the consolidating effect of a liquid phase (i.e., liquid fraction, solid/liquid interfacial energy, γ_{SL}, and solid/liquid solubilities). Finally, many models apply to isothermal heat treatment segments only, while neglecting the sintering and interdiffusion that might take place during the athermal heat-up segment.

Despite the limited practical use of such models, they provide an improved physical understanding of the morphological changes during the sintering process and its sensitivity to key parameters. Equation (2-5) clearly illustrates that densification is significantly affected by the sintering temperature (both directly and indirectly through D), and average particle size (d).

2.2. Process Variations

Figure 2-5 presents an overview of various sintering techniques. The major categories of sintering process variants are differentiated primarily by the use of pressure during the sintering cycle and whether or not a liquid phase is formed. The latter is primarily determined by the peak processing temperature chosen with respect to the phase diagram of the powder materials used.

Pressure-assisted methods can be used during the sintering cycle to obtain lower residual porosity. The external pressure is usually hydrostatic or uniaxial, and is applied by hot isostatic pressing (HIP) or forging/die-pressing respectively [2]. High-stress sintering employs pressures sufficiently high to cause plastic deformation and flow of the powders to achieve higher densities. However, most sintering is performed without an external pressure [2]. Pressure-assisted sintering will not be discussed in further detail here.

Pressureless methods do not employ HIP or die pressing *during* the sintering cycle. The starting powders are usually in loose contact prior to sintering (i.e., the green state), or they may be pressed/compacted (i.e., green-pressed). Green-pressing is often used to increase the initial density of the starting powders and/or to simply make compacted pre-forms of a desired shape.

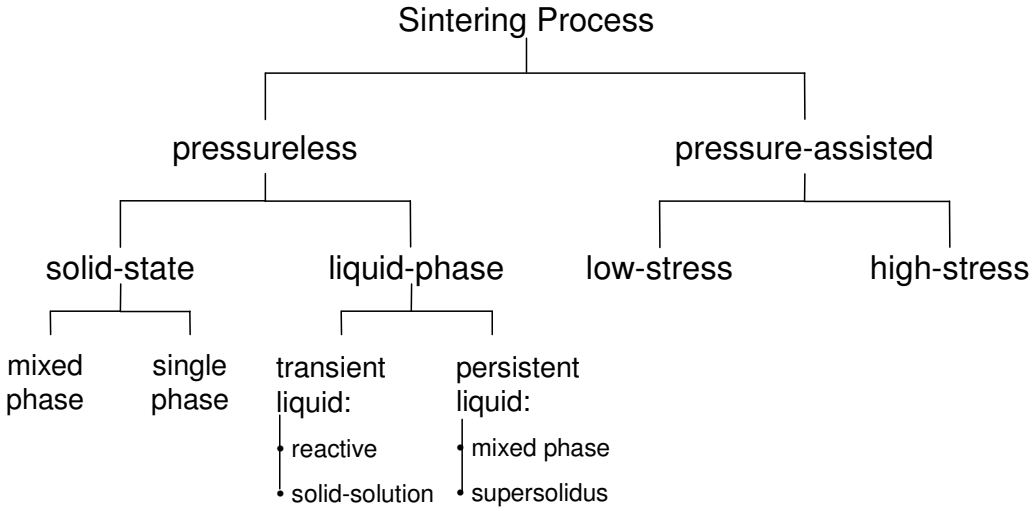

Figure 2-5: Sintering process variations.

Pressureless sintering processes can be further classified by the presence or absence of a liquid phase (i.e., liquid phase or solid-state sintering). Sections 2.3 and 2.4 will discuss phase diagram concepts and the relevant temperature regimes generally used for liquid phase or solid-state sintering variants.

2.3. Solid-State Sintering

Solid-state sintering (SSS) is performed at temperatures below the melting point, or solidus temperature, of the powders used whereas liquid phase sintering occurs in the presence of a liquid above the solidus. Basic SSS theory and sintering behaviour has been briefly discussed in the introductory sintering material (Section 2.1). Variants of solid-state sintering include mixed-phase and single-phase sintering. As illustrated in Figure 2-6, mixed-phase sintering utilizes mixtures of powders each consisting of a different phase (i.e., A and B in this case), whereas single-phase SSS utilizes only one powder. It is important to note that in both cases the powders used can be in either elemental (i.e., pure) or in pre-alloyed form. By

convention, powder A will be considered to be relatively rich an element A. It is also possible the prealloyed powder may consist of multiple phases within each particle, but for simplicity they will be considered as a single phase. Secondary phases will be represented by a different powder (i.e., B).

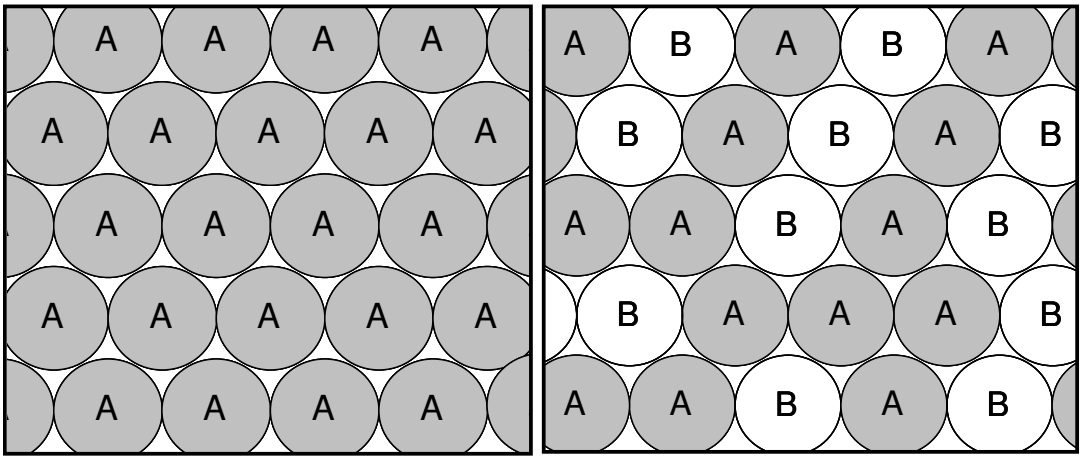

Figure 2-6: Powder arrays for: a) single-phase A powder, b) A and B mixed-phase powder mixtures.

Figure 2-7 presents simple binary phase diagram schematics to illustrate the sometimes subtle differences between mixed vs. single phase and solid vs. liquid phase sintering for A-B alloy systems, which exhibit a) eutectic or b) isomorphous phase diagrams. Important phase boundaries, or miscibility lines, are indicated on each diagram (i.e., the liquidus, solidus, and eutectic lines). The solidus line represents the lowest temperatures at which liquid first forms for A-B alloys, and coincides with the pure/elemental melting points (i.e., T_A and T_B) at the composition axis extremities. For eutectic systems, the lowest temperature at which a liquid can form is given by the eutectic line at T_E (Figure 2-7*a*). Figure 2-7*c* illustrates the segments and profile of a typical sintering cycle used for solid-state sintering, where the peak process temperature (T_P) is kept below the melting point, or solidus temperature of the powders used. It is important to note that the solidus temperature of the powders used is variable depending on the composition of the powder mixture composition (C_O).

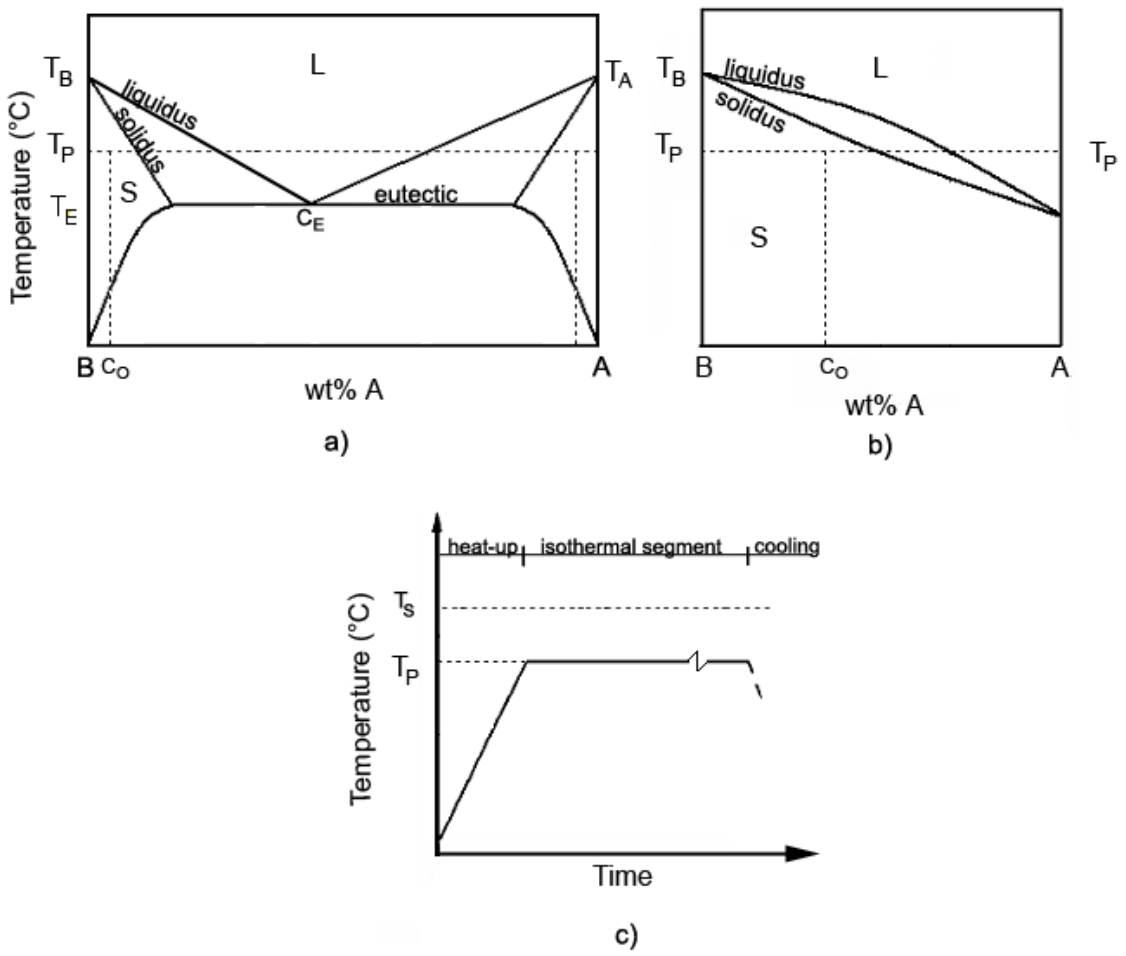

Figure 2-7: Schematic phase diagrams for SSS in: a) A-B eutectic system, and b) A-B isomorphous system. (c) Heat treatment temperature profile throughout typical sintering cycle.

Single-phase powder mixtures of pure B or pure A must be solid-state sintered at T_P below the elemental B or A melting points respectively (T_B or T_A), regardless of the phase diagram type exhibited. Alternatively, for a single-phase powder consisting of a pre-alloyed A-B solid-solution having some composition C_O (see Figure 2-7*a* and Figure 2-7*b*), the peak processing temperature must not exceed that given by the intersection with the sloped solidus line for the given composition ($T_{Solidus}$, or T_S). In isomorphous systems (as in Figure 2-7*b*), single-phase SSS can be performed over a broad range of compositions and temperatures whereas eutectic systems are restricted by limited solid-solubility regions (*S*).

In mixed-phase SSS, mixtures of elemental A and B powders can be used as well as mixtures of pre-alloyed powders of varying compositions (in wt %A). By convention, element A will be considered to be the lower melting point constituent of the alloy system (i.e., $T_A <$

T_B). For pre-alloyed powders, powder A will be considered to be relatively rich in constituent A (i.e. pure A or an A-rich alloy), and will thus have a lower melting point, or solidus temperature T_S. As such, elemental A and B powder mixtures must be heated below T_A to prevent melting in both eutectic and isomorphous A-B systems. However, an additional consideration in eutectic systems is the possible interaction of A and B powders during the initial heat-up segment to cause incipient melting and form a low-melting point eutectic below T_A at T_E. In this case the solidus temperature is effectively given by the eutectic line. In such systems T_P should remain below the eutectic temperature to prevent the formation of an incipient liquid having a eutectic composition (C_E). In general, mixed-phase SSS should take place at temperatures below any liquid phase regions (L) of the phase diagram exhibited by the powders of interest.

Solid-state sintering generally proceeds via the classical stages depicted earlier in Figure 2-4. Solid-state densification and shrinkage is fairly well understood in surface area-dominated sintering for non-interacting/alloying powders [2,4]. However, for the mixed-phase case, metallurgical interactions between the different powders such as interdiffusion and phase transformations can potentially occur during the sintering cycle. This complicates the sintering process and as a result, interacting mixed-phase sintering of heterogeneous mixtures is less well understood [4,33]. This will be further discussed in Section 2.5 with respect to the solid-state sintering stage of TLPS.

2.4. Liquid Phase Sintering

Many sintering cycles generate liquid phases due to the possible productivity and microstructural advantages that LPS can provide. The presence of a liquid in LPS techniques is often used to enhance densification and mass transport rate (vs. SSS) by exerting a capillary pull to rapidly re-arrange and consolidate powder particles within the mixture [2,3]. This liquid can form by full or partial melting of the initial powder(s) used (e.g., partial or complete melting of powder A in Figure 2-6*a* or *b*), or via the *in situ* formation of a low melting point phase during the sintering cycle (e.g. incipient eutectic melting at A-B contact points in Figure 2-6*b*). The tree diagram in Figure 2-5 showed that the two main variations of LPS are

distinguished by the duration of the liquid phase and its solidification mechanism (i.e., persistent or transient liquids).

Persistent liquids are used in conventional LPS, where the liquid phase exists throughout the high temperature portion of the sintering cycle and is solidified athermally by freezing during the cooling segment. To do so, the processing temperature must remain above the solidus temperature of the low melting point powders throughout the high temperature segment. Alternatively, in TLPS, transient liquids are removed *during* the high temperature portion of the sintering cycle by diffusional processes prior to cooling. Under the correct conditions, the liquid phase is isothermally removed by the formation of intermediate phases via a phase transformation (i.e., reactive TLPS) or by the formation of a solid-solution via diffusion and alloying (i.e., solid-solution TLPS). In this study the focus will be on the latter since the isomorphous systems aimed for investigation inherently do not form intermediate phases. A more detailed description of the TLPS process is provided in Section 2.5.

Variants of conventional persistent liquid phase sintering include mixed-phase LPS of A and B powder mixtures (as depicted in Figure 2-6*b*) and supersolidus liquid phase sintering (SLPS) of pre-alloyed single-phase powders (as depicted in Figure 2-6*a*). SLPS consists of partially melting a pre-alloyed powder by heating the alloy intothe two phase solid/liquid miscibility gap of the system's phase diagram. If these single phase particles have a pre-alloyed composition C_O (as shown in Figure 2-8), SLPS would consist of heating to a process temperature between the solidus and liquidus to cause a stable, yet partial powder melt. For mixed-phase LPS of A-rich and B-rich powder mixtures as depicted in Figure 2-6*b*, a liquid can be formed by partially or fully melting the low melting point A powders. For the liquid to be stable in this case, the total additive content of the entire mixture (i.e., C_O in Figure 2-8 is now taken as the bulk solute content of the mixture) must lie between the solidus and liquidus lines at the selected T_P. Due to the similar C_O constraint for single-phase SLPS and mixed-phase LPS, the two techniques are sometimes referred to interchangeably.

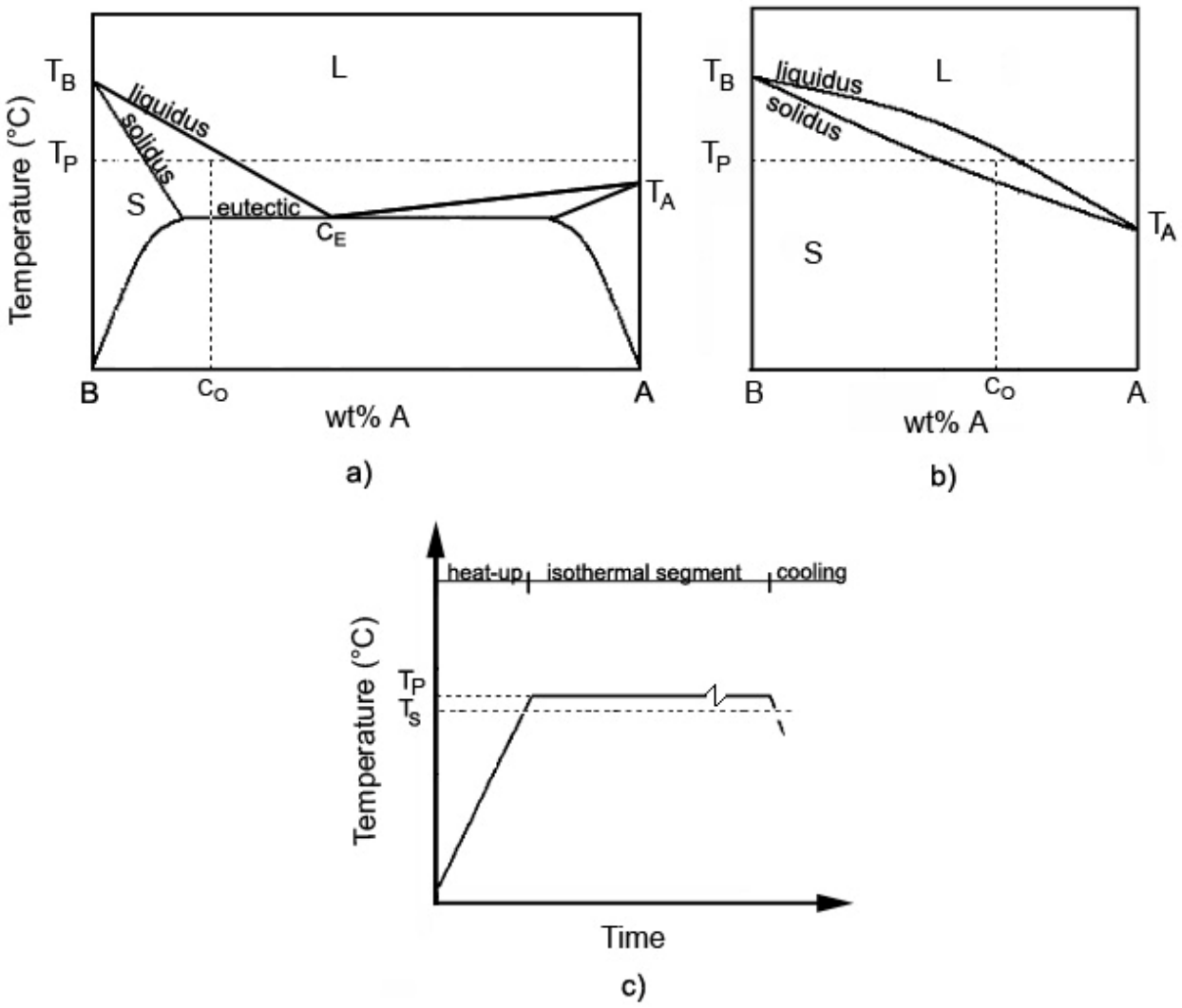

Figure 2-8: Schematic phase diagrams for persistent liquids in SLPS and mixed-phase LPS for: a) A-B eutectic systems, and b) A-B isomorphous systems. (c) Heat treatment temperature profile throughout a typical sintering cycle.

The liquid phase is persistent in conventional LPS processes because the bulk powder mixture composition (given by C_O, in wt% A) and processing temperatures are chosen such that the liquid and solid are both equilibrium phases under the selected conditions. In other words, sintering takes place within a two-phase region of the powder system's phase diagram. Figure 2-9 illustrates the classic LPS stages for mixed powders, where the liquid is persistent and non-reactive (i.e., sintering is dominated by surface energy effects and not chemical reactions) [2].

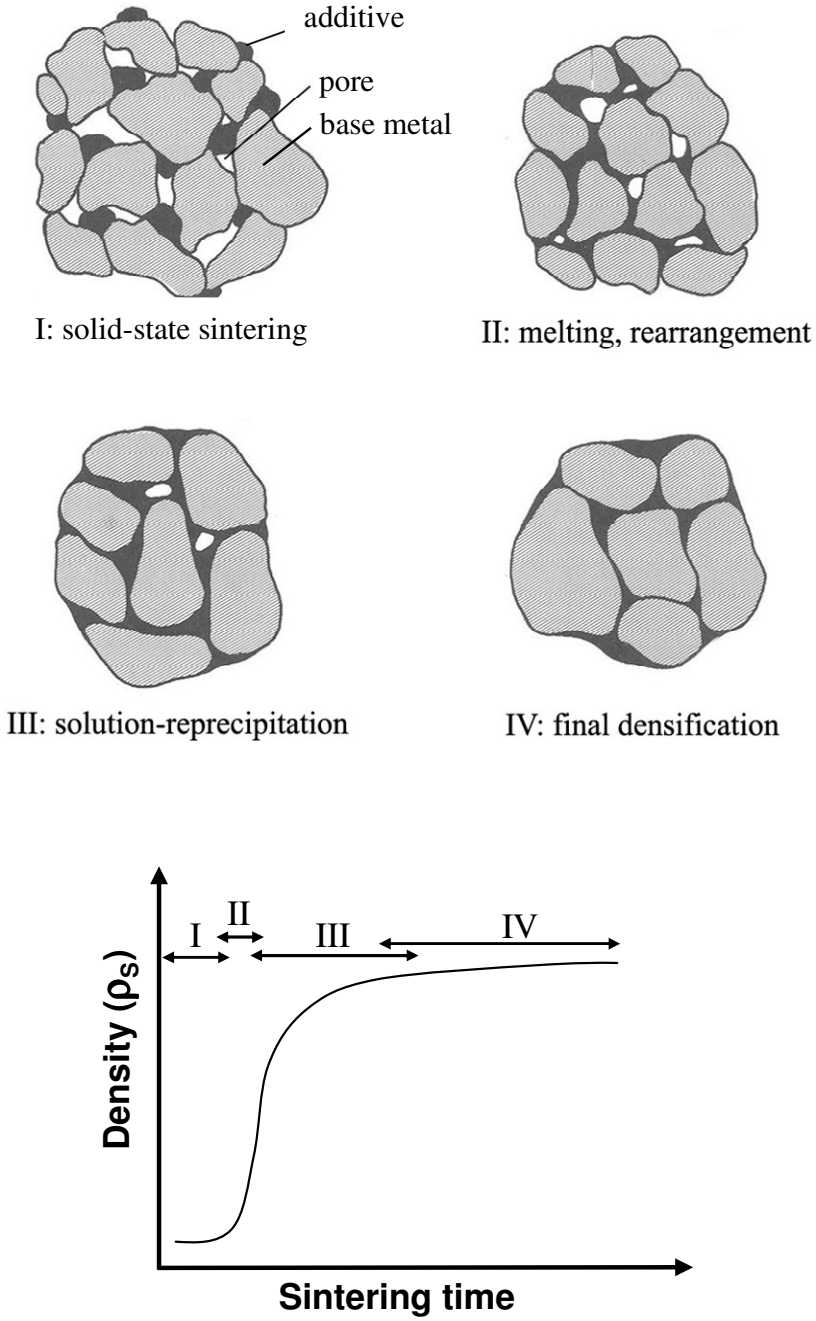

Figure 2-9: Illustration of classical stages and densification behaviour in persistent liquid phase sintering [adapted from 2].

Here, stage I consists of solid-state sintering and interdiffusion between contacting additive and base metal powder particles during the heat-up segment. Depending on the heating rates, relative particle sizes, and alloy system, the amount of solid-state interaction during heat-up can vary significantly. Stage II consists of additive melting, which causes a

rapid densification burst by capillary rearrangement for the base metal particles. Densification by the wetting liquid and re-arrangement have been reported to occur within the first second of melt formation [34,35,36].

During stage III, solution-reprecipitation processes dominate, which serve to decrease interfacial surface area and smoothen the particle surfaces. During this process, solution of smaller base metal particles into the liquid and reprecipitation onto adjacent larger particles allows further rearrangement and grain-shape accommodation to remove more pores and increase densification [2]. This process generates a coarsened microstructure with enlarged particles and a stable inter-particle liquid phase. During the final densification stage (stage IV), solution-reprecipitation processes have essentially ceased, and only solid-state sintering processes between adjacent base metal particles provide slow densification.

Stages II, III, and IV correspond to the initial, intermediate, and final stages of densification and morphological evolution identified for solid-state sintering (see Figure 2-4). It is important to note that these metallurgical processes overlap during LPS densification, but one is more dominant in each of the stages identified.

2.5. Transient Liquid Phase (TLP) Sintering

2.5.1. Process description and nomenclature

Transient liquid phase sintering involves the formation of a liquid by similar means to persistent LPS methods. However, in this case the liquid is removed by metallurgical powder interactions during the high temperature portion of the sintering cycle (vs. athermal freezing/solidification during cooling). Powder mixtures consisting of multiple phases must be used (as depicted in Figure 2-6*b*). Typically, TLPS is used with powder mixtures consisting of a low melting point powder (i.e., powder A) in the presence of a higher melting point base metal powder (i.e., powder B). Alternatively, low melting point phases can be incorporated as coatings on one of the powders. Once formed, the liquid isothermally solidifies by diffusion into the solid to form a solid solution (i.e., solid solution TLPS). TLPS is a complex and sensitive sintering process since it consists of a short SSS stage during heat-up and a transient LPS stage.

Figure 2-10 illustrates a schematic phase diagram for a binary-isomorphous alloy system that can be used as a basis for understanding TLPS in this study. A typical TLPS heating profile relating to the important phase diagram temperatures is shown and important stages are identified during the process. If we consider the initial powder system to consist of a mixture of pure A and pure B powders, then the relative proportions of A and B determine the bulk solute content C_O of the mixture (in wt% A).

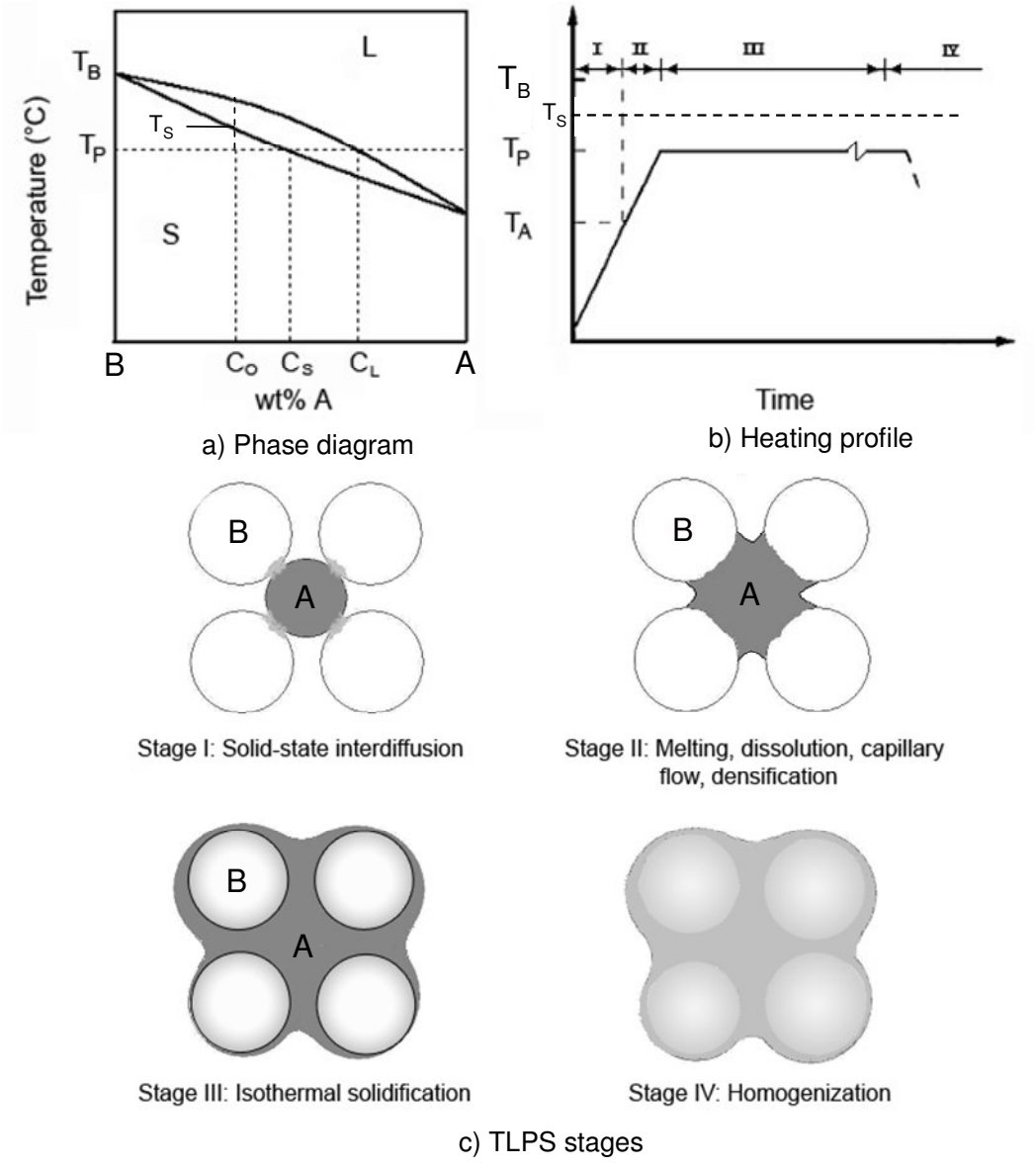

Figure 2-10: a) Schematic equilibrium phase diagram for a binary-isomorphous system and, b) typical heating profile showing important temperature used in TLPS.

For the liquid phase to be transient and TLPS to be possible, the liquid phase must not be persistent at the selected isothermal processing temperature and therefore the final equilibrium composition must lie within the single-phase solid region of the phase diagram. An important requirement for this to be possible is that the phase diagram for the alloy system chosen must exhibit a significant solubility for the additive in the base metal. Therefore, an important initial condition for TLPS is that the solute content of the mixture must be less than the maximum solid solubility (C_S) of the alloy at T_P (i.e., $C_O < C_S$).

Figure 2-10 shows the important stages that have been identified in TLPS [2,13]: I) solid-state sintering and interdiffusion occurs as A-B necks during the first athermal heat-up segment below the melting point of the additive powder (T_A); II) liquid formation through the melting of phase A and the dissolution of the B phase (if $T_P > T_A$). The liquid spreads through the powder mixture by capillary action, wets the base metal particles and causes rapid densification; III) gradual solidification of the liquid during an isothermal hold at T_P by solute diffusion into the base metal particles; and IV) continued solid-state interdiffusion at T_P eliminates compositional gradients and homogenizes the solid-solution mixture prior to cooling. Upon reheating, the TLP sintered mixtures should demonstrate a higher solidus corresponding to the post-sintered alloy at C_O (i.e., T_S in Figure 2-10*a*). The melting point shift is then given by $T_S - T_A$. Lower C_O values will also result in higher post-sintered melting point shifts as shown by the phase diagram, but will compromise liquid fractiosn and densification.

The significance of the heat-up stage (I) in regards to interdiffusion and consolidation depends on its duration as a result of the peak temperature and the heating rate used. However, the isothermal stage that follows the melting event is typically the stage of interest since the duration is usually much longer and the majority of the metallurgical and morphological changes take place during this prolonged treatment. However, the effects of the heat-up stage must still be considered in the sintering process. This is particularly true in high diffusivity, high solubility systems such as Ni-Cu since solid-state sintering can decrease the amount of liquid formed at T_A [11]. In the present thesis, the diffusional processes occurring during stages I, II, and III will be primarily investigated. The morphological changes during sintering shrinkage, liquid wetting, and the consolidation process will not be thoroughly investigated.

2.6. Non-DSC Studies and Important Process Parameters

In the context of a VMP braze, the amount of liquid initially formed is particularly important as it should be sufficient to densify the braze and bond the faying surfaces of the substrates to be joined, yet isothermally solidify within a reasonable, known time frame. For example, increasing the amount of additive powder should increase the amount of liquid formed and therefore increase consolidation levels. However, the amount of solute and liquid should be optimized such that a desired density can be achieved while minimizing the solidification time.

Base metal particle size (a_B) [11,25,26,37,38], relative diffusivities (D_A and D_B) [39,40], base metal grain size (d) [25], heating rate (R_H) [11,26,40,41], processing temperature (T_P) [37,38,40,41, 42], base/additive solubilities [26,40], powder purity/composition and morphology [26,40], and bulk alloy composition (C_O) [11,38,40-41], have all been found to significantly influence the amount of liquid formed and its duration during TLPS [10,11,13,26,38,40], which critically affects densification [13,38,40,42]. However, these non-DSC studies do not offer reliable quantitiative experimental results for the liquid duration and its diffusional solidification rate. The sensitivity of TLPS to the above variables has been typically investigated by dilatometry, chemical analysis and qualitative (or semi-quantitative) metallographic analysis. These methods provide useful information regarding the sintering behaviour of TLPS powder systems, but it is difficult to quantitatively determine the amount of liquid formed and its transient nature during sintering using these *ex situ* techniques.

The liquid phase and remnant solid-liquid interfaces can be difficult to identify once the specimens have been cooled to the solid-state and prepared for metallographic analysis of a single section. Furthermore, the inherently complex phase distribution and morphology in sintered specimens of fine particulate materials is statistically complex due to inhomogeneity and size distribution effects. As a result, a quantification of the kinetics of liquid removal (or isothermal solidification) has received little attention. As such, the sensitivity of TLPS to the above variables and how they specifically affect liquid formation and isothermal solidification kinetics is not well understood, particularly on a quantitative basis [25]. Instead, many experimental studies focus on the measurable macroscopic dimensional changes during sintering of bulk, compacted specimens (typically disc-shaped or cylindrical). Such dilatometric techniques measure sintering shrinkage/expansion *in situ* during the cycle using a

controlled dilatometer instrument or by manual measurements at various interruptions in the sintering cycle.

Lee and German [40] conducted sintering experiments with Fe and Al powders (Al being the additive) to investigate the shrinkage/expansion behaviour of pressed powder compacts and related these results to the observed *ex situ* microstructure evolution. Experimental variables included different heating rates, mixture composition (2.5-15wt% Al), Al powder composition (i.e., pure vs. pre-alloyed) and hold temperatures ranging from 1250 to 1300°C. They pointed out that the binary phase diagram for this system shows a eutectic Al-rich liquid at 655°C, a large solubility of Al in (Fe), as well as many intermediate intermetallic Fe-Al phases. Sintering experiments were performed in a dilatometer to measure specimen length changes during linear heating segments with rates of 10 and 200 °C/min. Net shrinkage/expansion measurements for all post-sintered specimens showed a net expansion as a result of swelling during sintering for samples containing ≥ 5wt% Al powder. This was attributed to the formation of the intermetallic phases around the original Al particles as well as significantly unbalanced diffusivities ($D_{Al} > D_{Fe}$), causing Kirkendall effect porosity in the prior Al particle locations. Samples with higher Al powder contents showed a gradual increase in net expansion.

Individual dilatometer expansion traces showed that an abrupt expansion occurred at the eutectic temperature during heat-up, where an Al-rich liquid should form. Lee and German suggested that this is due to the break-down of oxide films, which delayed the diffusive Kirkendall swelling at low temperatures, by the liquid formed at the eutectic temperature. However, the presence of the liquid (i.e., amount and duration) was not clearly distinguishable in micrographs presented due to the complex intermetallic phases and pore structure. However, differential thermal analysis (DTA) data did indicate a small melting peak with an onset near 655°C for one specimen studied using DTA. When 200°C/min heating rates were used (vs. 10°C/min), moderately less expansion swelling was measured. When Fe-50%Al pre-alloyed additive powder was used instead of the elemental Al powder, decreased net expansions were measured. This was attributed to the avoidance of the eutectic liquid region of the phase diagram, which likely enhanced intermetallic formation and interdiffusion once formed.

German and Dunlap [37] and Baek and German [38] have studied TLP sintering in the Fe-Ti system using dilatometric and metallographic techniques. This binary alloy system can potentially form two eutectic liquids during heat-up to high temperatures – a Ti-rich liquid at 1085°C and a Fe-rich liquid at 1289°C. German and Dunlap investigated TLP sintering of pure Fe and pure Ti mixed compacts (2-5 wt% Ti) at 1350°C in Argon under various conditions. Dilatometry data collected during the sintering cycle showed that the densification behaviour of all samples consisted of an initial swelling/expansion period during heat-up to the temperature range of the first eutectic (1085°C) followed by a significant shrinkage period during heating through the second eutectic point (1289°C).

By examining the *ex situ* microstructural evolution of post-sintered specimens, German and Dunlap [37] found that the initial swelling during heat-up resulted from pores formed within the Ti particles. This was attributed to alloying during heat-up and unbalance diffusion ($D_{Ti} > D_{Fe}$). Thus, outward Ti diffusion into the Fe particle matrix and away from the Ti particles leaves behind large pores within the Ti particles. Layers of FeTi and Fe_2Ti were also observed to form surrounding the Ti particles. The formation of the first eutectic liquid at 1085°C was evidenced by rounding of the interior Ti pores. Capillary spreading of this liquid was inhibited from consolidating the mixture by the surrounding intermetallic envelope layers. Metallographic data showed that once the samples reach the second eutectic temperature (1289°C) the formation of additional liquid successfully penetrates Fe grain boundaries, intermetallic layers, and interparticle pores – causing re-arrangement and consolidating the sample and causing shrinkage. German and Dunlap's findings indicated that the TLPS process has a considerable sensitivity to the following process variables [37]:

Heating rate and Ti content: Densification was found to increase with increasing Ti contents and heating rates. This is attributed to the fact that greater Ti contents appeared to form greater amounts of liquid. Also, higher heating rates diminished the effects of interdiffusion and intermetallic formation during heat-up, which should decrease the amount of liquid available for melting once the eutectic temperature was reached. Liquid fractions were not reported.

Particle size: It was found that homogenization of the compacts was more rapid with finer particles sizes. This is likely due to increasing surface/volume ratios and decreasing

diffusion depths for finer powders. Also, the shrinkage rate near 1289°C and net densification was higher for finer Fe powders. A discussion of these effects was not presented. However, other studies have also shown that finer particles result in suppressed liquid formations due to excessive interdiffusion during solid-state heat-up [26].

Temperature and hold time: Ex situ hardness and density measurements were taken for specimens TLP sintered at three different temperatures for increasing hold segments durations. Specimens held below the second eutectic temperature (1275°C) for 15-240 minutes showed that negligible density increases occurred due to insufficient or ineffective liquid formations. Sintering at 1300°C showed that 12% densification occurred after 15 minutes and this increased to 27% after 240 minutes. As a result, hardness was found to increase accordingly from 29 to 45HRB as a result of densification. Sintering at 1350°C gave the highest densities and hardnesses at 15 minutes (17%, and 40HRB) and 240 minutes (57%, 56HRB). The improved densities and mechanical properties obtained at higher T_P are likely due to the increased consolidation from greater degrees of melting and liquid formation. German and Dunlap go on to suggest that the amount of liquid formed is determined by the amount of Ti and the heating rate used, and this determines the liquid's duration.

Baek and German [38] conducted a similar dilatometric TLPS study with Fe and Fe_2Ti powder compacts. A pre-alloyed Fe_2Ti powder was used in this case to avoid the low-temperature swelling associated to the first Ti-rich eutectic liquid and pure Ti pore formation. In this study, it was reported that the degree of densification depends critically on the amount of liquid and its duration, as determined by several processing parameters: T_P, sintering time, particle size, heating rate, and the amount of additive (Fe_2Ti powder). These experiments found similar trends to those found by German and Dunlap. Interestingly, both studies indicate that there must be an optimal amount of liquid for peak densification since excessively high additive contents and heating rates resulted in decreasing densities after an observed maximum from dilatometry results. They propose that high heating rates or excessive Ti contents can cause excessive liquid formations that leave behind large pores (at previous Ti sites) and spread away from the previous additive powder locations. These dilatometric results and corresponding metallographic data indicated that the formation of liquid and its duration have a significant effect on sintered properties. However, the amount and duration of the liquid

is not quantitatively investigated or correlated to density and hardness measurements in these studies.

Lumley and Schaffer [26] conducted a more recent study on particle size effects and base/additive solubilities by conducting LPS experiments using three separate alloy systems. Pure Al powder and three different pure additive powders were used to give the following bulk compact compositions: Al-5wt%Sn, Al-10wt%Zn, and Al-5.5wt%Cu. All samples were mixed, pressed, and then heated to ~600°C in a high purity N_2 atmosphere at different heating rates and durations to cause the formation of a liquid phase having some transient characteristics. Quantitative image analysis was used to identify the area fraction of liquid found within polished and etched cross-sections to approximate the liquid fraction present in the post-sintered microstructures. The details of the area fraction measurements, such as liquid phase and interface identification were not presented. Also, the complication of intermediate phase formations (such as ZnAl or $CuAl_2$) is not discussed relative to area fraction measurements. In any case, this study provides one of the few attempts at quantifying liquid formation and removal in TLPS.

The Al-Sn system was chosen as an ideal persistent liquid system where the amount of liquid formed appeared to be independent of additive particle size. This is due to the fact that that there is very limited solid solubility for Al in Sn or Sn in Al and unlimited liquid solubility. As such, solid-state interdiffusion during heat-up at different heating rates had negligible effects on the liquid formation. Once the melting point of Sn was surpassed, the amount of liquid increases gradually. This is due to the high solubility of the base (Al) in the Sn melt, which causes Al particle dissolution. Once the peak temperature is reached, the amount of liquid moderately decreases with hold time. This likely occurs by some Sn diffusion in Al, but since Sn solubility is negligible in Al (1.2wt% Sn), a significant liquid phase persists.

Conversely for the next alloy system, Al has a high maximum solid solubility for Zn (~83wt% Zn) in the Al-Zn system. When fine additive Zn powders were used, the small initial liquid fraction formed (W_{Ao} = 0.03 at 525°C) was rapidly removed during heat-up to 580°C within 13 minutes after surpassing the Zn melting point (i.e., before reaching the isothermal processing temperature T_P = 620°C). The liquid was reportedly removed by absorption into

(Al) solid-solution, but compositional data was not reported for the Al particles. The final structure appeared unsintered and was very porous with limited connectivity due to small liquid formations – thereby complicating liquid area fraction measurement. When coarse Zn powder was used, significantly increased liquid fractions were measured (up to $W_A = 0.07$) and this was gradually removed at 620°C within 30 minutes (approximately three times longer than with fine Zn particles). The post-sintered macrostructures appeared denser and contained connected liquid networks. Similar metallographic results were obtained for the Al-Cu system, but quantitative results were not reported in this case. However, less than expected liquid formations were observed. It was suggested that this may be due to a diffusivity effect additional to the solubility effects above. Since the diffusivity of the additive in the base is higher than the reverse ($D_{Cu} > D_{Al}$), it is suggested that this may remove some pure Cu available for incipient liquid formation. However, the Cu melting point (1085°C) is much higher than that of Al (660°C), and the liquid phase likely forming in these experiments is a (Al)-$CuAl_2$ eutectic above 548°C. The formation of $CuAl_2$ as well as many other intermediate Al-Cu phases and their effect on the liquid fraction formed is not discussed. It is believed that the formation of such intermetallics may account for some liquid suppression.

Lumley and Schaffer [26] suggested that the low liquid fraction formed with finer additive powders in the Al-Zn system is due to increased interdiffusion (which causes homogenization and liquid suppression) during heat-up due to increased additive/base particle contact. Conversely, the use of coarse additive powders increases the amount of liquid formed and prolongs its existence. This occurs in systems having transient liquid aspects and appreciable solid-solubility of the additive constituent in the base metal. Low heating rates (1 vs. 40°C/min) were also found to decrease the amount of liquid formed due to increased solid-state interdiffusion prior to melt formation. At 1°C/min heat-up rates, TLPS was not possible in Al-Zn compacts since the liquid phase was completely suppressed – leaving a porous unsintered microstructure.

2.7. Ni-Cu Sintering Studies

The effects of unequal diffusive flux in base/additive couples have already been briefly discussed thus far. Smigelskas and Kirkendall [43] first investigated this phenomenon in the

Cu-Zn system and it was soon termed the Kirkendall effect. In this early study, a diffusion couple was created between pure Cu and brass (a Cu-30wt%Zn alloy). Since $D_{Zn} > D_{Cu}$, it was found that the brass plate thickness had decreased during high-temperature annealing due to the unbalanced Zn diffusion out of the brass alloy plate and into the previously pure Cu regions. Since this early investigation, many other studies have found that that such unbalanced diffusivities can also induce porosity and swelling in the high-diffusivity species since the rapidly diffusing atoms are not being replaced at an equal rate. The resultant mass-flux imbalance causes void formation and porosity near phase boundaries and high interdiffusion areas where concentration gradients are high. Such voids are commonly referred to as Kirkendall-type pores and are known to occur in the Ni-Cu system since $D_{Cu} > D_{Ni}$. In general it is found that materials with the lower melting point have higher relative diffusivities [31]. Solid-state sintering studies of Ni and Cu powders by Brand and Schatt [39] found that the unbalanced Cu diffusion stream caused porosity formation in the previous Cu particles and expansion of the Ni particles.

Fischer and Rudman [44] also conducted solid-state sintering studies of mixed pure Ni and pure Cu compacts where Kirkendall porosity was observed during isothermal heating at 750,850 and 950°C. Shrinkage, or densification, was observed after sintering for short hold times, which was attributed to the typical surface energy based sintering mechanisms exhibited by either pure element. However, after some time it was found that expansion occurred at all sintering temperatures and this resulted in a net expansion after long hold times. This was attributed to a developing Kirkendall pore structure with increasing interdiffusion and homogenization at longer hold times, which eventually dominated the shrinkage mechanism. Therefore, Fischer and Rudman suggested that the densification process in Ni-Cu solid-state sintering consists of two overlapping mechanisms: 1) surface energy dominated shrinkage as in pure powders - causing neck growth, pore rounding and filling; 2) expansion due to Kirkendall effect porosity formation. They also considered that the unbalanced Cu flux away from the Cu powder (caused by unequal diffusivities) can be considered as a net vacancy flux towards the Cu particles. Therefore vacancy accumulation and deposition as voids explained the formation of very stable intra-granular pores that are not removed even after prolonged sintering. Diffusive interactions like these complicate the sintering process and as a result, reliable knowledge about sintering of interacting powders such as Ni and Cu is still quite incomplete

relative to single-phase systems [4,33]. Sintering of interacting powders is even more complex in the presence of a liquid phase, particularly when the liquid is transient as in TLPS. It is expected that prolonged Ni-Cu TLPS experiments should also develop a Kirkendall pore structure.

Puckert *et al* have investigated the TLP sintering behaviour of Ni-Cu powders at T_P = 1260-1380°C in a reducing atmosphere [5,45]. Large Cu-coated Ni spheres (260μm in diameter) were specifically prepared for these experiments using a thermal vapour deposition process. Although not commercially available, this geometry provides an ideal concentric sphere model for uniform Cu coverage and particle distribution. The Cu layer thickness was varied (1.1-7.8 μm) to give relatively low solute contents ranging from C_O = 2.95-16.75 wt% Cu. Densification and pore formation were investigated by metallographic and dilatometric techniques [45], and liquid formation was investigated via metallography and diffusion profile calculations [5].

By measuring particle movement and morphological changes (via microscopy) at different times during isothermal sintering of planar single-layer arrays of contacting Ni-Cu spheres, Puckert *et al* found that heating rates of >30°C/min were necessary to form a liquid phase with the Ni core size and Cu layer thickness ranges studies [45]. Upon heating to 1260°C at 75°C/min., they reported that a liquid phase formed at the previous Cu layers, which formed liquid bridges at the previous interparticle necks. This rapidly caused particle rearrangement and densification within a few seconds [45]. This rapid densification was evidenced by dimensional shrinkage measurements of 6-8% at very short hold times immediately following melting. The liquation of the thin Cu layers rapidly filled inter-particle pores by capillary action and caused shrinkage by pulling adjacent Ni particles together. In doing so, this sometimes formed denser particle clusters that then became separated and created gaps or large pores between the clusters, which prevented complete densification. Although the liquid did abruptly increase density, the samples still appeared quite porous due to the low Cu contents used and these unfilled interparticle regions. Porous macrostructures are not suitable for PM parts or filler metal applications. Since relatively low Cu contents were investigated, it is believed that higher Cu contents could form more liquid and enhance

densification by filling more of there interparticle areas. However, the fraction of liquid formed was not quantitatively reported or correlated to the initial shrinkage measurements.

As in Fischer and Rudman's work [44], samples were found to begin slowly expanding/swelling with increasing hold time after ~10 minutes following the rapid initial densification/shrinkage stage attributed to liquid formation and spreading [45]. However, in this case, a moderate net shrinkage (~2%) was still found at completion (240min.) likely due to the presence of the density enhancing liquid phase in TLPS vs. SSS. They suppose that this expansion regime begins once the liquid is diffusionally removed. At this point they state that the isothermally solidified neck regions are still Cu-rich [45]. Increased hold times caused further solid-state interdiffusion to remove compositional gradients. This was found to cause swelling/expansion with increasing time due to the formation of particularly small pores in the interparticle neck regions. Again, this was attributed to the Kirkendall effect arising from a diffusive mass-flux imbalance in the neck regions, which are high interdiffusion areas due to the concentration gradients present.

By calculating the Cu and Ni mass flux rates in the neck area, Puckert *et al* [45], were able to determine an experimental measure of vacancy accumulations in this region. It was found that, indeed, these pores are likely diffusion-induced via a Kirkendall effect due to excess vacancy accumulations, causing voids which condense in the form of pores. Kirkendall pores are usually generated in high interdiffusion areas such as the neck/interface [45], where concentration gradients and therefore mass transfer rates are greatest in accordance with Fick's first law. Other studies have also shown that these Kirkendall-type pores will tend to nucleate and grow within the Cu-rich side of the interdiffusion region via excess vacancy accumulations from the imbalanced Cu diffusion stream [39,44, 46].

In another Ni-Cu TLPS study by Puckert *et al* [5], the effects of heating rate and higher processing temperature were investigated for similar monolayer arrays of Cu-coated Ni spheres. Sintering for varying durations took place in a N_2 atmosphere using heating rates of 1-100°C/min and T_P = 1260°C and 1380°C. Optical macrographs of the evolving particle array morphology showed that sintering at higher T_P resulted in greater particle rearrangement, pore filling, and densification. The melt bridges found at previous necks caused local contact flattening visible at the solid/liquid interface and the approach of the solid Ni particle centers.

This was attributed to increased liquid fractions as a result of Ni dissolution into the melt at higher temperatures [5]. Due to the low Cu contents used however (16.8wt% Cu), the amount of liquid formed was still not sufficient to remove many large pores.

Heating rates of 1°C/min. were found to generate no liquid phase, which was attributed to extensive solid-state interdiffusion during heat-up. Heating rates of 15°C/min were found to generate some visible liquid (evidenced by pore and neck/bridge rounding as well as increased rearrangement and density) in samples containing at least 16.8wt% Cu. Even higher heating rates (up to 75°C/min) were generally found to increase the observed amount of liquid. This was attributed to the diminishing effect of solid-state interdiffusion during shorter heat-up segments with faster heating rates.

Optical micrographs revealed residual pores within the large Ni cores (from the starting spheres). Compositional analysis showed that one such pore contained a significant amount of Cu-rich material (~50wt% Cu). It was proposed that this partial pore filling occurred via grain-boundary infiltration by the Cu melt and penetration deeply into the Ni sphere [5]. However, the large size of this pore (~20μm) and the lack of results for other occurrences of internal pore-filling or grain boundary penetration raises some questions. It is possible that this pore was partially filled by polishing debris during the preparation of the metallographic specimens.

Chemical analysis of concentration gradients in the neck region between connected particles was undertaken for one sample to better understand TLP sintering behaviour in regards to the evolving solute distribution. Electron probe x-ray micro-analyser (EPMA) measurements made within a sample sintered at 1320°C for a short period (5 min.) showed that the neck, or liquid bridge, region no longer consists of pure Cu after melting – as might be expected from the equilibrium liquidus. They found that the concentration profile contained three regions within the bridge/neck area separating the two Ni particles: 1) a central area that is mostly Cu-rich and has compositions approximating the liquidus at 1320°C; 2) a 'greater neck area' on either side of the central area, which has compositions near the solidus; and 3) the initial Ni particles that are still fairly pure. The greater neck area likely corresponds to the diffusionally solidifying phase at T_P; however, direct experimental evidence for liquid removal via isothermal solidification is not presented. After 120 minutes at 1320°C, the sample appeared completely homogenized since composition was uniform at 16.8wt% Cu. Therefore,

at some point during this hold segment the liquid must have been removed by diffusional processes. Unfortunately, metallographic and dilatometric results could not elucidate the transient character of the liquid phase.

2.8. Modelling of TLPS

Analytical and numerical models have been developed to predict interdiffusion during the different stages of the sintering process. These models are important because they develop an understanding of the influence that important process variables have on TLPS. In this study, modelling of the isothermal solidification stage (as well as the influences of solid-state interdiffusion and dissolution) is emphasized since it is of primary interest.

2.8.1. Mathematics of Binary Diffusion

Since the solidification of the liquid phase in TLPS is diffusion-controlled, understanding the mathematical relationships of diffusion is important for modelling the different stages. Fick recognized that mass transfer via diffusion could be quantified by Fourier's equation for heat conduction since both processes were based on the mechanism of random molecular motion [31]. The derivation of Fick's equation for solute diffusion through an element volume can be better understood with reference to Figure 2-11, which illustrates a volume element at point *P* within a planar sheet having some compositional gradient *C(x)* in the *x* direction. This figure also shows the unit volume having the dimensions *2dx, 2dy, 2dz* and a mass flux (*J*) diffusing through it.

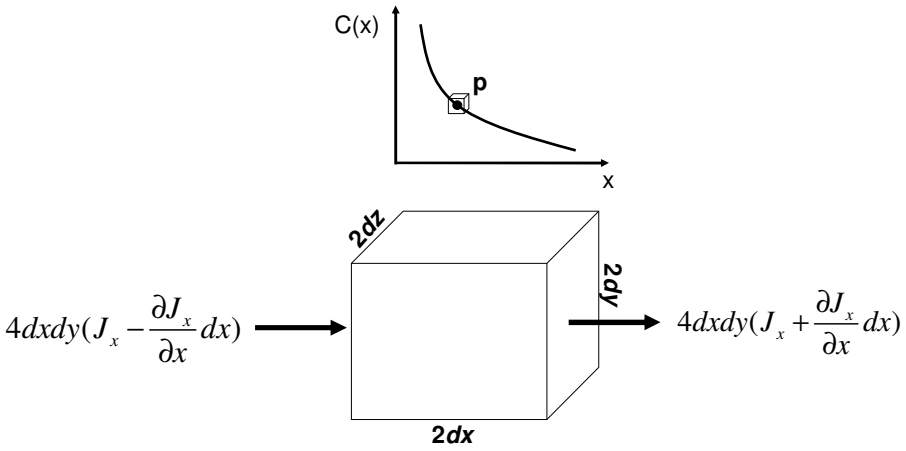

Figure 2-11: Element volume with compositional gradient *C(x)* and mass-flux imbalance.

The solute concentration at the centre of the element (point *P*) is given by *C(x,y,z,t)*. *J* gives the mass flux per unit area that is diffusing normal to a plane in the volume. This flux is proportional to the solute concentration gradient normal to the section. Fick's first law gives the mass flux of the diffusing solute in the *x* direction:

$$J_x = -D\frac{\partial C}{\partial x} \tag{2-6}$$

This expression shows how mass flux is proportional to compositional gradients and diffusivity, which is a temperature dependent parameter. The rate of solute entering the volume in the *x*-direction is given by:

$$4dydz(J_x - \frac{\partial J_x}{\partial x}dx) \tag{2-7}$$

and the rate of solute leaving the volume is given by:

$$4dydz(J_x + \frac{\partial J_x}{\partial x}dx) \tag{2-8}$$

The imbalance of these two flux terms generates a net flux of solute into the element, which is equal to:

$$-8dydz(\frac{\partial J_x}{\partial x}dx) \tag{2-9}$$

The contributions from the other directions can be similarly obtained, which will cause an accumulation, or decrease, of solute within the element. The rate of solute content increase in the element is given by:

$$8dxdydz(\frac{\partial C}{\partial t}) \tag{2-10}$$

Where *C* is the concentration of solute per unit volume at *P*. If each of the above terms is summed for all directions, we immediately have:

$$-\left(\frac{\partial J_x}{\partial x} + \frac{\partial J_y}{\partial y} + \frac{\partial J_z}{\partial z}\right) = \frac{\partial C}{\partial t}$$
$$\text{or,} \quad \frac{\partial C}{\partial t} = -\nabla \cdot J \tag{2-11}$$

If the diffusion coefficient is assumed to be constant (i.e., diffusivity is not concentration dependent) and J_x, J_y, J_z are given by Fick's first law, Equation (2-11) becomes:

$$\frac{\partial C}{\partial t} = D\left(\frac{\partial^2 C}{\partial x^2} + \frac{\partial^2 C}{\partial y^2} + \frac{\partial^2 C}{\partial z^2}\right) \quad \textbf{(2-12)}$$

For a one-dimensional system this reduces to:

$$\frac{\partial C}{\partial t} = D\left(\frac{\partial^2 C}{\partial x^2}\right) \quad \textbf{(2-13)}$$

and in spherical coordinates, $\frac{\partial C}{\partial t} = D\left(\frac{\partial^2 C}{\partial r^2} + \frac{2}{r}\cdot\frac{\partial C}{\partial r}\right)$

This equation is a simplified form of Fick's second law of diffusion using average diffusivity. Equations (2-6) and (2-13) serve as the foundation for modelling of mass transfer in diffusion-controlled processes such as TLPS. These differential equations can be solved analytically or numerically to give solute concentration profiles and rates of solute uptake for different geometries and boundary conditions.

2.8.2. Analytical Solution for Spherical Particles

Closed analytical solutions to Fick's second law have been developed by Crank [47] for spherical particles of radius *a* (Figure 2-12). In this case, solute atoms from the surrounding additive phase (A) diffuse across the solid-liquid interface (represented by the dashed circle) and into the base metal particle (B).

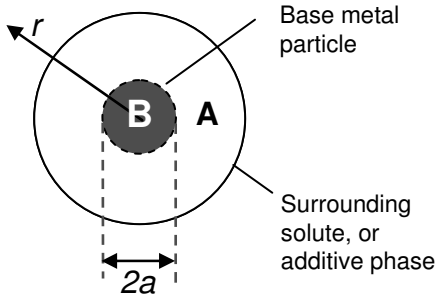

Figure 2-12: Base metal particle (B) surrounded by additive phase (A).

In order to simplify the solution of Equation (2-13*b,* this partial differential equation can be reduced by the following transformation:

$$U(r) = C(r)r \tag{2-14}$$

Equation (2-13) then becomes:

$$\frac{\partial U}{\partial t} = D\left(\frac{\partial^2 U}{\partial r^2}\right) \tag{2-15}$$

which is a simpler differential equation. The boundary and initial conditions used by Crank are shown below.

$U = aC_S$,	$C = C_S$,	$r = a$,	$t > 0$	**(2-16)**
$U = 0$,	C,	$r = 0$,	$t > 0$	**(2-17)**
$U = 0$,	$C = 0$,	$0 < r < a$,	$t = 0$	**(2-18)**

Where $2a$ is the average particle diameter as defined in Figure 2-12, r is the radial distance from the particle center, and t is the isothermal hold time.

These conditions are relevant to TLPS during isothermal solidification. In Equation (2-16), a constant composition is assumed at the particle surface (i.e., C_S at radial position $r = a$). This boundary condition applies local equilibrium conditions at the solid/liquid interface (as predicted by the solidus and liquidus compositions in the relevant phase diagram) and is valid as long as liquid is present. The boundary condition at $r = 0$ given in Equation (2-17) assumes no mass flux across the center of the particle, which is valid for symmetric particles and compositional profiles with $\partial C/\partial r = 0$ at $r = 0$. The initial condition given in Equation (2-18) assumes that a dilute B particle exists at $t = 0$. This is valid for cases when no significant solute diffusion has yet taken place.

Crank's solution for the compositional profile within the B particle under these conditions is provided below.

$$\frac{C(r,t)}{C_s} = 1 + \frac{2a}{\pi r}\sum_{n=1}^{\infty}\frac{(-1)^n}{n}\sin\left(\frac{n\pi r}{a}\right)e^{-Dn^2\pi^2 t/a^2} \tag{2-19}$$

Where r, a, and t are as defined above, D is the relevant diffusion coefficient, $C(r,t)$ is the solute concentration as a function of time and position, and C_S is the fixed surface composition at the interface. However, the concentration profile within the particle is not immediately of interest. Rather, the total amount of solute that has entered the sphere at a given time (M_t) is of

interest for quantifying the amount of liquid (A) remaining in TLPS. The solute uptake at a given time t can be found by:

$$M_t = \int_{t=0}^{t} J_r dt \qquad \textbf{(2-20)}$$

Substituting Equation (2-6), $$M_t = -\int_{t=0}^{t} D\frac{\partial C}{\partial r} dt \qquad \textbf{(2-21)}$$

Similarly, the quantity of solute diffused at $t = \infty$ is given by:

$$M_\infty = -\int_{t=0}^{t=\infty} D\frac{\partial C}{\partial r} dr \qquad \textbf{(2-22)}$$

Crank has shown that substitution of Equation (2-19) allows the determination of fractional solute uptake by the B particles (defined as M_t/M_∞, hereafter referred to as M_t/M_f).

$$\frac{M_t}{M_f} = 1 - \frac{6}{\pi^2}\sum_{n=1}^{\infty}(-1)^n e^{-Dn^2\pi^2 t/a^2} \qquad \textbf{(2-23)}$$

Some of the key assumptions of this solution include:

1. D is constant and independent of solute concentration (i.e., the dilute alloy assumption).
2. The particle's boundary concentration is constant at C_S - Equation (2-16).
3. No solute diffuses through the centre of the particles - Equation (2-17).
4. The particle boundary, or interface, is fixed since the location of the interface is held constant at $r = a$ by Equation (2-16).
5. There is initially no solute in the particle at $t = 0$, Equation (2-18).

The implications of these assumptions, particularly 4 and 5, on the modelling of isothermal solidification kinetics will be further discussed in Sections 2.8.3 and 6.

2.8.3. Simplified TLPS Isothermal Solidification Model

Corbin has developed a stepwise analytical model for the rate of liquid removal during isothermal solidification for binary-eutectic TLPS systems [25]. This diffusion-based model employs Crank's solute uptake equations and shows good agreement with experimental DSC results for the Pb-Sn system [11,13,28].

In Corbin's model [25], the low melting point additive powder is an A-B eutectic alloy. This powder is considered as constituent A and has a eutectic composition given by C_E. The melting point of the additive powder is given by the alloy system's eutectic temperature (i.e., $T_A = T_E$). The high melting point base metal powder (considered to be constituent B) is assumed to have a solute content of 0 wt% A prior to heating. The TLPS system is then defined as the homogeneous mixture of A and B powders having the desired bulk solute content (C_O). It is important to note that a different notation is adopted in Corbin's model. Compositions are represented by X rather than C as in this study (e.g., X_O is equivalent to C_O).

The initial weight fraction of liquid that forms (defined as W_{Ao}) at the processing temperature (T_P) is assumed to spread uniformly through the powder mixture to instantaneously produce an array of base metal particles coated with a liquid layer of uniform thickness. The kinetics of isothermal solidification was analyzed with the aid of Figure 2-13, which illustrates a representative unit cell for isothermal solidification.

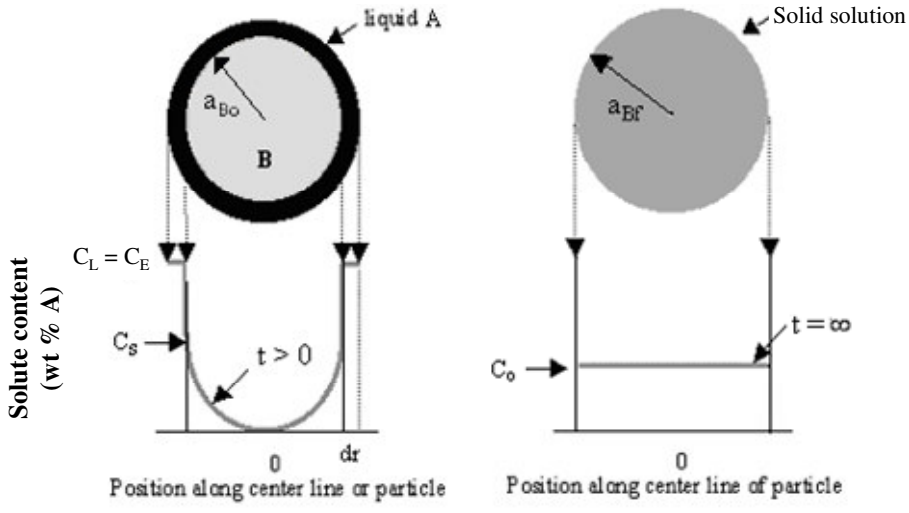

a) $0 < t < \infty$ b) $t = \infty$

Figure 2-13: Unit cell for Corbin's isothermal solidification model showing the solute distribution: a) after a short time *t* after melting, b) after a long hold time where the only a homogeneous solid-solution exists, which has a uniform composition C_O [adapted from 25].

Since solid-state sintering and interdiffusion are ignored during heat-up, the initial solute content in the particle, $C(r,0)$, is zero and the particle radius is a_{Bo} at the onset of melting (t = 0). Upon melting, local equilibrium is assumed to exist at the interface. The liquid side of the interface has a composition of C_L and the solid side of the interface is at C_S, which corresponds to the maximum solubility of solute within the solid-solution particle (given by the solidus line). Since the eutectic temperature (T_E) is taken as the process temperature, the liquid has a eutectic composition (i.e., $C_L = C_E$). It was assumed that rapid diffusion in the liquid causes this phase to obtain a uniform composition. In cases where $T_P > T_E$, some dissolution of the base metal particles is required to obtain a composition of C_L, which will cause a reduction in the size of the solid particle diameter. However, Corbin's model does not take dissolution into account since isothermal predictions were at $T_P = T_A = T_E$ [25]. As the mixture is held at the processing temperature, solute diffusion through the interface creates a compositional profile in the particle as shown in Figure 2-13*a*. At short times, a steep compositional profile exists at the surface of the particle and no solute has diffused through to the centre. As time increases, the liquid remains at C_L, yet diffusion of solute atoms through the interface causes an increase in total solute content within the particle and the profile within the particle becomes flatter. The solute mass flux imbalance at the interface causes gradual B particle growth and a reduction in the liquid weight fraction W_A (i.e., isothermal solidification). Eventually, no liquid phase remains and the B particle begins to undergo homogenization until all compositional gradients are removed and a uniform composition C_O is obtained.

The mass balance of solute content in the solid and liquid phases at a time t is given by:

$$C_O = C_A W_A + C_B W_B \qquad \textbf{(2-24)}$$

where $C_A W_A$ and $C_B W_B$ are the solute contents of the liquid phase and solid base metal particle respectively, W_A and W_B are the weight fraction of each phase in the mixture, and C_A and C_B are the average solute composition of each phase in wt% A. After melting, the compositon of the additive phase C_A can be approximated as the liquid composition C_E according to the assumption stated above. Rearrangement of Equation (2-24) then gives:

$$W_A = (C_O - C_B W_B) / C_E \qquad \textbf{(2-25)}$$

The eutectic solder systems studied by Corbin exhibited negligible solid-state interdiffusion during heating [11,13,25]. Thus, from Equation (2-25), an expression for the initial liquid fraction formed at $t = 0$ (W_{Ao}) can be obtained since $C_B \approx 0$ prior to melting (i.e., no solute within B particles).

$$W_{Ao} = C_O / C_E \tag{2-26}$$

Substituting Equation (2-26) into Equation (2-25) gives Corbin's simplified governing equation for isothermal solidification. This expression is used to predict the weight fraction of liquid, which is normalized by W_{Ao}.

$$W_A / W_{Ao} = (C_O - C_B W_B) / C_O \tag{2-27}$$

From Equation (2-27), the normalized liquid fraction remaining after a given isothermal hold time t at T_E can be determined by knowledge of the solute content absorbed in the solid base metal particles ($C_B W_B$), provided that the bulk composition C_O and liquid composition C_L are specified. Crank's expression for fractional solute uptake by a sphere (Equation (2-23)) can be used to obtain $C_B W_B$ by the following relationship:

$$M_t / M_f = C_B W_B / C_{Bf} W_{Bf} \tag{2-28}$$

where C_{Bf} is the average composition of phase B at $t = \infty$, W_{Bf} is the weight fraction of phase B at $t = \infty$, and $C_{Bf} W_{Bf}$ is the solute content of phase B at $t = \infty$. In the Crank solution, $t = \infty$ corresponds to the time where the spherical particle is completely saturated with solute and has a uniform composition equal to the surface boundary condition (i.e., $C_{Bf} = C_S$) [47]. In a TLPS problem, the Crank solution is truncated at a time $t < \infty$, and thus only a portion of the M_t/M_f solution is used until the point where no liquid remains ($W_{Af} = 0$, *or* $W_{Bf} = 1$). The Crank solution for M_t/M_f is applicable to TLPS problems because solute uptake by the base metal, which has a fixed boundary condition at C_S, will continue until the liquid phase is completely removed. This will result in incomplete saturation of the particles and thus only part of the solution will be utilized (i.e., up to a time $t < \infty$). Only when $C_O = C_S$ will the full solution for M_t/M_f be used for the isothermal solidification solution. The implications and limitations of the Crank solution with respect to this problem are discussed below and in Section 6. Rearrangement of Equation (2-28) and substitution of these values gives:

$$C_B W_B = (M_t / M_f) C_S \tag{2-29}$$

Finally, substituting this expression into Equation (2-27) gives:

$$W_A / W_{Ao} = \left[C_O - (M_t / M_f) C_S \right] / C_O$$
$$\text{or, } W_A / W_{Ao} = \left[1 - (M_t / M_f) \frac{C_S}{C_O} \right] \tag{2-30}$$

Equation (2-30) can be use to calculate the normalized liquid fraction due to solute uptake, which is a function of *t, a_B, T,* and *D*. This approach is only valid for C_O values less than or equal to C_S, otherwise a persistent liquid will result. Unlike the full Crank solution, incomplete saturation occurs at the end of the process (unless $C_O = C_S$). This is due to the insertion of the M_t/M_f term into the mass balance equation at T_p. Also, this approach can only be used to model diffusion processes once the liquid phase is present (i.e., *t = 0* at the onset of melting) and the boundary condition at C_S is valid.

As predicted by mass conservation arguments and as shown in Figure 2-13, liquid absorption is accompanied by a gradual particle growth. However, the Crank solution is based on a stationary liquid/sold interface, and therefore a fixed base metal particle size. The effect of particle size has been shown to have a significant impact on the rate of liquid absorption [2, 11, 26,]. For a given bulk mixture composition, larger base metal particles offer less total surface area available for interdiffusion, and thus longer solidification times are required. Therefore, the solution of this model for a specific TLPS system must incorporate base metal particle growth. Thus, the solution of Equation (2-30) must be iterative because the *a* term in the M_t/M_f calculation must be updated at *t* increments as isothermal solidification takes place.

Particle growth was accounted for by first relating liquid weight fractions to liquid volume fractions by $V_A = W_A/\rho_A$ as follows:

$$V_A / V_{Ao} = \frac{W_A / \rho_A}{W_{Ao} / \rho_{Ao}} \tag{2-31}$$

Where V_{Ao} and W_{Ao} are the initial liquid volume and weight fractions respectively and ρ is density. Similarly, the solid B phase volume fraction is give by:

$$V_B / V_{Bo} = \frac{W_B / \rho_B}{W_{Bo} / \rho_{Bo}} \tag{2-32}$$

Where V_{Bo} and W_{Bo} are the initial base metal volume and weight fractions respectively. But, for each successive time step, they represent values from the previous step. It was assumed that solute diffusion doesn't change the density of the solid particles. Equation (2-32) then becomes:

$$V_B/V_{Bo} = W_B/W_{Bo} \tag{2-33}$$

Conveniently, Cu and Ni have very similar atomic radii and densities (8.93 and 8.902 g/cm^3 respectively) [1]. Therefore, alloying does not significantly change the density of the growing solid phase and this assumption is reasonable. From Equation (2-33), the B particle size after some liquid absorption is:

$$a_B = a_{Bo}(W_B/W_{Bo})^{\frac{1}{3}}$$
$$\text{or, } a_B = a_{Bo}\left[(1-W_A)/(1-W_{Ao})\right]^{\frac{1}{3}} \tag{2-34}$$

where W_A is be determined by Equation (2-30).

To summarize, the rate of isothermal solidification in this TLPS model is a function of t, C_O, W_{Ao}, a_{Bo} and T_P (which determines C_S and D). The gradual decrease in liquid fraction (normalized as W_A/W_{Ao}) can be predicted starting at the isothermal process temperature T_P, which is restricted to T_E. In the absence of solid-state interdiffusion effects during heat-up, the initial liquid fraction W_{Ao}, is assumed to be equal to C_O at $t = 0$. Therefore, $W_A/W_{Ao} = 1$ is an assumed initial condition at $t = 0$. The input parameters required for predictions include T_P, D, C_S, C_L, C_O, and the starting B particle size (a_{Bo}).

The liquid fraction present at a given isothermal solidification time, or dimensionless time (Dt/a^2), is calculated via a stepwise procedure where M_t/M_f is first calculated using Equation (2-23). W_A/W_{Ao} is then calculated by Equation (2-59). The particle size a_B is then updated by Equation (2-63) for the next calculation sequence after some incremental increase in time Δt. Figure 2-14 shows a visual representation of the stepwise solution procedure.

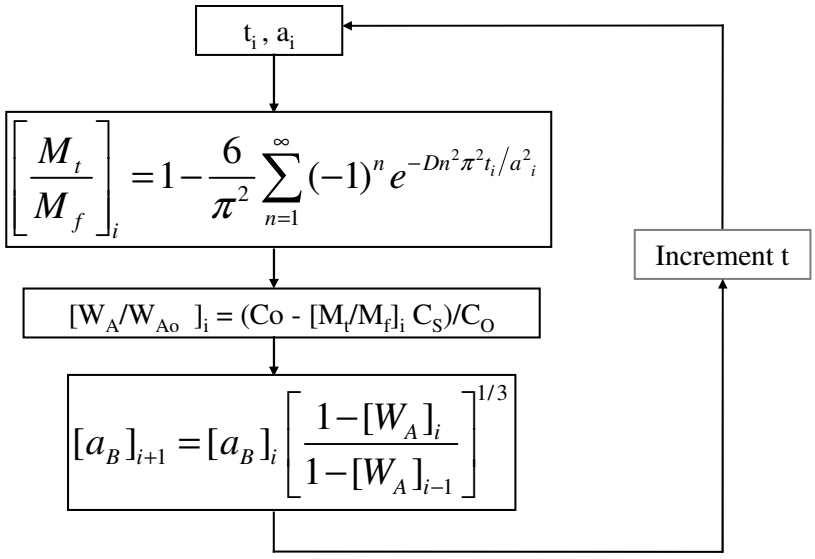

Figure 2-14: Stepwise solution technique for simplified isothermal solidification model

2.8.4. Numerical Modelling

The complex particle and mixture geometries, non-uniform particle size/shape distributions, and possible inhomogeneity in real powder mixtures significantly complicates analytical solutions to Fick's second law Equation (2-13). Thus, analytical solutions, and even most numerical solutions, are often restricted to simplified geometry and boundary conditions in order to reduce the mathematical complexities encountered [48,49]. As such, the concentric sphere-type geometry illustrated in Figure 2-13 serves as the basic unit cell for most sintering models – analytical [25] and numerical [5,48,49].

Larsson and Karlsson [48,49] have developed finite difference models for one-phase and two-phase diffusion problems having concentric sphere geometries that could be suitable for modelling base/additive interdiffusion during the heating stage and the isothermal solidification stage. The merits of such numerical methods are less restricted boundary conditions such as a non-fixed solid/liquid interface, concentration-dependent diffusivity that can be calculated for each element at every time step and the facilitated incorporation of particle size distribution functions. These advantages can be attributed to the relative computational ease of solving Fick's second law directly for *N* elements using a numerical scheme.

Larsson and Karlsson's concentric sphere solid/liquid model consisted of an α particle uniformly surrounded by a β phase (see Figure 2-15), which are equivalent to B and A in the current study. Rapid diffusion is assumed within the liquid for LPS predictions where a liquid phase is present, causing no compositional gradients within this phase [49]. Fixed interface compositions are assumed at the solid/liquid phase boundary (i.e., the α/β interface) due to local equilibrium at the interface. As such, the $C_{\alpha/\beta}$ and $C_{\beta/\alpha}$ boundary concentrations are equivalent to C_S and C_L. Figure 2-15 illustrates these concentrations at the interface and the concentration profiles assumed in Larsson and Karlsson's concentric sphere model.

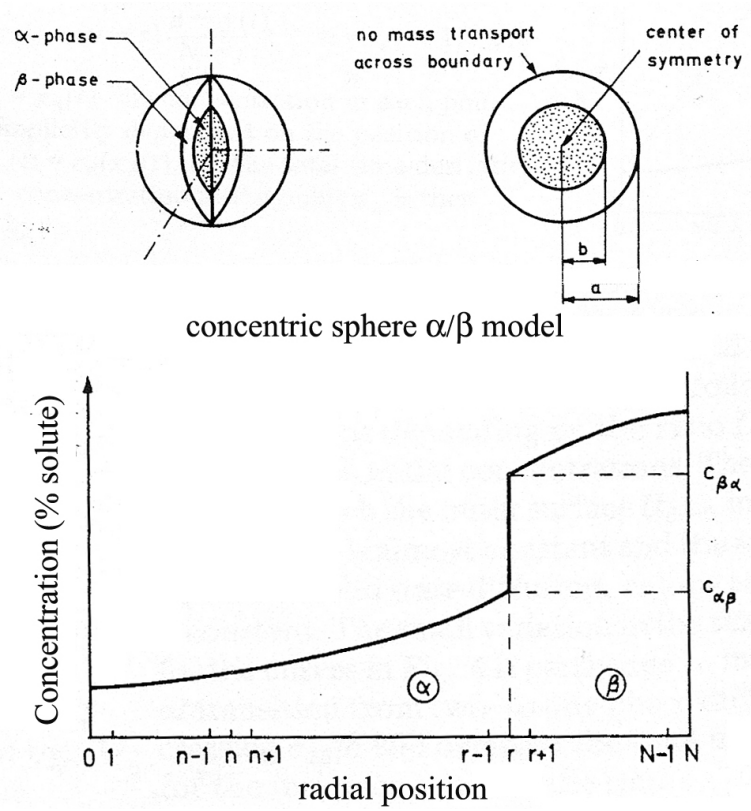

Figure 2-15: Concentric sphere model used by Karllson and Larsson [49] for concentration profile calculations within the α and β phases.

As a first approximation of the melting event, Puckert *et al* [5] developed a'crude' but simple quantitative method for roughly estimating the initial amount of liquid formed at different T_P. This model is based on the experimentally observed liquid bridges formed during TLP sintering of Cu-coated Ni particles (see Section 2.7 for experimental description). This was done to attempt to predict the effects of solid-state interdiffusion on the melt-forming Cu-

shell in order to determine if liquation would occur at all. The melting event of pure Cu at 1085°C and dissolution were not directly predicted. This method is based on a mass balance of Cu that assumes an infinite heat-up rate and therefore negligible solid-state interdiffusion during the heat-up segment. Equation (2-35) simply states that the initial amount of solute should equal the amount of solute within the new liquid at T_P, which has a composition given by C_L

$$C_{shell}W_{shell} = C_L W_L \tag{2-35}$$

Where C_{shell} is the initial compositon of the pure Cu shell (i.e. weight fraction Cu = 1) and W_{shell} is the initial weight fraction of additive (i.e., given by the bulk solute content C_O in wt% Cu). C_L is the liquid compositon (taken as the phase diagram solidus) and W_L is the weight fraction of liquid formed at T_P. Rearrangement gives

$$W_L = \frac{W_{shell}}{C_L} \tag{2-36}$$

This solute mass balance approach is similar to that proposed by Corbin in Equation (2-26) for simplified eutectic systems with negligible solid-state interdiffusion. This expression simply adjusts the initial weight fraction of the pure Cu shell by the diluted composition of the liquid at T_P. As T_P increases, the liquidus composition decreases from C_L = 1 to some lower value as the Ni solubility within the liquid increases. Therefore, the amount of liquid (W_L) must increase to accommodate the increased Ni content. The density of Ni and Cu are very similar and it was assumed that the density of the solid does not change during melting. As such, Equation (2-7) becomes:

$$V_L = \frac{2}{z}\frac{V_{shell}}{C_L} \tag{2-37}$$

Where V_L and V_{shell} are the volume fractions of the liquid bridges formed and the initial pure Cu shell respectively. This expression is in the form reported by Puckert *et al* [5]. A coordination number term (z) is included to account for the number of interparticle liquid bridges formed. For every 2 particles there may be z liquid bridges. Values of z = 2 were used to calculate the initial liquid volumes. The inclusion of this term can potentially void the mass balance upon which this expression is based. For example, if a z value >2 is used (i.e., $z/2$ becomes less than unity), then the volume of liquid formed decreases artificially based on the

arbitrary selection of z. Puckert *et al* [5] found that this method overestimated the initial liquid fractions formed in comparison to experimental liquid bridge volume data. This may be due to solid-state interdiffusion in the samples (which used finite heating rates) and resulted in suppressed liquid formations. However, the method for determining liquid bridge volumes from experimental specimens was not discussed. This type of three-dimensional measurement should be difficult for arrays of liquid phase sintered particles.

In order to better understand liquid formation Puckert *et al* [5] also developed a somewhat more refined finite difference numerical method for solving Fick's second law when applied to the idealized concentric sphere model. The diffusivity of Cu alone was considered for diffusional mass transport and the resultant concentration redistribution process. Predictions consist of solute profiles (in wt% Cu vs. radial position) that have developed during the heat-up segment within the Ni core and Cu shell. The predicted profiles first assume no melting up to some T_P, which is above T_A, and therefore represent a hypothetical solute distribution within the Cu phase, which isn't stable for $T_A < T < T_P$. As such, this method does not directly account for, or predict, the melting event at 1085°C or the subsequent dissolution of Ni above 1085°C. Dissolution by Ni migration into the liquid (due to decreasing solid-solubility C_S) is expected to decrease the Ni particle size and increase the liquid fraction in addition to the that already accounted for by lower C_S intersection of the calculated profile. Furthermore, the low bulk additive contents (C_O) studied resulted in the formation of small liquid fractions in the form of predicted inter-particle liquid bridges. This liquid morphology, which forms at $T_A < T < T_P$, is quite different from the idealized concentric sphere geometry assumed for predictions up to T_P.

However, this numerical method provides an alternative approach for the determination of initial liquid fractions, which is reported to be more accurate than the 'crude' analytical method shown in Equation (2-35). The calculated profiles can be used to determine the locations of the profile that would melt at T_P. In other words, the regions of the predicted profile having solute concentrations $C > C_S$ (i.e., above the intersection with the solidus composition) are expected to melt. Liquid fractions can be estimated by calculating the fraction of the profile length that is expected to melt (i.e., the fractional length of the radial profile where $C > C_S$). Predictions showed that higher heating rates should produce more

liquid since the Cu shell remains more Cu-rich during heat-up. Liquid removal during the isothermal solidification process can not be generated with this model.

In both of these numerical models, the concentric sphere geometry is adopted to approximate the powder system. The initial and boundary conditions assumed are similar to Corbin's model; however, predictions are not directly relevant to this TLPS problem since transient liquid fractions are not predicted, as well as the effects of solid-state interdiffusion during heat-up and dissolution on the melting event itself. However, further development and coupling of Larrson and Karlsson's one-phase [48] and two-phase [49] concentric sphere models could provide numerical solutions for interdiffusion during heating and isothermal solidification for $T_P > T_A$. The ease by which concentration-dependence can be incorporated for each element along concentration profiles is a significant benefit. However, the transition from a one-phase diffusion problem to a two-phase problem after melting would have to be carefully considered (i.e., numerically modelling liquid melting/formation, dissolution, and re-solidification). The numerical models by Puckert *et al* and Larsson and Karlsson will also be referred to in this work, but a numerical scheme will not be developed due to the complexity of the melting event and coupling of the solid-solid and solid-liquid interdiffusion solutions. Since Corbin's analytical model was developed specifically for TLPS problems and showed good agreement with low temperature eutectic powder systems, it will be used as a basis for developing a TLPS model for high temperature binary isomorphous systems.

2.9. Mass Transport Considerations

During sintering, many diffusion mechanisms can contribute to the mass transport process for densification and solute re-distribution, or homogenization. These mechanisms include surface diffusion, volume diffusion (also commonly referred to as lattice diffusion), and grain boundary diffusion. SSS studies with Ni and Cu mixtures by Fischer and Rudman found that, prior to appreciable interdiffusion, Cu envelops Ni particles by surface diffusion during heat-up [44]. This diffusion mechanism is relatively fast due to the less restricted atomic movement across free surfaces. However, this mechanism cannot solely explain bulk sintering behaviour since it is isolated to surface areas. Rather, this diffusion path assists in neck formation and sinter-bonding at the early stages of sintering. As such, most diffusion-

based sintering models do not consider this mechanism to be a significant contributor for long sintering treatments.

During long isothermal sintering treatments, atoms must diffuse through the bulk of the powder particle mass for significant consolidation and interdiffusion to occur. Figure 2-16 illustrates a micrograph of a solid-state sintered Ni-Cu powder mixture that has been etched to reveal the grain structure within Ni particles. Cu diffusion within the Ni particle during sintering can occur by volume diffusion through the lattice of the Ni grains, or via inter-granular boundaries. Grain boundaries offer a less obstructed path for atomic movement relative to the dense lattice since grain boundaries consist of more open, imperfect pathways between adjoining grains, or lattices.

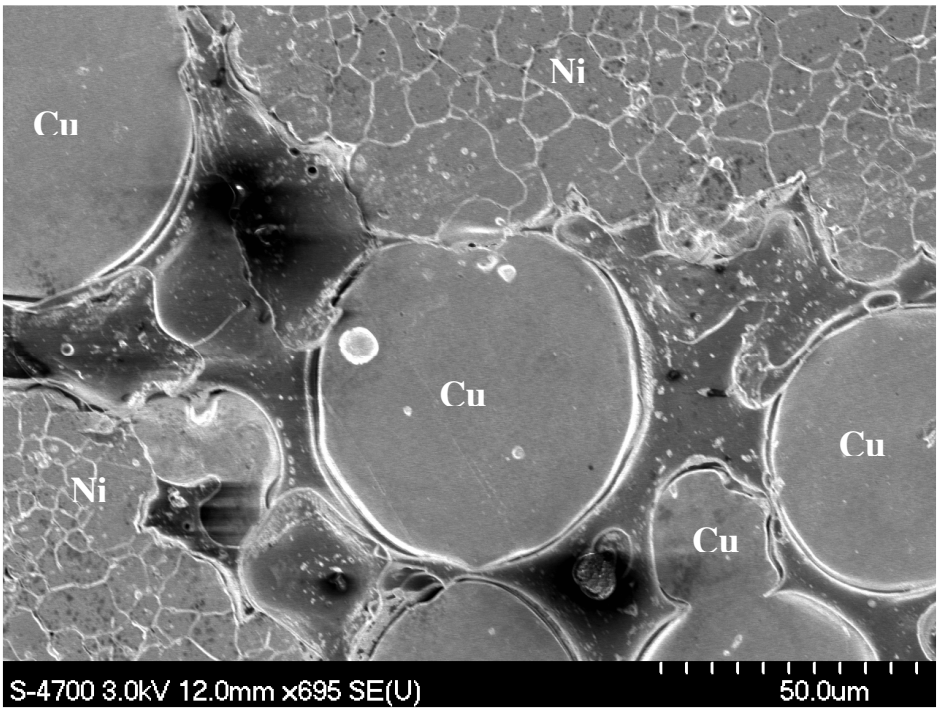

Figure 2-16: Example of the grain structure within Ni powder particles that have been solid-state sintered with Cu particles.

Diffusivities for all three mechanisms can be expressed by the Arrhenius-type relation shown in Equation (2-4) such that pre-exponential factors ($D_{O,s}$, $D_{O,b}$, $D_{O,l}$) and activation energies (Q_s, Q_b, Q_l) can be used to calculated surface, boundary, and lattice diffusivities (D_s, D_b, D_l).

$$D = D_O e^{\frac{-Q}{RT}} \tag{2-38}$$

For solute atoms to diffuse through a lattice of solvent atoms, closely-bound adjacent solvent lattice atoms must be displaced. This imposes a larger energy barrier relative to the migration along a free surface or grain boundary, which must be overcome by a larger activation energy Q. Therefore, atoms migrating across a free surface or through grain boundaries require lower activation energies (Q) since less energy is required for atomic movement relative to lattice diffusion. As such, grain boundaries and surfaces are considered to be high diffusivity pathways relative to the lattice and these low activation energy mechanisms are more significant at low temperatures whereas lattice diffusion becomes more dominant at higher temperatures.

2.9.1. Grain Boundary Effects

Lattice diffusion data for Cu in Ni can be found in many sources [1,50]. However, it is more difficult to obtain grain boundary diffusivity data for most solute-solvent alloy systems since these boundaries are very narrow (~0.5 nm) and complicate D measurements [31]. In FCC metals such as Ni and Cu alloys, it is generally found the $Q_b \sim 0.5 Q_l$ [31]. Grabovetskaya *et al* [51] have measured grain boundary diffusivity parameters for Cu in Ni. Diffusivities were calculated from Cu concentration profiles measured by secondary-ion mass spectroscopy (SIMS) within planar Ni-Cu diffusion couples. These were previously heated to temperatures of 500-600°C, where the contribution of lattice diffusion was assumed to be negligible. It is likely that some lattice diffusion is included in their measurements, yet its contribution to the net interdiffusion process and solute profile development is small at these temperatures. As a simple comparison between lattice and boundary diffusion at 500°C and 1000°C, Table 2-1 shows how grain boundary diffusivities can be several orders of magnitude greater than lattice diffusivities.

Table 2-1: Lattice and boundary diffusivity data for Cu in pure Ni [1,51]

	Lattice	Boundary
D_o (m^2/s)	5.70E-05	1.10E-04
Q (J/mol)	258300	124700
$D_{500°C}$ (m^2/s)	1.9917E-22	6.5364E-17
$D_{1000°C}$ (m^2/s)	1.4313E-15	5.4200E-11

It is important to note that, at a given temperature, the contribution of grain boundary diffusion to the overall solute transport process is determined by the fraction of grain boundaries within the solvent material. In a material completely free of grain boundaries, this rapid mechanism is not available and lattice diffusion dominates (see single-grained powders illustrated in Figure 2-2). Fine-grained materials will have more grains, and therefore grain boundaries, causing a relative higher net flux due to a higher grain boundary contribution. Also, the different D_o and Q values of each mechanism cause varying temperature dependencies for each. In general, $D_b > D_l$ at all temperatures since $Q_b < Q_l$, but the difference decreases with increasing temperatures [31].

Isothermal solid-state sintering studies of Ni and Cu elemental powders have found that grain boundary diffusion contributes significantly to the interdiffusion process [Rudman 44, Puckert 5]. In Fischer and Rudman's work [44], it was found that lattice diffusivities alone could not account for the rapid interdiffusion observed, thus bringing them to conclude that grain boundary diffusion mechanisms must be active and significant. However, the contribution of boundary diffusion to the overall mass transport process in sintering is complex due to the geometrical considerations of grain boundaries, solute concentrations within them, as well as the differing temperature dependence of lattice and grain boundary diffusion. Diffusion-based models such as Corbin's TLPS model for example, require a single diffusivity value which accurately estimates the net mass transport process.

One approach used to account for both contributions is to consider an effective, or apparent diffusivity (D_{app}), which was originally proposed by Hassner [52], and has been adopted by others [31,52,53,54]. This approach accounts for both mechanisms using the simplified grain geometry shown in Figure 2-17 [31].

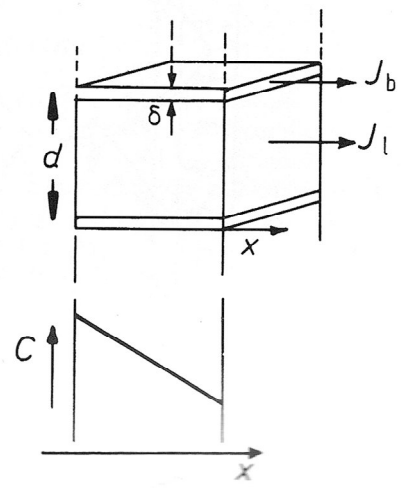

Figure 2-17: Apparent diffusivity model [31].

For simplicity, Figure 2-17 illustrates an isolated grain of size *d,* which is separated from adjacent grains by boundaries of width δ. The effective width of a grain boundary is ~0.5nm and grain sizes are significantly larger and can vary from ~1-1000 μm [31]. The solute concentration gradient *C(x)* in the region of the grain results in diffusive solute fluxes along the grain boundary (J_b) and through the grain's lattice (J_l). Assuming that the concentration gradients along the boundary and through the lattice are identical, J_l and J_b are:

$$J_l = -D_l \frac{dC}{dx} \qquad J_b = -D_b \frac{dC}{dx} \tag{2-39}$$

The contribution of grain boundary diffusion to the total flux (J) will depend on the relative cross-section area through which the solute is migrating. If we consider the grain to have unit thickness and that the grain size is much larger that the boundary width (i.e., $\delta >> d$), we have:

$$J = (J_l d + J_b \delta) / d \tag{2-40}$$

By substituting Fick's expression for J_l and J_b from Equation (2-39) we have,

$$J = -\left(\frac{D_l d + D_b \delta}{d} \right) \frac{dC}{dx} \tag{2-41}$$

Thus, the term within brackets in this case can be considered as an apparent diffusion coefficient such that the grain boundary contribution is scaled by δ/d.

$$D_{app} = D_l + \frac{\delta}{d} D_b \qquad \textbf{(2-42)}$$

It is important to note that grain boundary diffusion provides an enhancing, yet complex contribution to the net mass transport process in real materials. The migration of solute along thin grain boundaries is generally not well understood due to various geometrical considerations (e.g., grain orientations), particularly in PM materials, as well as other transient effects that are difficult to isolate experimentally. These effects are briefly described below.

- Grain growth during isothermal treatments at elevated T_P will cause variations in d. Also, the varying grain boundary orientations will affect boundary flux efficiency.
- In the case of liquid/solid couples, Zhou and Gale have shown that grain boundary grooving causes an increased δ at the interface and this affects the solute transport process [55].
- In many alloy systems, including Ni-Cu, the penetration of solute within base metal grain boundaries can cause diffusion induced grain boundary migration (DIGM) to occur [56]. Solute transport via grain boundaries into the base metal, sometimes leave behind a solute enriched region in the wake of the migrating solute-rich grain boundary. This results in shifting boundary orientations and solute concentrations within the lattice adjacent to the boundary, yet below the interface.
- DIGM is sometimes accompanied by diffusion induced recrystallization (DIR), which occurs in small zones near migrating grain boundaries when solute concentrations exceed a critical value [56]. This process consists of the nucleation and growth of new small grains adjacent to the solute-rich grain boundary or the interface itself. The relevant conditions and driving forces for DIGM and DIR are not well understood [56]. Den Broader and Nakahara first observed DIR zones within DIGM regions near the interface in Ni-Cu planar couples system [57]. Since then, numerous studies have observed DIR [53,56,58,59] and DIGM [60] in the Ni-Cu system at temperatures below 1000°C. However, the occurrence criterion for DIR/DIGM as well as the mechanisms and driving forces for these

processes is still under debate [56,61]. DIGM regions are usually quite small if they occur (< 10 μm thick), and DIR zones occupy a small fraction of these regions in the wake of the migrated boundaries [57]. However, as a resultant effect, Moriyama and Kajihara [62] and Schwarz *et al* [53] reported that the occurrence of DIR at low temperatures (< 800°C) caused accelerated Cu diffusion rates, and this increased Cu penetration rates within planar Ni samples.

- Liquid film migration (LFM) in liquid/solid couples is similar to DIGM [56]. In this case a liquid phase penetrates grain boundaries, causing them to migrate [56]. This can significantly enlarge the boundary, dissolve and round adjacent grains, and increase solute levels [63]. LFM has been observed in Al brazing alloys [64,65], Ni-Cr alloys [66], Co-Cu alloys [63], Ni-Mo and Cu-Zn alloys [67] among other systems; however, liquid film penetration or LFM in the Ni-Cu system has not been reported in literature.

- The accumulation of solute within grain boundaries may cause concentrations to vary in a complex manner for different boundary thicknesses, orientations, or depths within the base metal. Furthermore, the concentration dependence of D_b will affect diffusivity rates at different solute concentrations. These enriched boundaries may also act as sources from which solute can diffuse into the adjacent grains via lattice diffusion.

- Finally, in cases where there are two or more diffusing species (i.e., solute and solvent atoms), unequal diffusivities can result in an unbalanced mass flux and cause Kirkendall effect porosity [43]. This effect is typically considered for lattice diffusion, and is known to occur in Cu-Ni couples since $D_{Cu} > D_{Ni}$ [31]. The vacancies produced by this unbalanced mass flux will coalesce to form pores and can also accumulate at grain boundaries, which act as vacancy sinks. It has been suggested that unequal diffusivities can also occur within grain boundaries and induce grain boundary migration (DIGM) [56]. In effect, DIGM might be a grain boundary form of the Kirkendall effect [56]. In any case, this effect is not completely understood, but the production of vacancies will undoubtedly affect the diffusion field within the lattice and possibly within grain boundaries as

interdiffusion of multiple species accumulates. It is believed that DIR/DIGM arising from unequal diffusivities will tend to increase apparent diffusivities via shifting boundaries and decreases in *d*. However, the concomitant vacancy coalescence and pore formation will decrease mass transport rates since these regions can no longer transmit a mass flux

Many of the effects discussed above are not well understood, difficult to measure and quantify in terms of effective mass transport, and occur only under certain conditions. As such, the apparent diffusivity model shown in Equation (2-42) can provide a simple approximation of grain boundary contributions to mass transport considering the above effects. The contribution of grain boundary diffusion to the apparent diffusivity can be scaled as a function of δ/d. Furthermore, Hassner [52] and Schwarz *et al* [53] include an additional factor (k) which varies from $0.5 < k < 1.5$. This factor accounts for the varying grain boundary contribution due to geometrical effects such as grain boundary orientation and some of the effects described above.

$$D_{app} = D_l + k\frac{\delta}{d}D_b \qquad \textbf{(2-43)}$$

2.9.2. Concentration Effects

Figure 2-18 shows the variation of lattice diffusivity for Cu (D_{Cu}) and Ni (D_{Ni}) at 1000°C within alloys of homogeneous composition ranging from pure Cu to pure Ni [31]. These data clearly show that $D_{Cu} > D_{Ni}$ for the entire composition range. The same is likely true for boundary diffusion. The lattice diffusivity of each species varies by over an order of magnitude over the compositional range, indicating a significant compositional dependence. This is particularly important in TLPS for isomorphous systems such as Ni-Cu (in comparison to limited solid-solubility eutectic systems) because the solid-solution base metal particles can obtain fairly solute-rich compositions depending on the isothermal processing temperature and corresponding solidus composition. Therefore, the dilute alloy assumption, which is used in many analytical models such as Corbin's TLPS model, may not be a valid assumption in this alloy system.

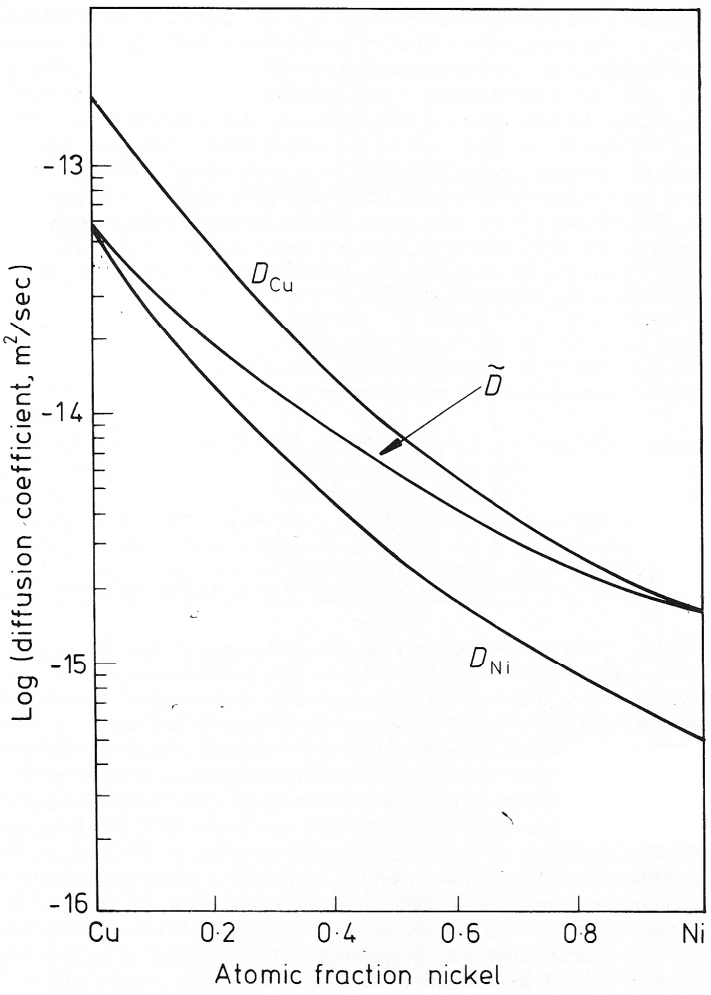

Figure 2-18: The variation of lattice diffusion coefficient in the Cu-Ni system at 1000°C [31].

Figure 2-18 also shows the variation of an interdiffusion coefficient ($\widetilde{D}$) which accounts for the diffusion of both A and B constituents in substitutional alloy systems such as Cu-Ni. In isomorphous alloy systems, the constituent atoms have similar atomic radii and must therefore diffuse substitutionally (vs. interstitially). Figure 2-19 illustrates a planar A-B diffusion couple having a composition gradient (*dC/dx)* near the interface. Due to their similar size, A and B atoms cannot occupy interstitial sites between lattice atom positions and must diffuse substitutionally to vacant atom sites. Therefore the compositional gradients of A and B atoms are equal and opposite ($dC_A/dx = -dC_B/dx$). As such, from Fick's first law, the flux of A and B atoms *relative to the lattice* is given by:

$$J_A = -D_A \frac{dC_A}{dx} \qquad J_B = -D_B \frac{dC_B}{dx} = D_B \frac{dC_A}{dx} \tag{2-44}$$

Figure 2-19 illustrates that the diffusion of A or B is accompanied by the diffusion of a vacancy in the opposite direction (i.e., $-J_A$ and $-J_B$). When, for example, $D_A > D_B$ there will be a net vacancy flux in the negative/left direction. This net vacancy flux causes the lattice reference frame to shift relative to the sample reference frame and also gives rise to vacancy accumulation and the Kirkendall effect.

$$J_V = -J_A - J_B \tag{2-45}$$

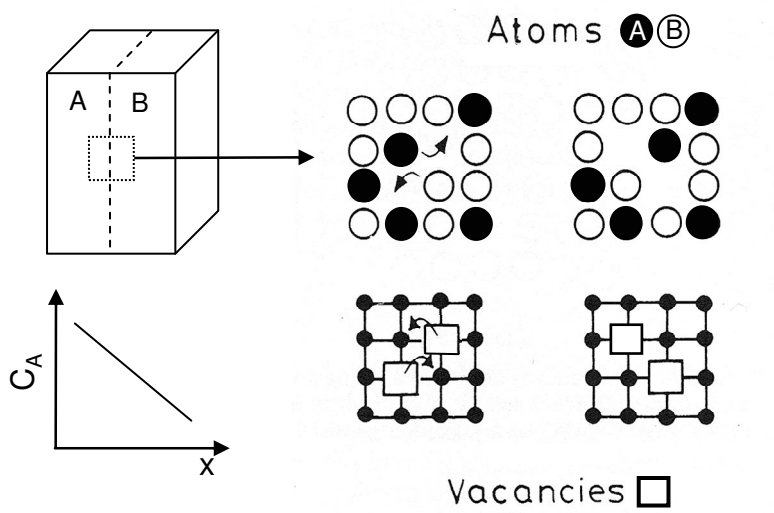

Figure 2-19: Substitutional diffusion of A and B atoms near the interface of an A-B diffusion couple [adapted from 31].

Porter and Easterling [31] continue to show that the flux of A in substitutional diffusion can be given by:

$$J_A = -(X_B D_A + X_A D_B)\frac{dC_A}{dx} \tag{2-46}$$

Where the X_A and X_B are the mole fractions of A and B respectively. This equation can be simplified by defining an interdiffusion coefficient ($\widetilde{D}$, shown in Figure 2-18) which accounts for the interdiffusion of both constituents as a function of composition in substitutional alloys.

$$\widetilde{D} = X_B D_A + X_A D_B \tag{2-47}$$

The factors D_O and Q that determine $\widetilde{D}$ in solute rich alloys are uncertain and there is no simple atomistic model for a concentrated solution [31]. Yet, knowledge of D_A and D_B at a

given composition and temperature can allow the estimation of $\widetilde{D}$ via Equation (2-47). However, many diffusion-based models consider only the diffusivity of the migrating solute species and do not employ $\widetilde{D}$. In dilute B alloys for example (i.e., low A contents, X_A ~0), $\widetilde{D}$ ~ D_A, and thus only A diffusivity in dilute B is considered.

2.10. Differential Scanning Calorimetry

A differential scanning calorimeter (DSC), is a thermal analysis tool used to identify and quantify thermal events (e.g., phase transitions) within small samples [68]. DSC is a variation of differential thermal analysis (DTA) and is sometimes referred to as calorimetric DTA or heatflux DSC. DSC and DTA instruments are typically configured in a similar fashion as shown in Figure 2-20. This schematic shows an empty reference crucible (R) and a sample crucible (S) that contains the specimen under investigation. These thin-walled crucibles are placed on a sample holder, or carrier, which supports the specimens within the hot zone of a furnace which is temperature and atmosphere controlled. Thermocouple sensors are used to measure the sample and reference temperatures throughout the experiment, where both are subjected to a desired temperature program.

In classical DTA, the thermocouple junctions, or sensors, are sometimes placed directly within the sample crucible. In DSC however, the thermocouple sensors are bonded to the carrier - typically directly below the crucibles. This induces some thermal resistance but avoids sample/thermocouple interactions. Temperature calibration of instruments with this configuration is necessary for accurate temperature measurement for a given crucible material.

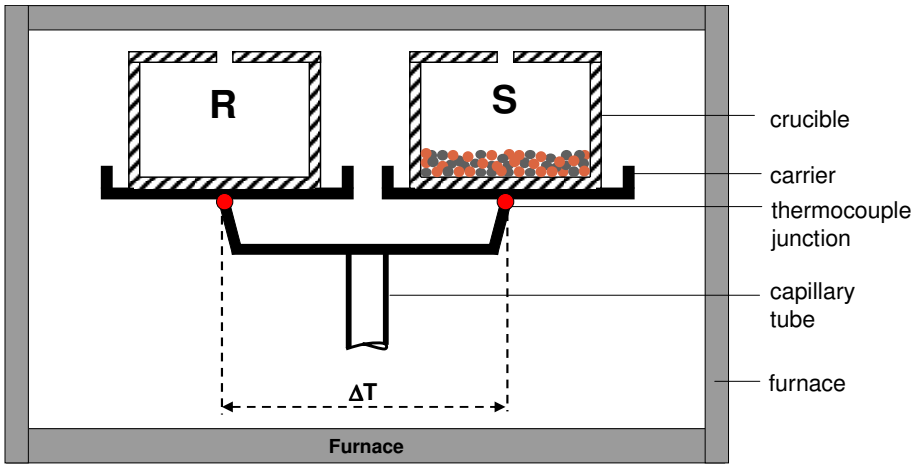

Figure 2-20: Schematic of DSC configuration and differential temperature measurement (ΔT)

In DSC, the heatflow into or out of the sample is measured throughout the temperature program. This heat-flow measurement is based on the temperature difference that exists between the sample cell and the empty reference cell when endothermic or exothermic thermal events take place within the sample. In DTA, only the differential temperature signal between the sample and reference (ΔT) is measured during an experiment. This is accomplished by simultaneously tracking the sample temperature (T_S) relative to the adjacent reference (T_R).

$$\Delta T = T_R - T_S \tag{2-48}$$

A thermal event within the sample will induce a temperature difference or lag with respect to the empty, more responsive reference cell. If the thermal event is endothermic (e.g., melting the sample temperature (T_S) will lag behind the reference temperature (T_R) and a positive ΔT will be measured. Conversely, if the reaction is exothermic (e.g., freezing or intermetallic formations), ΔT will be negative. If we consider the solid→liquid transition during melting for example, a temperature lag occurs since this is a transient process. This phase transition causes a temporary thermal arrest since an additional heat influx (relative to the reference) is required to satisfy the material's latent heat/enthalpy of fusion (h_f) requirements for complete melting to occur.

The measurements of ΔT throughout the temperature program can be plotted as a function of time or temperature (T_S or T_R). Temperature resolved plots are useful in identifying the important onset temperatures of the thermal events. As shown in Figure 2-21, thermal events appear as deviations, or peaks, from the baseline of the DTA trace in either an

exothermic or endothermic direction. A peak in the endothermic direction is considered as an endotherm, and exothermic peaks are referred to as exotherms. These peaks are characterized by their onset temperatures and the areas under them. The onset temperature can be used to identify the reaction taking place with reference to a phase diagram for the material being analyzed (if it is available or known). The area under the peak is related to the heat-flow, or enthalpy change (ΔH), for the reaction.

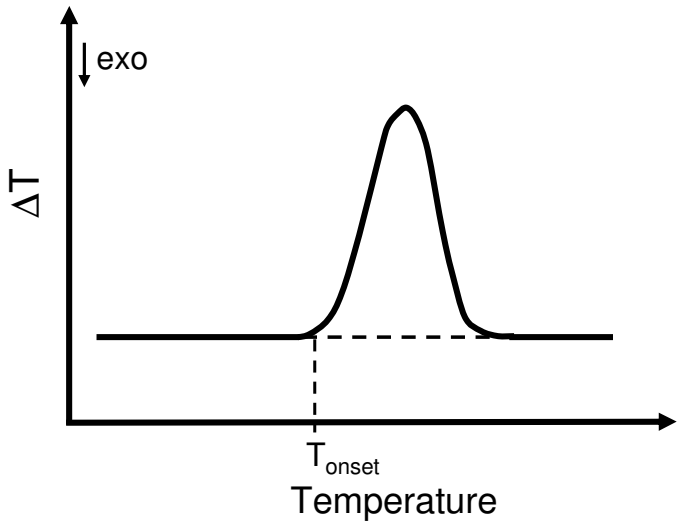

Figure 2-21: Sample DTA curve showing a differential temperature signal during an endothermic event such as melting

The material in the reference cell should have the same thermal conductivity and heat capacity as the sample cell and should undergo no thermal events during the temperature program [68]. Also, it is important to use inert crucibles that do not interact with the carrier as well as the sample itself. The sample crucibles and carrier should also be thin and constructed of conductive material. These DTA/DSC design considerations are important for accurate temperature measurement and determination of enthalpy changes. When high-temperature liquids are formed, ceramic crucibles are typically used since the liquid will not wet or interact with the crucible.

In both DTA and DSC techniques, the measured signal is generated by the thermocouples (T_S and T_R). In classical DTA, the temperature signal is obtained from thermocouples placed directly within the sample reference crucibles. In heatflux DSC (or calorimetric DTA), the samples are placed on top of a conductive sample carrier which has thermocouples attached to its base (see Figure 2-20). This configuration has the advantages

that the output signal is less dependent on the thermal properties of the sample and is not affected by sample-thermocouple interactions [68]. However, the measured thermal response is slower in DSC [68].

The principles of heat-flux DSC operation can be understood by examining the following equations. Equation (2-49) gives the heat-flow rate (*dq/ds*) into the sample crucible according to Newton's law where: R is thermal resistance; T_h is the heat source temperature, and T_{sm} is the sample temperature measured at the monitoring station (i.e., carrier base).

$$\frac{dq_s}{dt} = \frac{1}{R} \cdot (T_h - T_{sm}) \tag{2-49}$$

Similarly, for the reference side:

$$\frac{dq_r}{dt} = \frac{1}{R} \cdot (T_h - T_{rm}) \tag{2-50}$$

Heat-flow to the sample side will heat the sample and the monitoring station. In the absence of thermal events, the temperature changes of the sample side in relation to this heat-flow are given by Equation (2-51) , where C_{sm} is the heat capacity of the monitoring station, C_s is the heat capacity of the sample and crucible [68].

$$\frac{dq_s}{dt} = C_{sm} \cdot \frac{dT_{sm}}{dt} + C_s \cdot \frac{dT_s}{dt} \tag{2-51}$$

Similarly for the reference side:

$$\frac{dq_r}{dt} = C_{rm} \cdot \frac{dT_{rm}}{dt} + C_r \cdot \frac{dT_r}{dt} \tag{2-52}$$

Subtracting Equation (2-49)-(2-50) gives the differential temperature as a function of *R* and the differential heatflow.

$$\Delta T = T_{rm} - T_{sm} = R \cdot \left(\frac{dq_s}{dt} - \frac{dq_r}{dt} \right) \tag{2-53}$$

For ideal instruments where the monitoring station is a single structure holding both the sample and reference, it is assumed that $C_{sm} = C_{rm}$ and that the heating rate is uniform in the hot zone ($dT_r/dt = dT_s/dt = dT/dt$). Also, $C_s \neq C_r$ since the reference side does not contain a sample. Further manipulation by substituting Equations (2-51) and (2-52) gives Equation (2-63), the measured signal from the thermocouples in the absence of thermal events.

$$\Delta T = T_{rm} - T_{sm} = R \cdot \frac{dT}{dt} \cdot (C_s - C_r) \quad \textbf{(2-54)}$$

This expression shows that the measured differential temperature (in the absence of thermal events) is a function of the instrument's thermal resistance, the heating rate (*dT/dt*) and the difference in specific heats between the sample and reference. The DSC trace baseline is primarily controlled by C_s since the effect of C_r is effectively removed by the symmetry of the instrument and identical crucible set-up (i.e., the only difference between the sample and reference cells is the actual specimen).

In DTA, the *R* term is an accumulation of many thermal resistance terms for the instrument and sample, which are not always known. In DSC, since the thermocouple junctions are outside the specimen (i.e., attached to the carrier base), *R* is dependent only on the instrument and not on the sample's thermal characteristics [68]. However, since *R* is a function of temperature, the DSC must be temperature-calibrated using various standard materials with know melting points over the temperature range of interest. With *R* and the differential temperature know, the differential, or relative, heatflow can be obtained from Equation (2-63). As such, some heat-flux DSC manufacturers incorporate electronic compensation for the temperature dependence of *R*, as well as the conversion of the instrument output signal to units of power within the instrument control module - thus providing a relative heatflow output signal [68].

If a thermal event takes place, the measured output will be affected by the change in enthalpy of the sample (*ΔH*) and the DSC trace will deviate from its baseline to form a peak (as shown in Figure 2-21). The area under DSC peaks, which can be measured by integration, is related to the amount (or mass) of the sample as well as the enthalpy of reaction for the thermal event such as a phase transition. The integrated area (*A*) is assumed to be proportional to the enthalpy change for the thermal event [68]:

$$\Delta H = A\left(\frac{K}{m}\right) \quad \textbf{(2-55)}$$

Where m is the sample mass and *K* is an enthalpy calibration constant. This factor can be determined by correlating known enthalpy changes to measured peak areas from standard calibration materials [68]. The temperature dependence of the thermal resistance of the

instrument *(R)* and the enthalpy calibration constant (*K*) are accounted for by performing multiple calibration experiments over the operating temperature range of the instrument. The melting and solidification of pure metals having different melting points (such as indium, gold, silver, etc.) is used for enthalpy and temperature calibration (i.e., ΔH and T_{onset} calibration).

The integration of DSC endotherms or exotherms to measure peak areas requires a straight horizontal baseline. However, the DSC trace will not return to the original baseline after a thermal event if the heat capacity of the sample changes during the event. Under these circumstances, the peak area must be measured by establishing an approximate baseline. A correction file can be used to decrease baseline drift. The correction file is created by performing a DSC trial experiment using the desired temperature and empty reference and sample crucible. The recorded heatflow signal captures the thermal response of the system without the sample present. The DSC sample trial is then conducted with the sample in place for the identical temperature program. The correction file data is used by the DSC controller to subtract the thermal response of the system from the sample data. This effectively reduces baseline drift inherently introduced by the system. A more detailed discussion of baseline correction methods will be presented in Section 3.2 with respect to this experimental work.

2.10.1. Using DSC to Measure TLPS Kinetics

The onset temperature of DSC peaks is very useful in identifying specific phase transformations. For example, the melting of a certain phase at a specific onset temperature (say a pure metal A) should coincide with the melting point of that phase A (i.e., T_A). Heat-flux DSC is particularly useful since this technique can also quantify enthalpy changes during these phase transformations. If the latent heat of fusion of pure A is known ($\Delta H_{f,A}$), DSC results can be used to determine the weight fraction of a multi-phase specimen that is involved in a given melting or solidification event. For example, if a mixture of pure A and pure B powders is heated to cause only the A powder to melt, the enthalpy change during melting of the A regions can be measured by integrating the DSC endotherm area. In the mixed A+B case, the measured melting or solidification enthalpy (ΔH_m in J/g) will be smaller than the pure A case since only a portion of the mixed specimen is melting. If other thermal events do not

overlap the DSC peaks of interest, the weight fraction of liquid phase A formed in the sample is given by:

$$W_A = \frac{\Delta H_m}{\Delta H_f} \tag{2-56}$$

This approach can also be used to determine the weight fraction of liquid solidifying after a certain heat treatment. In this case, the measured exothermic solidification peak enthalpy (ΔH_s) is used instead of ΔH_m in Equation (2-66).

It has been shown that DSC is capable of identifying phase transitions as well as quantifying the enthalpy change during a change of state. Numerous studies have utilized the onset and end temperatures of DTA and DSC peaks to identify liquidus and solidus temperatures of experimental powder systems [26, 40, 42]. This allows the determination of the appropriate TLPS processing temperatures as well as the identification of the melting phase. From the peak area, it is clear that DSC enthalpy measurements can also be a very useful tool in determining the mount of liquid formed and characterizing the process kinetics during TLPS [26]. However, most LPS or TLPS studies in literature do not employ DSC to its full potential as a tool for the quantitative measurement of transient liquid fractions. Rather, peak positions, onset temperatures and *ex situ* metallographic data are used to characterize TLP sintering behaviour in many cases.

Previous research has shown that enthalpy-based DSC can be used to successfully develop a technique for quantifying the extent of isothermal solidification of the transient liquid phase during TLPS [11,13,15,28,69]. Much of this work is based on the DSC technique developed by Corbin and Lucier [13] for determining the relative amount of liquid remaining after an isothermal hold. These TLPS experiments were conducted with mixtures of Pb powder and Pb-Sn eutectic powder (the low melting point additive powder, T_A = 183°C) [11,13]. The relative amount of liquid remaining as a function of hold time at 186°C was determined by comparing the measured area of the initial melting endotherm to that of the diminished solidification exotherm measured at the end of multiple interrupted isothermal hold experiments [11,13].

$$\textit{Liquid fraction remaining } (\Delta H\%) = \frac{\Delta H_s}{\Delta H_m} \bullet 100\% \tag{2-57}$$

This method shows the percent of the initial liquid that is remaining upon solidification after a certain hold time. This approach generally shows $\Delta H\%$ values beginning at 100% at $t = 0$. However, the actual weight fraction of liquid initially formed is less that 1 (or 100%) since only a fraction of the mixtures consists of the low-melting point eutectic powder that forms the liquid. As such, this method does not directly quantify the absolute initial weight fraction of liquid formed within the eutectic powder mixtures studied. However, it was found that negligible solid-state interdiffusion occurred during heat-up and therefore it was assumed that the initial liquid fraction was equal to the fraction of low-melting point eutectic powder used in the mixture. This assumption may be valid for certain low temperature eutectic systems with limited solubility, but it is expected that significant solid-state interdiffusion occurs during heat-up for high-temperature unlimited solubility systems such as Ni-Cu [11].

This work provides a very useful method for quantifying diffusional liquid removal in TLPS relative to the initial amount formed. From this work, an experimental method for quantifying isothermal solidification during TLPS of Ni and Cu powders will be developed. Furthermore, the extent of solid-state interdiffusion during heat-up and its impact on the liquid formation and its removal will be measured. Actual liquid weight fractions will be calculated using Equation (2-65). The main advantage of DSC is the *in situ* quantitative measurement of enthalpy (and thus liquid fraction) for bulk powder mixtures. This is generally very difficult using *ex situ* metallographic analysis of small polished specimen cross-sections that may not be representative of the bulk powder microstructure, which is inherently variable due to powder size, morphology, and distribution variations.

2.11. X-ray and Neutron Diffraction Techniques

X-ray diffraction (XRD) and neutron diffraction (ND) are terms used to describe diffraction phenomena with x-rays and neutrons respectively, as well as the techniques used to study them. Diffraction techniques are typically used to study periodic structures in materials (i.e., crystal lattices, layered microstructures, precipitates, etc.). An important advantage of these methods is that quantitative structural/crystallographic information can be obtained from characteristic diffraction patterns generated during a diffraction measurement.

X-rays and neutrons are different in x-rays are a form of electromagnetic radiation while neutrons are a subatomic particles. However, de Broglie's formula shows that neutrons and as x-rays exhibit a wave/particle duality where they have a specific wavelength with associated mass and velocity.

$$\lambda = \frac{h}{mv} \tag{2-58}$$

These properties allow both neutrons and x-rays to be used as diffraction probes. The wavelengths of these probes are on of the order of interatomic distances in condensed matter ($0.5\text{Å} < \lambda < 5\text{Å}$) and this permits the measurement of periodic structures [70]. However, neutron and x-ray beams are energetic since the beam energy is inversely related to its wavelength. As such, irradiation of the specimen is an important consideration, particularly with neutron techniques due to activation of the sample.

X-ray and neutron diffraction are inherently similar since both phenomena consist of a sample material which scatters an incident beam of radiation in a particular manner such that diffraction occurs. Both techniques consist of measuring these diffraction patterns using similar instruments (i.e., diffractometers) that are designed having the same basic configurations. As such, both techniques are similar in principle (i.e., relating to Bragg diffraction theory), but they differ significantly in practice. The differences arise from the beam source (i.e., x-ray tube vs. nuclear reactors or pulsed neutron sources) and the nature of the scattering event. Both techniques were used in the current study. For the sake of simplicity, the following description of the powder diffraction technique and diffraction theory will not significantly differentiate between XRD and ND methods until the end of this section.

2.11.1. Powder Diffraction Theory

The powder diffraction method [71] will be discussed here since it was employed in this study. This technique utilizes a monochromatic incident beam (i.e., single wavelength λ) and polycrystalline powder specimens. Figure 2-22 presents a simplified schematic of a typical diffraction instrument configuration where the source, specimen and detector are identified.

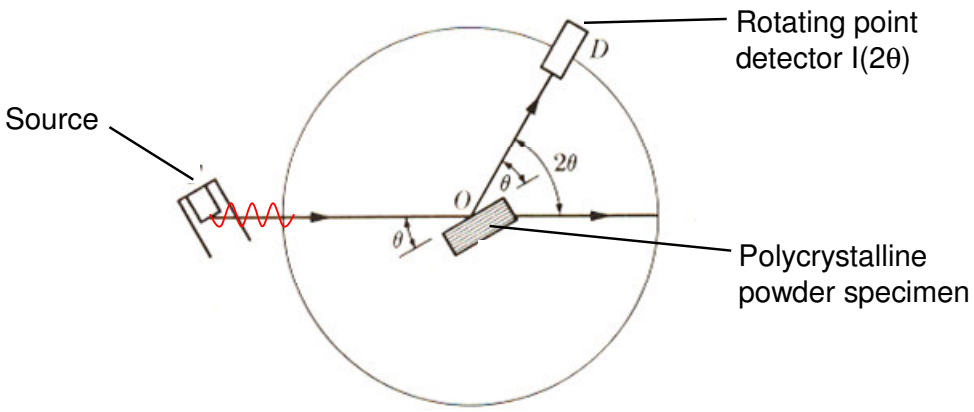

Figure 2-22: Schematic diagram of a typical x-ray diffractometer with a rotating point detector.

The wavelength of the incident beam is determined by the source and monochromating devices used. The incident beam is scattered by the specimen at point '*O*' (i.e., the diffractometer center) and the scattered beam is then detected by a moveable counter at *D*. The figure shows a point-type detector that scans through a range of scattering angles to produce a spectrum of intensity vs. 2θ. Curved stationary detectors may also be designed to scan a large range of angles simultaneously, facilitating rapid measurements.

Figure 2-23 illustrates a sample XRD pattern collected for three specimens – pure Cu, pure Ni, and Ni-65wt% Cu alloy powders. These data clearly illustrate sharp diffraction peaks (also referred to as reflections) that occur at specific 2θ angles, which are distinguishable from the low background signal corresponding to uniform incoherent scattering. The *hkl* Miller indices of the (111), (200) and (220) crystallographic planes are also shown to label the three sets of similar *hkl* peaks present in the diffraction patterns. In this case all three specimens have FCC crystal structures and therefore exhibit similar FCC-type diffraction patterns. The exact peak positions vary according to the lattice parameter of each material, which is similar for Ni, Cu, and its alloys. It is important to note that the lattice parameter of isomorphous alloys varies continuously as a function of composition. This will be further discussed below. Note: a shorter XRD data collection time was used for the alloy specimen in Figure 2-23, thus explaining the lower intensity levels recorded.

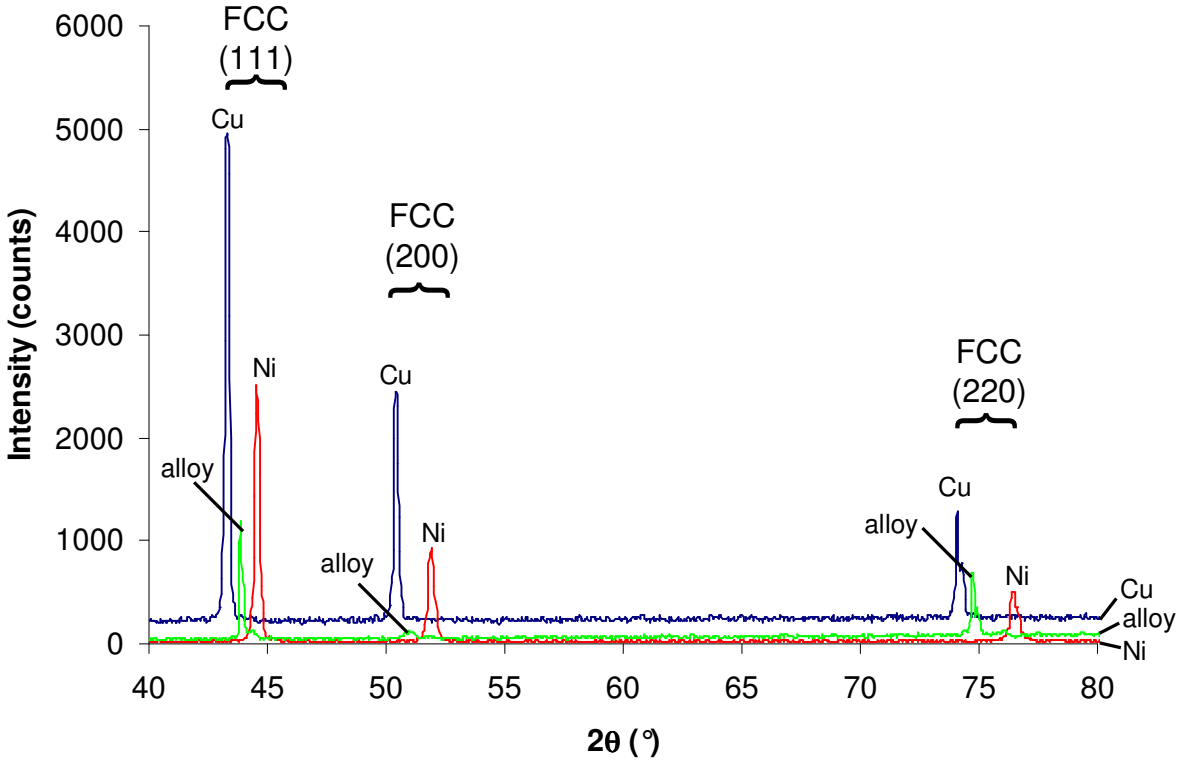

Figure 2-23: Sample XRD pattern for FCC materials (Cu, Ni, and a Ni-65wt% Cu alloy. A shorter data collection time was used for the alloy specimen, thus explaining the lower intensity levels recorded

To understand how these diffraction patterns are generated it is necessary to examine the scattering event. When the incident beam impacts the sample it is partially scattered, absorbed, and transmitted through the target. The absorbed and transmitted portions do not contribute to diffraction, and in some case they are detrimental since the scattered beam is significantly attenuated. Scattering is a general term used to describe elastic and inelastic beam interactions with the sample. Figure 2-24 illustrates a particular scattering condition by atoms within similar *hkl* planes of a single grain or crystal, which is properly oriented with respect to an incident x-ray beam to cause diffraction.

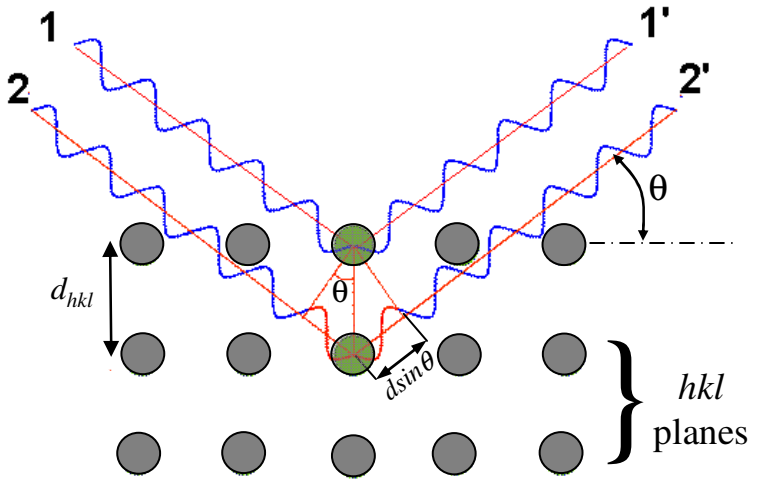

Figure 2-24: Diffraction of a monochromatic beam by a single crystal

Two incident x-rays are shown (1 and 2), which are coherent, and in-phase (same λ and no phase shift). Ray 1' is scattered by an atom in the first plane of the specimen. Scattering occurs in all directions, but we are concerned with the direction that is coplanar with the incident beam, the scattering plane normal, and the detector. Relative to Ray 1', Ray 2' has traveled an extra path length *(2dsinθ)* after it is scattered by an equivalent atom in the adjacent plane. The planes are separated by the characteristic plane spacing for the material's crystal structure (d_{hkl}). If rays 1' and 2' are out of phase, they deconstructively interfere and cancel. Thus, no x-ray peak is detected under these conditions. In the condition that ray 2' is scattered in-phase with ray 1', both rays constructively interfere, and their amplitudes add to reinforce and strengthen the measured signal. This scattering condition is called diffraction and it only occurs at specific angles for a given *hkl* plane.

This diffraction condition is mathematically given by Bragg's law, which simply states that the extra path length traveled by ray 2' (i.e., 2dsinθ) must be an integer value of λ (i.e., nλ) for rays 1' and 2' to be in phase.

$$\lambda = 2d_{hkl}\sin\theta \qquad \textbf{(2-59)}$$

Where λ is the known incident beam wavelength, θ is the *hkl* peak location in a measured diffraction pattern, and d_{hkl} is the interplanar spacing for the plane. An additional requirement for Bragg diffraction is that the scattering event must be elastic. This implies that

the beam energy (and thus wavelength) is unchanged during the scattering event (i.e., $\lambda_{incident} = \lambda_{scattered}$). Equation (2-58) is an extremely useful expression since it defines the angles (also referred to as Bragg angles) where reinforced, in-phase scattering occurs (i.e., diffraction) for the various crystallographic planes of a phase within the specimen. Therefore, the different crystallographic planes of a given material's lattice, having specific plane spacing (d_{hkl}), will cause diffraction peaks to form at characteristic angles in a diffraction pattern.

Figure 2-24 illustrates a Bragg diffraction condition for a fixed incident beam on one crystal or grain. To detect other *hkl* reflections, the crystal would have to be rotated with respect to the incident beam. Polycrystalline specimens on the other hand, have a random orientation of numerous crystals that are typically much smaller than the beam. Therefore such samples are better able to provide diffraction peaks for all important planes without crystal alignment/orientation issues. Powdered/particulate specimens are particularly well suited for providing full texture-free diffraction patterns, which is the primary advantage of powder diffraction methods.

The sample powder XRD pattern shown in Figure 2-23 illustrates how materials having similar crystallographic structures generate similar sets of characteristic peaks. As will be shown in Section 2.11.2, the locations of these peaks are determined by the crystal structure type and size of the crystal lattice. Since Ni, Cu and Ni-Cu alloys have face-centered cubic (FCC) crystal structures, the powder diffraction patterns are very similar in each case (i.e., the number of peaks detected and their *hkl* indices are identical). However, according to Bragg's law (Equation (2-59)), close-packed planes having low d_{hkl} will diffract the incident beam at higher angles. As will be shown in Section 2.11.2, the size of the crystal lattice determines the d_{hkl} spacing of the different planes in a given structure. Therefore, materials having smaller crystal lattice parameters, for a given structure, will cause diffraction peaks to form at greater 2θ angles in a diffraction pattern. This explains the small difference in the diffraction angles of the (111) reflection for Ni and Cu in Figure 2-23 for example, since Ni and Cu have similar, yet slightly different lattice size parameters, a_o ($a_{Ni} < a_{Cu}$) [1]. Alloying and interdiffusion effects on the location and shape of diffraction peaks will be further discussed in Section 2.11.6.

Another important attribute of diffraction patterns is the intensity of the observed peaks. The maximum peak intensity is affected by scanning time, the inherent scattering characteristics of the material, and the volume fraction of the material present in the sample. The width of a peak is determined by experimental artifacts and the materials itself. For example, each diffraction instrument will contribute a certain degree of instrumental broadening due to a finite beam width, detector resolution, detector misalignment, sample displacement, beam divergence, and other geometrical factors. Residual stresses, compositional gradients, temperature gradients, and very fine grain sizes within the material can also contribute to broadening since these cause variations in a, or d_{hkl}, within the material itself [72,73].

Equation (2-60) provides a simple model used for predicting the x-ray diffraction intensity (I) for a given phase [72]. This basic model can also be used to conceptually explain some of the important factors affecting neutron diffraction as well [73].

$$I = \left|F\right|^2 P\left(\frac{1+\cos^2 2\theta}{\sin^2\theta\cos\theta}\right)e^{-2m} \qquad \textbf{(2-60)}$$

Where F is the structure factor, P is the multiplicity factor, e^{-2m} is the temperature factor, and the remaining θ terms are the Lorentz-polarization factor. The structure factor describes the effect of the atom and crystal structure on diffraction intensity. Equation (2-61) presents an expression for determining the structure factor [72].

$$\left|F\right|^2 = \sum_j f_j e^{2\pi i(hu_j+kv_j+lw_j)} \qquad \textbf{(2-61)}$$

Where f is the atomic scattering factor of the j^{th} atom within a plane having hkl Miller indices. The coordinates of the atom within the plane, and thus the lattice, are determined by the fractional Cartesian coordinates $u,v,$w. The inherent scattering intensity of different atoms/elements differs due to their characteristic nuclear and electronic structures, thus the atomic scattering factor varies depending on the atom and the type of incident beam. In XRD for example, since x-rays are scattered by the atom's electrons, heavier atoms have higher atomic scattering factors since they have a greater number of electrons. This causes high atomic number elements to tend to form stronger peaks in XRD patterns relative to lighter

elements. In neutron diffraction, the incident beam is scattered by the atom nucleus and not its electronic structure. As such, the atomic scattering factor will differ significantly between the two techniques, as will be discussed in Section 2.11.3 and Section 2.11.4. However, in both techniques, the atomic scattering factor generates intensity contrast between phases with different compositions since they contain different amounts of certain atoms.

The later terms of the structure factor in Equation (2-61) account for the geometric effects of the crystal structure and the individual atom positions within each *hkl* plane of the diffracting phase. This relationship is applicable to both ND and XRD since it relates to geometric conditions. The experimental XRD pattern in Figure 2-23 shows how FCC materials only generate peaks for planes having unmixed *hkl* Miller indices (i.e., all even or all odd: 111, 200, 220, 311, etc.). This is due to the specific positions of atoms within certain crystal planes, which cause destructive interference with other co-planar atoms, thus preventing diffraction from occurring for certain planes. This results in a null structure factor and intensity for such peaks. To illustrate this, the different atom positions for the FCC lattice (*uvw:* 000, ½½0, ½0½0, and 0½½) have been substituted into Equation (2-61) and the expression has been simplified to give:

$$\text{For FCC materials: } \left|F\right|^2 = f_j[1+e^{2\pi i(h+k)}+e^{2\pi i(h+l)}+e^{2\pi i(k+l)}]$$

$$\left|F\right|^2 = 4f \text{ for unmixed } hkl \qquad \textbf{(2-62)}$$

$$\left|F\right|^2 = 0 \text{ for mixed } hkl$$

The multiplicity factor *P* in Equation (2-60) accounts for the fact that certain planes are equivalent in symmetric crystals. For example, (200), (020), and (002) planes in FCC materials are symmetrically equivalent, and are considered to constitute the {200} group of reflections. These peaks have the same d-spacing and will intensify, or multiply, the measured (200) reflection. The temperature factor (e^{-2m}) accounts for the effect of sample temperature on the diffraction peak intensity in the pattern, where *m* is a complex function of 2θ angle and temperature. At all temperatures atoms are undergoing thermal vibrations about their nominal positions *uvw* within the lattice. As temperature increases the atoms vibrate at greater amplitudes. The effect of this vibration decreases peak intensities since the material slightly deviates from the idealized Bragg diffraction condition (i.e., stationary atoms/planes) [72]. The

Lorentz polarization factor accounts for the θ dependence of the diffraction peak height and width. This geometrical factor acts to decrease peak intensities at intermediate angles and increase peak width at high angles. A more thorough review of diffraction principles can be obtained elsewhere [72,73]

2.11.2. Lattice Parameter Measurement

Typically, we are less interested in the plane spacing of particular *hkl* peaks, but more so in the characteristic size of a given phase's crystal lattice. The interplanar spacing of similar *hkl* planes (d_{hkl}) within a crystal is related to the size of the lattice and the type of plane. Geometrical relationships between d_{hkl} and lattice size parameters are known for many crystal structures. The materials examined in this study have FCC (Ni, Cu) and hexagonal close-packed (HCP) (Al_2O_3) crystal structures. Their geometric relations are provided below [72, 73].

For FCC materials (e.g., Ni and Cu), d_{hkl} is related to a single lattice parameter *a* by:

$$d_{hkl}{}^2 = \frac{a^2}{h^2 + k^2 + \ell^2} \tag{2-63}$$

For HCP materials (e.g., Al_2O_3), d_{hkl} is related to two lattice parameters for the *a* and *c*-axis lengths:

$$\frac{1}{d_{hkl}{}^2} = \frac{4}{3}\left(\frac{h^2 + hk + k^2}{a^2}\right) + \frac{l^2}{c^2} \tag{2-64}$$

For FCC materials, every observed diffraction peak having known *hkl* indices and 2θ position can be used to calculate *a.* By substituting Equation (2-59) (Bragg's law) into Equation (2-63), we can obtain a simple relationship for calculating the FCC lattice parameter (*a*) for different *hkl* reflections.

$$a^2 = \frac{\lambda^2}{4\sin^2\theta}(h^2 + k^2 + \ell^2) \tag{2-65}$$

Similarly for HCP materials, by substituting Bragg's law into Equation (2-64) we get:

$$\sin^2\theta = \frac{\lambda^2}{4a^2}\left(\frac{4}{3}(h^2+hk+k^2)+\frac{l^2}{(c/a)^2}\right) \quad \textbf{(2-66)}$$

Since the HCP structure is more complex than the cubic FCC structure, solving Equation (2-66) for the *a* and *c* lattice parameters requires using 2 peaks and solving a set of 2 equations. A specific *a/c* axis ratio can sometimes be assumed. Alternatively, the values of *a* and *c* can be directly obtained by examining certain types of reflections if they are available [72]. The value of *a* can be calculated by examining *hk0*-type reflections. When *l=0* is substituted into equation (2-66), we obtain.

$$a^2 = \frac{\lambda^2}{3\sin^2\theta}\left(h^2+hk+k^2\right) \quad \textbf{(2-67)}$$

Similarly, *c* can be calculated by examining *00l*-type reflections.

$$c = \frac{\lambda}{2\sin\theta}l \quad \textbf{(2-68)}$$

2.11.3. X-ray Diffraction (XRD)

In XRD, an x-ray tube is usually used as the radiation source in typical laboratory environments. The wavelength of the incident x-ray beam is usually in the area of λ ~0.7-2.2 Å [72] depending on operating voltage and the tube's target material. Figure 2-25 illustrates the essential components of a modern x-ray tube. Electrons are first produced by heating a tungsten electrode (i.e., the cathode) via a heating current. By imposing a sufficiently high voltage across the cathode and the tube's target material (i.e., the anode), electrons are emitted from the cagthode and accelerated towards the anode/target. These high velocity electrons collide with the water-cooled target. This collision causes the ejection of target material electrons from their characteristic energy levels. The loss of energy during this interaction manifests itself in the production of x-rays [72, 73]. The x-rays exit the x-ray tube through a small Beryllium (Be) window, which has a low absorbtivity for x-rays.

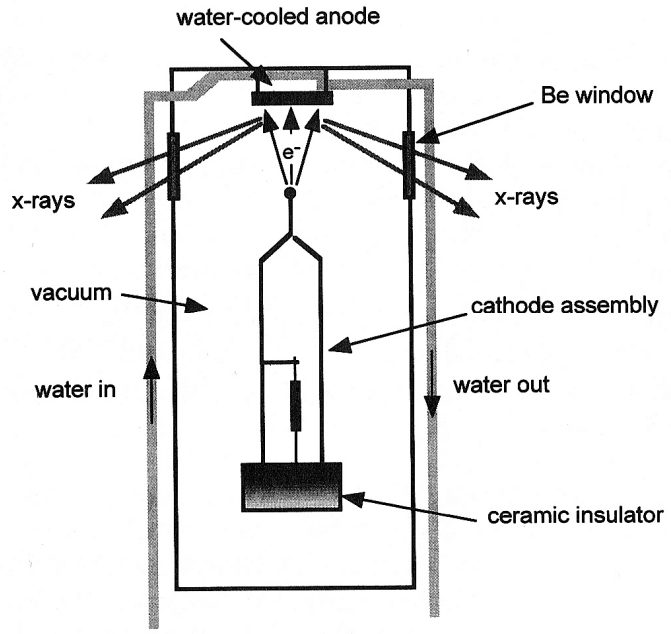

Figure 2-25: Schematic of a modern x-ray tube [72].

Common target materials used in x-ray tubes include Cu, Cr, Fe and Mo, which will emit characteristic x-ray spectra, as illustrated in Figure 2-26 for Mo [72]. The intense x-ray peaks in these spectra are used to form the incident beam in x-ray diffraction (i.e., K_α and K_β rays). The K_β and $K_{\alpha 2}$ rays (shown in the expanded scale of Figure 2-26) are undesirable since they prevent the formation of a monochromatic beam having a single wavelength. These additional x-rays are observed in experimental x-ray patterns by the manifestation of double diffraction peaks, or 'doublets' at off-angles. These additional x-rays can be removed by filters, monochromating crystals, and slits [72]. Figure 2-27 shows the arrangements of slits which can be used to refine the beam's parallelism, adjust its dimensions, and remove doublets. This is done to decrease instrumental broadening effects that can artificially broaden diffraction peaks and add extra doublet peaks to the diffraction pattern. CuK_α radiation is the most common radiation type used in x-ray diffraction studies because of its high intensity [72]. The energy of the x-rays is given by Equation (2-69), which applies to various forms of EM radiation.

$$E = \frac{hc}{\lambda} \tag{2-69}$$

Where h is Planck's proportionality constant and c is the speed of light.

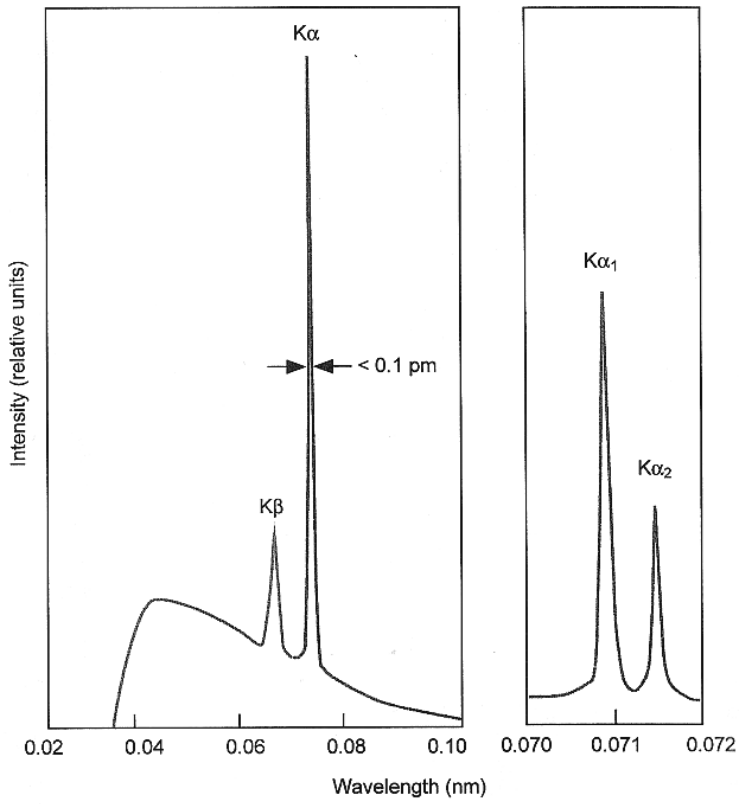

Figure 2-26: X-ray spectrum of molybdenum at an acceleration voltage of 35kV (expanded scale shown at right) [72].

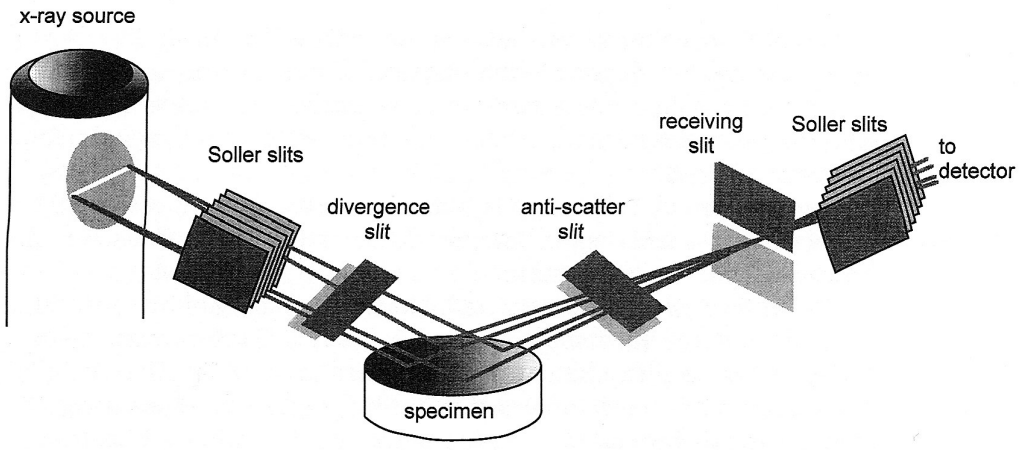

Figure 2-27: Schematic arrangement of slits in a diffractometer [72].

In a typical XRD experiment, a thin layer of polycrystalline powder (usually a few milligrams) is spread onto a planar substrate, which is placed at the diffractometer center. The x-ray interaction with the specimen results in the beam being partially absorbed, scattered, and diffracted. X-rays typically have a low penetration, or sampling depth, within the specimen due

to the nature of the beam-sample interaction (as will be shown in Section 2.11.4). Since x-rays have an associated electromagnetic field, they interact with the charged electrons orbiting the atomic nuclei. Incident x-rays cause sample electrons to oscillate about their mean position. This disturbance causes the electron to decelerate and emit x-rays [72]. This process of absorption and re-emission of electromagnetic radiation effectively scatters the incident beam. The portion of the beam that is elastically scattered having the same wavelength as the incident beam can generate diffraction at specific angles with respect to the beam and crystal planes. Some elements absorb and scatter x-rays more strongly depending on their electronic density. Atoms with higher atomic numbers (Z) have more electrons and higher electronic densities. Light elements for example, which have fewer electrons, scatter x-rays less intensely [72].

As previously mentioned, two main detector configurations are used in x-ray diffractometers to measure x-ray intensity (in counts) versus diffraction angle 2θ. As shown in Figure 2-22, moving point detectors can scan over a 2θ range at desired resolution increments. Alternatively, curved array detectors can be used to collect diffraction patterns over the 2θ range simultaneously. Three main types of x-ray detectors can be used to measure the scattered x-ray intensity (proportional, scintillation, and solid-state). More detail on x-ray detector technology can be obtained elsewhere [72].

2.11.4. Neutron Diffraction (ND)

When a neutron beam is incident on a specimen, the Bragg diffraction concepts by periodic structures previously discussed are also applicable to the neutron beam interaction. The key differences between neutron and x-ray methods are that neutrons can generate a highly penetrating, neutral beam that can penetrate through ancillary equipment and allow the measurement of larger sample volumes [74]. The larger sampling volume can provide improved statistics in comparison to x-ray methods, yet more time is sometimes required for measurement since the probe intensity is weaker in reactor-based sources [77]. Higher intensity accelerator-type sources can be used to avoid this problem. As such, another very important difference relative to X-ray methods is the cost and limited availability of neutron

sources. Nuclear reactor-based neutron sources will be discussed here since this type was used in the present study.

Nuclear fission reactions within scientific nuclear reactors can be used to generate neutron beams used for analytical purposes. The production of neutrons by the fission reaction of uranium rods is illustrated in Figure 2-28. Incident neutrons are absorbed by ^{235}U atoms, which then become unstable and split into lighter elements and releases energy as well as more high-energy neutrons. These neutrons can then cause a chain reaction, releasing more neutrons which can also be used to form the neutron beam.

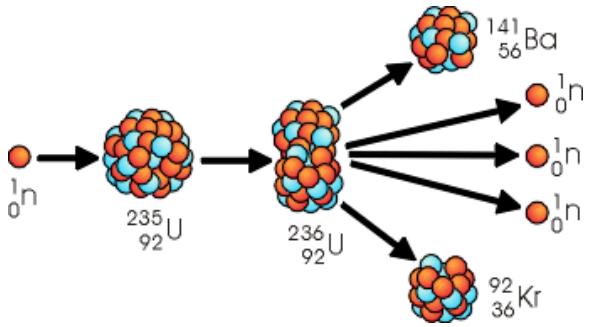

Figure 2-28: ^{235}U nuclear fission reaction.

This reaction takes place in a moderating fluid (graphite or usually water) within the reactor core, which serves to slow the emitted neutrons and control the reaction. The temperature of the moderator serves to control the energy (i.e., velocity) and resultant wavelength distribution of the neutrons and neutron beam. These properties are related by [74]:

$$E = 0.08617T = 81.81\left(\frac{1}{\lambda^2}\right) \qquad \textbf{(2-70)}$$

Sources operating at 60K< T <1000K are considered to produce *thermal* neutrons (vs. *hot* or *cold* neutrons), which have low energies favourable for ND [74]. CANDU (CANadian Deuterium Uranium) reactors, use a heavy water moderator maintained at 25-50°C to efficiently slow down, or moderate, neutrons for controlled power generation as well as for research purposes. Heavy water (i.e., D_2O or $^{2}H_2O$) is water that is enriched with the hydrogen isotope deuterium (^{2}H), which contains an extra proton. This fluid is particularly well suited as a moderator due to its lower absorbtivity for neutrons. The NRU reactor for example (located

in Chalk River ON, Canada) is a 135 MW, heavy water reactor used for neutron scattering and diffraction research [75]. The moderated neutron beams exit the reactor core via beam ports that are connected to diffractometer instruments within the nuclear lab facility.

Thermal neutrons offer a unique combination of properties for probing various periodic structures in materials. The mass of thermal neutrons results in a de Brogle wavelength which is similar to that of x-rays ($0.5Å < \lambda < 10Å$) [70,74]. The low temperature of the moderator, which reduces neutron velocities, significantly decreases the beam energy such that thermal neutrons are considered to provide a generally non-destructive probe [70]. However, neutron beams are more energetic than x-rays due to the inverse relationship with $1/\lambda^2$. As such, proper shielding of the instrument, its optical system, and personnel is an important safety consideration. Another, important hazard of neutron radiation is activation, which is the ability of neutrons to induce radioactivity in most substances they encounter. ND specimens must therefore be carefully analyzed for radioactivity after experiments and allow sufficient time to become inactive.

Since neutrons are neutral particles, they are scattered by the nuclei of the specimen atoms, unlike x-rays which are scattered by the charged electronic structure of the atom. Since the nucleus occupies a very small fraction of atomic volumes (as illustrated in Figure 2-29 for hydrogen), atoms appear much more transparent to neutrons. Thus, incident neutrons are able to penetrate the sample to much greater depths in comparison to x-rays [70,74,75,76]. Consequently, the use of complex sample environments such as cryostats, furnaces, and pressure cells is greatly facilitated [70], which enables *in-situ* studies under varying conditions. Table 2-2 provides comparative data for the penetration depth of x-rays and neutrons through various materials. The penetration depth is considered to be the depth (in mm) at which the beam in 90% attenuated.

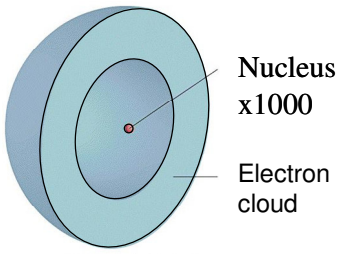

Figure 2-29: Illustrated cross section of a hydrogen atom showing the volume occupied by the nucleus (exaggerated by ~ 1000x) and the atom's electron cloud.

Table 2-2: Penetration depths ($I = 0.1I_O$, in mm) of thermal neutrons and x-rays in various materials [74].

Material	Neutrons	X-rays (1.54Å)
Be	24.9	9.372
C	37.4	1.886
Al	220.4	0.175
Fe	19.1	0.009
Cd	0.2	0.011
Pb	61.9	0.008

Since neutrons are scattered by the atom nucleus and not the electrons, scattering intensity is not a monotonic function of atomic number Z, or atomic mass, as found in XRD. Consequently, elements will have very different atomic scattering factors for neutrons and x-rays (f_i in Equation (2-61)). Figure 2-30 illustrates the erratic variation of neutron scattering intensity for various elements as well as their isotopes. These data show that certain light elements scatter neutrons as strongly as some heavier atoms. This results in useful contrast effects which include sensitivity to light elements and the ability to better distinguish between neighboring elements in the periodic table [70,76, 70]. It is also worth noting that the intrinsic scattering intensity of most elements is lower than that for x-rays. Furthermore, the neutron flux delivered by most reactor-based sources in lower than typical x-ray sources [77]. Therefore, lower diffraction intensities are important practical consideration for neutron diffraction studies – highlighting the compromise between resolution and intensity in practice [77].

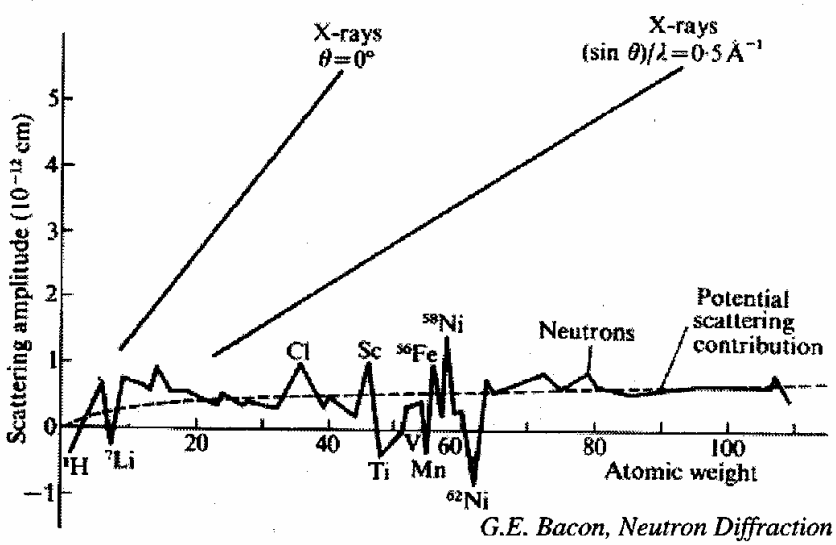

Figure 2-30: Scattering intensity of x-rays and neutrons for different elements [76].

The key differences between neutron and x-ray properties have been briefly described above. Inherently, the radiation source and detector technology are different. The large penetration depth of neutrons due to the nuclear scattering mechanism is also a particularly important differentiating characteristic. However, the basic powder diffractometer instrument configuration shown in Figure 2-22 is used in both neutron diffraction as well as XRD. This is because the concepts of Bragg diffraction apply to both beam types due to their wave/particle nature. As such, scattering of monochromatic radiation (x-ray or neutron) by the periodic structure of polycrystalline/powdered materials will generate peaks at specific Bragg diffraction angles in XRD and ND patterns. To illustrate this similarity, Figure 2-31 shows a comparison of experimental XRD and neutron diffraction patterns for the same specimen before and after oxidation during service (a Ti cathode material in this case) [75]. In the oxide-free specimen (Figure 2-31*a*), both patterns show similar peaks that form at different angles due to the difference in beam wavelength λ. The patterns differ more significantly for the oxidized material (Figure 2-31*b*). The ND data includes many strong Ti-oxide peaks whereas the XRD pattern is very similar in both the oxidized and oxide-free cases since light elements scatter x-rays poorly.

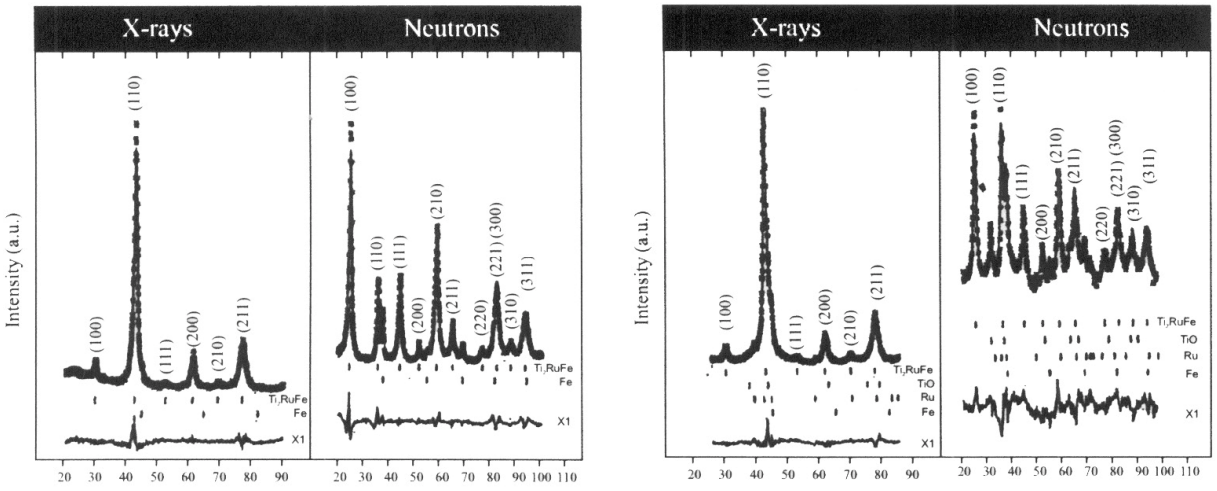

Figure 2-31: XRD and neutron diffraction spectra for a cathode material in pre- and post-oxidized states [75].

2.11.5. Temperature Effects3

Upon heating, most materials expand by different degrees depending on their coefficient of thermal expansion (CTE), which is a function of temperature. A material's linear expansion ($\Delta L/L_o$) over a temperature range can be used to calculate its linear CTE (α).

$$\alpha = \frac{\Delta L}{L_O \Delta T} \tag{2-71}$$

Metals typically have CTE values that are notably higher than ceramics such as alumina. This is primarily due to the higher interatomic bond strengths of ceramics (i.e., covalent vs. metallic bonds), which is indicated by their high melting points [1]. As an atom gains energy during heating, it increasingly vibrates about its nominal position and occupies more space. As previously discussed, the temperature factor (e^{-2m}) in Equation (2-60) can account for the decreased peak intensities caused by these thermal vibrations. However, another effect of increasing thermally-induced vibrations is the increase of interatomic distances, which causes the lattice to expand [1]. Bragg's law indicates that lattice expansion will cause the location of *hkl* reflections to shift towards lower 2θ angles for diffraction patterns collected at increasing temperatures. Furthermore, temperature gradients within a specimen will cause lattice parameter gradients, which result in peak broadening [72]. This effect may complicate the accurate *in situ* determination of peak locations during the transient, athermal segments of diffraction experiments.

In randomly oriented polycrystalline materials having a cubic structure, the thermal expansion of the crystal lattice during uniform heating is representative of the material's linear expansion in any direction. The degree of lattice expansion can be measured via diffraction techniques. By determining the lattice parameters of a phase from diffraction patterns collected at elevated temperatures and at room temperature (a_o), the simple expression in Equation. (2-72) can be used to calculate FCC lattice expansion.

$$\text{FCC: } a\text{-axis expansion} = \frac{\Delta a}{a_O} \tag{2-72}$$

For more complex crystal structures with unequal lattice parameters, the different parameters (e.g. *a* and *c* in HCP materials) may expand to different degrees during heating. As such, the thermal expansion measurement of the HCP lattice must consider both parameters.

$$\text{HCP: } a\text{-axis expansion} = \frac{\Delta a}{a_O}$$
$$c\text{-axis expansion} = \frac{\Delta c}{c_O} \qquad \textbf{(2-73)}$$

Since neutron and x-ray diffraction techniques are capable of accurately determining lattice parameters, numerous studies have been found in the literature where the thermal expansion behaviour of materials has been investigated [78,79,80,81,82]. Furthermore, thermal expansion data for various materials is available in the literature. A comprehensive review of lattice parameter expansion data has been compiled by Touloukian *et al* for metallic and ceramic materials [81,82]. This source provides a thorough review of numerous literature sources for the *a*-axis expansion of Ni, Cu and Al_2O_3. The averaged data and corresponding polynomial curve fits determined by Touloukian *et al* are presented in Figure 2-32.

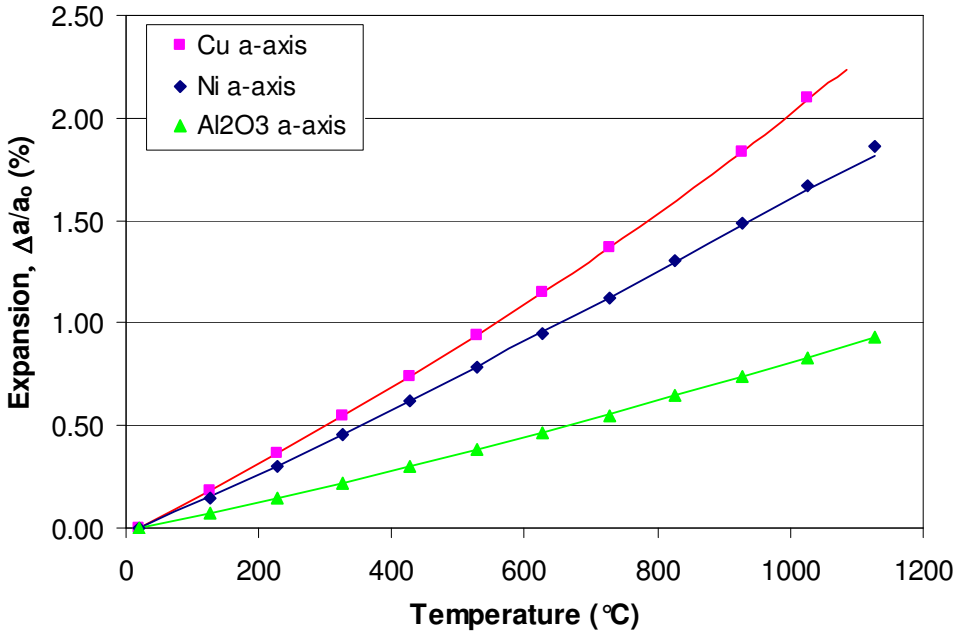

Figure 2-32: Thermal expansion data for the Ni, Cu and Al_2O_3 lattice [81,82].

Mathematical expressions for the curve fits determined by Touloukian *et al* are provided in Equations (2-74), (2-75), and (2-76) [81,82]. Temperatures are in K units in these expressions and a_o is the reference room temperature lattice parameter measured at 293K for each phase.

Cu thermal a-axis expansion:

$$(293 < T < 1300) \quad \Delta a/a_o = 1.685\times10^{-3}(T-293) + 2.702\times10^{-7}(T-293)^2 + 1.149\times10^{-10}(T-293)^3 \qquad \textbf{(2-74)}$$

Ni thermal a-axis expansion:

$$(293 < T < 895) \quad \Delta a/a_o = 1.362\times10^{-3}(T-293) + 4.544\times10^{-7}(T-293)^2 - 1.806\times10^{-10}(T-293)^3$$

$$(895 < T < 1500) \quad \Delta a/a_o = 0.944 + 1.713\times10^{-3}(T-895) + 1.283\times10^{-7}(T-895)^2 + 1.447\times10^{-10}(T-895)^3 \qquad \textbf{(2-75)}$$

Al_2O_3 thermal a-axis expansion:

$$(293 < T < 1190) \quad \Delta a/a_o = -0.176 + 5.431\times10^{-4}T + 2.150\times10^{-7}T^2 - 2.810\times10^{-11}T^3 \qquad \textbf{(2-76)}$$

These expressions enable the comparison of measured lattice expansions (from experimental diffraction peak positions) to predicted expansions with respect to measured thermocouple temperatures during high temperature experiments. Furthermore, they allow the determination of the actual temperature of each phase by substituting the measured lattice expansion in Equations (2-74), (2-75), and (2-76). This can be important during high temperature *in situ* diffraction experiments since thermocouple sensors can not always be placed directly within the specimen to provide accurate sample temperature measurements.

This verification scheme permits the use of internal standards during high temperature diffraction experiments. It is important that the phase used as the internal standard material is inert and does not interact with the specimen. Otherwise alloying or phase transformations will also contribute to peak shifting and broadening. Alumina crucibles for example are often used as inert containers for powder specimens. These crucibles inevitably contribute Al_2O_3 peaks to the measured diffraction patterns due to their proximity to the specimen and presence in the incident beam. As shown by Bull *et al*, the shifting locations of these peaks during the thermal expansion of the Al_2O_3 lattice can be tracked to accurately determine lattice parameter expansions and therefore the actual sample temperatures [80].

2.11.6. Interdiffusion and Alloying Effects/Studies

The alloying of a given phase by solute atoms to form a solid-solution will cause the position and shape of peaks to be altered due to the change in the solvent material's lattice parameter, which now accommodates different atoms. Compositional peak shifting in diffraction patterns must therefore be considered for interacting specimens. The sample powder XRD pattern shown in Figure 2-23 illustrates how alloying of Cu by Ni causes all *hkl* peak locations to shift. For example, a Ni-65wt% Cu alloy sample generates FCC peaks located between the elemental Cu and Ni peaks (i.e., between the 111, 200, and 220 FCC peak groups shown in the figure). This occurs because the addition of solute atoms in a solid-solution, which have different atomic radii, will cause the lattice size parameter to change as the solvent lattice accommodates more solute atoms – thus changing the peak position 2θ.

Alloying can also cause the diffraction intensity to vary with composition since solvent and solute atoms have different scattering factors (f_i). In this case, the alloyed Ni-65wt% Cu peaks are particularly weaker than the elemental Ni and Cu peaks due to the fact that a shorter data collection time was used. Nevertheless, this sample data illustrates some of the effects of alloying in Ni and Cu powders.

Since Ni and Cu form an isomorphous alloy system, by definition, their solid-solutions maintain the FCC structure over the full compositional alloy range between pure Cu and pure Ni. Since the atomic radius of Cu is somewhat larger than that of Ni (r_{Cu} =1.278Å, r_{Ni} =1.243Å) [1], the substitution of Cu in the Ni lattice causes an increase in the solid-solution lattice parameter with increasing Cu contents. This variation is shown in Figure 2-33 for various isomorphous alloy systems at room temperature [83]. The Ni-Cu data (shown as individual points) illustrates that the lattice parameter of Ni-Cu alloys varies almost linearly from a_{Cu} to a_{Ni}.

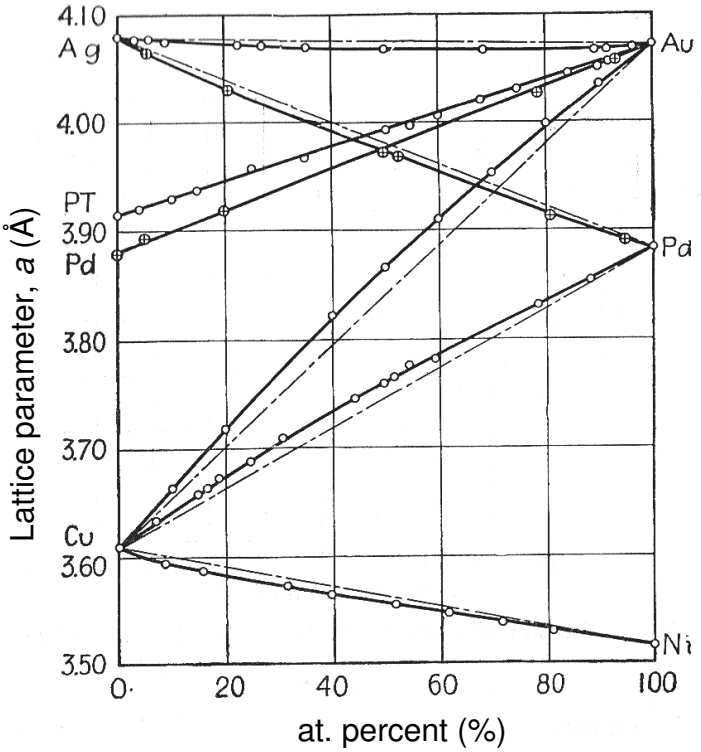

Figure 2-33: The variation of lattice parameter as a function alloy composition for various alloys at room temperature [83].

A simple approximation of alloy lattice parameters (a_{alloy}) can be obtained by the linear relationship assumed in Vegard's law.

$$a_{alloy} = a_{Cu}C_O + a_{Ni}(1 - C_O) \tag{2-77}$$

Where a_{Cu} and a_{Ni} are the lattice parameters of pure Cu and pure Ni respectively and the fractional composition of the homogeneous solid-solution is given by C_O. If Bragg's law and the lattice geometry (Equation (2-65)) are substituted into Equation (2-77), the variation of *hkl* peak location for Ni-Cu alloys can also be approximated by Equation (2-78).

$$\sin\theta_{alloy} = \left(\frac{C_O}{\sin\theta_{Cu}} + \frac{1 - C_O}{\sin\theta_{Ni}} \right)^{-1} \tag{2-78}$$

Where θ_{Cu} and θ_{Ni} are the diffraction angles of the pure Cu and pure Ni *hkl* reflections respectively. θ_{alloy} is the diffraction angle of the same *hkl* reflection for the homogeneous Cu-Ni alloy having a fractional Cu content C_O. This indicates that Ni-Cu alloys can cause diffraction over the entire 2θ region separating sets of similar *hkl* peaks (i.e., θ_{Cu}-θ_{Ni}) As such,

the 2θ axis in diffraction pattern plots is analogous to alloy compositions between θ_{Cu}-θ_{Ni} (or 100-0 wt% Cu). According to Equation (2-65) and Equation (2-78), as the lattice parameter of a homogeneous alloy shifts from a_{Ni} to a_{Cu} for increasing Cu contents, the FCC *hkl* peaks will shift to lower diffractions angles. As shown by the Ni-65wt%Cu alloy peaks in Figure 2-23, alloys having compositions rich in Cu will form peaks closer to the pure Cu locations. Similarly, Ni-rich alloys will form peaks closer to the pure Ni location. Since no intermediate phases can form in this isomorphous system, the formation of new peaks at different angles, as a result of phase transformations, is not expected.

An additional consideration is the effect of non-uniform alloying on the shape of diffraction peaks, which is expected in sintering experiments with interacting dissimilar powders. If compositional gradients are present within solid-solution regions of a specimen, this causes asymmetric broadening of peaks since there is a variation in *a* within the material, thus complicating their quantitative interpretation. This is particularly important in the Ni-Cu system since solid-solutions can form exceptionally broad, diffuse diffraction signals between the pure Ni and Cu peak locations, which will correspond to the Ni- and Cu-rich regions of the specimen.

The combined broadening and shifting effects of alloying on diffraction patterns can be useful in the investigation of the transient interdiffusion and phase transformation processes during sintering of dissimilar powders. Fischer and Rudman performed an XRD study where the effect of Ni-Cu interdiffusion on XRD diffraction patterns was investigated [84]. Mixtures of elemental Ni and Cu powders (~5 μm in diameter) were solid-state sintered at temperatures below the melting point of Cu for increasing durations (750-1050°C). The post-sintered specimens were then analyzed by XRD to examine the changes in diffraction pattern profile at the various times. Figure 2-34 presents Fischer and Rudman's XRD data for the (220) peak evolution after sintering at 780°C for increasing times. Conveniently, a secondary x-axis is included that indicates the composition of the corresponding diffraction angle. It is worth noting that the 2θ axis in Rudman's data is reversed relative to typical diffraction patterns plots (i.e., plotted from high to low 2θ angles from left to right). Also, thes data contain $K\alpha_2$ doublets, which required removal, and was obtained *ex situ* on post-sintered mixtures heated in the solid-state only.

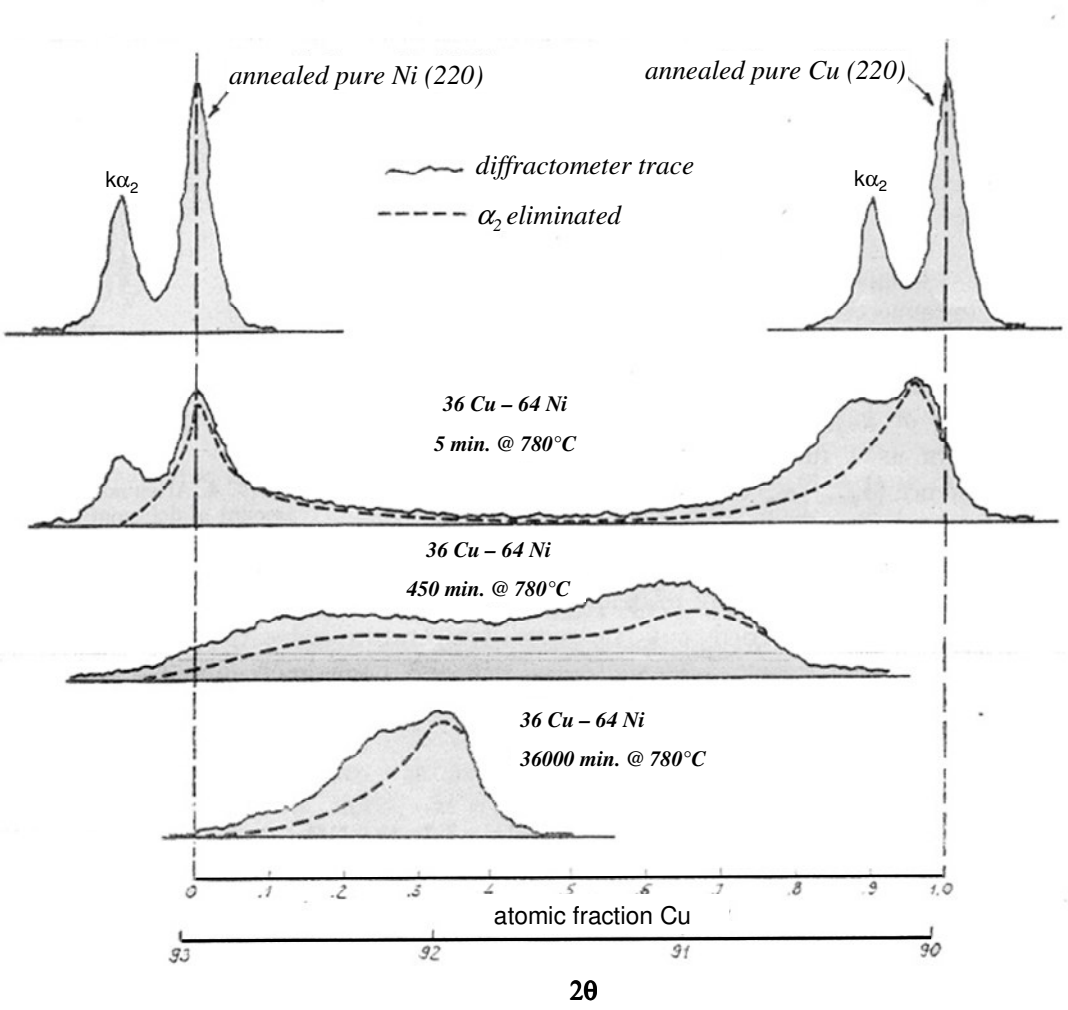

Figure 2-34: XRD patterns for solid-state sintered Ni-Cu powders collected after solid-state sintering for increasing times [84]

The initial elemental Cu and Ni powder peaks were found to gradually broaden asymmetrically and shift inwards at short hold times (see the 5 minute pattern). Concurrently, the diffraction intensity from the intermediate 2θ region between the elemental peaks gradually increases as the volume fraction of alloyed regions increases within the specimen. At intermediate hold times the elemental peak intensities significantly decrease and a large, broad alloy peak develops. Near the end of the sintering process, homogenization of the sintered alloy acts to decrease compositional gradients. This decreases the measured alloy peak width and increases its maximum intensity at an intermediate 2θ position. The center of the final peak at 36000 minutes corresponds to the bulk mixture composition (i.e., Ni-36wt%Cu in this case). However, this peak is still relatively broad and asymmetric in comparison to the starting

elemental peaks. This indicates that small compositional gradients are still present. This is also due in part to the $K\alpha_2$ doublet.

It is important to remember that the 2θ position of a particular intensity measurement is determined by composition (through *a*) and the intensity is determined by the volume fraction of the material which has that composition. Based on the intensity distribution, or profile, of above XRD data, Rudman developed a technique for calculating normalized concentration profiles from the x-ray intensity profiles [85]. The measured x-ray profiles contained Cu$K\alpha_2$ peak doublets, which were removed from the diffraction patterns by a $K\alpha_2$ stripping technique that was developed (see dashed lines in Figure 2-34). In Rudman's method, these concentration profiles were then used to elaborately calculate quantitative parameters indicating the degree of homogenization, or interdiffusion, for each profile during the solid-state sintering process. This analysis indicated that grain boundary diffusion was significant at the temperatures studied.

In a more recent related study by Delhez *et al*, similar *ex situ* XRD measurements of compacted mixtures of fine Ni and Cu powders were obtained after solid-state sintering at 800, 900, and 1000°C [86]. Delhez *et al* similarly tracked the evolution of {220} peak profiles. In this case, the degree of homogenization during sintering was determined by measuring relative peak position shifts. These data were compared to a concentric sphere model for Ni-Cu interdiffusion and solid-state homogenization, which is based on Crank's equations [47]. Their findings showed that some degree of interdiffusion and alloying takes place during the heat-up segment. The rate of homogenization during isothermal sintering at these temperatures was also found to be significantly affected by surface, grain boundary, and volume diffusion mechanisms.

The *ex situ* XRD studies by Rudman and Delhez provide an experimental basis for investigation of the solid-state interdiffusion behaviour of Ni and Cu diffusion couples via powder diffraction methods. As such, this work provides a good indication of the neutron diffraction pattern evolution expected during solid-state sintering (SSS) experiments and the first stage of TLPS experiments (i.e., solid-state sintering and interdiffusion during the athermal heat-up segment prior to Cu melting). However, the liquation of Cu, which is

necessary in TLPS, is expected to remove Cu peaks and significantly alter the diffraction pattern evolution during isothermal sintering above 1085°C.

Neutron diffraction approaches, which can penetrate complex sample/furnace environments and irradiate larger sample volumes relative to XRD, have the potential to provide additional information about these transient processes. As such, this technique is well-suited for *in situ* analysis. Diffraction patterns collected *during* sintering experiments, rather than from post-sintered specimens, can provide similar structural information but at the times/temperatures where the metallurgical interactions take place.

In doing do, insight can be gained for time-resolved synthesis pathways, reaction mechanisms, and reaction kinetics at the actual temperatures of interest [78]. For example, the self-propagating high-temperature synthesis (SHS) of Ti_5Si_3 intermetallics from pure Ti and Si thin films was studied via high-speed *in situ* neutron diffraction by Riley *et al* [87]. This reaction is poorly understood due to its speed (~0.5s in Riley's data) and the difficulty in making *in situ* observations with other techniques. However, the evolution of diffraction patterns collected during the process, which were acquired using a high-flux neutron diffractometer (D20 at l'Institut Laue-Langevil, ILL, Grenoble France) at 0.9s time intervals, allowed a clearer determination of the reaction pathway. It was found that the formation of Ti_5Si_3 intermetallic material via SHS (as indicated by the abrupt formation of Ti_5Si_3 peaks) was immediately preceded by a $\alpha \rightarrow \beta$ transformation in the Ti powder, which apparently initiated interdiffusion and triggered the SHS ignition.

The synthesis of Ti_3SiC_2 [88] and Ti_3AlC_2 [89] ceramics via reactive sintering of starting elemental powder mixtures has also been carefully analyzed by Wu and Kisi via *in situ* neutron powder diffraction. *In situ* diffraction measurements were carried out on a medium-resolution neutron powder diffractometer (Australian Nuclear Science and Technology Organization, ANSTO, Menai Australia). The relatively slower (on the order of hours) yet complex multi-phase reactions comprising the synthesis paths of these high-temperature ceramics were elucidated by time/temperature-resolved ND patterns. The significance of applying ND techniques arises from its ability to reveal structural and compositional information about the phases present - providing an ideal tool for the *in situ* study of transient phases and interdiffusion. However, in nearly all *in situ* time/temperature-resolved diffraction

experiments, one is often forced to compromise between signal quality and time/temperature resolution [77,78]. For example, the beam-refining optical systems and longer collection times desired for high quality measurements inherently reduce the neutron beam intensity and time/temperature resolution of the measurements respectively [78]. The acceptable balance is a function of the source/instrument available, the accuracy required, and the system studied. This consideration is more important for *in situ* ND studies using most reactor-based thermal neutron sources, where neutron fluxes are relatively low in comparison to XRD and intense accelerator-based neutron sources [77].

2.11.7. Quantitative Analysis and Sources of Error

The first step in the analysis of XRD and ND data is to index the diffraction pattern. This involves identifying the phases present in the pattern, and assigning the correct *hkl* Miller indices to each peak. This requires knowledge of the phases present and their crystal structure. The absence of unknown peaks must also be verified to ensure accurate results. In XRD methods, most diffractometer systems and analysis software packages contain large experimental databases of XRD peak locations for many materials and incident x-ray wavelengths. This reference data can be superimposed onto experimental XRD patterns to quickly identify the phases and peaks present in an experimental pattern. Such databases are not commonly used or available for ND methods since neutron scattering facilities are much less prominent. In such cases, the predicted peak locations for known phases must be calculated and compared to the experimental data. This can be done manually based on the equations in Sections 2.11.1 and 2.11.2 or via an appropriate computer application.

Once a pattern has been indexed, the 2θ locations of the peaks can be used to experimentally determine the actual lattice parameter of a pure specimen, or the individual phases within a multi-phase specimen. As illustrated in Figure 2-35, the location of a diffraction peak can be determined at its centroid, which is the 2θ position of the peak center at half of its maximum intensity M (i.e., the center of its full width at half-maximum, FWHM).

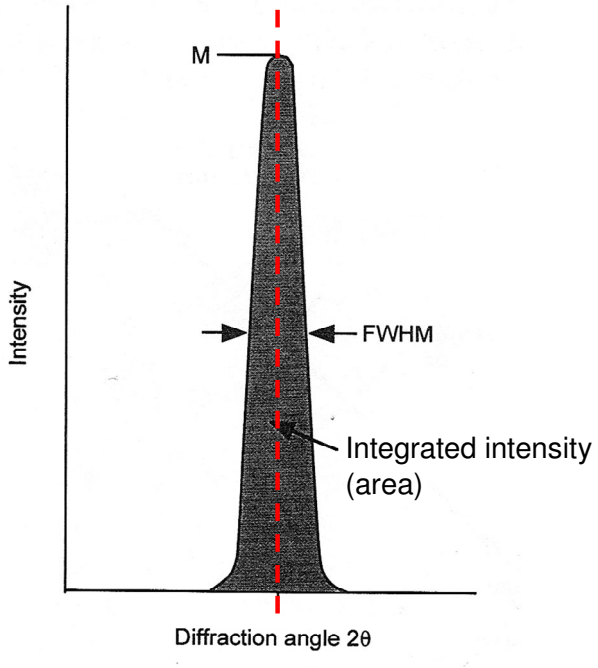

Figure 2-35: Typical diffraction peak profile [72].

The accurate determination of peak locations and lattice parameters requires diffraction data that are free of systematic errors. For example, a poorly aligned diffractometer will measure peaks at incorrect angles. Diffractometers are periodically calibrated using precise standard materials with know diffraction patterns for this reason. This permits the 2θ calibration of the detector position.

Sample displacement from the diffractometer center is another important source of alignment error. This is typically the largest single systematic error in XRD and ND experiments, but it can be corrected with internal standards [72]. Figure 2-36 illustrates schematics of properly aligned and poorly aligned samples. In the first case, the sample is properly placed at the diffractometer center *O*, bisecting the incident beam (*I*) and the diffracted beam that is measured by the detector, which has a radius *R*. At a certain 2θ angle (measured between the transmitted beam *T* and diffracted beam), Bragg-oriented grains will form an intense diffraction peak. If the sample is displaced from the diffractometer center by some value *r* in the x-y plane (see Figure 2-36b), the same diffraction peak will be erroneously measured at a location offset by some angular displacement $\delta\theta$. Consequently, care must be taken to place the sample at the diffractometer center. The use of internal calibration standards

within the specimen is useful for sample displacement verification. When this error is detected, the diffraction pattern can be shifted, or 're-zeroed' by the measured angular displacement $\delta\theta$. Figure 2-36 also illustrates how the beam width, its parallelism, and the 2θ resolution of the detector can contribute to instrumental broadening. Modern diffractometers utilize complex systems of slits, and other optical components to refine the beam and limit these effects.

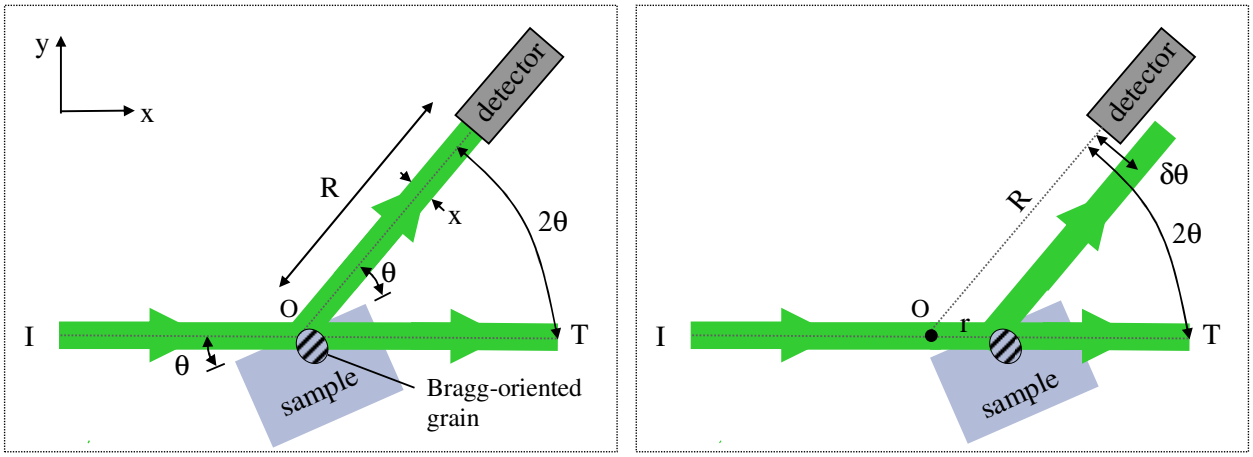

a) properly aligned

b) poorly aligned (misalignment = r)

Figure 2-36: Schematic of properly and poorly aligned samples

Computer applications can be used to predict the peak locations and peak profiles for complex diffraction patterns containing many phases. The general approach of such programs is to calculate a predicted diffraction pattern based on multi-parameter models for the diffraction profile contribution of each phase included. These models have a physical basis derived from the expressions in Section 2.11.1 and 2.11.2, which include important parameters such as the crystal structure, lattice size, atom positions, and instrument settings. Numerous physically-based profile fitting parameters (~20) are also incorporated to predict peak shapes (i.e., peak width and height). A least squares optimization technique is used by these programs to iteratively adjust these parameters and the predicted profile to improve its agreement, or fit quality, with the observed experimental pattern. The quantity minimized in the least squares refinement scheme is the residual, S_y [90].

$$S_y = \sum_i w_i (y_{oi} - y_{ci})^2 \qquad \textbf{(2-79)}$$

Where $w_i = 1/y_{oi}$, y_{oi} is the observed intensity of the i^{th} 2θ increment, y_{ci} is the calculated intensity of the i^{th} 2θ increment, and the sum is over all diffraction pattern data points over the recorded 2θ range. Once a stable solution is reached that minimizes S_y, the model's refined parameters can provide an estimation of the properties of the diffracting phases in the specimen (e.g., peak identification and location, lattice parameters, phase fractions). Such predictions require the input of a starting crystal structure for phases known to be present in the pattern. Instrument settings (incident beam wavelength, configuration, etc.) must also be input to accurately predict patterns and instrumental broadening effects.

GSAS (Generalized Structure Analysis System) is one such application developed by A.C. Larson and R.H. von Dreele that is commonly used for the detailed quantitative analysis of XRD and ND data [91]. A thorough description of GSAS can be obtained elsewhere [92]. Rietveld or LeBail profile fitting methods can be used to model diffraction patterns – each having different profile functions that can be used. Rietveld models can be used to calculate diffraction patterns fitting the experimental peak locations (for lattice parameter determination), and peak profiles (i.e., the integrated intensity of peaks) for phase fraction determination [90]. LeBail models can be used to determine lattice parameters by fitting the peak positions only. This model is useful when lattice parameters are of primary interest

Figure 2-37 shows an example of a Rietveld fit (using GSAS) to an experimental XRD pattern collected for a powder mixture containing Si and Al_2O_3. The observed experimental data are shown as individual points and the calculated diffraction pattern profile is shown by the solid curve approximating the experimental data. The corresponding *difference* between the observed and calculated data is also plotted at the bottom over the 2θ range. This provides an indication of fit quality. The *hkl* indices of individual peaks from the phases present were also identified using GSAS and labeled manually. The agreement between calculated and observed data in the figure shows a good fit quality. The parameters refined by the model (e.g., lattice parameters) therefore provide a good estimation of the specimen's phase characteristics.

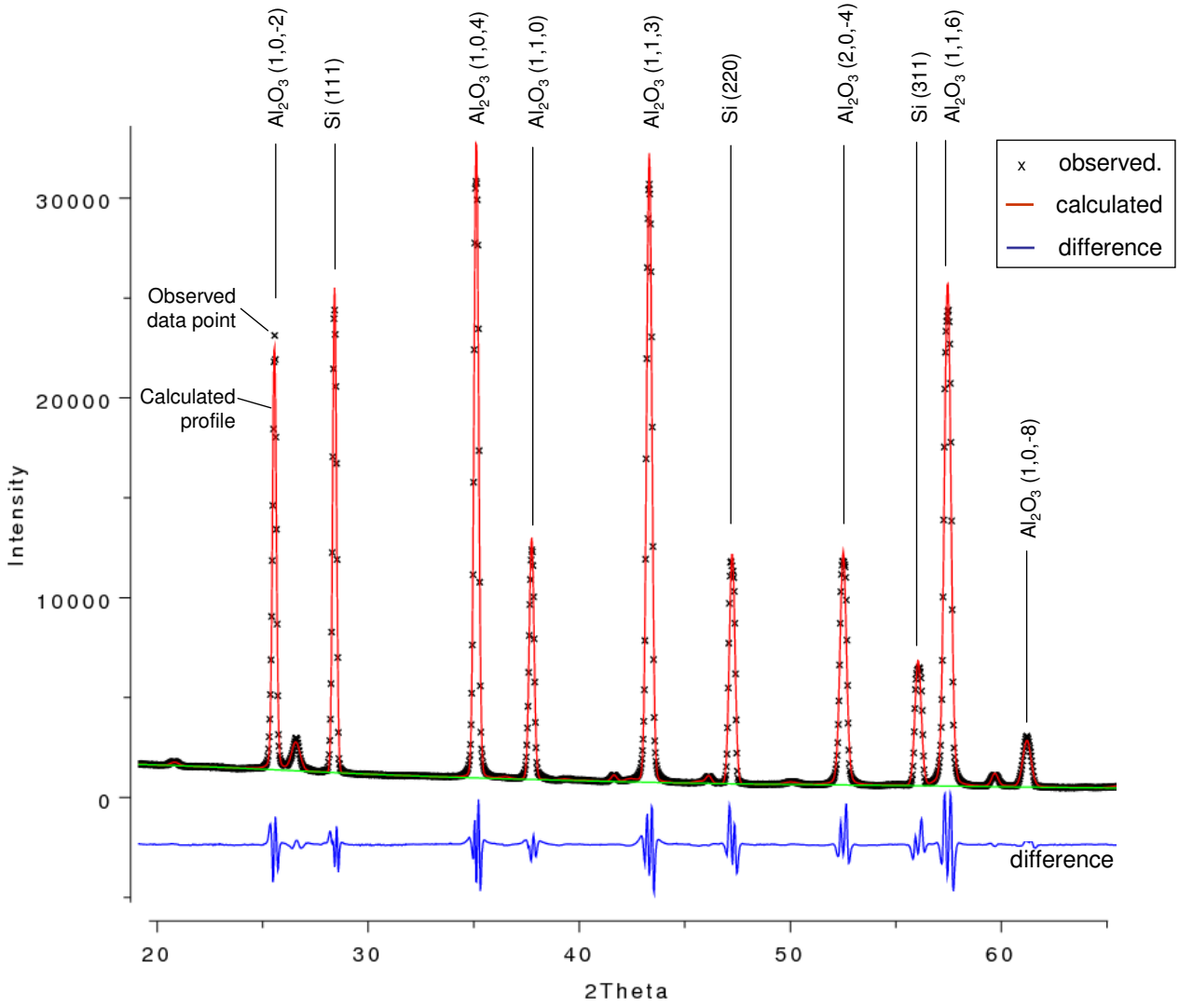

Figure 2-37: Sample GSAS Rietveld fit to an XRD pattern collected for an Al_2O_3 powder mixture

The accuracy of the data obtained from the fit parameters is determined by the quality of the full profile fit. Various fit criteria can be used to determine the quality of calculated profiles. The following residual terms, or *R* values, are commonly used and cited as quantitative indicators of fit quality.

$$R_P = \frac{\sum_i (y_{oi} - y_{ci})}{\sum_i y_{oi}} \qquad \textbf{(2-80)}$$

$$wR_P = \left(\frac{\sum_i w_i (y_{oi} - y_{ci})^2}{\sum_i w_i y_{oi}^2} \right)^{\frac{1}{2}} \quad \textbf{(2-81)}$$

Where $w_i = 1/y_{oi}$, y_{oi} is the observed intensity of the ith 2θ increment, y_{ci} is the calculated intensity of the ith 2θ increment, and the sum is over all diffraction pattern data points. Both of these residual terms apply to powder diffraction data, which is designated by the subscript *'p',* which differentiates them from single crystal fit criteria. Conceptually, both fit indicators provide a ratio of the observed-calculated intensity difference to the observed intensity, which is summed over the entire diffraction pattern. Therefore small R values indicate better fits (typically ranging from 0.05-0.15 depending on data and fit quality). The weighted wR_p term is considered to be more meaningful since the numerator is the actual residual being minimized by the least squares refinement scheme (S_y in Equation (2-79)). From a mathematical perspective, the wR_p term is also typically higher than R_p since the observed-calculated difference is squared. Furthermore, the w_i weighting term allows strong peaks to contribute less to the residual sum, but noisy backgrounds will contribute relatively more.

The accurate fit of experimental patterns via applications like GSAS for quantitative analysis is suited for defined, fairly homogeneous phases. Distinct, sharp peaks are predicted according to each phases' crystal structure. In the case of solid solutions with significant compositional variations, the measured experimental patterns can have significant compositional broadening, which is difficult to account for by profile fitting functions and least squares refinement of a variable lattice size. This is particularly true for isomorphous alloys such as Ni-Cu, where the entire 2θ region separating identical FCC peaks increasingly contributes to the very broad diffraction profile. As such, quantitative analysis using profile fitting applications like GSAS is limited for solid-solutions [107]. However, as in Rudman and Fisher's work as well as Delhez *et al*, the peak positions and qualitative analysis of the peak profile can provide valuable interdiffusion insight.

2.12. Justification of Current Work

The Ni-Cu system was selected for experimentation partly because it is an ideal model system with a simple, isomorphous equilibrium phase diagram. No intermediate phases exist in the alloy system and experimental diffusivity data are available for lattice and grain boundary mechanisms. From processing and commercial perspectives for future TLPS brazes, the Ni-Cu system is attractive for the following reasons: 1) Cu-based alloys are commonly used in brazing applications for their wetting ability, and conductivity [93, 94]; 2) increased high temperature strength and increased corrosion resistance from Ni alloying [93, 94]; 3) the binary isomorphous phase diagram allows significant processing flexibility in terms of additive content and processing temperature; 4) the unlimited solubility exhibited in the Ni-Cu system prevents the formation of undesirable intermediate phases during sintering (e.g., intermetallics); 5) large melting point shifts are possible by using a low sintering temperature (T_A = 1085°C) and the large range of available bulk composition (C_O) below solidus line; 6) Ni and Cu elemental powders are readily available in spherical form and varying sizes. Also, Ni-Cu-based alloys are common filler metal choices in joining steels because of their excellent corrosion resistance and high temperature properties [95]. Products such as aircraft turbine components, hydraulic fittings, automotive parts, heat exchangers, and honeycomb structures are some examples of components fabricated using Ni-Cu-based filler metals [94, 95].

A reliable experimental method for accurately and quantitatively characterizing TLPS process kinetics (i.e., during solid-state sintering and isothermal solidification) has the potential to reduce process parameter development time for the future applications of TLPS. This is particularly true in liquid rich mixtures where the amount and duration of the liquid phase are important to optimize the sintered material (e.g., density, composition) as well as the process itself (i.e., processing temperature and time). The value of accurate experimental data is amplified when similar studies are not available or accurate predictions cannot be generated using available models. The important contributions of accurate experimental data and the development of appropriate models are: 1) an improved understanding of the underlying science and mechanisms explaining the behaviour of the system studied; as well as, 2) the extension of this knowledge to similar bi-phase diffusion-controlled interactions; 3) a streamlined process optimization; and, 4) increased adoption of TLPS processing for suitable applications.

TLPS studies reported in the literature have primarily utilized dilatometric or *ex situ* metallographic analyses, which offer indirect evidence of the isothermal solidification process and the amount and duration of liquid formed. Experimental dilatometric studies [4,26,37,38] of powder mixture expansion/shrinkage have been used to infer information about the presence of a liquid phase during the sintering cycle. Similarly, metallographic analyses of specimens after the sintering cycle also provide indirect, qualitative information about the *ex situ* post-sintered microstructure. The amount of liquid initially formed as well as the amount which was present at T_P prior to cooling is difficult to determine by analyzing metallographic specimens once cooled to room temperature. This requires the identification of a previous solid/liquid interface at T_P for numerous representative particles as well as the amount of frozen liquid present. This approach is complicated and prone to error since the previous solid-liquid interfaces may have irregular shapes and may be obscured by preparation artefacts, intermediate phases formed during freezing, or further interdiffusion during cool down [96]. The latter complication is particularly important in isomorphous systems because only one solid solution phase is present after cooling below T_A due to the unlimited solid solubility of these systems. As a result, the two-phase diffusion problem of interest during isothermal solidification at T_P, which has a definite solid/liquid interface, is reduced to a single phase diffusion problem, which does not exhibit an interface, as the liquid solidifies and cools to room temperature. This limits metallographic analysis of isomorphous TLPS systems because microstructural evidence of the previous solid-liquid interface and the liquid regions are difficult to identify and measure after cool down. This emphasizes the importance of thermal techniques such as DSC to directly quantify the amount of liquid.

Differential scanning calorimetry studies with TLPS solders [10, 11, 13, 28] have shown that DSC allows the measurement of the amount of liquid formed at T_A as well as the amount present immediately after an interrupted isothermal hold at T_P by measuring the enthalpy of the melting and solidification/freezing reactions respectively. Thus, this method can provide more accurate, quantitative information about the amount of liquid formed and its rate of removal. However, in these previous studies [10, 11, 13, 28], DSC was primarily used to investigate isothermal solidification kinetics (excluding solid-state interdiffusion and dissolution effects) for binary eutectic systems aimed at low temperature solder applications. There is a current lack of literature presenting similar quantitative work for binary isomorphous systems, Ni-Cu

being included. The current study aims to implement and adapt the DSC technique for a higher temperature binary isomorphous system in order to quantify liquid formations and their rate of removal.

Unfortunately, the DSC technique can not provide direct *in situ* A-B interdiffusion information *during* the different stages of TLPS. Interdiffusion taking place during the initial heating and isothermal solidification stages do not generate measurable effects in DSC results [27, 96]. Instead, phase transitions such as the melting and freezing events are measurable at high temperatures near T_A. Previous DSC results for TLPS solders [10, 11, 13, 28] have found that only athermal melting and freezing/solidification events can be quantified for small specimens after specified individual hold times at T_P. This allows the measurement of the amount of liquid present at discrete points in the sintering cycle – i.e., the amount formed during melting and then solidified upon cooling. The measured change in the amount of liquid is used to determine the amount isothermally solidified over that time period. Therefore, multiple specimens are required for sintering experiments of varying isothermal hold time durations in order to characterize the rate of liquid removal during the entire isothermal stage. Limited information is provided about the mechanisms of interdiffusion explaining the solid-state sintering and isothermal solidification processes.

Neutron powder diffraction techniques offer a potential means of obtaining structural and compositional information for large specimens within controlled furnace atmospheres due to the large penetration depth of neutrons [74]. Structural and compositional information derived from neutron diffraction spectra collected *during* the athermal *and* isothermal segments (i.e., not only during the melting and freezing events) can provide clear indications of phase transformations and developing A-B concentration gradients arising from the diffusional processes assumed to be responsible for isothermal solidification. The significance of applying a neutron powder diffraction technique arises from the ability to probe bulk mixtures with a neutron beam throughout the sintering cycle to obtain *in situ* structural and compositional information. This information is not limited to discrete points in the sintering cycle and can provide a better understanding TLP sintering behaviour, A-B interdiffusion processes, and the isothermal solidification mechanism. The combination of DSC and NPD for analyzing TLPS processes, which has not been reported in literature (particularly for binary isomorphous liquid-rich systems), can provide very useful quantitative and *in situ* information.

2.13. Scope, Criteria and Constraints

This study is constrained to binary alloy cases in order to limit the complexity of the resulting analysis. Ternary and higher order systems, although potentially feasible for future commercial brazing applications, will not be considered. The potential barriers to interfacial interactions between the liquid and solid phases during sintering (e.g., impurities and oxide layers) must be minimized. However, flux ingredients to remove oxides will not be used as they can complicate the interpretation of results and densification. Fluxless brazes are commercially viable since they simplify preparation and reduce costs, but a fluxing agent is often required in practice. This additional complication will be avoided in this study since preliminary work with Cu and Ni powders sintered in high purity inert atmospheres indicates that this is feasible.

The powder materials and mixture compositions selected for the experimental work must be commercially available and suitable for isothermal solidification at processing temperatures within the limits of the DSC equipment. Furthermore, TLPS process kinetics must be sufficiently rapid to be measured with good resolution within a reasonable time frame.

This study aims to characterize the TLP sintering process for a high-temperature binary isomorphous system, which has potential applications as a braze filler metal. The development and mechanical testing of experimental TLP sintered joints is outside the scope of this study. This investigation will be approached using experimental and analytical modelling methods to characterize the different stages of TLPS, while focusing on the isothermal solidification stage. Experimental work will consist of studying powder mixtures using thermal analysis (DSC), diffraction techniques (x-ray and neutron), optical microscopy, scanning electron microscopy (SEM), and energy dispersive x-ray spectroscopy (EDS) for metallographic analysis.

In this study, the diffusional processes occurring during stages I-III will be primarily investigated in regards to quantifying liquid formation and the mechanism of its removal during isothermal solidification. The morphological changes during sintering shrinkage, liquid wetting, and the consolidation process are not the focus of this study and will not be thoroughly investigated.

3. Experimental Methods

3.1. Materials

With the study criteria outlined in Section 2.13 in mind, the powder constituents chosen for experimentation were selected based on the following criteria:

- The alloy system must have an isomorphous phase diagram where the melting point of the additive phase is within the operating range of the DSC instrument (1500°C) and the neutron diffractometer furnace (~2000°C).
- The constituent powders must attain a safe level of radioactivity shortly after neutron diffraction experiments in order to permit further manipulation and analysis.
- The constituents must be readily available in spherical form of varying sizes.
- The diffusivity of the solute in the base metal particles must not be too low. Furthermore, under the experimental conditions selected, TLPS process kinetics must be sufficiently slow to be measured with good resolution, yet within a reasonable time frame.
- The constituents must not be too reactive in air so that a fluxless process, with clean inert gas, can be used during sintering.
- Diffusivity and phase diagram data must be available in literature.
- The constituents chosen must be relevant to commercial brazing filler metals and applications.
- Previous TLPS studies using the same materials would be advantageous.

The copper(Cu)-nickel(Ni) system was found to be well suited for DSC and ND experiments based on the above criteria as well as the inherent attributes of a simple isomorphous system, which will be described below. Cu-based brazes are common braze filler materials due to good wetting and flow characteristics [94]. Previous TLPS studies with the

Cu-Ni system have been completed by Puckert et al [5,45]. This work, which includes some numerical modelling and experimental results (non-DSC), will be useful in the interpretation of results. From the binary isomorphous Ni–Cu phase diagram (Figure 3-1), Cu will be the additive phase, or melting point depressant and Ni will be the base metal. The respective melting points of each pure powder are 1085°C and 1455°C and Cu-Ni solid-solutions will melt over a temperature range bounded by the liquidus and solidus lines forming the miscibility gap for alloyed compositions.

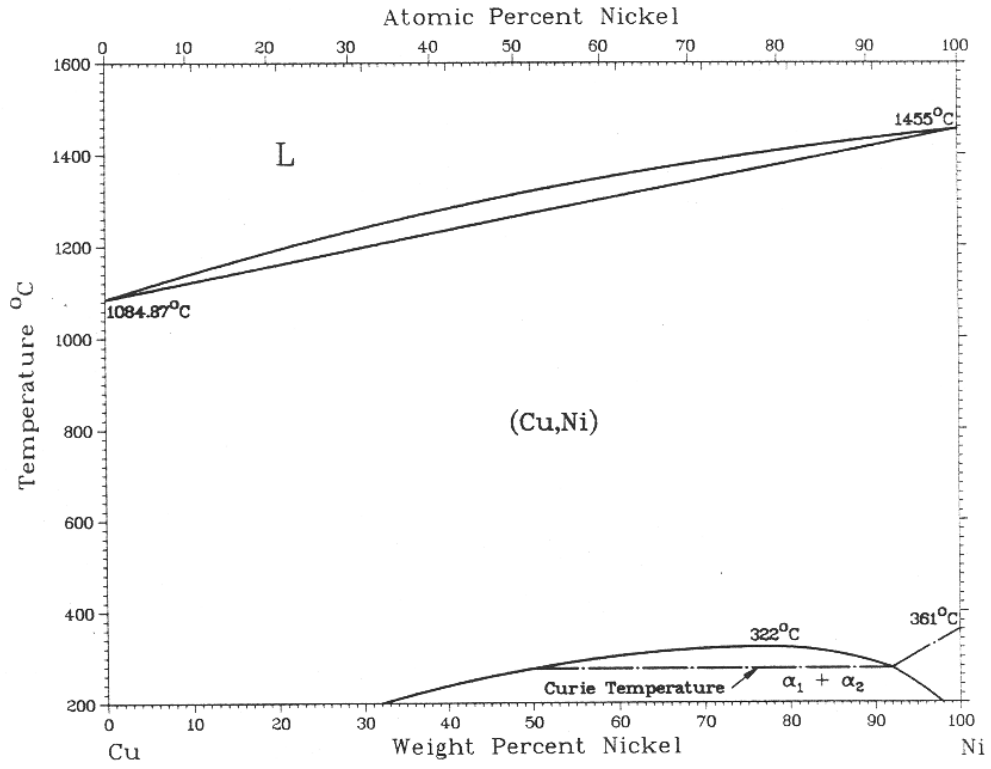

Figure 3-1: Cu-Ni phase diagram [97]

The Cu-Ni binary isomorphous system was chosen since it represents a simple model system for TLPS investigations with no intermediate phases, while having practical importance as a commercially viable braze material. As the phase diagram illustrates, this system provides significant TLP processing flexibility. Cu-rich liquids can be isothermally solidified in mixtures having bulk, or average, Cu contents over a wide range. Accordingly, a large range of sintering temperatures can also be used. The large melting point difference between Ni and Cu also indicates the large melting point shift potential of isothermally solidified mixtures.

Specimens were prepared from elemental Cu and Ni powder mixtures. Spherical, high-purity Cu and Ni powders were obtained from Alfa Aesar. The commercial availability of these powders at various sizes facilitated the preparation of specimens. Table 3-1 lists the powders used and their relevant characteristics as stated by the supplier. Each powder was stored in a nitrogen chamber prior to use in order to avoid long-term oxidation.

Table 3-1: Powder data

Powder	Purity (metals basis)	Specified size	Avg. size (*a*)	Shape	Supplier
Cu	99.9% <1000 ppm O	-170+400 mesh	23.09μm	spherical	Alfa Aesar
Ni	99.9% pure	-48+150 mesh	80.50μm	spherical	Alfa Aesar
Ni	99.9% pure	-100+325 mesh	57.51μm	spherical	Alfa Aesar
Ni	99.9% pure	dia. = 3-7μm	3.39μm	spherical	Alfa Aesar

The average size of the as-received powders (particle radius, *a*) was measured using a Horiba CAPA-700 particle size analyzer with the exception of the coarsest Ni powder, which was determined via optical microscopy due to its excessive size. The absence of impurities within the powders was verified via XRD and energy dispersive x-ray spectroscopy (EDS) analysis. The morphology of the powders was verified via optical microscopy and SEM (Figure 3-2). The Cu power was found to be very spherical with smaller non-spherical satellite particles – typical of a gas atomization fabrication process. The Ni powders were also found to have fairly spherical morphologies, but with a rough surface typical of powders fabricated via hydrometallurgical processing (i.e., the Sherritt process) [98]. The fine Ni powder was found to have a spherical, yet more spikey morphology – typical of Ni powder produced by the thermal decomposition of nickel tetra-carbonyl gas [98]. The rough surface projections of these Ni powders suggest that they are not completely dense particles. Furthermore, the non-smooth surfaces may affect liquid distribution and removal (vs. the ideally spherical case) since this surface morphology increases the surface area/volume ratio of the powders – thus affecting interdiffusion and liquid wetting processes.

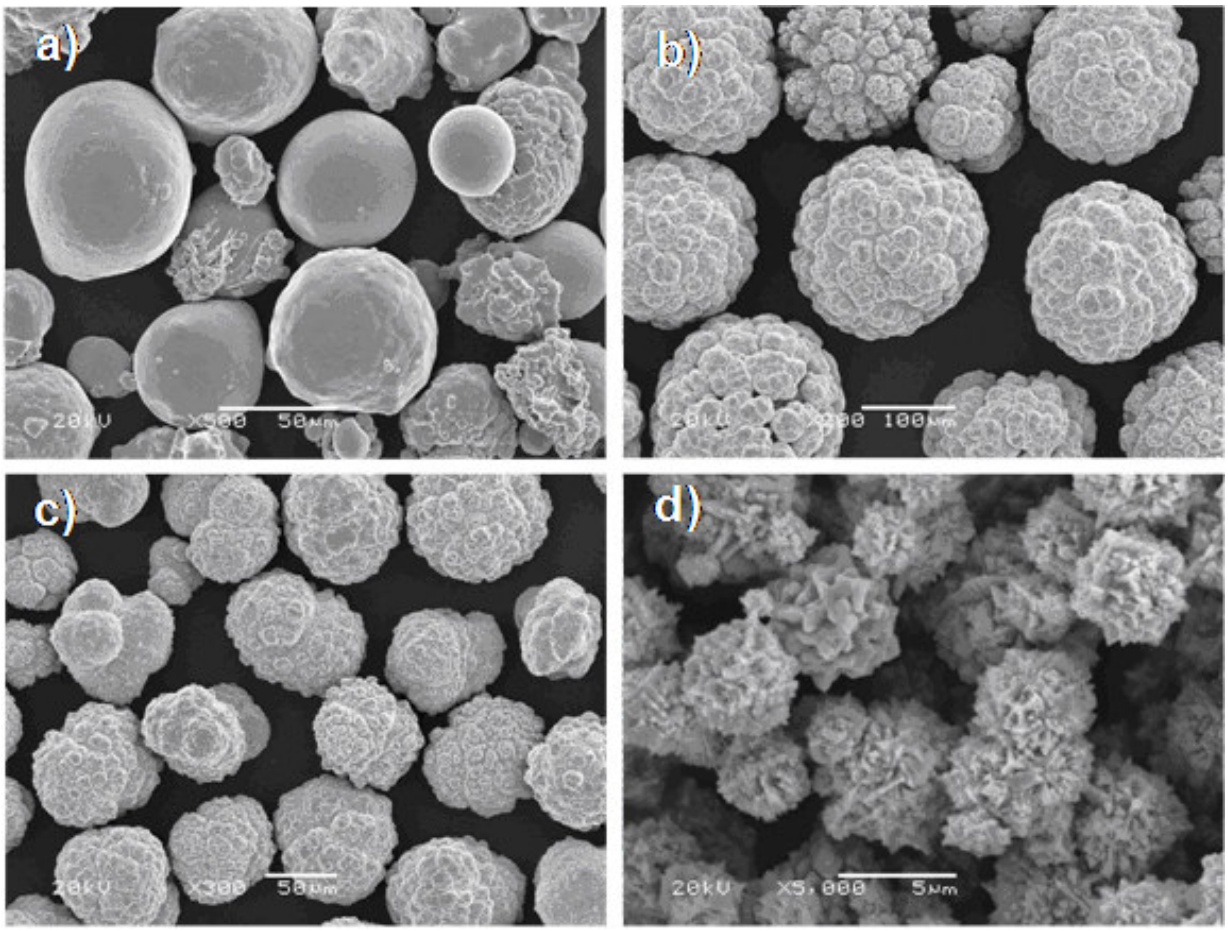

Figure 3-2: SE macrographs of: a) pure Cu powder, b) coarse Ni powder, c) medium Ni powder, d) fine Ni powder

3.2. DSC Experiments

3.2.1. Equipment

A temperature and enthalpy calibrated Netzsch 404C-Pegasus differential scanning calorimeter (DSC) was used for all TLPS experiments (see Figure 3-3). This system is comprised of: a heatflow measurement cell within a controlled cylindrical furnace; vacuum system; shielding gas delivery system; power supply; controller; and system computer. These sub-systems are well integrated within the commercial Netzsch DSC package – enabling time/temperature-controlled experiments, data collection, and data analysis. This instrument essentially allows the measurement of heatflow to or from a sample as a function of

temperature and time, while the sample is subjected to a controlled temperature program and atmosphere.

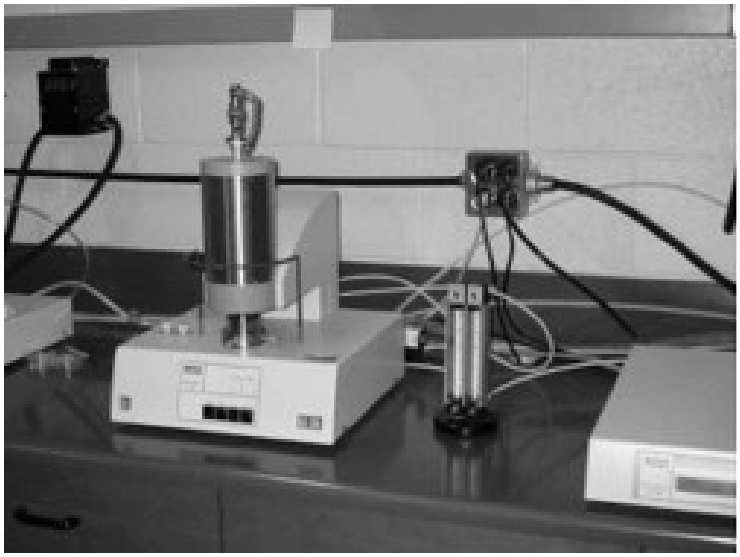

Figure 3-3: Netzsch 404C differential scanning calorimeter

The sample environment is contained within a tube furnace. The heat-flux measuring head supports the sample within the hot zone of the tube furnace. This DSC is capable of a 1500°C maximum temperature and linear heating rates ranging from 0.1-50°C/minute below 1200°C. The furnace can be evacuated to provide a vacuum and remove atmospheric contaminants prior to processing. Static atmospheres can be used as well as dynamic/flowing atmospheres of inert or reducing gases. The shielding gas is supplied from an external gas supply bottle equipped with a two-stage pressure regulator. The gas flow is controlled by an internal solenoid within the DSC and a manual flow control valve, which was set to a flow rate of 50 ml/min. in these experiments. High purity N_2 gas (99.998%, grade 4.8 supplied by Praxair) was used as a shielding gas for all experiments.

Temperature control and heatflow signal acquisition is performed by the TASC 412/3A thermal analysis system controller. Up to 64 individual temperature segments can be programmed into the controller with segment durations ranging 1 minute to 100 hours. The functions of the controller are temperature control and temperature linearization during isothermal and athermal segments. The TASC 412/3A is capable of sample temperature control (STC), which minimizes deviations from the nominal program temperatures via PID control. The temperature resolution is 0.1°C and accuracy is calibrated to within < ±3.0°C

using the melting onset temperatures of five elemental standard reference materials (SRMs) - namely indium (In, T_m = 156.6°C), Tin (Sn, T_m = 231.9°C), aluminum (Al, T_m = 660.3°C), silver (Ag, T_m = 961.8°C), and gold (Au, T_m = 1064.2°C). Au was specifically chosen since its melting point coincides with the temperature range of interest for Cu melting in TLPS experiments.

The sample holder consists of a heatflux measurement head (Netzsch model DSC-Cp) that is supported in the hot zone by an alumina capillary tube on which radiation heat shields are mounted (Figure 3-4). The DSC-Cp measuring head uses a type-S thermocouple (Pt/Pt-10%Rh) with a maximum temperature of 1650°C. The accuracy of this measuring head for specific heat and enthalpy determination are ±2.5% and ±3.0% respectively up to 1400°C. The stated measurement reproducibility of this system is < 1.5% for enthalpy changes and 0.3°C for temperatures below 1000°C [99]. Heatflow baseline reproducibility is < ±2.5 mW. Enthalpy calibration was performed prior to TLPS experiments using the measured melting enthalpies and known latent heats of fusion for the standard reference materials mentioned above.

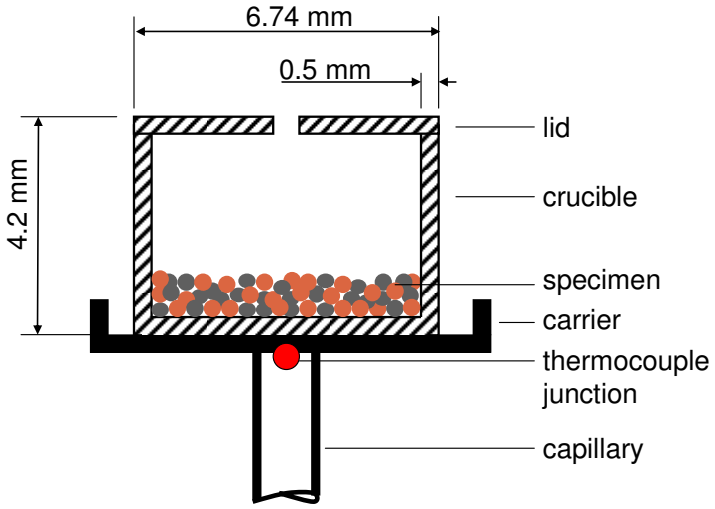

Figure 3-4: Schematic set-up of powder specimen within Al_2O_3 crucible placed on the measuring head of the DSC sample carrier

Alumina (Al_2O_3, or corundum) crucibles were supplied by Netzsch for sample containment (Figure 3-4). Ventilated lids were placed on top of the crucibles. The sensors (i.e., thermocouple measurement junctions) are located in the measuring head below the crucibles. Thermal events occurring within the sample, such as melting or solidification, cause an

endothermic heat influx or exothermic efflux relative to the adjacent empty reference crucible. The enthalpy of these phase transformations is conducted through the crucible and measured by the thermocouples. Although the conductive properties of alumina are not ideal, this thin-walled ceramic oxide material is well suited for this application since it is very stable at high temperatures. As such, alumina provides inert sample containment free of metallurgical interactions with the specimen. Metal crucibles, such as Pt and Al, have improved conductivity but dissolution by the powder melt and cost considerations restricted their use.

Al_2O_3 crucibles are reusable after cleaning. The cleaning process consisted of soaking for 30 minutes in a hot aqua-regia solution freshly prepared from concentrated acetic and nitric acids in equal parts. The crucibles were then rinsed and ultrasonically cleaned in acetone for 30 minutes. The crucibles were then rinsed in distilled water and then baked in air at 1475°C to burn off any remaining contaminants.

3.2.2. Sample Preparation Techniques

The initial liquid content of TLPS samples was varied by a change in bulk composition of the mixtures (C_O) from 35 to 75 wt.% Cu. However, after a preliminary liquid formation and densification study, the remainder of the work focused on a Ni-65wt% Cu composition. Initial liquid distribution was varied using the two following preparation techniques (Type A and B), which will be examined in detail in Section 4.1:

A) Layered/pressed powders: Cu and Ni powders were individually poured directly into a die in the correct proportion and then uniaxially pressed at 165MPa to form 100mg, layered disc-shaped compacts 4.75mm in diameter. This created a Cu powder layer that was poorly distributed amongst the Ni powder and therefore a segregated liquid distribution

B) Loose/mixed powder mixtures: Cu and Ni powders were mixed to the desired bulk composition (C_O) and milled for 1 hour. This created a well distributed Cu powder amongst the Ni powders which would in turn lead to a well distributed initial liquid. Particle segregation was a concern in Cu-Ni mixtures containing the coarse Ni powder due to size mismatch. As such, samples containing this powder combination were individually prepared and mixed to ensure accurate bulk compositions.

The mass of powder specimens was measured using a Scientech SA-210 auto-calibrating analytical balance with a readability of 0.1mg. All samples were prepared to have nominal masses of 100 mg, which varied by ±1 mg from sample to sample. The composition of the mixtures was controlled to within ±1 wt%. The total specimen mass was entered in the sample mass field of the DSC control program in order to enable normalized enthalpy measurements in units of J/g. Once a sample was weighed and placed into an Al_2O_3 crucible, the experiment details were then programmed into the DSC.

3.2.3. DSC Operation and Temperature Programs

Individual experiments were first set up using a personal computer that uses an IEEE 488 interface connection with the TASC 413/3A DSC controller. Temperature segments, shielding gas conditions and instrument settings are programmed via a Netzsch DSC-specific graphic user interface. Netzsch Thermal Analysis Data software (version 3.6) is also used for data interpretation and analysis.

The function of this correction file is to remove background instrumental and crucible effects from the experimental results. Figure 3-5 illustrates the temperature programs used for all sintering cycles in DSC experiments – consisting of athermal heat-up and cooling segments separated by isothermal segments of varying duration. In all cases a heating and cooling rate of 40°C/min. was used during athermal segments. Isothermal processing temperatures (T_P) of 1090°C (i.e., just past the melting point of pure Cu) and 1140°C were used during TLPS experiments. Isothermal segment durations ranged from 0 to 360 minutes. Data acquisition rates were set at 1 pt./s during all athermal and isothermal segments. At the end of the heat-up segments, transient overshoots of the isothermal processing temperature by the DSC controller were measured to be within 7°C of the nominal T_P and these were damped within 5-10 minutes.

High heating and cooling rates near the capability limits of the Netzsch DSC (i.e., 50°C/minute) were desirable in order to minimize Ni-Cu interdiffusion accrued during the athermal segments. A drawback of using high DSC heating/cooling rates is increased baseline shifting of heatflow measurements during these segments. However, previous DSC results indicated that 40°C/minute heating rates were experimentally feasible and sometimes

necessary to form measurable liquid fractions when using highly soluble, interacting powders such as Ni and Cu [11].

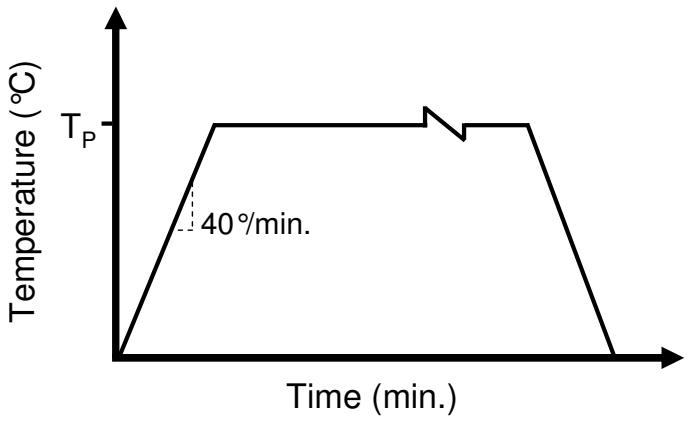

Figure 3-5: Temperature program used in DSC experiments

As such, 40°C/minute heat-up rates were chosen in order to minimize solid-state sintering and Ni-Cu interdiffusion in order to maximize liquid formations, which are desirable from a flowable braze filler metal perspective. Similarly, 40°C/minute cooling rates were used after the isothermal sintering segment in order to best preserve the high-temperature microstructure for metallographic analysis.

Isothermal segments at T_p = 1090°C were aimed at determining the effects of solid-state interdiffusion and sintering on the initial liquid fraction formed. Numerous specimens were isothermally held at T_P for varying hold times and then cooled to interrupt the isothermal solidification process and measure the remaining liquid solidification. Similar experiments at 1140°C were aimed at investigating the effects of increased T_P on the amount of initial liquid formed (as affected by melt-back and dissolution processes) and the rate of liquid removal. In addition to the two heating profiles described above, some samples were heated just below the Cu melting point (1070-1080°C) and cooled to observe the solid-state sintered 'pre-melt' structure. A selection of samples that had already been sintered were also re-heated to 1300°C to characterize the degree of homogeneity and altered re-melt behaviour due to the TLP sintering process.

Before a DSC experiment can be conducted, a correction file must be generated by performing a DSC trial using the desired temperature program in the absence of the sample. This is done to record the measured thermal behaviour of the DSC instrument and crucibles

(both empty) throughout identical temperature programs to be used for experimental trials for actual samples. The purpose of a correction file is to record, isolate and remove the thermal behaviour of the instrument and crucibles when analyzing data collected from experiments where the sample is included in the sample crucible. The intention is to obtain is flatter baselines that are less affected by experimental artifacts which can cause signal shifts. Figure 3-6*a* illustrates a typical correction file, which was obtained for empty crucibles heated to 1140°C for 2 minutes. The corresponding temperature history is also included (dotted line).

Once the correction trial was complete and experiment details were entered into the Netzsch control program, the crucible containing the powder sample was loaded into the sample carrier within the DSC measurement cell. The empty reference crucible was then loaded into the slot adjacent to the sample crucible. After the DSC furnace was lowered into position, the furnace chamber was evacuated using a mechanical pump and then backfilled with the N_2 purge gas. This purge cycle was repeated to ensure the atmosphere was free of oxygen and as inert as possible. Temperature programs were initialized at 20°C with the purge gas turned on. Once a purge gas flow was visually confirmed by the flow control indicator and positive pressure within the furnace chamber was established, the furnace exhaust valve was manually opened. This enabled the dynamic flow of shielding gas and prevented the backfilling of the sample environment with air. The experiment was then started using the control software.

The recorded DSC data was in the form of heatflow traces plotting Heatflow (mW or Mw/mg of sample mass) as a function of process time and temperature during the temperature program. Figure 3-6*b* illustrates typical DSC traces (corrected and uncorrected) for a pure Cu sample that was heated using the identical temperature program via the previously obtained correction file. The correct DSC trace clearly shows flatter baselines in the heatflow signal. The temperature segments and endothermic/exothermic peaks will be further discussed in Section 3.2.4. Once the trial was complete, the samples were removed and visually inspected using an optical stereoscope for any defects or initial observations prior to detailed metallographic analysis using SEM/EDS.

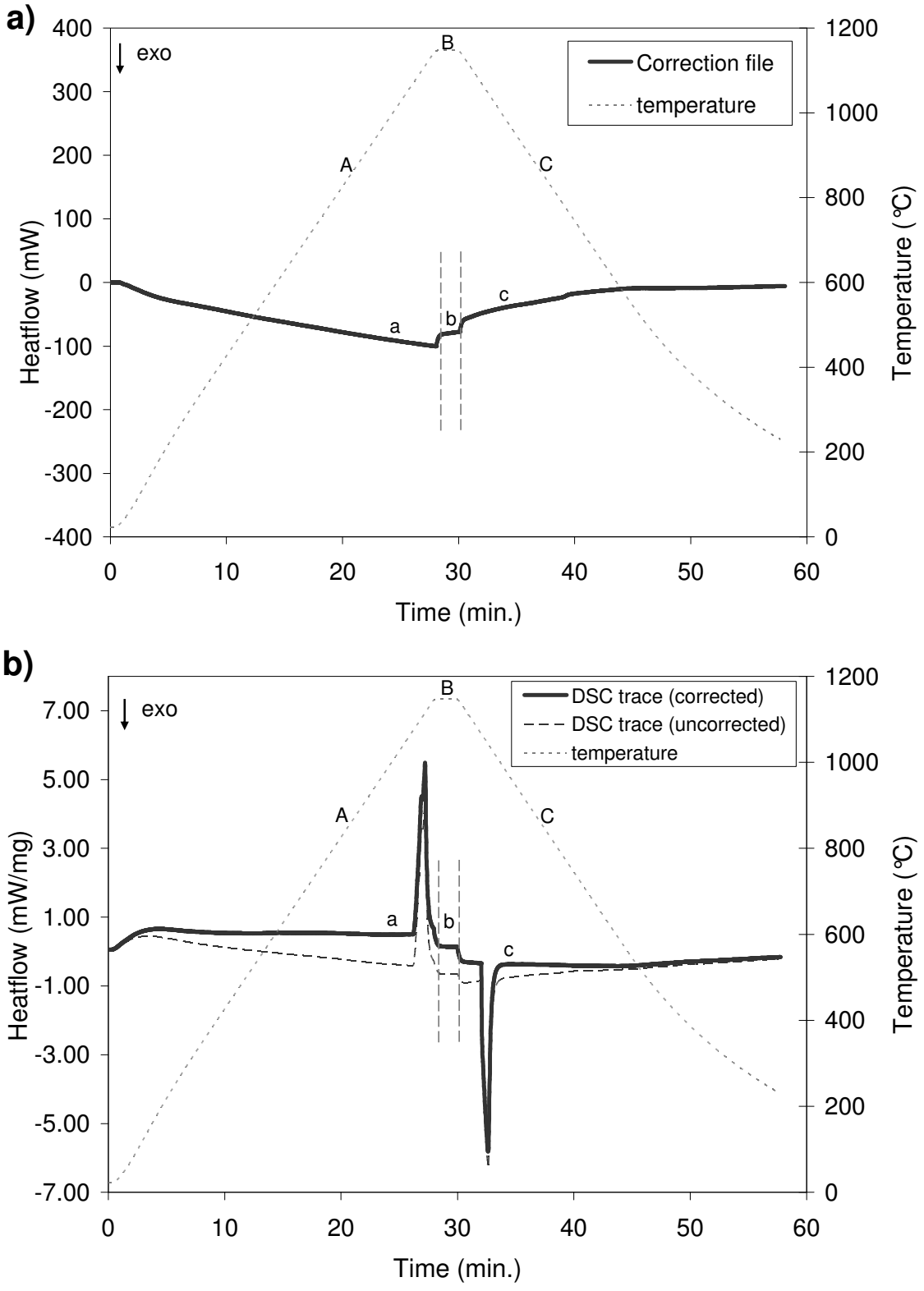

Figure 3-6: a) Typical correction file and corresponding temperature history for empty crucibles heated to 1140°C and held for 2 minutes. b) DSC trace (corrected and uncorrected) for a pure Cu specimen heated using identical temperature program. Individual temperature segments are labeled A-C and the corresponding heatflow segments are labeled a-c.

3.2.4. Analysis of DSC results

Once a DSC trial was complete, the Netzsch Thermal Analysis software (version 3.6) was used to interpret and analyze the acquired results, which are in the form of a time/temperature-resolved heatflow trace. Individual segments of DSC traces can be isolated and manipulated for comparison and measurement of important attributes such as reaction onset temperatures and reaction enthalpies. Figure 3-6*b* presents a typical time-resolved DSC trace for a pure Cu powder specimen isothermally held at 1140°C for 2 minutes. The measured temperature history is shown by the dotted line and the DSC heatflow trace is shown as the solid line. Individual temperature program segments have been labelled as A (heat-up), B (isothermal), and C (cool down). The corresponding segments of the heatflow trace are labelled *a-c*. By convention, the exothermic heatflow direction is down on the ordinate axis. As such, phase transformations such as melting, which require a heat influx to achieve a higher energy state, will create positive deviations from the DSC trace baseline – forming upward melting peaks.

In Figure 3-6*b,* the heat-up segment of the DSC trace (*a*) shows some initial drifting at low temperatures due to the rapid heating rate employed. However, 10 minutes into the segment a stable baseline is established. A large endothermic peak, also referred to as an endotherm, is visible at the end of the heat-up segment just below the isothermal hold at T_P. The onset of this peak was measured at 1085.8°C, which coincides with the Cu melting point. The isothermal segment (*b)* of the DSC trace is flat and does not show any interesting features since the Cu melt is free of metallurgical interactions within the inert Al_2O_3 crucible. The cool-down segment (*c)* shows a large exothermic peak, or exotherm, which corresponds to Cu solidification. At low cool-down temperatures (< 400°C) the DSC furnace is seen to be incapable of maintaining a 40°C/min. cooling rate and DSC trace baseline drifting is also visible. However, this behaviour is not a significant concern at these low temperatures (i.e., well below the solid/liquid regime of primary interest) since the sample is in the solid-state and free of phase transformations.

Figure 3-6 shows that DSC baseline shifts occur at the transitions between athermal segments and isothermal segments. These shifts coincide with the sudden changes in heating rate (*dT/dt*) between segments and are attributed to the normal hysteresis of the DSC trace baseline. These transitional baseline shifts can complicate the analysis of DSC peaks when the

start or end of a peak overlaps this instrumental effect. For example, the post-melt baseline on the right side of the melting peak in segment *a* is shifted due to the *a*-*b* segment transition. A similar baseline shift is found at the *b*-*c* segment transition upon cooling, yet in this case the solidification peak is not affected due to undercooling below the Cu melting point.

To identify temperature-specific phase transition such as melting, the athermal segments of DSC heatflow traces can be plotted as a function of temperature. Figure 3-7 illustrates ideal melting endotherms that are temperature-resolved. Case 1 illustrates how the onset temperature (T_{onset}) of a melting peak was calculated using the Netzsch Thermal Analysis software. The onset temperature was determined at the intersection of the extrapolated baseline and peak onset tangent.

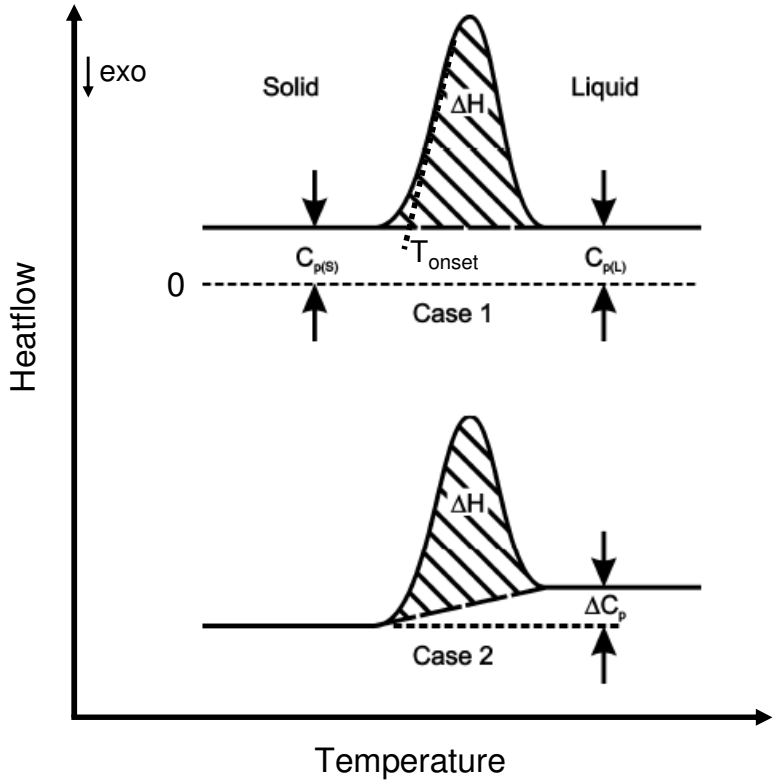

Figure 3-7: An illustrative comparison DSC endotherms when there is no baseline shift between the solid and liquid (case 1: $C_{p(L)} - C_{p(S)}$) and when there is (case 2: $\Delta C_P = C_{p(L)} - C_{p(S)}$) [adapted from 100]

The specific heat of the specimen, which is defined as the heat influx required to raise the material's temperature by one degree, determines the location of the baseline in regions of the DSC trace having no phase transition peaks (as plotted in Figure 3-7) [68]. The flat DSC trace

for case 1 in Figure 3-7 illustrates how an ideal material having a constant C_P will generate a flat baseline relative to the natural baseline of the DSC at heatflow = 0 J/g (a case where no sample or crucibles are present). Case 2 in Figure 3-7 illustrates how baseline shifts can occur across a DSC peak during phase transitions as a result of a C_p change in the liquid phase for example. Both cases in Figure 3-7 assume that C_P is temperature independent for illustrative purposes, but in reality C_P is a function of temperature.

The enthalpy of the observed melting, or solidification, phase transitions can be determined by measuring the area under DSC peaks. The magnitude of this measurement (ΔH_m in J or J/g) can provide an indication of the amount of liquid formed or solidified. It is important to note that the entire sample mass, as entered into the DSC control program, is typically used to calculate ΔH_m values in units of J/g. Case 2 in Figure 3-7 illustrates how C_P changes during the phase transition can complicate the determination of ΔH_m since baseline shifts across a DSC peak affect the area on integration. In the case of melting, this shift can be attributed to a change in specific heat (C_p) between the solid and liquid phase ($\Delta C_P = C_{p(\mathrm{L})} - C_{p(\mathrm{S})}$). Additionally, improved thermal contact between the new liquid phase and crucible after melting (relative to powder-crucible thermal contact resistance before melting) may also contribute to baseline shifting across the melting endotherm [96].

In this study, the area of DSC peaks was found by integration using the Netzsch Thermal analysis software. As illustrated in Figure 3-8, there are a variety of methods available for DSC peak integration and baseline interpolation in the presence of baseline shifting across a peak [68]. These include: a) linear, b) tangential sigmoidal, c) horizontal left or right starting, and d) horizontal split. The integration limits were manually selected using the Netzsch Thermal Analysis software and examination of the first and second derivatives of the DSC trace. The start of a peak was considered to be the point where the first and second derivatives began to increase as the DSC trace departed from the baseline. The end of a peak was determined at the point where the second derivative was zero. At this point the slope of the trace is no longer changing and the baseline can be considered to be re-established after the thermal event.

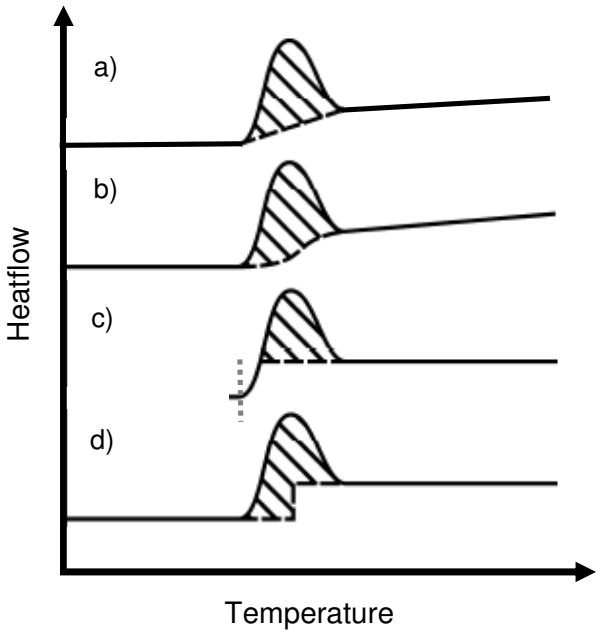

Figure 3-8: Baseline interpolation methods

Since the exact nature of baseline shifting across the peak due to thermal contact resistance and C_P effects is not well known, a linear interpolation method (*a*) was used in cases where a stable baseline is available on either side of the peak. Method (*c*) was employed in cases where only one stable baseline was available on either side of the peak for the given segment. This occurred when peaks are in close proximity to segment transitions that have unstable baselines and significant baseline shifts. As found in Figure 3-6 for the segment *b-c* transition as well as the endotherm at the *a-b* transition, these instrumental baseline shifts would falsely contribute to the peak area if a linear interpolation scheme were used. Method (*d*) was employed in cases where the segment transition was directly within a peak and therefore two horizontal baselines were used. This topic will be revisited in more detail with respect to preliminary TLPS experiments in Section 4.

3.3. Neutron Diffraction Experiments

The neutron diffraction experiments described in this work were performed on the C2 neutron powder diffractometer located at the Chalk River Labs (CRL) in Chalk River, Ontario, Canada. Access to this facility was achieved through the acceptance of a research proposal submitted to the Canadian Neutron Beam Centre (CNBC) [101], which is operated by the

National Research Council of Canada (NRC). Modifications of the experimental set-up at the CRL as well as the development of the experimental technique to study TLPS kinetics was a collaborative effort between NRC scientists (I. Swanson, L. Cranswick, and M. Watson) and the author. The experiments were conducted over two separate one week periods.

3.3.1. Material Characterization

Loose powder mixtures of coarse Ni powder and oxide-free Cu powder (see Table 3-1) were used for all ND experiments (65wt% Cu, 2.5g total powder mass). During the entire sintering cycle, these powder mixtures were contained within new alumina crucibles, which differed in size from those used in DSC experiments (see Figure 3-9). These long crucibles were designed to accommodate larger powder specimens and fit within the cylindrical sample environment of the C2 diffractometer furnace. All crucibles were specially manufactured by Anderman Ceramics Inc. (Burlington VT, USA) for this study. Larger powder samples (in comparison to DSC experiments) were desired in order to occupy a large incident beam cross-section and thus generate a sufficiently strong diffracted beam signal. This is an important consideration in reactor-based sources where the neutron flux is relatively low in comparison to pulsed accelerator sources.

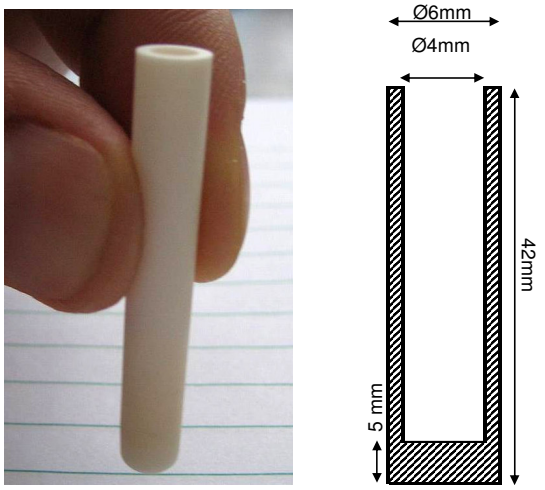

Figure 3-9: Alumina (Al_2O_3, or corundum) crucibles used in ND experiments

Additionally to providing inert sample containment, these crucibles would inevitably contribute to the measured diffraction patterns due to their proximity to the sample. As such, the Al_2O_3 peaks conveniently served as internal standards for the interpretation and analysis of

the evolving Ni-Cu diffraction patterns. Al_2O_3 diffraction peaks were used as a common reference for diffraction pattern alignment as well as a means of verifying the measured thermocouple temperatures during the high temperature portions of the sintering cycles. Since corundum is a very stable aluminum-oxide ceramic and has no sample interactions within the temperature range studied (as found with current DSC studies), the observed Al_2O_3 peak shifts during high temperature experiments can be used to determine the thermal expansion of the Al_2O_3 lattice at a given temperature. The comprehensive compilation of thermal expansion data by Touloukian [81, 82] was then used to determine the theoretical temperature necessary to cause the measured degree of thermal expansion. This temperature could be compared to the measured thermocouple temperature. This technique necessitated the accurate measurement of the starting Al_2O_3 lattice parameters in order to verify the room temperature lattice size of the crucible material, which is the reference point for thermal expansion calculations (i.e., the denominator in $\Delta a/a_O$).

High resolution XRD measurements were performed at the University of Waterloo in order to verify the purity of the crucibles as well as to obtain high accuracy Al_2O_3 lattice parameter measurements. Two different powder diffractometers were used as shown in Table 3-2 (i.e., Inel XRG 3000 and a Bruker D-8 Advance). Furthermore, a silicon powder internal calibration standard was used with both diffractometers in order to establish a high degree of confidence in the Al_2O_3 lattice parameter measurements. The Si powder used was a high accuracy standard reference material (SRM) obtained from the National Institute of Standards and Technology (NIST), which is intended for use as a standard for calibration of diffraction line positions and shapes for powder diffraction. The certified lattice parameter for this powder (NIST 640c Si powder) is 0.54311946 nm ± 0.00000092 nm at 22.5°C [102].

Table 3-2: X-ray diffractometer specifications

Specification		Bruker D-8	Inel XRG 3000
Radiation λ:	Cu Kα1	1.5406 Å	1.5406 Å
	Cu Kα2	1.5444 Å	removed by slits
	Configuration	Bragg-Brentano	Curved position sensitive
	Detector	scanning point detector	detector array
	2θ Range	20-120°	0-112°
	2θ Resolution	0.02°	0.03°
	Sample holder	Al flat plate	rotating Al flat plate
	Atmosphere	air, 24°C	air, 24°C

Prior to XRD measurements, an alumina crucible was first hand-crushed using an agate mortar and pestle. This powder was then ground in acetone using a McCrone Micronizing Mill located at the Chalk River Labs to obtain a very fine powder that was free of possible texture effects. The extracted alumina powder was then mixed with 15 wt% NIST Si powder, which would serve as a highly accurate internal standard for XRD data analysis. XRD measurements were then performed on both diffractometers with the mixed Al_2O_3 and NIST Si powders. The XRD sample environment temperature was measured to be 24°C for both diffractometers. The 1.5°C deviation from the NIST Si 640c certificate temperature of 22.5°C was found to create a negligible thermal expansion of the Si lattice according to Touloukian *et al* data for Si [82].

The recorded XRD patterns were analyzed using GSAS [91] least-squares refinements in LeBail fitting mode using peak positions to determine lattice parameters. Peak intensity and shape fitting was not necessary in this case since the weight fractions of Al_2O_3 and Si powder were not of interest. GSAS refinements of the LeBail fits were performed by fixing the Si lattice parameters to the NIST 640c certificate values and allowing the Al_2O_3 lattice parameters to be refined until a stable, converging fit is obtained that minimizes the difference between the observed and calculated data. In doing so, the NIST Si powder served as a highly accurate internal 2θ° calibration. Figure 3-10 and Figure 3-11 show the observed diffraction patterns obtained from the Inel and Bruker diffractometers respectively (observed, experimental data is shown as individual points). The calculated profile fit from GSAS is shown as the solid curve that approximates the experimental data points. The corresponding difference between the calculated and experimental data is shown at the bottom of both figures over the 2θ° range (i.e., *difference* = observed – calculated). These figures are included to simply illustrate and compare the fit quality of both patterns using the known phases present. Therefore the numerous peaks formed are not individually labeled since observing the fit quality and the *difference* plots is primarily of interest here.

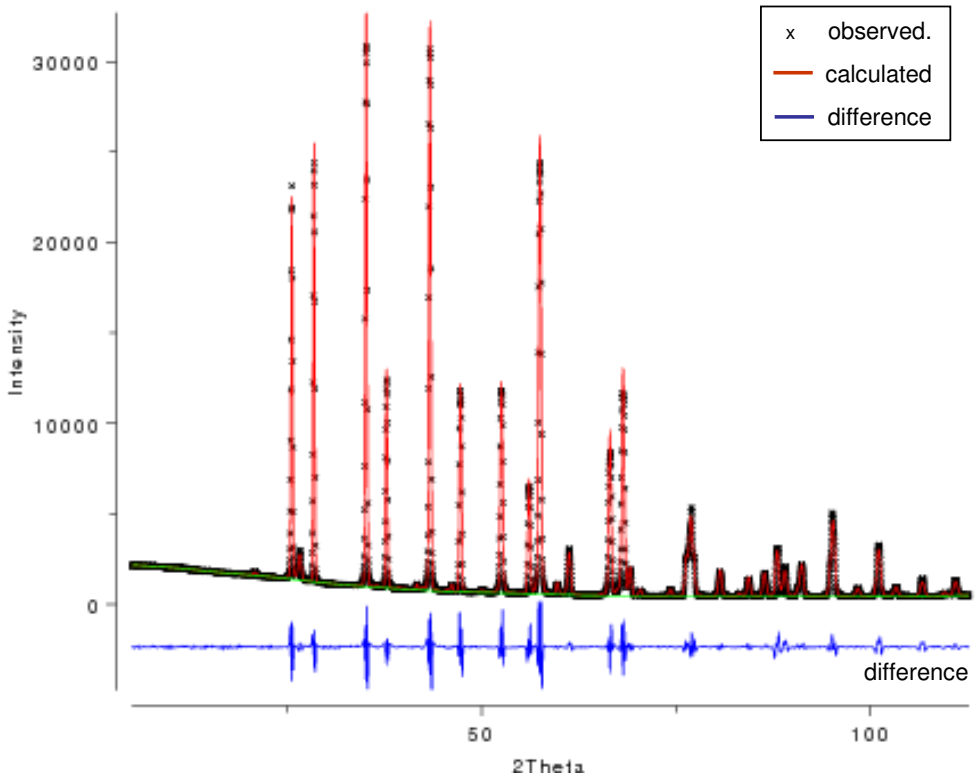

Figure 3-10: GSAS fit of INEL XRD data for Al_2O_3 crucible material.

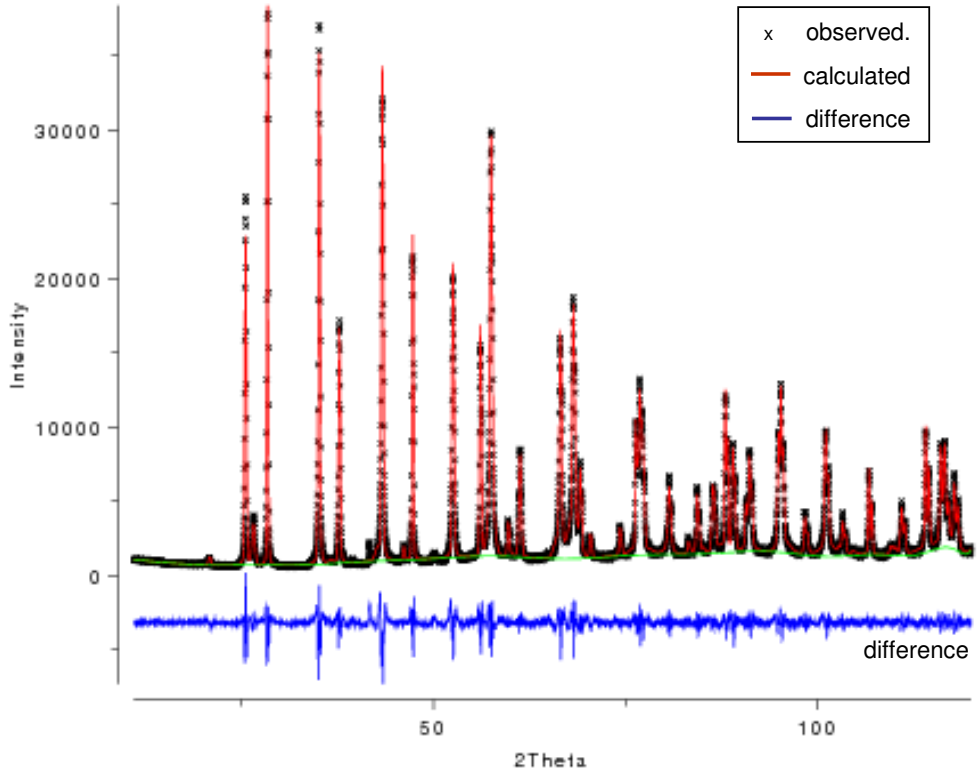

Figure 3-11: GSAS fit of Bruker-D8 Advance XRD data for Al_2O_3 crucible material.

Both patterns in Figure 3-10 and Figure 3-11contain only Al_2O_3 and Si peaks, with the exception of initially unknown low intensity peaks found at ~26° and 50°. This phase was identified as silica (SiO_2), which was introduced to the powder mixture in small amounts during the hand grinding process. It was observed that crushing the Al_2O_3 crucibles resulted in abrasion of the agate mortar and pestle surfaces during hand grinding. This can be expected since alumina is harder than silica, which is a major constituent of agate. The absence of Si or SiO_2 in the as-received crucibles was verified by SEM/EDS analysis.

Figure 3-10 and Figure 3-11 show that both diffraction patterns can be predicted using GSAS and the appropriate instrument parameter data. However, a comparison of the observed diffraction data reveals some of the inherent configuration and design differences of the two XRD instruments (see Table 3-2). For example, the Inel peak intensities decrease significantly at higher angles. This is believed to be due to the curved stationary detector array and rotating sample of the Inel instrument. Comparatively, the Bruker XRD pattern contains many more peaks that are stronger at higher angles. The additional peaks are due to the presence of unfiltered Cu$K\alpha_2$ incident radiation from the x-ray source. This is common in some commercial diffractometers. Unfiltered incident CuK_β and Cu$K\alpha_2$ radiation causes overlapping peaks or shoulders at low angles and smaller $K\alpha_2$ double peaks, or doublets, at higher angles. These peaks are not found in the Inel data since this diffractometer filters this portion of the signal using slits.

Detailed observations of the curve fits in Figure 3-10 and Figure 3-11 at high and low angles indicate good agreement between the calculated profiles and observed data. This is further supported by the low R terms shown in Table 3-3, wR_p and R_p (weighted and unweighted respectively). Table 3-3 also provides the calculated Al_2O_3 lattice parameters and their corresponding estimated standard deviations from GSAS. The GSAS fits of both data sets generated very similar *a* and *c* values, which differ only in the fourth decimal place and within one respective standard deviation. These values are also quite similar to those found in other studies (a = 4.76050 Å, c = 12.99560 Å) [103]. As such, the experimentally measured lattice parameters are assumed to be sufficiently accurate for the actual Al_2O_3 crucible material used in this study. It was decided to utilize the Bruker data as the internal reference values (a =

4.76032 Å, c = 12.99472 Å) due to its marginally better agreement with literature values, yet more so due to the availability of the Bruker XRD for further measurements in future work.

Table 3-3: GSAS LeBail fit results for INEL and Bruker XRD data

	Alumina lattice parameters				Residual terms	
Data Source	**a (Å)**	**σ_a (A)**	**c (Å)**	**σ_c (A)**	**wRp**	**Rp**
INEL XRD	4.76025	0.00007	12.99414	0.00027	0.0783	0.0563
Bruker XRD	4.76032	0.00005	12.99472	0.00020	0.1035	0.0758
Lutterotti *et al*	4.76050		12.99560			

3.3.2. C2 Neutron Powder Diffractometer

Figure 3-12 provides a general layout of the NRU reactor and the six spectrometers at the Chalk River Labs. The C2 and C5 spectrometers, which are named after the beam ports they utilize, are incorporated into a large DUALSPEC instrument. The C2 spectrometer (shown in the photograph in Figure 3-13) is a powder diffraction class instrument which uses a monochromatic incident beam to probe particulate, polycrystalline materials. Table 3-4 lists the important specifications and configuration used during this study.

Table 3-4: C2 Neutron powder diffractometer specifications

Neutron beam λ	1.33069 Å
Detector	curved stationary array
2θ Range	20-100°
2θ Resolution	0.1°
Sample holder	cylindrical crucible
Atmosphere	furnace controlled

A planar silicon single crystal monochromator (Si531) was used at a take-off angle of 92.7° to generate a monochromatic incident beam having a wavelength of 1.33069Å. Calibration and alignment of the instrument were performed by CNBC-NRC staff. The incident beam wavelength of the experiments was calibrated using Rietveld GSAS analysis with an external standard of NIST Si 640c powder at room temperature. The samples were placed into vanadium canisters of 6 mm diameter. These were centered/aligned in the furnace body over the rotation axis of the sample stage using a dial gauge to minimize sample displacement from the diffractometer center [104].

The diffracted neutrons are detected by a curved 800-wire BF_3 position sensitive detector which spans an 80° 2θ range. The detector wire spacing provides 0.1° angular resolution over

the 80° diffraction angle range, which is measured simultaneously. This instrument uses stationary, adjustable, and oscillating Soller slits to refine the incident and diffracted beams and limit beam broadening effects. The detector floats a few thousandths of an inch over an epoxy dance floor with the aid of a high-pressure air supply. Its position can be adjusted by a small harmonic drive coupled to a rubber wheel on the epoxy floor, providing positional reproducibility of approximately 0.002º 2θ [104]. The resulting diffraction patterns are acquired and recorded throughout an experiment in the form of neutron counts (intensity) vs. angular position (2θ°) via a computerized data acquisition system referred to as ATRANS.

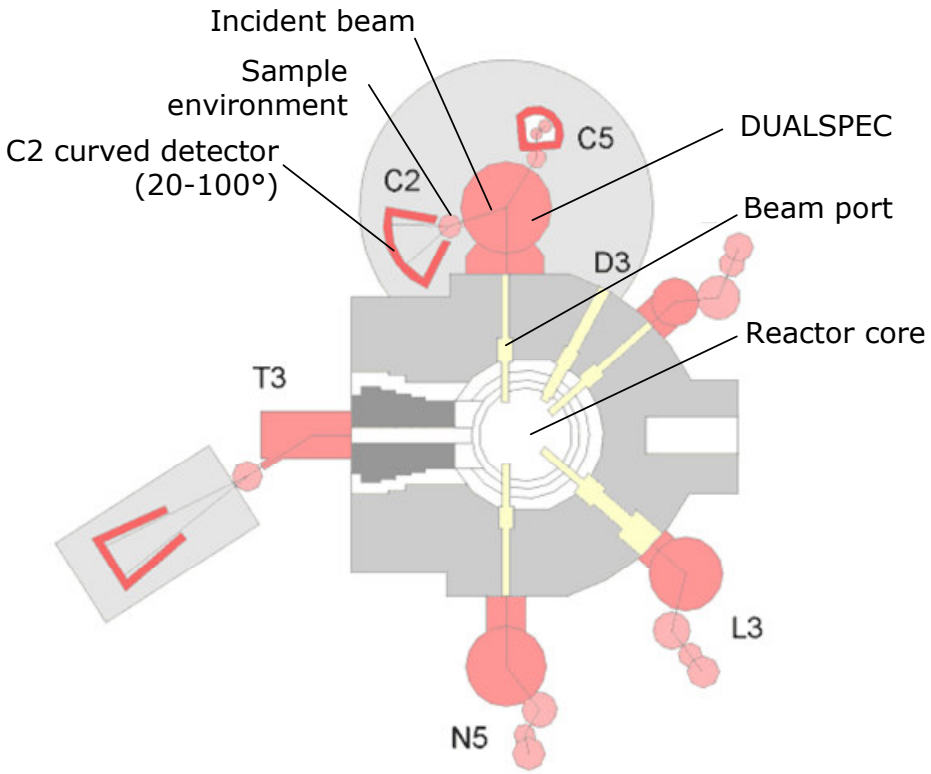

Figure 3-12: Top view layout of NRU reactor and ancillary spectrometers (Chalk River Labs, Chalk River ON) [75].

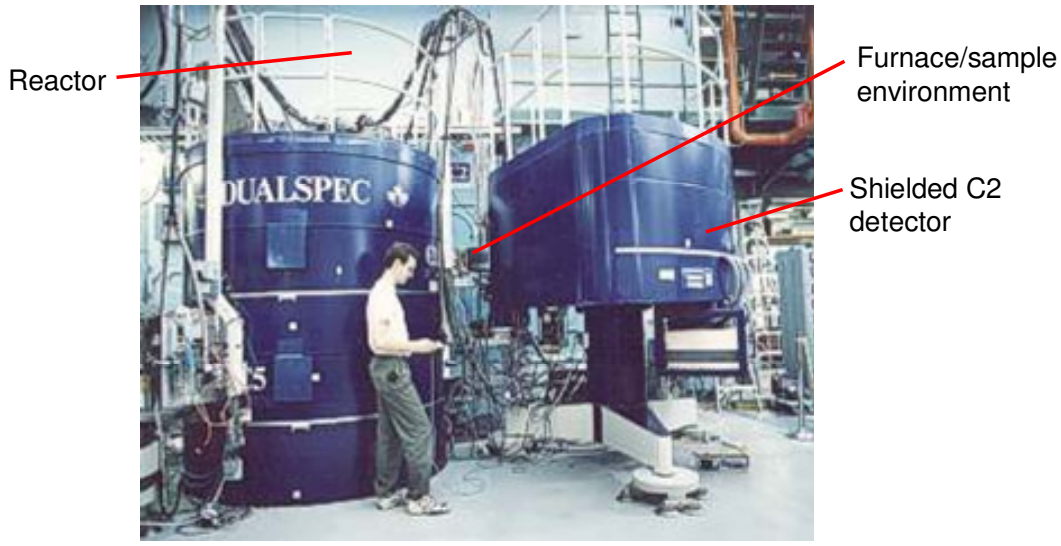

Figure 3-13: Photograph of C2 diffractometer [75].

3.3.3. C2 Sample Environment and Temperature

Figure 3-14 presents a photograph of the cylindrical furnace used in the ND experiments and Table 3-5 provides important furnace specifications and conditions, which will be described below. Figure 3-15 shows a 3D model of the C2 furnace, which was designed by M. Watson (CNBC-NRC). This model includes the important internal and external components of the high temperature furnace, which is capable of providing a vacuum sample environment during sintering, or if a sample canister is inserted inside the vacuum vessel (as shown in Figure 3-16) this furnace can also provide a gas atmosphere surrounding the specimen. In this configuration, the high vacuum (~3E-6 Torr) surrounding the sample canister provides thermal insulation for the heated area (i.e., hot zone). The vacuum restricts atmospheric conductive and convective heat transfer from the hot zone to the nearby furnace components, which can not support high heat loads (e.g., the Al furnace casing) - thus, the only remaining heat transfer mode is radiant. For convenience, the incident and diffracted neutron beams are also illustrated in Figure 3-15 as they penetrate through the different furnace components and sample.

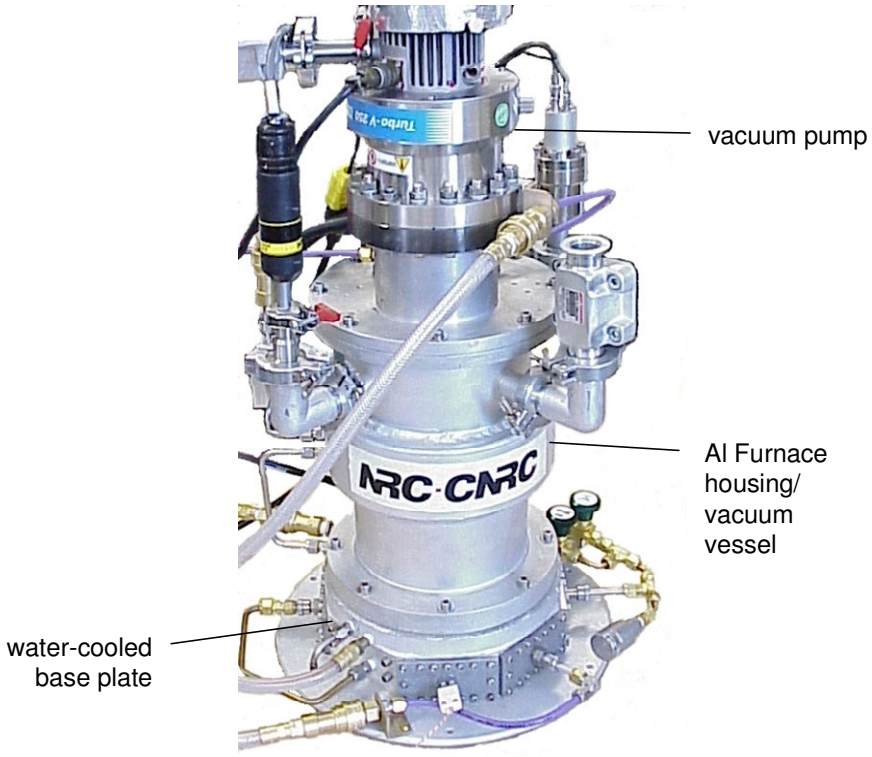

Figure 3-14: Photograph of C2 furnace used at the Chalk River Labs

Table 3-5: C2 Furnace conditions

C2 Furnace Conditions	
Sample atmosphere	N_2
Purity	99.998%, Grade 4.8
Flow rate	5 ml/min.
Pressure	1 atm.
Thermocouples:	Type-K (OMEGA-KMQXL) Ø0.04" sheathed wire, exposed jcn. 0℃ reference cell (OMEGA-TRCIII)
Heating rates:	10-40℃/min
Isothermal hold temp.	1085-1200℃
Vacuum pressure:	3E-6 Torr

Figure 3-15 shows the mounting flange for the vacuum pump used to evacuate the aluminum vacuum vessel. The vacuum vessel casing has a wall thickness of 3mm and is fabricated from 6061-T6 aluminum (Al). The relatively large diameter of the Al casing is sufficiently large to not contribute to the measured diffraction patterns since it is far from the aligned sample position. Thinned sections of the Al wall, which are not illustrated, provide 'beam windows' to further limit Al attenuation of the beam and the contribution of Al peaks to the measured diffraction patterns. Controlled resistive heating of a cylindrical tantalum heating element (0.125mm thick), which surrounds the vanadium sample canister, provides the

necessary heating rates. The Al furnace casing and vanadium canister are connected to the base of the furnace, which is water-cooled to prevent overheating of the purge gas lines and other furnace components. The hot zone of the furnace near the Ta heating elements is surrounded by multiple layers of molybdenum foil (0.00025 mm thick). These foils serve to reflect radiant heat back towards the hot zone to prevent heat losses, prevent overheating of the furnace housing and base, and to assist in providing a uniform temperature distribution. Aluminum, molybdenum (Mo) and vanadium (V) are suitable construction materials due to their high temperature properties and relatively low neutron scattering cross-sections, thus offering minimum attenuation of the beam and diffraction peaks [105]. They are considered to be relatively neutron-transparent materials. Although Ta has a relatively high neutron cross section, it is the material of choice for the radiant heater because of its high resistivity and low cost [106].

Figure 3-16 illustrates a sectioned 3D view of a vanadium canister, which reveals the sample environment inside. A flowing N_2 atmosphere is generated by a coaxial supply/return purge gas line entering at the bottom of the canister. The purge gas tube enters the canister from a sealed hole at the bottom of the sample environment (as shown in the 2D section diagram in Figure 3-17). The Al_2O_3 crucibles were placed at the top of the V canister such that the incident beam irradiated the specimen inside. The crucible bottom was supported by a small Mo foil spacer (not shown in Figure 3-17) and separated from the N_2 purge gas line (~30 mm). These measures were taken to reduce the convective cooling effects of the incoming purge gas and the conductive cooling effects of the water-cooled base.

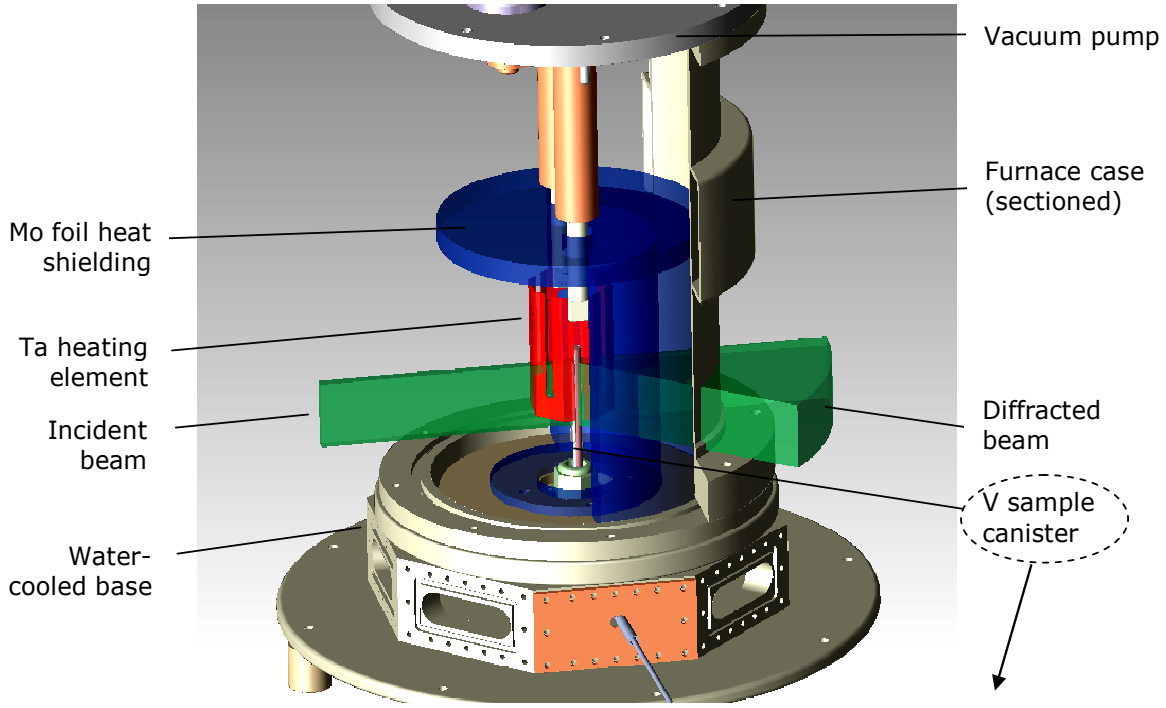

Figure 3-15: 3D Model of C2 furnace assembly [from 106]

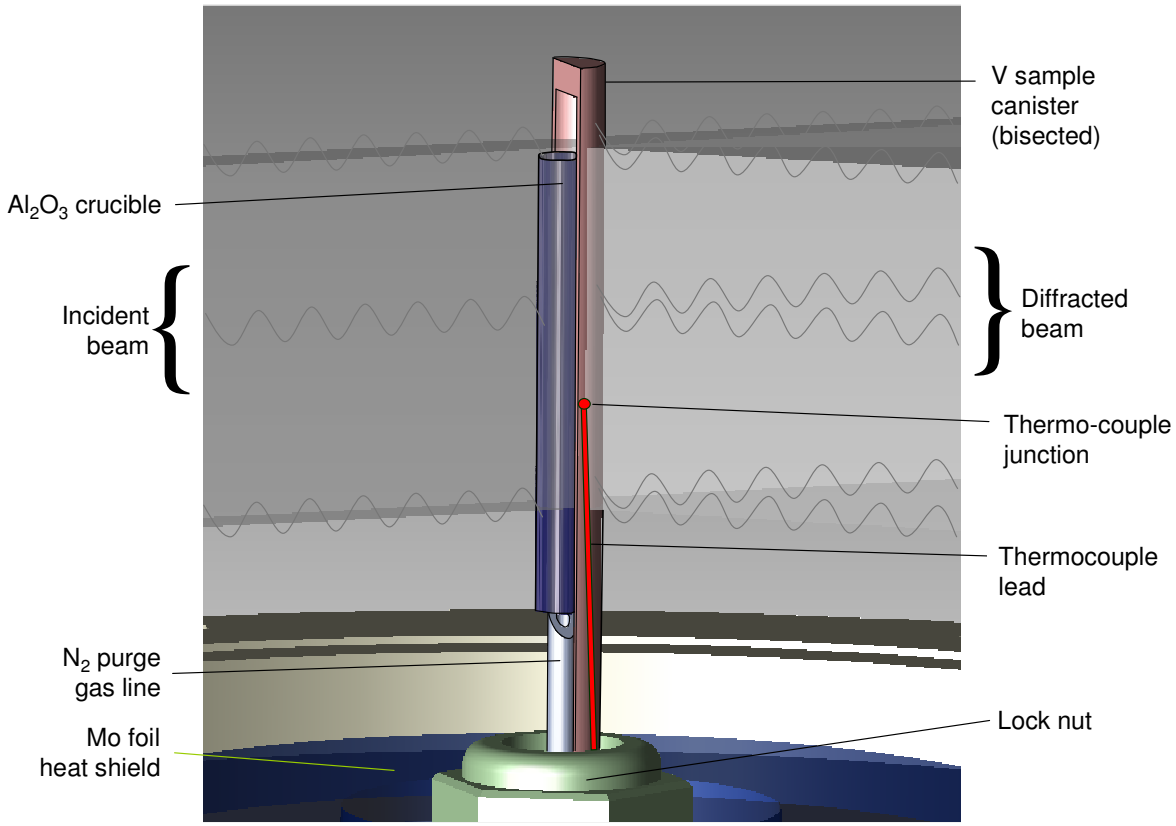

Figure 3-16: 3D Model of sample environment [from 106]

The V canister was secured to the furnace base by a large swage nut and Cu gasket, which seals the N_2 atmosphere from the vacuum vessel. Figure 3-17 also shows the position of the thermocouple measurement points used to measure the temperature at the mid-height of the vanadium canister surface. The exposed junctions of K-type thermocouple wires were securely attached to the V canister wall by tightening Ta wire around the canister and junction. A primary thermocouple (hereafter referred to as the control thermocouple) was used for feedback control of the sample temperature via the furnace control system. A secondary thermocouple (hereafter referred to as the secondary/read thermocouple) was placed adjacent to the control thermocouple to provide redundant temperature measurements for consistency and in the eventuality of erroneous readings or thermocouple failures. A precision refrigerator (Omega TRCIII, 0°C +/- 0.1°C) was used as an ice point reference cell for accurate thermocouple temperature measurements.

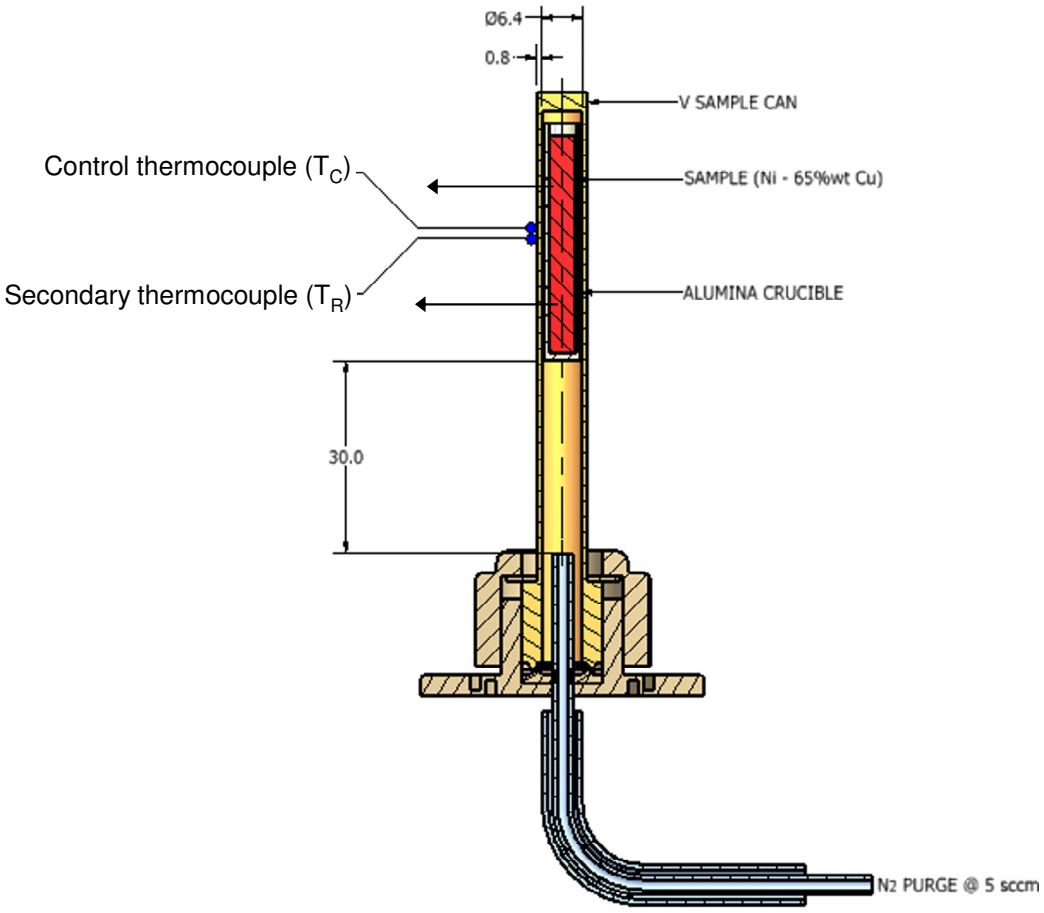

Figure 3-17: 2D section of sample environment and thermocouple placement for TLP sintering experiments [from 106].

Since the actual sample temperature inside the crucibles could not be directly measured and the fact that temperature gradients are inevitable in this furnace configuration, it was expected that the measured control and secondary temperatures (T_C and T_R respectively) would not necessarily provide accurate sample temperature readings. However, as previously mentioned, the measured *in situ* diffraction profiles were used to provide a means of internal temperature verification for each specimen. Al_2O_3 thermal expansion peak shifts and the removal of Cu peaks during Cu melting will be shown to provide good internal sample temperature references.

3.3.4. Temperature Programs

Figure 3-18 illustrates the typical temperature program used for ND experiments to study TLP sintering. Within the practical limits of the CRL equipment, the important aspects of the DSC temperature program (i.e., T_p and heating rates) were duplicated (as in Figure 3-5). Isothermal processing temperatures (T_P) nominally varied from 1085°C to 1200°C. Linear 40°C/minute heating rates were used during the heat-up segment as per DSC experiments. However, as will be discussed in Section 5, the furnace control system was not capable of providing this nominal rate in one experiment. Quenching from T_P after varying hold times was achieved by rapid furnace cooling. This was done in an attempt to quench and preserve the high temperature microstructure.

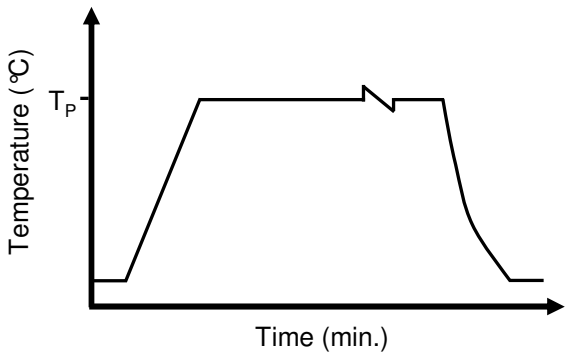

Figure 3-18: Temperature programs used for ND experiments

The temperature programs used for ND experiments were intentionally designed to be somewhat different than the DSC programs in certain aspects due to the nature of the analysis technique. For example, since the ND technique can provide *in situ* structural information

throughout the entire sintering cycle there was no need to perform multiple interrupted isothermal hold experiments. In this case, much longer isothermal segments were employed (ranging from 30-1040 minutes), which were used to study the TLPS process through to its completion (i.e., the formation of a homogeneous alloy). Another difference with respect to the DSC temperature programs was that short, isothermal hold segments (e.g. 30 minutes at 27°C) were appended to the beginning and end of the TLPS experiments. This was done in order to obtain stable room temperature diffraction patterns representing the pre- and post-sintered conditions. This room temperature data served as a consistent reference point for comparisons and was necessary to determine the degrees of peak shifting and thermal expansion.

3.3.5. Data Acquisition

The diffraction patterns can be obtained on the C2 diffractometer by continuously measuring neutron intensities over the 2θ range for desired scan duration. Typically, as scan time increases, the measured diffraction peaks become sharper and more distinct from the background signal since the signal/noise ratio (or peak vs. background intensity ratio) improves as more neutrons are detected. For *in situ* studies, numerous sequential diffraction patterns were recorded at specific time increments throughout the sintering cycle - generating individual Intensity vs. 2θ data sets sometimes referred to as scans. Each file had an associated time stamp corresponding to the end of the scan (i.e., the time when the data file was recorded) in order to accurately determine the elapsed time of each data set. The C2 control and data acquisition system permits two different means of recording numerous sequential diffraction patterns: 1) Recording data sets at specified time intervals (Δt), which commence once the experiment has started; 2) Recording data sets once a specific total scattered neutron intensity count (ΔI) has been reached for the full scattering angle range during a given scan interval.

The second approach was chosen since this would ensure that each pattern would have similar peak intensities and signal quality (i.e., peak/background signal ratio) [107]. This permitted the relative comparison of different data sets for various experiments since the total neutron count for each data set was constant. Since the NRU reactor power was nominally constant (~100MW), the thermal flux was also consistent (~ 5.26E09 n/cm^{2}s), a ΔI value was

determined that corresponded to a desired scan time interval Δt (i.e., $\Delta I \propto \Delta t$) [75]. The time stamps of the individually recorded diffraction pattern files were then used to verify the scan interval times and total elapsed time after each experiment. In some experiments, discrete, unavoidable reactor power fluctuations were encountered at the NRU facility (e.g., temporary shutdowns or reactor faults). This would cause immediate decreases in the beam's neutron flux and result in time gaps between the collected data sets. Fortunately, these gaps could be detected by verifying the time stamps and plotting the elapsed times of the sequential scans. This is explained in more detail in Section 5 Appendix A.

In the current study, diffraction patterns were acquired at short time intervals of 1 minute throughout the sintering cycle of each experiment to capture transient structural changes such as thermal expansion and phase transitions. This short time interval was selected based on a compromise between: 1) the time resolution limit of the C2 diffractometer to be able to generate accurate and resolvable peaks and 2) the desired time resolution deemed necessary based on the rapid isothermal solidification kinetics indicated by DSC results (i.e., rapid liquid removal and solute diffusion within the first few minutes of the isothermal segment). Preliminary trials done by CNBC-NRC scientists prior to TLP sintering experiments showed that 1 minute scans of 65wt% Cu powder mixtures at room temperature generated diffraction patterns with resolvable peaks representative of the mixture composition (described further in Section 5.1.1) [107]. If needed during the analysis of the data, these acquired 1 minute scans could be summed over longer time intervals (e.g., summing every 5 data sets), thus offering the flexibility of improving signal quality at the expense of time resolution.

The experiments, which had total durations ranging from 30 minutes up to 3500 minutes (~58 hours), generated numerous sequential diffraction pattern data sets as well as a 'summary' file describing each data set condition at the time of acquisition (time, temperature, neutron count). Figure 3-19 illustrates a sample of a small portion of a summary file generated at the end of an experiment. Individual diffraction patterns are numbered as sequential data sets within each row of the table. The associated date, time, and thermocouple temperatures of each data set during the sintering cycle are listed in the vertical columns. The time and temperature fields were important for verifying that the desired temperature program and scan

intervals where achieved. The 'monitor' field corresponds to the calibrated total neutron count (ΔI = 78600 detected neutrons), which approximately corresponded to a 1 minute scan interval.

Data set no.	Date	Time (hr:min:s)	No. of points	Monitor	T_C (°K)	T_R (°K)
1	18-OCT-2005	08:15:35	800	78600	291.4	291.2
2	18-OCT-2005	08:16:39	800	78600	295.3	295.0
3	18-OCT-2005	08:17:44	800	78600	299.9	299.9
4	18-OCT-2005	08:18:48	800	78600	300.4	300.8
5	18-OCT-2005	08:19:52	800	78600	300.0	300.4
6	18-OCT-2005	08:20:56	800	78600	299.9	300.2
7	18-OCT-2005	08:22:00	800	78600	300.1	300.3
8	18-OCT-2005	08:23:05	800	78600	300.2	300.4
9	18-OCT-2005	08:24:09	800	78600	300.2	300.4
10	18-OCT-2005	08:25:13	800	78600	300.2	300.3
11	18-OCT-2005	08:26:17	800	78600	300.1	300.3
12	18-OCT-2005	08:27:23	800	78600	330.4	330.7
13	18-OCT-2005	08:28:29	800	78600	357.5	359.6
14	18-OCT-2005	08:29:33	800	78600	387.2	391.7
15	18-OCT-2005	08:30:37	800	78600	409.1	416.3
16	18-OCT-2005	08:31:41	800	78600	425.4	434.2
17	18-OCT-2005	08:32:45	800	78600	437.1	446.9
18	18-OCT-2005	08:33:50	800	78600	442.1	452.0
19	18-OCT-2005	08:34:54	800	78600	445.3	454.8
20	18-OCT-2005	08:35:59	800	78600	447.3	456.3

Figure 3-19: Sample of summary file generate by ATRANS for a given experiment.

The original summary files generated by ATRANS did not contain an elapsed time field or temperatures in °C. Furthermore, ATRANS was found to be limited to recording a maximum of 400 sequential data sets per experiment. This limit corresponds to a maximum time of 400 minutes, or 6.7 hours. Since most TLP sintering cycles were intended to investigate homogenization at long hold times that exceeded this limit, sequential experiments were programmed into the data acquisition system for a given sample to circumvent this problem. This permitted the collection of well over 400 diffraction patterns per sample, but added some complexity to the file naming system and data interpretation. Figure 3-20 shows an example of a modified summary file which contains elapsed time calculations and temperatures in °C for N+1 ATRANS experiments/summary files for a given sample and TLPS sintering cycle.

Sample no. (N)	Data set no.	Date	Time (hr:min:s)	Elapsed time (min)	No. of points	Monitor	T_C (°K)	T_R (°C)	T_R (°K)	T_R (°C)
Experiment N	1	18-OCT-2005	08:15:35	0.00	800	78600	291.4	18.3	291.2	18.0
	2	18-OCT-2005	08:16:39	1.07	800	78600	295.3	22.1	295.0	21.9
	3	18-OCT-2005	08:17:44	2.15	800	78600	299.9	26.7	299.9	26.7
	↓									
	400	18-OCT-2005	14:56:00	400.42	800	78600	300.1	26.9	300.3	27.2
Experiment N+1	1	18-OCT-2005	14:57:04	401.48	800	78600	300.2	27.0	300.4	27.3
	2	18-OCT-2005	14:58:08	402.55	800	78600	300.2	27.0	300.4	27.3
	3	18-OCT-2005	14:59:13	403.63	800	78600	300.2	27.0	300.3	27.2
	↓									
	400	18-OCT-2005	21:38:08	802.55	800	78600	387.2	114.1	391.7	118.6

Figure 3-20: Sample of a modified summary file for a given sample consisting of multiple ATRANS experiments.

3.3.6. Analysis of ND Results

Once recorded by ATRANS, the raw ND pattern data sets were converted to the necessary formats (*.xy format for Powder3D analysis and *.GSA format for GSAS analysis). This was also done for 1-minute data and summed 5-minute data. GSAS [91] was used to identify individual phases and peaks within the indexed diffraction patterns as well as for verifying the phase fractions present when desired.

Powder3D [108] was used to analyse individual patterns and determine peak centroid positions at FWHM (i.e., a peak's centre 2θ position at half-maximum intensity). This application was also used for viewing large arrays of diffraction patterns since it provides powerful graphical presentation and analysis tools that greatly facilitated observations of the pattern evolution during sintering. Figure 3-21*a* illustrates a sample 3D plot constructed from individual 2D diffraction patterns that are plotted sequentially along the y-axis, which is analogous to elapsed time during the sintering cycle. The z-axis and x-axis plot intensity and 2θ data respectively. Figure 3-21*b* illustrates a corresponding 2D 'film plot' which consists of a 2D projection of the 3D plot, where peaks appear as dark lines evolving along the y-axis due to intensity contrast with respect to the background signal. As shown in Figure 3-21*c*, the film plot presentation method provides a clear top-view interpretation of diffraction pattern evolution by tracing the shifting peak positions over time. General observations of peak

locations, peak shifts, and broadening are more easily interpreted with respect to the 2θ axis for large ND data set arrays using this 2D projection method.

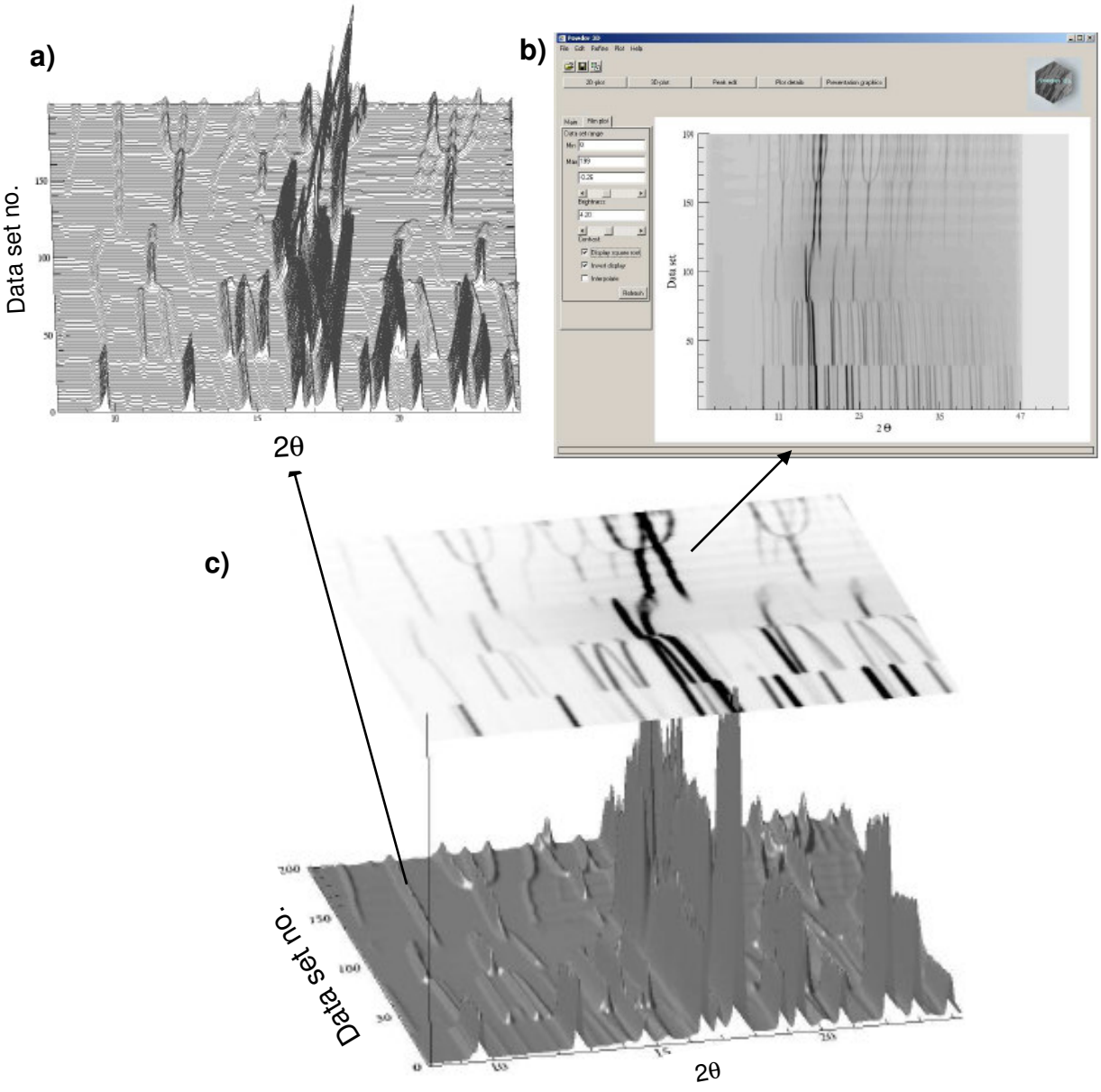

Figure 3-21: Sample outputs of Powder3D:. a) 3D line plot, b) 2D film plot showing projected intensity contrast, c) 3D surface used to project peak intensity contrast onto 2D film plot [109]

3.4. Metallographic Analysis

DSC and ND sample microstructures and compositions were analyzed by SEM/EDS and optical microscopy. Metallographic samples were prepared by typical metallurgical techniques as described below. However, once neutron diffraction sintering experiments were completed, ND samples could not be collected or handled immediately for metallographic analysis. These samples required approximately 1-2 weeks to become inactive and be deemed safe for manipulation and shipping by CRL staff.

3.4.1. Sample Preparation

Following DSC and ND experiments, the sintered specimens were mounted, polished, and etched if necessary. A polished cross section of the TLPS specimens was then obtained through bisecting the samples along their diameter. This was achieved by gradually polishing through the specimens, which were mounted in epoxy resin or conductive bakelite resin. Complete, unsectioned specimens were mounted for polishing in order to evaluate large, more representative areas of the entire sample microstructure.

The mounted samples were then manually ground using progressively finer SiC paper. Each specimen was ground to 1200 grit then cleaned ultrasonically in water prior to fine polishing. Fine polishing consisted of using progressively finer suspensions of diamond particles (6 μm, and then 1 μm) and lubricant on a Struers Labopolish5 machine. In some cases a slurry of Al_2O_3 particles was used. If the samples were to be etched, a diluted solution of equal parts nitric and acetic acid was prepared. The polished section was etched by immersing the sample in the etchant for 1 to 3 seconds depending on the sample size and rate of etching.

3.4.2. Optical Microscopy

The polished cross sections of the TLP sintered specimens were examined using optical microscopy. Images were captured with a digital camera at magnifications ranging from 10-1000X. An Image Pro image analysis software package was used for analyzing the collected images where appropriate.

3.4.3. Scanning Electron Microscopy

A JEOL 6460 scanning electron microscope (SEM) was used for high magnification metallographic examination of specimens. A 20kV electron gun acceleration voltage was used. Secondary electron (SE) imaging was used to interpret the morphology and topographical contrast of the sections. However, backscatter electron (BSE) imaging was primarily used since this mode provided chemical contrast between Ni and Cu rich regions. This SEM is equipped with an Oxford energy dispersive x-ray spectrometry (EDS) analysis system. EDS was used to quantitatively analyze the chemical composition of the samples at various locations on the cross section.

4. DSC experiments

A primary objective of this study is to develop an experimental DSC technique to measure the liquid fractions formed and their removal by isothermal solidification at T_P. Corbin and Lucier [13], used DSC to quantify these TLPS processes for Pb-Sn solder pastes, which constitute a relatively limited solid-solubility, low-temperature eutectic alloy system. Solid-state sintering, interdiffusion, and dissolution effects were not investigated since they were found to not be significant in this or other similar TLPS studies with eutectic powder systems performed at $T_P \approx T_{eutectic}$ [11,13,25]. Nonetheless, these DSC studies have shown that this technique is capable of quantifying the amount of liquid more accurately than the typical methods of visual inspection or other metallographic techniques which are inherently qualitative in nature. However, it is expected that solid-state interdiffusion during heat-up and dissolution at elevated T_P will affect the initial liquid and its removal in the isomorphous Ni-Cu system and therefore the DSC method must be validated for these effects.

4.1. Results and Analysis

Thi chapter will first present results from preliminary trials aimed at characterizing the thermal behaviour indicated by DSC traces for pure Cu specimens and Cu-Ni TLPS specimens. A method for quantifying liquid formations and removal at varying T_P will then be presented in the following section. The results will be presented systematically according to the stages of TLPS, namely 1) solid–state sintering, 2) melting/dissolution, 3) isothermal solidification and 4) homogenization. A description of these important TLPS stages was provided in Section 2.5.

4.1.1. Characterization of Pure Cu Powder Melting

The melting and solidification behaviour of the pure Cu powder was analyzed by performing repeated trials at T_P = 1090°C and 1140°C. A typical time-resolved DSC trace for such an experiment was previously shown in Figure 3-6. Figure 4-11 plots the temperature-resolved DSC trace for this 100 mg pure Cu specimen heated to 1140°C and held for 2 minutes prior to cooling. As shown, C_p was measured by the baseline difference during the athermal

segments. At 300°C, C_P was found to be 0.396 $Jg^{-1}K^{-1}$, which is in reasonable agreement with typical values of 0.386 $Jg^{-1}K^{-1}$for pure Cu in literature (within 2.84%) [1]. The onset of the endothermic peak was measured at 1085.8°C, which coincides with the Cu melting point. The width and moderate bi-modal character of this endotherm is attributed to the transient nature of the melting event as peripheral regions of the powder melt first, followed by regions in the center of the crucible. The sudden baseline shift upon transition to the isothermal segment is shown by the dashed DSC trace segment connecting the heat-up and cool-down athermal segments.

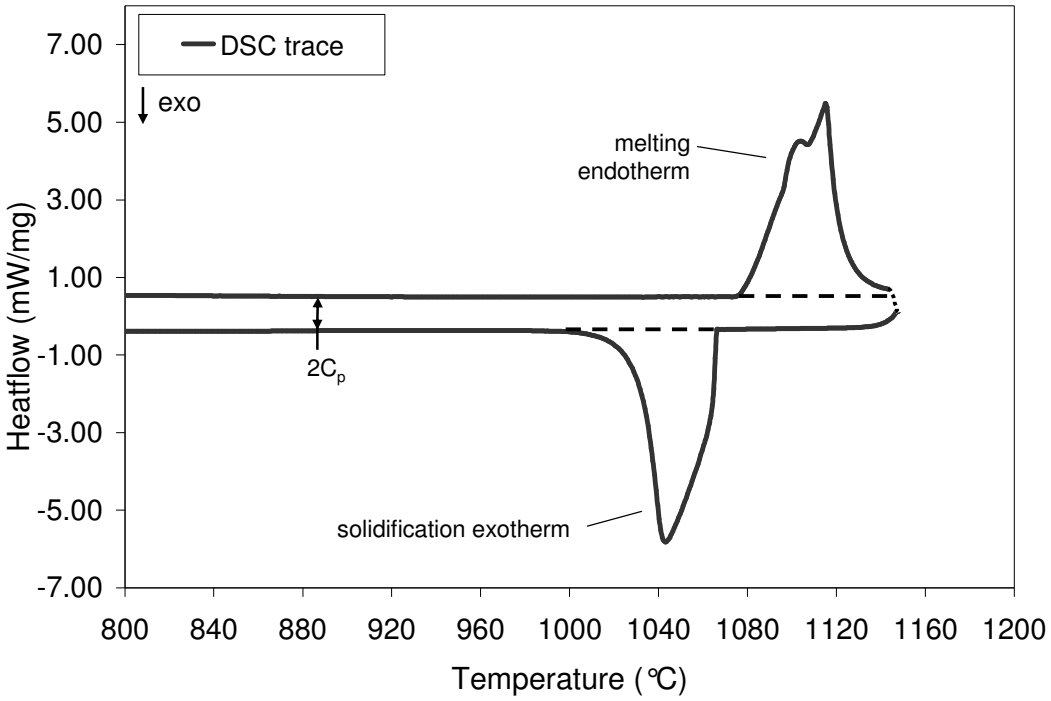

Figure 4-1: Typical temperature-resolved DSC trace for a pure Cu powder specimen heated to 1140°C and held for 2 minutes prior to cooling.

The delayed onset of the solidification peak in the cooling segment was measured at 1060.3°C due to undercooling of the liquid. Undercooling is required to overcome solid nucleation barriers and cause athermal freezing of the liquid metal [110]. This is typical of pure liquid metals and confirms that the Cu sample was fully liquid prior to cooling. The powder sample was also found to have formed a fully dense solid ball after the experiment. The presence of a solid/liquid 2-phase mixture in TLPS experiments (i.e., Cu-rich liquid and solid

Ni particles) is expected to particularly affect the endothermic peak size and the solidification mechanism indicated by the exotherm.

In order to quantify the amount of liquid formed during Cu-Ni TLPS experiments with DSC, it is necessary to determine the transformation enthalpy, or latent heat of fusion (ΔH_f) for pure Cu powder under identical experimental conditions. Table 4-1 and Table 4-2 list measured endotherm and exotherm enthalpies for five repeated DSC trials using pure Cu specimens isothermally held at T_P = 1090°C and 1140°C respectively under identical experimental conditions (i.e., acquisitions rates, purge gas, heating rates).

Table 4-1: Measured enthalpies (ΔH_m) for pure Cu powder heated to T_P = 1090°C.

	$T_{melt\ onset}$	Integrated intensity, ΔH_m (J/g)	
Trial	(°C)	Endotherm	Exotherm
1.0	1083.7	195.9	195.1
2.0	1085.2	205.1	212.8
3.0	1086.3	195.6	198.2
4.0	1084.6	196.0	201.4
5.0	1085.9	193.6	203.6
average	1085.1	197.2	202.2
σ (%)	0.10	2.28	3.33

Table 4-2: Measured enthalpies (ΔH_m) for pure Cu powder heated to T_P = 1140°C.

	$T_{melt\ onset}$	Integrated intensity, ΔH_m (J/g)	
Trial	(°C)	Endotherm	Exotherm
1.0	1086.1	209.5	212.9
2.0	1083.2	206.5	205.0
3.0	1084.6	205.4	197.1
4.0	1084.4	193.2	196.6
5.0	1085.8	204.7	205.6
average	1084.8	203.9	203.4
σ (%)	0.11	3.06	3.33

The onset of melting was found to be coincident with the expected Cu melting point (1085°C) and very repeatable. At both T_P the melting and solidification enthalpies were similar and quite repeatable (standard deviation, σ = 2.28-3.33%). The average measurements are assumed to provide an accurate approximation to the Cu latent heat of fusion (ΔH_f) under these experimental conditions. At 1090°C, the endotherm area is somewhat underestimated since a portion of the peak overlaps the *a-b* segment transition and isothermal segment (see

Figure 3-6). As such, method *c* (as described in Figure 3-8 and shown in Figure 4-1) was used to provide a consistent method for melting and solidification enthalpy measurements.

4.1.2. Initial Characterization of DSC traces for Cu-Ni TLPS Mixtures

Three identical DSC trials were performed by heating Type B loose powder mixtures of coarse Ni powder and Cu powder (C_O = 65 wt% Cu) to 1140°C for 45 minutes prior to cooling. These repeated trials were done to characterize any divergent melting/solidification behaviour relative to exclusive pure Cu specimens, and to investigate the repeatability of the DSC for TLPS experiments involving liquid/solid mixtures. Figure 4-2 shows these three time-resolved DSC traces as well as the temperature program used. The inset shows an expanded-scale view of the exotherms to be analyzed.

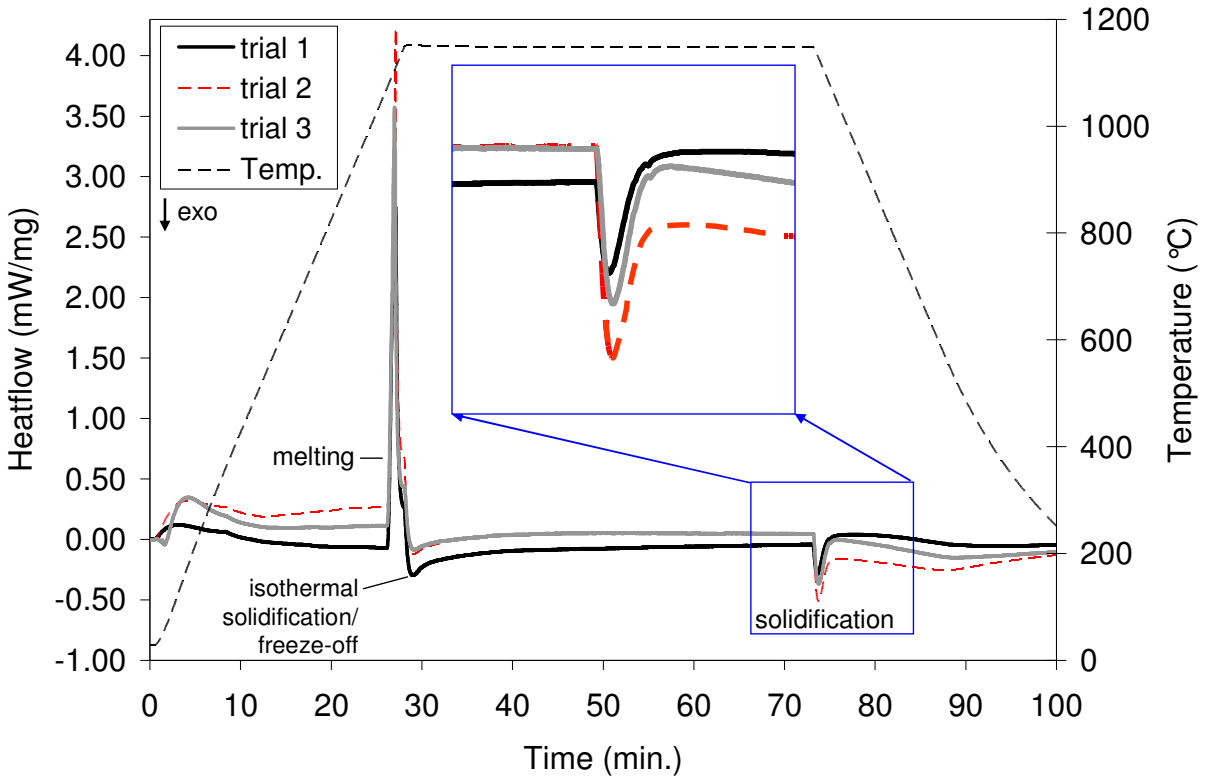

Figure 4-2: Time resolved DSC traces and temperature history for three repeated samples (C_O = 65 wt% Cu) heated to 1140°C and held for 45 minutes prior to cooling.

The heat-up segments in Figure 4-2 show varying baselines and large melting endotherms at 1085°C (see temperature-resolved DSC traces in Figure 4-3 as well). Figure 4-2 shows a small exothermic peak that overlaps the melting endotherms on the right. It is

suggested that this is due to rapid redistribution of the Cu liquid, which quickly solidifies by interdiffusion with the previously unaffected Ni particle surfaces. This process is sometimes referred to as 'liquid freeze-off' and marks the beginning of the gradual exothermic isothermal solidification process of the liquid at T_P. The isothermal segments show no important features aside from a slow endothermic drift – further supporting a gradual isothermal solidification process. This endothermic drift and the rapid freeze-off peak following the melting event are also apparent in the temperature-resolved traces in Figure 4-3 (see overlapping isothermal segment data at highest temperatures). The cooling segments show significantly diminished exothermic solidification peaks relative to the initial melting endotherm areas. This indicates that much less liquid was present at the end of the 45 minute hold segment and provides direct evidence of the isothermal solidification process in TLP sintered Cu-Ni powder mixtures.

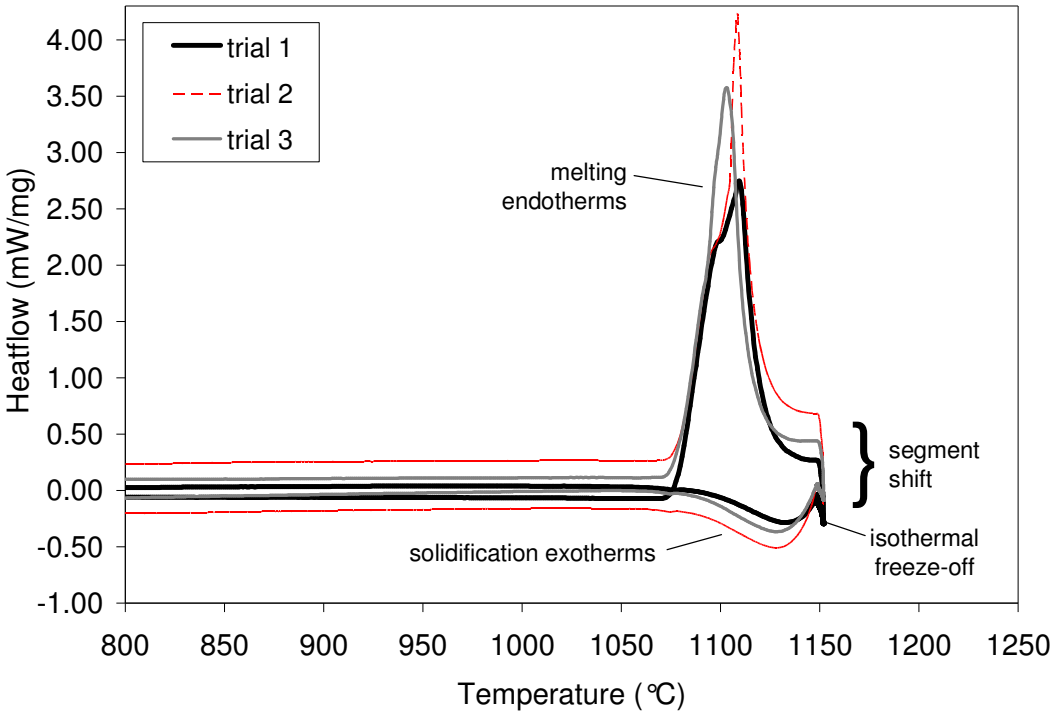

Figure 4-3: Temperature-resolved DSC traces for three repeated samples (Type B, C_O = 65 wt% Cu) heated to 1140°C and held for 45 minutes prior to cooling.

Prior to further analysis, it was important to investigate the nature of the athermal solidification event indicated by the DSC endotherms (see inset in Figure 4-2 and the temperature-resolved DSC traces in Figure 4-3). All solidification peaks have onsets coinciding exactly with the isothermal-cooling segment transition. Firstly, this indicates that

solidification begins immediately upon cooling without the need for undercooling, which was observed for fully liquid Cu specimens (Figure 4-1). This is attributed to the fact that the specimen consists of a 2-phase mixture at T_P prior to cooling (solid Ni particles surrounded by Cu-rich liquid). Upon cooling, the Ni particles provide stable nucleation sites for liquid solidification. As such, a smaller driving force (i.e., undercooling) is required to overcome nucleation energy barriers for solidification to be initiated [31]. Secondly, the inset in Figure 4-2 and the temperature resolved DSC traces in Figure 4-3 clearly show variable baseline shifts after the solidification peaks for these otherwise identical specimens. This is attributed to varying degrees of instrumental baseline shifting at temperature segment transitions (as observed for the *b-c* transition in the pure Cu specimen of Figure 3-6). In these Cu-Ni mixtures, the immediate onset of solidification peaks overlaps this transition, thus shifting the athermal segment baseline as well as the DSC peak itself. Clearly, if the isothermal segment baseline is used for peak area integration (i.e., the left baseline in the Figure 4-2 inset, which is not visible in the temperature-resolved plot in Figure 4-3), this will cause aberrations in measured ΔH_m values since the instrumental baseline shift will contribute to the integrated area.

Therefore, as done for pure Cu enthalpy measurements (ΔH_f, Section 4.1.1), the athermal segment baseline was used for area integration since it is free of instrumental shifting effects from segment transitions and the fact that the temperature-resolved DSC traces do not have a stable baseline on the right of the solidification peak (Figure 4-3). As such, a left-starting horizontal baseline interpolation method was consistently used for peak integration and ΔH_m determination, as described in Section 3.2.4. Table 4-3 shows that this method provided repeatable enthalpy measurements for 65 wt% Cu specimens. The melting peaks coincided with the Cu melting point, and the endotherm enthalpies indicate that less liquid Cu has formed relative to the pure Cu powder experiments in Table 4-2 (i.e., 128.6 J/g vs. 203.9 J/g), as expected with partial melting of these 100 mg specimens that contain only 65 wt% Cu. Relative to the endotherms, the exotherm enthalpies are much smaller (21.2 J/g vs. 128.6 J/g) – providing a measure of the amount of liquid isothermally solidified by diffusional processes during the 45 minute hold at 1140°C. Relative to the initial liquid formation, the diminished exotherm area indicates an 83.5% reduction in the amount of liquid.

Table 4-3: Measured enthalpies (ΔH_m) for 65 wt% Cu Type B mixtures heated to T_P = 1140°C.

Trial	$T_{melt\ onset}$ (°C)	Integrated intensity, ΔH_m (J/g) Endotherm	Exotherm
1	1086.1	127.4	21.4
2	1083.2	130.1	20.6
3	1084.6	128.3	21.7
average	1084.6	128.6	21.2
σ (%)	0.13	1.07	2.68

These data strongly indicate that the DSC technique is capable of measuring the amount of liquid remaining when it athermally freezes after an interrupted isothermal hold. Further experiments were necessary with varying isothermal segment durations to interrupt this process during different stages of completion. Numerous experiments were conducted to capture the rate of liquid removal until completion of the isothermal solidification process under different processing conditions (T_p, and preparation technique). However, it was first desired to determine the effects of solid-state sintering on the absolute amount of liquid initially formed for different mixture compositions (C_O).

4.1.3. Solid-State Sintering and Interdiffusion

Figure 4-4 illustrates macrographs of solid-state sintered Ni-65wt% Cu powder mixtures made by the Type A and B methods after heating to 1075°C followed by immediate cooling. The different distribution of Cu powder amongst the Ni powder in the two mixing cases is clearly visible with BSE imaging contrast. These macrographs also illustrate the relatively low density of the powder compacts prior to liquid formation. Figure 4-5 shows an isolated Ni-Cu contact from the Type A mixture after solid-state sintering at 1075°C. This micrograph shows that the Cu regions appear relatively denser than the Ni particles, which contain residual porosity from the as-received powder. The EDS line scans for Cu and Ni clearly indicate that significant diffusion of Cu into Ni particles and vice versa (i.e., *inter*diffusion) has occurred in the sintered neck regions – forming a typical diffusion couple concentration profile. The interdiffusion region on the Cu-rich side of the sintered neck will not melt if heated to 1085°C since any Ni alloying of pure Cu increases its solidus temperature (see Figure 3-1).

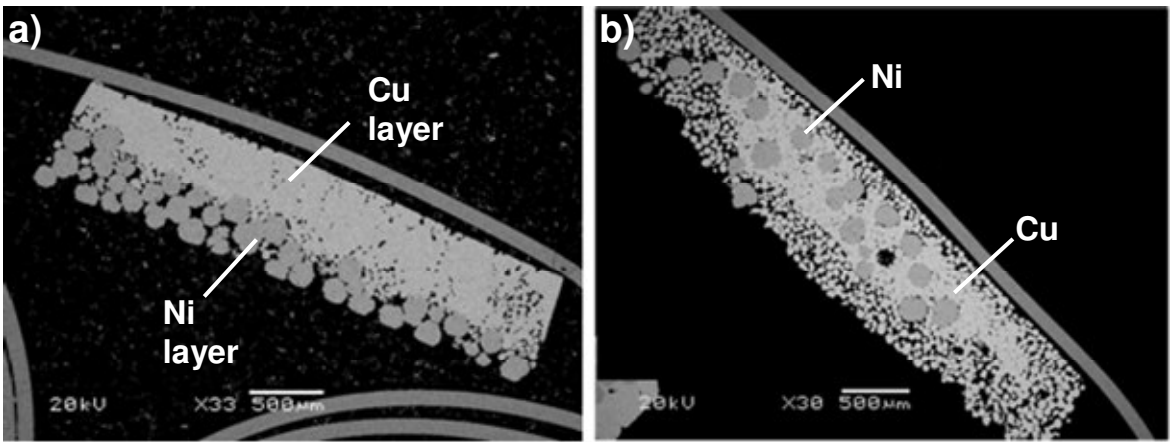

Figure 4-4: BSE micrographs of Ni-65wt% Cu powder mixtures heated to 1075°C and immediately cooled to illustrate the pre-melt condition of both techniques: a) Type A: layered/pressed, b) Type B: mixed/loose.

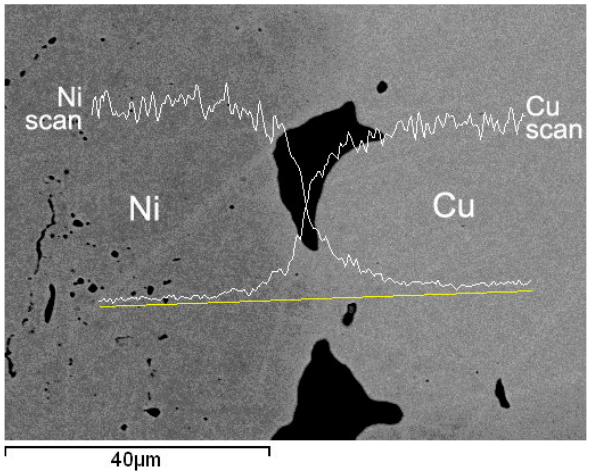

Figure 4-5: BSE micrograph with qualitative EDS line scans of a Ni-65wt% Cu powder mixture heated to 1075°C.

4.1.4. Melting & Dissolution

The extent of solid-state interdiffusion illustrated in Figure 4-5 can be quantified using DSC by examining the initial liquid formation, since significant levels of solid-state interdiffusion during heat-up should cause measurable decreases in the volume of liquid formed at T_P. Figure 4-6 shows heat-up segment DSC traces for Type A Cu-Ni mixtures having different bulk Cu contents (C_O) that were heated to 1140°C and immediately cooled. The endothermic peaks found upon heating indicate that the onset of melting occurred at 1085°C (i.e., pure Cu melting). The variation of peak areas indicates that the amount of liquid

formed increases as the bulk Cu content of a mixture increases, which would be expected [7,12-14].

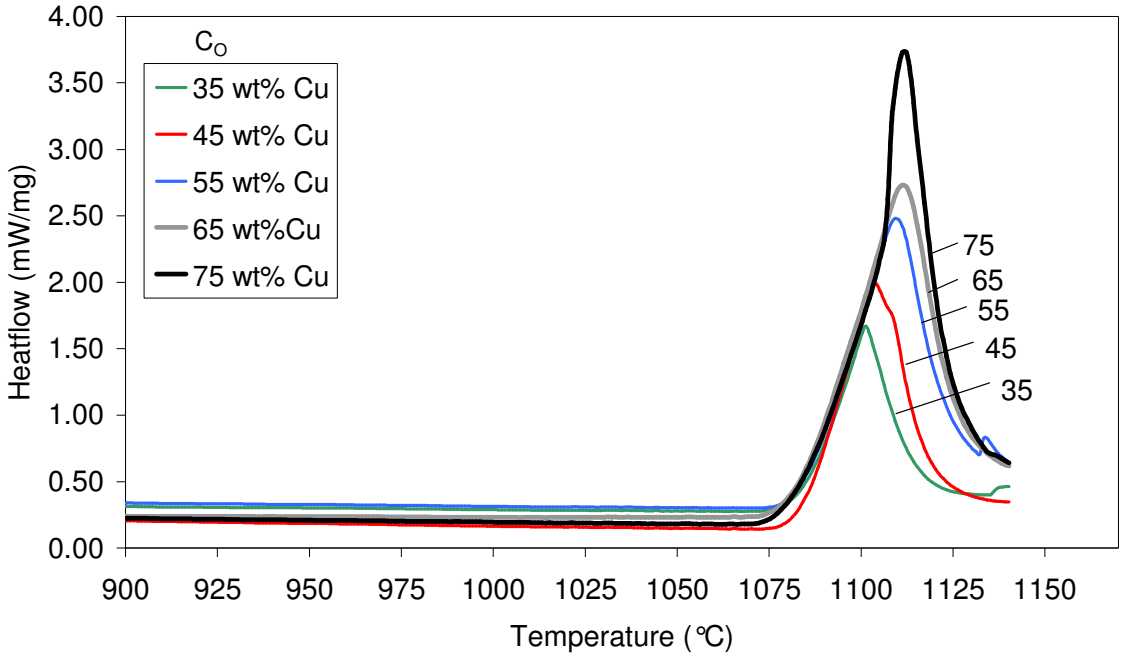

Figure 4-6: DSC traces showing initial melting endotherms for layered/pressed brazes (Type B) heated to 1140°C with varying Cu contents.

The initial liquid weight fraction formed from additive melting (W_{Ao}) can be determined by measuring the area under the endothermic peaks and dividing this measured endothermic energy (ΔH_m) by the expected endothermic energy if the sample had been 100% Cu (i.e., the latent heat of fusion, ΔH_f, for Cu), as per Equation (4-1).

$$W_A = \frac{\Delta H_m}{\Delta H_f} \qquad \textbf{(4-1)}$$

The latent heat of fusion value (ΔH_f) for the pure Cu powder was determined by DSC under identical experimental conditions as the mixtures (Table 4-2). In the absence of solid-state interdiffusion all of the Cu within the sample should melt in its pure form when heated above 1085°C. In this case W_{Ao} would be equal to the Cu content in the mixture, C_O. Therefore the degree to which the experimentally measured $W_{Ao} < C_O$ is a measure of how much interdiffusion took place prior to melting. A summary of ΔH_m values measured via DSC for Cu-Ni mixtures along with the corresponding W_{Ao} values are given in Table 4-4 for a series of

compositions heated to T_P = 1140°C. Type B mixtures heated to 1090°C and 1140°C are also included.

Table 4-4: DSC and density data for Type A and B mixtures heated to T_P and immediately cooled.

C_O (wt% Cu)	Temperature T_P (°C)	Preparation technique (Type)	Endotherm enthalpy, ΔH_m (J/g)	Liquid fraction, $W_{Ao} = \Delta H_m/\Delta H_f$	Density D_{theo}
35	1140	layered/pressed (A)	36.4	0.18	0.87
45	1140	layered/pressed (A)	62.8	0.31	0.92
55	1140	layered/pressed (A)	85.5	0.42	0.95
65	1140	layered/pressed (A)	103.4	0.51	0.96
75	1140	layered/pressed (A)	123.5	0.61	0.98
65	1090	layered/pressed (A)	88.7	0.45	0.92
65	1140	mixed/loose (B)	124.9	0.61	0.96
65	1090	mixed/loose (B)	102.8	0.52	0.92
100	1090	Pure Cu mixture - ΔH_f	197.2	1.00	1.00
100	1140	Pure Cu mixture - ΔH_f	203.9	1.00	1.00

These data are also plotted in Figure 4-7 as a function of the Cu content, C_O. A theoretical curve corresponding to $W_{Ao} = C_O$ (i.e., the absence of solid-state interdiffusion) is also shown for comparison. As expected, ΔH_m (and therefore initial liquid wt. fraction, W_{Ao}) increases as the Cu content within the mixture increases. However, comparison with the theoretical curve indicates that W_{Ao} is always less than C_O. This clearly indicates that interdiffusion prior to melting occurs and reduces the amount of liquid which initially forms in the powder compacts. The overall impact of interdiffusion on liquid formation is largest at low Cu compositions where W_{Ao} is less than 50% of the C_O value.

Metallographic results by Puckert *et al* for planar arrays of Cu-coated Ni spheres have shown that Ni dissolution occurs at neck regions during TLPS above 1085°C [5]. Optical macrographs clearly showed increased Ni melting and a decreased Ni particle sizes at higher sintering temperatures. Unfortunately, unlike the above results, these qualitative observations cannot quantify how the liquid fraction is affected.

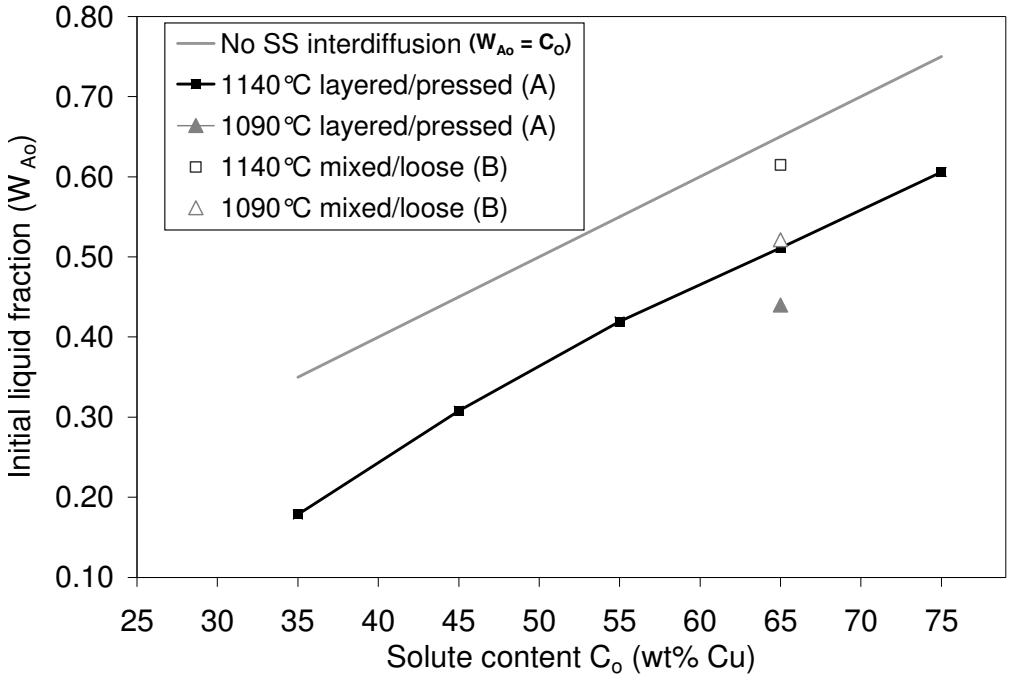

Figure 4-7: Initial liquid fraction formed (W_{Ao}) for Type A and B brazes heated to 1140°C and 1090°C at 40°C/min.

The impact of dissolution on the amount of liquid formed can be determined by comparing the DSC results at 1090°C and 1140°C for the 65 wt% Cu samples in Figure 4-7. At 1090°C the liquidus composition is 99 wt% Cu and therefore any dissolution and melting of Cu-rich regions alloyed with Ni will be negligible in terms of their contribution to liquid formation. By comparison, the liquidus composition at 1140°C is 92 wt% Cu. Therefore, melt-back of previously interdiffused Cu-rich alloyed regions as well as Ni dissolution (from increased Ni solubility in the liquid), would be expected to have an impact on the initial liquid formation. A comparison of ΔH_m and W_{Ao} measurements for 65 wt% Cu Type A mixtures at the two temperatures in Table 4-4 and Figure 4-7, clearly indicates that dissolution does cause more liquid to form - increasing ΔH_m from 88.7 J/g (or W_{Ao} = 0.45) at 1090°C (where no dissolution occurs) to 103.41 J/g (or W_{Ao} = 0.51) at 1140 °C. Similarly, Type B mixtures also form less liquid at 1090°C. However, it is worth noting that even at 1140°C, $W_{Ao} < C_O$ indicating that dissolution does not fully recover the entire alloyed Cu. The Ni regions alloyed below the solidus composition of 86 wt% Cu still remain stable in the solid phase and do not melt at 1140°C.

***Consolidation*:** An example of the macrostructures of Type A and B samples sintered at 1090°C and 1140°C for 0 minutes is shown in Figure 4-8. Comparing these structures with the 'pre-melt' samples heated to 1075°C (Figure 4-4) indicates that liquid formation has caused rapid particle rearrangement and increased density within ≤ 1 minute of liquid duration. This is consistent with metallographic and dilatometric Ni-Cu TLPS studies by Puckert *et al* which showed that the initial densification process occurs by rapid liquid redistribution through capillary action and base metal rearrangement [5,45]. German suggests that this process can occur within the first few seconds of melt formation [2].

Figure 4-8 illustrates that the more segregated starting structure of the compacted Type A mixtures has not prevented densification of the sintered material, again indicating the effectiveness of particle rearrangement. These layered/pressed mixtures seem somewhat denser and less distorted than the loose Type B mixtures. This is likely due to the initial presence of a pressed and solid-stated sintered Ni skeleton prior to melt infiltration. However, this relatively dense-pressed rigid particle network has resulted in decreased liquid fractions (indicated by DSC) and visibly increased shape retention in Type A mixtures – both of which are undesirable characteristics from a flowable braze filler metal perspective. In comparison, the loosely mixed Type B mixtures formed more liquid, which was less restricted for Ni particle rearrangement.

Comparison of both sintering temperatures for layered/pressed Type A mixtures (Figure 4-8*a* and *b*) reveals that specimens sintered at 1140°C appear more distorted owing to the increased liquid formation. This was less evident in the loose Type B specimens, which all showed similar levels of particle rearrangement and shape distortion owing to the less restrictive loose powder contact. However, it was observed that in both A and B types, specimens heated to 1140°C showed moderately decreased Ni particle sizes owing to dissolution at higher temperatures, as observed by Puckert *et al* [5].

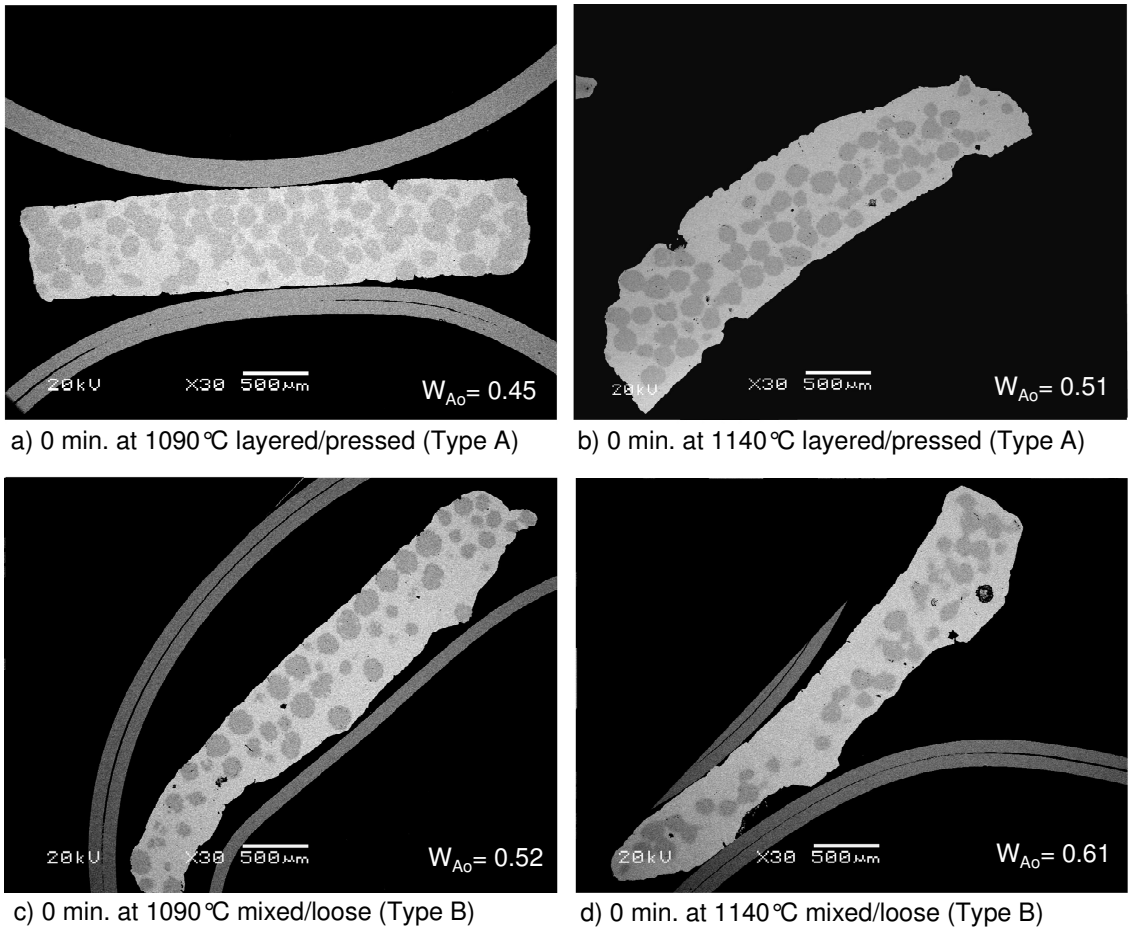

a) 0 min. at 1090°C layered/pressed (Type A)

b) 0 min. at 1140°C layered/pressed (Type A)

c) 0 min. at 1090°C mixed/loose (Type B)

d) 0 min. at 1140°C mixed/loose (Type B)

Figure 4-8: BSE macrographs of layered/pressed (Type A) and mixed/loose (Type B) specimens after heating to 1090°C or 1140°C and immediately cooled. The initial liquid fraction measured by DSC is identified at the bottom right corner.

Bulk sintered density measurements ($\rho_{sintered}$) were performed on these post-sintered Type A and B mixtures prior to sectioning via the Archimedes method by weighing in oil and air. These density measurements can be expressed as fractions of full density (D_{theo} = $\rho_{sintered}/\rho_{full}$), where full density corresponds to a sintered braze with no voids. These data are plotted in Figure 4-9, which illustrates how the densification level increases as the initial liquid fraction formed increases. The corresponding C_O values of specimens shown in Figure 4-7 are also plotted for each data point. Fractional density measurements for the 65 wt. % Cu specimens ranged from 0.92-0.96 depending on processing conditions (see data encircled by dashed line), which is expected based on the high levels of consolidation exhibited in the macrographs for these specimens (Figure 4-8).

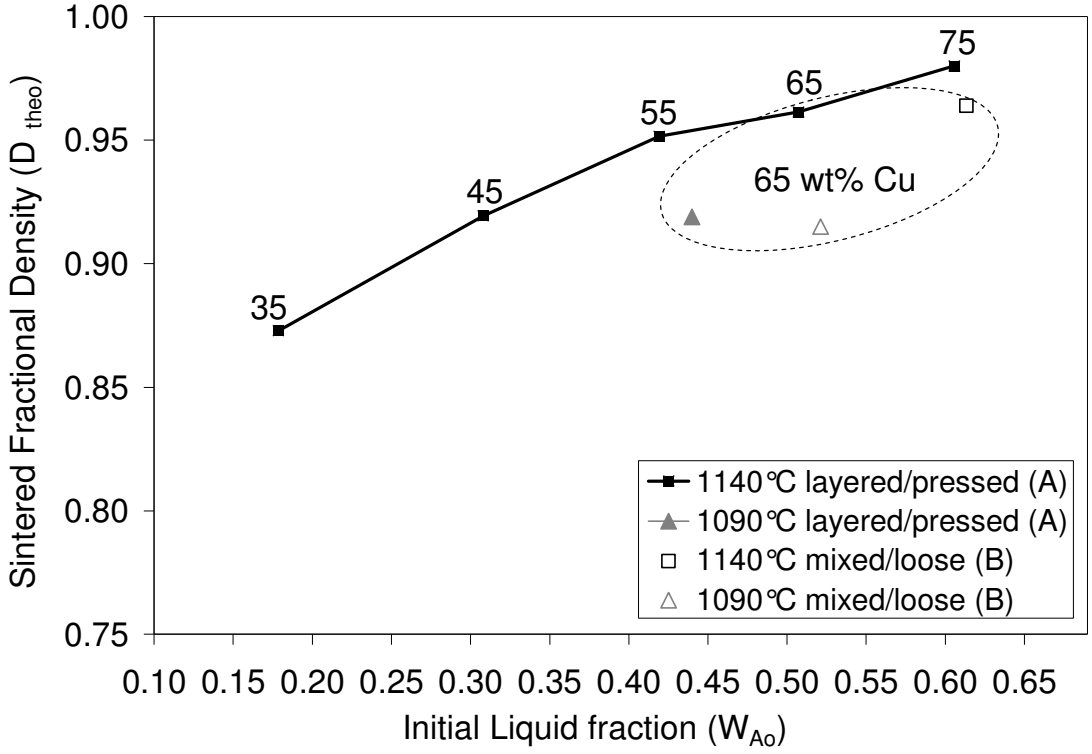

Figure 4-9: Fractional density (D_{Theo}) vs. initial liquid fraction formed for Type A and B brazes heated to 1140°C and 1090°C at 40°C/min and immediately cooled.

The 1140°C data shown in Figure 4-9 indicates that Type A powder mixtures containing approximately 40 wt% liquid (i.e., 55wt% Cu) or more will have consolidation levels in excess of 95 % theoretical. Full density was not achieved even at higher Cu contents, due to the presence of residual Ni pores from the starting Ni powder (Figure 4-5) and large pores within the Cu regions (visible in Figure 4-8). The large pores associated with liquid regions are likely due to trapped gas. Additionally, unequal diffusivities ($D_{Cu} > D_{Ni}$) [1,110] can cause a mass flux imbalance that gradually generates Kirkendall-type 'diffusion pores' and swelling at long sintering times [39,45,44]. However these types of pores will make a more significant contribution once greater degrees of interdiffusion have taken place at longer sintering times. As such, Kirkendall-type pores are not expected to be the main source of porosity in the data of Figure 4-9, which were collected after a 0 minute hold at the sintering temperature. However, specimens TLP sintered at longer times are expected to exhibit more Kirkendall porosity due the accruing mass-flux imbalance near the interface.

An additional influence on density is related to solid-state interdiffusion and dissolution, which can be discussed by comparing the consolidation results at 1090°C and 1140°C. Within

the dashed area of Figure 4-9, data for mixtures of the same bulk composition of Ni-65wt% Cu are included. However, differences in the 4 separate data points include the peak temperature (i.e., 1090°C and 1140°C) and preparation technique of the powder mixtures (i.e. layered/pressed versus loosely intermixed). It is clear from the figure that, while loosely intermixed powders (B) generate more initial liquid; this does not result in higher sintered densities at the same peak temperature. Type A specimens achieved similar densities with lower liquid fractions due to the higher starting green densities from pressing. However, regardless of the mixing method, a peak temperature of 1140°C always results in higher density. Therefore, density is more sensitive to peak temperature than to liquid fraction or initial powder distribution. This is due to increased dissolution and melt-back of the sintered and interdiffused rigid network created at lower temperatures. This allows more particle rearrangement of the mixture and higher densities.

4.1.5. Isothermal Solidification

Based on the DSC data in Figure 4-9, it was decided to investigate higher density mixtures for further isothermal solidification studies (i.e., 65 wt% Cu). The consolidation levels observed and significant melting point shift potential of the 65 wt% Cu mixtures are desirable characteristics for potential VMP braze filler metals. Figure 4-10 shows DSC traces for 65 wt% Cu Type A specimens heated to 1140°C, held isothermally for different durations, and then cooled to interrupt the isothermal solidification process. All brazes were found to exhibit very similar endothermic melting peaks at 1085°C. Upon cooling, solidification peaks that are significantly smaller than the melting peaks were found. As indicated in the preliminary data presented in Section 4.1.2, this shows that isothermal solidification of the liquid phase occurs at the processing temperature and this appears to be a gradual process. Cooling segment traces for samples held at longer times show progressively less liquid solidification. The flat DSC trace for the mixture held for 240 minutes indicates no liquid solidification upon cooling. Therefore complete isothermal solidification took place between 160 and 240 minutes.

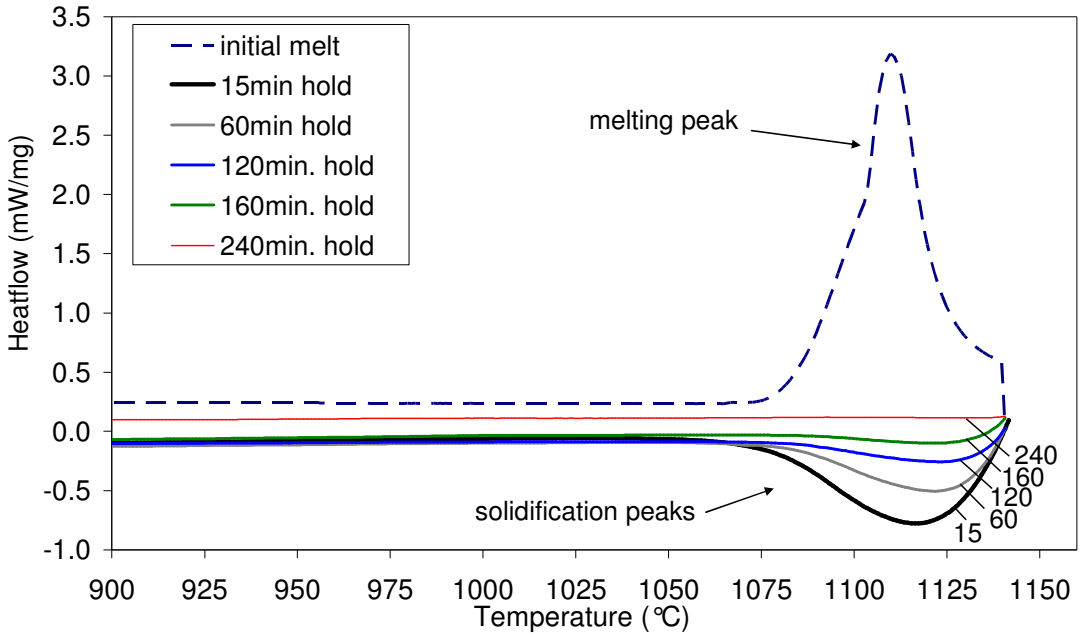

Figure 4-10: DSC traces for 65wt% Cu Type A mixtures heated to 1140°C and held for different isothermal hold times.

The exothermic solidification enthalpies after specific interrupted isothermal hold times were quantitatively measured by DSC (i.e., the area under the solidification peaks, ΔH_m). Equation (4-1), was used to calculate the liquid fraction present (W_A) as a function of hold time t. By convention, the start of the isothermal segment is considered as the initial condition at t = 0 minutes (or t_O relative to the total elapsed time). In the case of sintering at 1140°C, the liquid is actually present approximately 1.4 minutes earlier since initial melting occurs at 1085°C. Table 4-5 provides a large summary of ΔH_m and liquid fraction data from numerous DSC experiments interrupted after increasing hold times for Type A and B mixtures TLP sintered at 1090°C and 1140°C. At the initial melting condition (taken as t = 0 minutes), the ΔH_m value given is the average enthalpy of all melting endotherms for a given experimental condition (Type and T_P).

Table 4-5: Exotherm enthalpy, ΔH_m (J/g) and liquid fraction (W_A) data from DSC at increasing hold times for Type A and B mixtures TLP sintered at 1090°C and 1140°C.

		Exotherm enthalpy ΔH_m, J/g (Liquid fraction, W_A)			
		Layered/pressed (A)		Mixed/Loose (B)	
C_O (wt% Cu)	Hold time (min.)	1090°C ΔH_m (W_A)	1140°C ΔH_m (W_A)	1090°C ΔH_m (W_A)	1140°C ΔH_m (W_A)
65	0*	79.71 (0.45)	103.41 (0.51)	102.80 (0.52)	124.64 (0.61)
65	2	63.70 (0.32)	91.52 (0.45)	73.94 (0.37)	95.52 (0.47)
65	5	39.80 (0.20)	87.30 (0.43)	48.82 (0.24)	66.07 (0.32)
65	15	15.57 (0.08)	45.15 (0.22)	13.22 (0.07)	39.40 (0.19)
65	30	11.65 (0.06)	34.03 (0.17)	6.60 (0.03)	16.62 (0.09)
65	45			0.00 (0.00)	21.23 (0.10)
65	60	8.15 (0.04)	21.63 (0.11)		9.09 (0.04)
65	75				4.04 (0.02)
65	90	3.40 (0.02)	8.94 (0.04)		0.40 (0.00)
65	120	2.09 (0.01)	7.43 (0.04)		
65	150	0.00 (0.00)	5.71 (0.03)		
65	160		2.73 (0.01)		
65	240		0.00 (0.00)		

*at t = 0 min., ΔH_m = the average of all melting endotherms for a given condition (Type &T_P)

Figure 4-11 plots the W_A values vs. isothermal hold time for mixtures sintered at 1090°C and 1140°C. Data sets for Type A and B specimens (i.e., pressed/layered and loose/mixed) are shown in Figure 4-11*a* and Figure 4-11*b* respectively. Each data point represents a different specimen (data from Table 4-5). All data sets illustrate similar transient liquid trends – the large liquid fractions initially formed upon heating are rapidly reduced with hold time at temperature due to diffusional (or isothermal) solidification. The rate of this solidification (i.e., the slope of each curve) is initially very rapid but decreases significantly near the end of the solidification process. For the mixed/loose powders (Type B), the net solidification rate is more rapid at 1090°C compared to 1140°C, resulting in complete removal of the liquid phase in half the time at the lower temperature. The time required for complete liquid removal (t_C) is also shorter at 1090°C for the layered and pressed powders (Type A). However, the times for complete liquid removal are similar at both temperatures for Type A mixtures and considerably longer than that measured for the mixed/loose (Type B) counterparts. This data will be further discussed in a Sections 4.3.

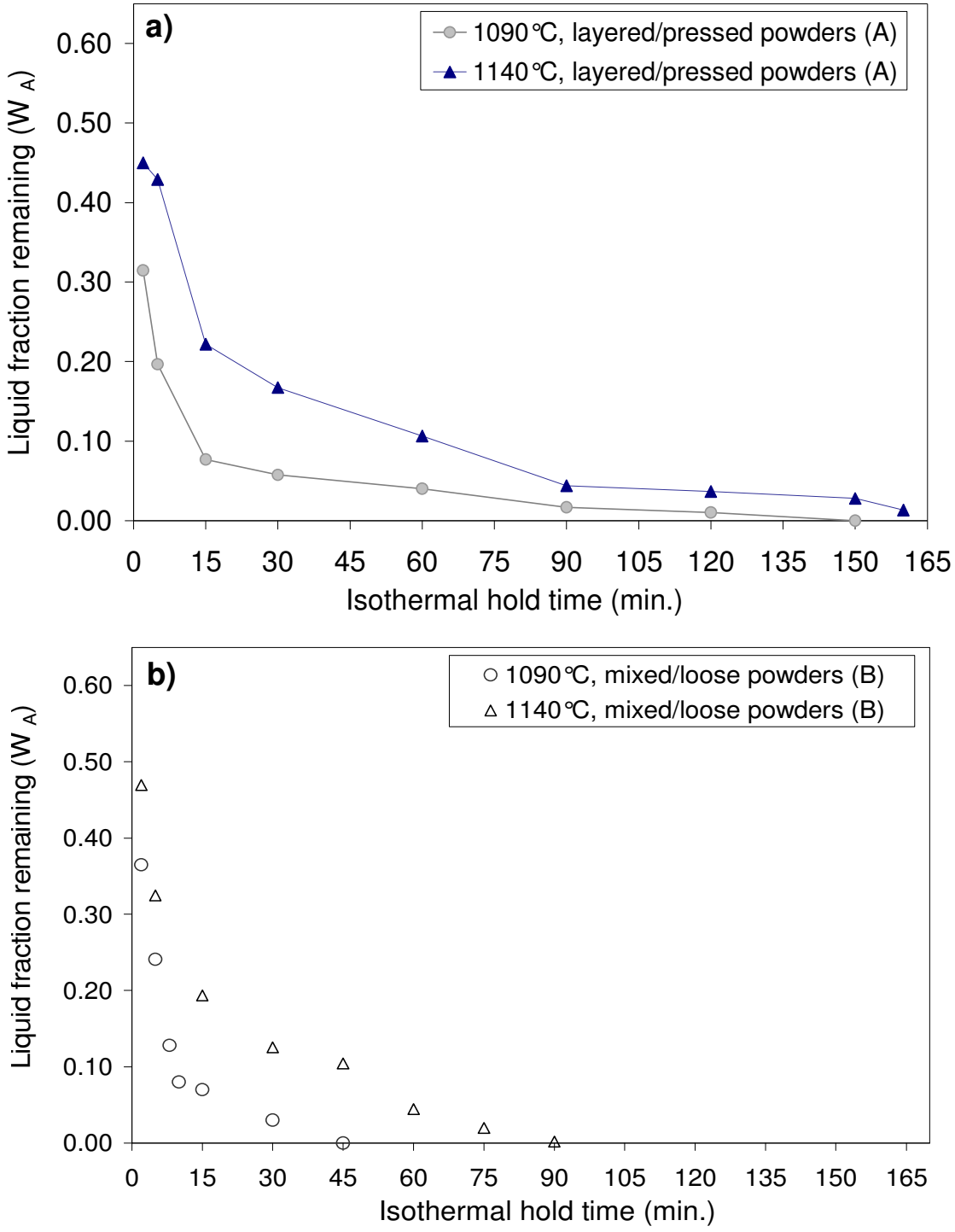

Figure 4-11: DSC results showing the fraction of liquid remaining after interrupted isothermal holds at 1090°C and 1140°C for 65wt% Cu mixtures: a) Layered/pressed mixtures (Type A), b) Mixed/loose mixtures (Type B).

Microstructural evidence of the isothermal solidification mechanism. Figure 4-12 shows BSE macrographs of Type A and B specimens at the end of the isothermal solidification process at 1090°C and 1140°C. Figure 4-12*b* shows a polished section in the plane of the sintered disc-shaped specimen. All specimens show that some large pores are still visible, which are attributed to stable trapped gas pores in the liquid (Figure 4-8), which are too large for removal during TLPS. However, all samples in Figure 4-12 show increased porosity levels in comparison to the high consolidation levels initially observed after melting (Figure 4-8). This porosity is attributed to the accrued mass flux imbalance for the duration of the hold segments. The unbalance Cu diffusion stream due to unequal diffusivities $D_{Cu} > D_{Ni}$ caused the gradual formation of Kirkendall-type diffusion pores and macroscopic swelling [39,45,44]. Numerous studies on this solid-state phenomenon have been conducted in Ni-Cu alloys since Kirkendall's first characterization of this effect for the Cu-Zn system [43]. As clearly illustrated by comparing the macrographs in Figure 4-8 and Figure 4-12, these diffusion pores make a more significant contribution once greater degrees of interdiffusion have taken place at longer sintering times.

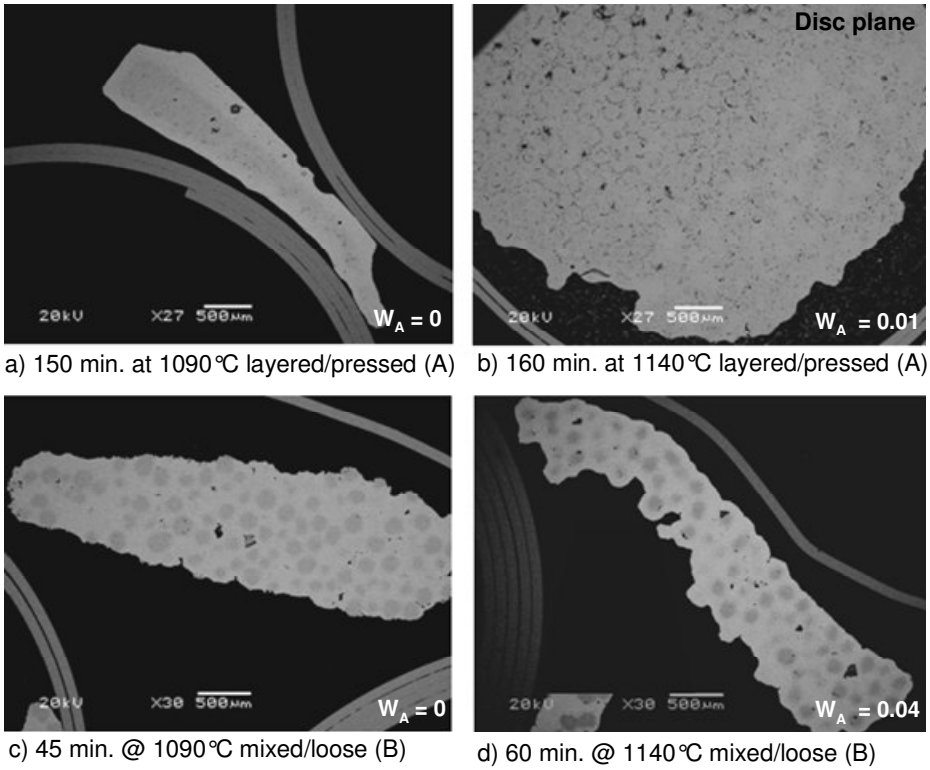

a) 150 min. at 1090°C layered/pressed (A) b) 160 min. at 1140°C layered/pressed (A)

c) 45 min. @ 1090°C mixed/loose (B) d) 60 min. @ 1140°C mixed/loose (B)

Figure 4-12: BSE macrographs of layered/pressed (Type A) and mixed/loose (Type B) specimens after complete isothermal solidification at 1090°C or 1140°C. The initial liquid fraction measured by DSC is identified at the bottom right corner.

The macrographs for Type B mixtures in Figure 4-12*c* and Figure 4-12*d* show decreased chemical contrast between the darker Ni particle cores and lighter Cu-rich regions relative to that observed immediately after melting (Figure 4-8*c* and *d)*. This indicates diminished compositional gradients and shows that interdiffusion has taken place. However, the fact that Ni-rich particles are still distinguishable indicates that significant compositional gradients are still present.

The layered/pressed Type A mixtures in Figure 4-12*a* and Figure 4-12*b* also exhibit decreased chemical contrast after solidification, but the individual Ni particle locations are much less visible or distinguishable from the Cu-rich regions. Figure 4-12*a* shows the presence of a dark Ni-rich mass in the center of the sintered compact. This Ni-rich region corresponds to the previous, densely packed Ni-skeleton formed in the layered/pressed green compact. This packed Ni skeleton was infiltrated by a smaller portion of the Cu melt (vs. mixed/loose powders) and the remainder appears to have pooled in peripheral regions of the compact. The inhomogeneous distribution of these relatively large peripheral Cu-rich regions, as well as the decreased total Ni surface area from pressing, offer a good explanation for the significantly slower isothermal solidification rates found at longer hold times in the pressed/layered specimens (Figure 4-11). Figure 4-12*b* shows an etched section in the plane of a disc-shaped compact that was sintered at 1140°C. A distributed Kirkendall pore network is evident and it is difficult to distinguish individual Ni particles in this relatively large cross-section view.

BSE micrographs were obtained at the particle size scale (Figure 4-13) for Type B mixtures to closely examine microstructural evolution during TLPS. Type A mixtures, which differed macroscopically, exhibited similar microstructures at this scale. In the 'pre-melt' condition at 1075°C, the BSE micrograph in Figure 4-13*a* illustrates the typical solid-state sintered structure prior to melting. Cu particles have formed many sintered necks densely surrounding the Ni particles. The composite BSE/SE image in Figure 4-13*b* shows chemical/topographical contrast for a single particle that was etched to reveal its grain structure. This specimen was heated just below the Cu melting point (1083°C), which explains the high degree of densification and flow at the onset of melting. The backscatter imaging mode (BSE, left) delineates a fairly equiaxed Ni grain structure and porosity in the solid-state sintered neck regions. Topographical contrast from the secondary electron imaging mode (SE,

right) reveals the Cu grain structure, which is very coarse due to accelerated grain growth and mass transport rates at such a high homologous temperature.

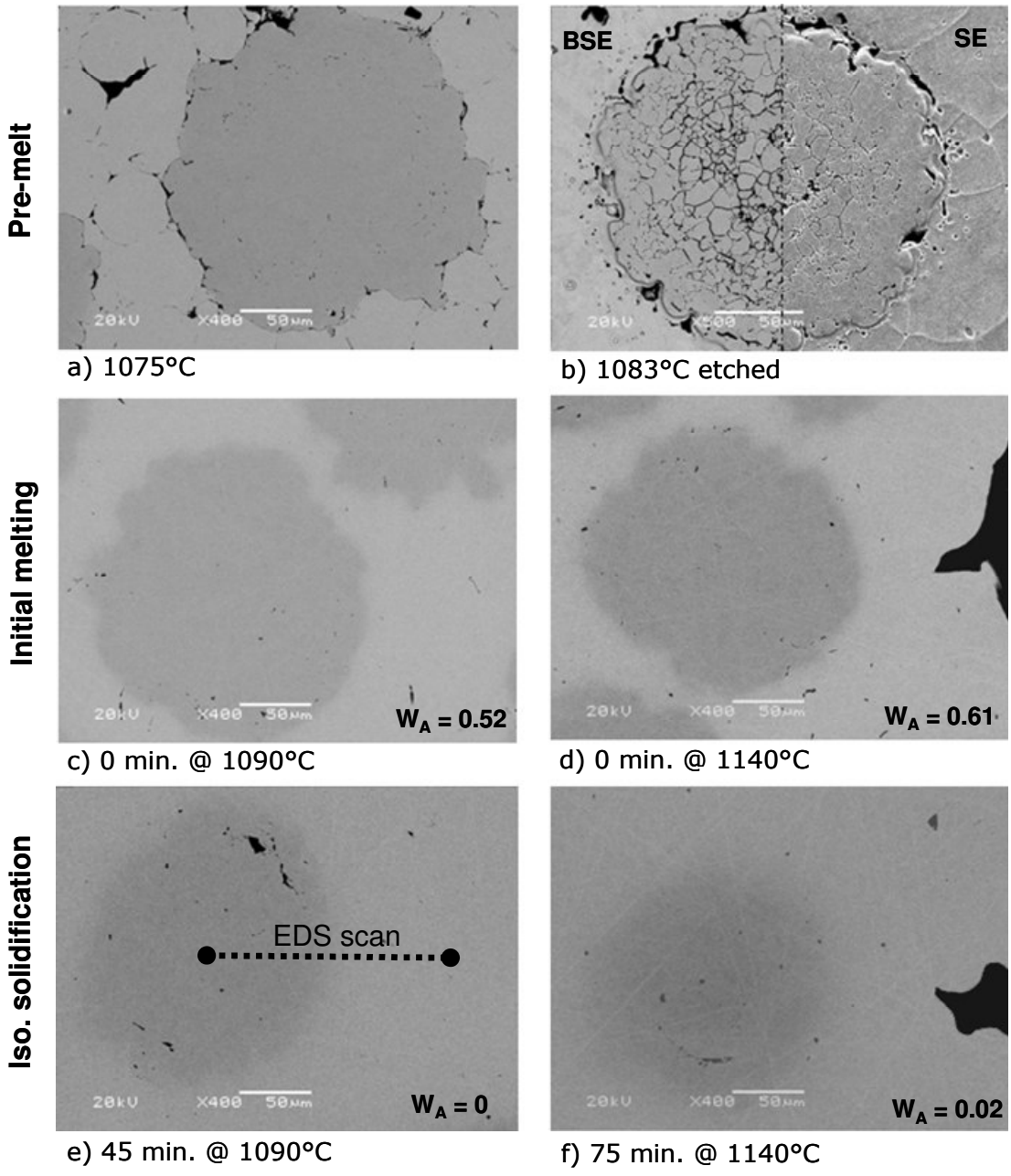

Figure 4-13: Micrographs showing microstructure evolution during TLPS of 65 wt% Cu Type B mixtures at 1090°C and 1140°C: a) BSE image before melting, b) composite BSE/SE image of etched specimen before melting, c)-f) BSE images at initial melting and the end of isothermal solidification. The liquid fraction present from DSC is identified at the bottom right corner.

After the initial melting event (t = 0 minutes) the Cu liquid has completely enveloped the Ni particles and caused densification (Figure 4-13*c* and *d*). No interface or boundary is found between the Ni particles and frozen Cu regions, yet significant compositional contrast is shown by BSE imaging. Comparison of Figure 4-13*c* and *d* shows that the Ni particle size is somewhat decreased at 1140°C and that a smoother, rounded shape is generated. This supports the melt-back and dissolution effects believed to explain the increased liquid fraction measured by DSC at 1140°C.

At the end of isothermal solidification (Figure 4-13*e* and *f)* the BSE images indicate somewhat decreased compositional contrast from interdiffusion and similarly, a smaller Ni particle size at 1140°C. However, the apparent Ni particle/core sizes, as indicated by the still distinguishable dark areas, remain in the size range observed at initial melting (i.e., a_B ~ 80μm). As such, these Ni-rich core regions do not appear to have grown to a size representative of ~52-61wt% liquid absorption. It is important to remember that isothermal liquid removal can theoretically occur by two simultaneous mechanisms: 1) solute penetration into the Ni core by diffusion within this Ni-rich solid-solution – causing growth and saturation of the original particle; and 2) interfacial motion leaving behind a solute-rich phase growing epitaxially on the original Ni particles. The above metallographic observations suggest that the isothermal solidification mechanism may be dominated by interfacial motion and does not require significant saturation of the original Ni particles by Cu.

Metallographic techniques such as BSE imaging allow an effective interpretation of the solidified microstructures, but observations made are limited to qualitative comparisons and discussion. Of particular importance is the fact that it is difficult to microscopically verify the frozen liquid fraction present in these post-sintered specimens since a distinct boundary corresponding to solid-liquid interface is not distinguishable. Since Ni and Cu are completely soluble in the solid phase, the two-phase solid/liquid couple that is present above 1085°C becomes a one-phase diffusion couple below 1085°C. This inherent isomorphous characteristic, combined with ongoing interdiffusion during cooling from T_P, serves to obscure the structural and compositional remnants of the boundary/interface between the solid solution particle and the frozen liquid. It is therefore difficult to distinguish between isothermally and athermally solidified liquid regions.

Rapid quenching from T_P, which the current DSC is incapable of, may remedy this difficulty in future experiments and better preserve interface remnants. However, metallographic techniques are inherently limited for the interpretation of isothermal solidification in TLP processing since they rely on the identification of distinct and uniform phase boundaries/interfaces [96]. Powder size and shape distributions as well as mixture inhomogeneity effects further complicate these techniques, which necessitate large sample sizes for statistical significance. These difficulties explain the lack of quantitative transient liquid fraction data reported in literature for TLP sintered PM alloys. This reinforces the value of thermal analysis via DSC for quantification of the isothermal solidification stage.

Nevertheless, useful quantitative compositional information can be obtained via EDS microprobe analysis regarding the degree of interdiffusion within the post-sintered, single-phase DSC specimens. Radial compositional profiles were measured (in wt% Cu) using aligned spots originating from the Ni particle cores, as illustrated in Figure 4-13*e*. These data can provide an improved understanding of the diffusional solidification process by examining the evolving distribution of solute in the base metal particles and in the adjacent isothermally solidified regions. Figure 4-14*a-d* show EDS compositional profiles for Type A and B samples TLP sintered at 1090°C and 1140°C. A range of hold times during the isothermal step for each condition are given in each plot. Profiles from samples heated to just below the point of Cu melting (i.e. 1075-1080°C) are shown to illustrate to starting pre-melt solute distribution. Profiles at the end of isothermal solidification are included last for each condition to illustrate the solute distribution at the end of TLPS. These data were obtained by EDS spot analysis consisting of radially-aligned analysis points at 10μm increments from the Ni core (at r = 0μm). All efforts were made to minimize positional errors by analyzing similarly sized, spherical particles (i.e., radius a ~ 80.5μm). Repeated measurements on multiple particles per sample (2-3) were obtained to ensure repeatable and representative measurements.

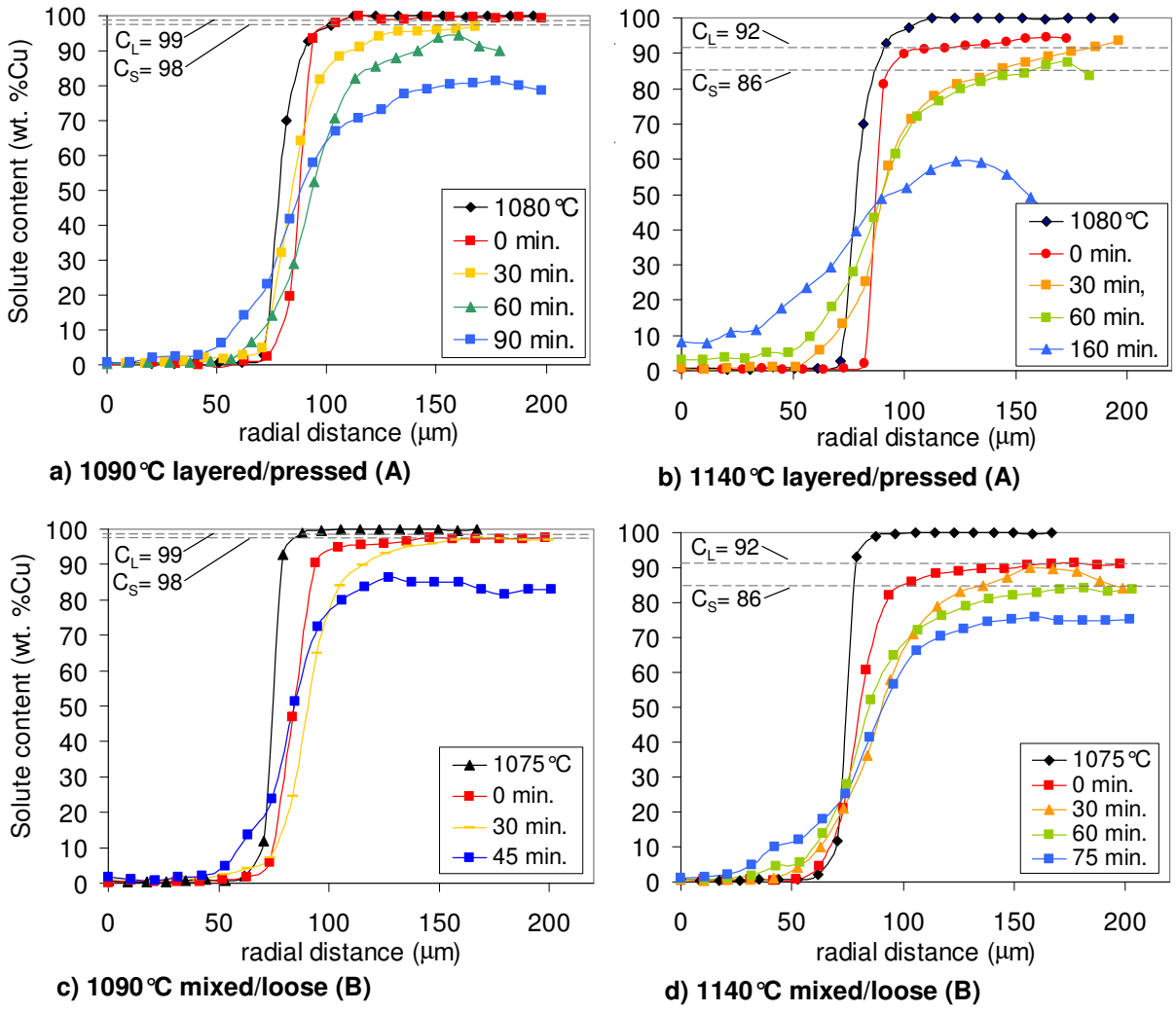

Figure 4-14: Evolution of radial concentration profiles from the Ni core - measured by EDS for 65wt% Cu Type A and B specimens TLP sintered at 1090°C and 1140°C.

For all data sets shown in Figure 4-14, the profiles obtained for specimens prior to melting show some Cu penetration into the Ni particle (and *vice versa*) as well as a sharp compositional gradient near the original interface. This is consistent with the solid-state interdiffusion evidence given in Figure 4-5. A uniform concentration of approximately 100 wt% Cu is found in the un-melted Cu regions. Immediately after melting at 1090°C (0 min., curves in Figure 9*a* and *c*), the frozen liquid composition is still quite uniform and was measured to be approximately 99-100 wt% Cu – corresponding to the equilibrium liquidus at 1090°C (C_L). After initial melting at 1140°C (0 min. curves in Figure 9*b* and *d*), the frozen liquid regions are shown to have rapidly obtained uniform compositions near 92-93 wt% Cu (≤ 1 minute) due to high diffusivity rates in the liquid. This is also consistent with the equilibrium

liquidus composition at 1140°C. At this point certain Cu-rich regions have obtained composition at or below the solidus composition C_S, indicating that they were solid-phases at T_P (i.e., isothermally solidified). Interfacial compositions constrained by local equilibrium at C_S/C_L were also observed by Puckert *et al* in the Ni/Cu system [23].

If we closely examine the Type B data of Figure 4-14*c* and *d*, even at a 0 minute hold time, a large portion of the Cu-rich microstructure has obtained a Cu concentration at or below *Cs* – suggesting that it isothermally solidified. For example, at 1090°C and 1140°C a concentration of $C < Cs$ occurs at radial positions of 150 and 130 microns respectively. These solid-solution regions are larger than the initial Ni particle radius of 80.5 microns and support the diminished initial liquid formation measurements of Figure 4-7 (i.e., $W_{Ao} < C_O$). Furthermore, the relatively larger $C < C_S$ solid-solution region at $t = 0$ minutes for 1090°C vs. 1140°C is consistent with the decreased initial liquid fraction (or increased solid fraction) measured by DSC at 1090°C – owing to solid-state sintering and dissolution effects previously discussed. The curves at successively longer hold times show decreased Cu contents at longer radial distances from the Ni core. This is a result of solute diffusion across the moving solid-liquid interface and into the isothermally solidified regions. For the 30 min. hold curves at 1090°C and 1140°C (Figure 4-14*c* and *d)* compositions close to C_L remain at radial distances of 150 μm and above. This indicates the continued presence of liquid phase in these samples, as indicated by the DSC results of and Figure 4-11*b*. After 45 minutes at 1090°C (Figure 4-14*c)* and 75 minutes at 1140°C (Figure 4-14*d)*, all compositions were measured below *Cs*, supporting complete isothermal solidification (Figure 4-11*b)*. The results for Type A samples show similar solute distribution behaviour and are also consistent with the DSC measurements of Figure 4-11, given that the DSC measures bulk behaviour whereas the EDS results are for isolated particles. Liquid distribution effects, which are significantly contrasted in Type A and B samples, will be further discussed in Section 4.3.3.

It is interesting to note from all cases in Figure 4-11 that Cu penetration deeply into the Ni base metal particles is slow and the Cu concentration gradients near the original interface (~80μm) remain sharp even at long hold times. This indicates the lack of long range diffusion into the Ni core, which remains very Ni-rich during isothermal solidification - even when effectively no liquid remains after 75 minutes at 1140°C for example (Figure 4-14*d)*.

Furthermore, a fairly solute-rich 'layer' has formed surrounding base metal particles having Cu-rich compositions near C_S. This further indicates that isothermal solidification of the liquid primarily occurs by epitaxial growth of the alloyed base metal particles via the progression of the solid-liquid interface - leaving behind a Cu-rich solid-solution that is constrained at C_S by local equilibrium at the moving interface.

4.2. Homogenization and Reheating

Three layered/pressed powder mixtures were selected for re-heating experiments to study the influence of hold time duration on the degree of homogenization and melting point shift. For these experiments samples were initially heated to 1140°C and underwent ~100% isothermal solidification after different hold segment durations (i.e., 150, 240, and 360 minutes). These samples were cooled to room temperature after TLPS and then re-heated well past the liquidus temperature of the bulk mixture composition (1300°C) to cause complete re-melting and then finally cooled again to room temperature. The re-heat profiles of these samples after the isothermal holds at 1140°C are shown in Figure 4-15. Also included for comparison is a heating segment showing the initial melting behaviour of the powder mixtures at 1085°C and the absence of an exothermic solidification peak after the initial TLPS treatment. The melting endotherms during the re-heat segments of all three specimens indicate higher onset temperatures, which correspond to melting point shifts. The re-heated melting endotherms are also much broader than the initial melting endotherms. Table 4-6 shows the measured re-melt onset temperatures for these three samples, as well as the corresponding melting point shifts and melting ranges.

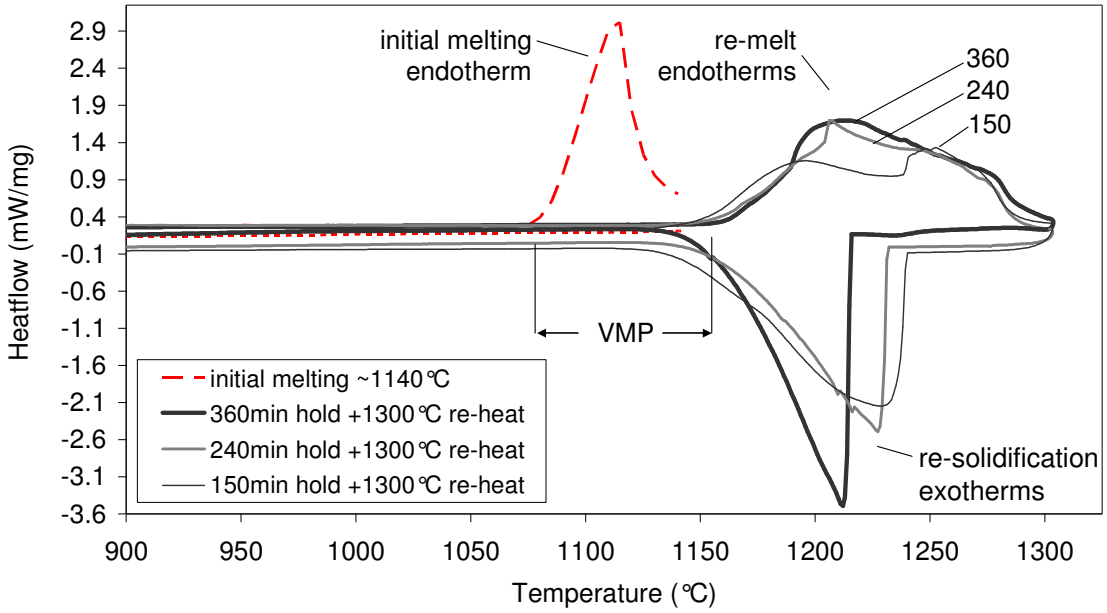

Figure 4-15: DSC traces for 65wt% Cu pressed/layered mixtures (Type A) that were initially TLP sintered to remove the liquid and cooled (150, 240, and 360 minute hold segments). These were re-heated to 1300°C showing different melting point shifts and degrees of homogenization.

Table 4-6: Melting point shift data for layered/pressed mixtures (Type A).

Hold time at 1140°C (min.)	New melting point (°C)	Melting point shift (°C)	Melting range (°C)
150	1150.0	65.1	140.8
240	1157.2	72.3	135.6
360	1168.7	83.8	132.1

The broad melting range of these reheated samples is due to the incomplete homogenization that exists after isothermal solidification, as evidenced by the EDS compositional profiles in Figure 4-14. For example, the compositional profile for the Type A specimen TLP sintered at 1140°C for 160 minutes in Figure 4-14*e* (i.e., 10 minutes longer than the first re-heated specimen in Figure 4-15) clearly shows that a very uneven solute distribution is present at this point. Upon re-heating, this causes progressive melting through compositional gradients within the specimen as the temperature is increased up to 1300°C. The very non-uniform EDS compositional profiles observed at the end of isothermal solidification clearly explain why the re-heat DSC traces for the 150 minute specimen contained a double peak. Re-melting first consisted of melting the peripheral Cu-rich regions, which are followed by melting of the Ni rich core regions at higher temperatures. In comparison, the 240 and 360 minute DSC traces show single-peak melting endotherms that are progressively narrower due to increased homogeneity

4.3. Discussion

In summary, DSC data presented in Section 4.1 allowed the quantification of the liquid fraction present during different TLPS stages. The supporting *ex situ* metallographic analysis indicates that the isothermal solidification mechanism may be dominated by interfacial motion and does not require significant saturation of the original Ni particles by Cu. At completion, a Kirkendall pore structure has developed, which affects the diffusion field – likely slowing mass transport rates.

4.3.1. Temperature Effects

The results for the various TLPS stages in Section 4.1 can be discussed with the aid of a conceptual model that is illustrated in Figure 4-16, which depicts a base metal Ni particle having an initial radius a_{Bi} surrounded by a pure Cu matrix. This concentric sphere model is a reasonable assumption for a representative unit cell (see Figure 4-13*a* and *b*) since the particle size of Ni is much larger than the surrounding Cu powder. The effects of the developing Kirkendall-type pore structure and inter-particle densification will not be discussed in order to simply illustrate the liquid removal process within a single unit cell. Prior to heating, no interdiffusion between the as-received powders is shown by the square, dashed profile in Figure 4-16*a*. During athermal heating to process temperatures $T_P \leq T_A$ (T_A being the melting point of the additive phase, Cu - 1085°C), a solid-state sintered interdiffusion region and corresponding profile develops (see dark solid curve and the solid grey phase region labelled 'SS' having radius a_{Bss} in Figure 4-16*b*). This region represents any material that is slightly alloyed to no longer consist of pure Cu. The original Ni particle size is identified by the darker core and original square compositional profile.

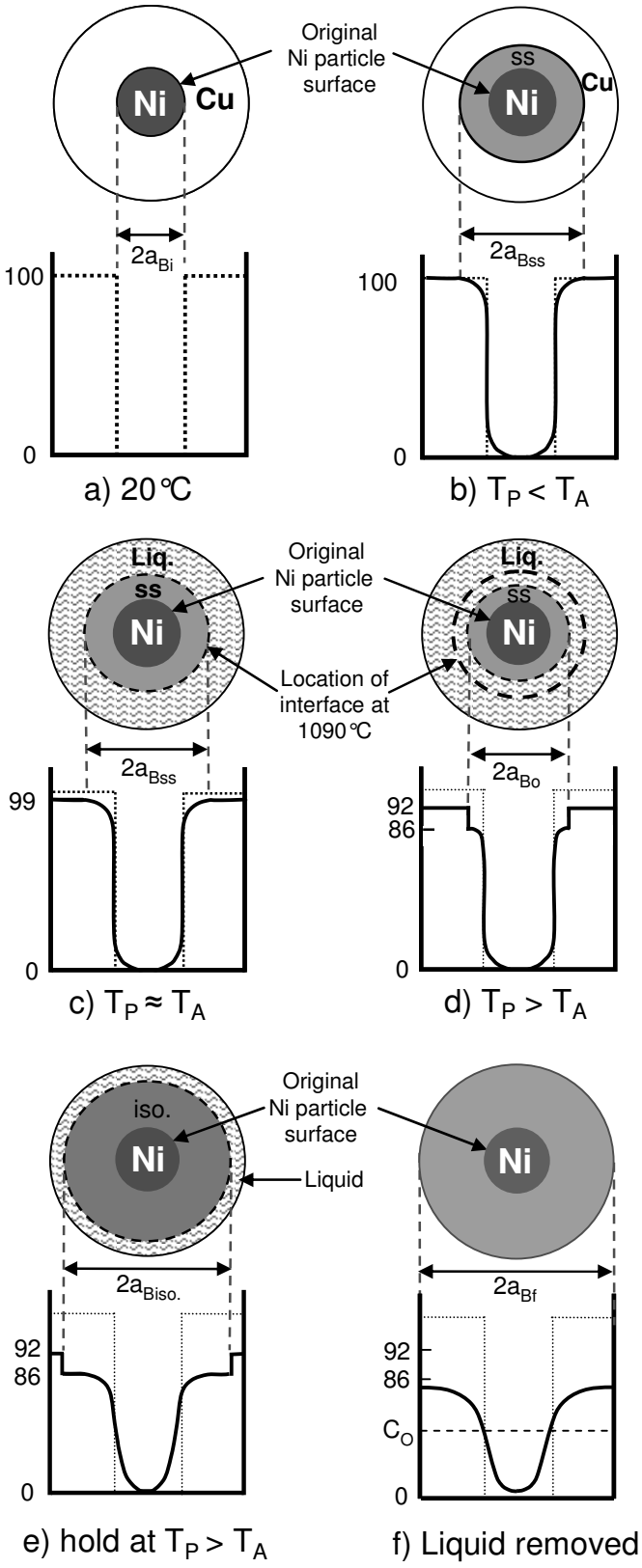

Figure 4-16: Simplified concentric sphere model showing solid/liquid fractions and solute concentration profile evolution during TLPS.

Once $T_P \approx T_A$ (e.g. 1090°C in Figure 11*c*), only the most Cu-rich regions of the solid-state sintered profile having compositions ranging from C_L to pure Cu (99 to 100 wt% Cu) will melt (illustrated by the hatched region). The solid-liquid interface is represented by a dashed circle and the diameter of the bounded solid-solution region (i.e., the new solid particle with radius a_{Bss}) is extended onto the compositional gradient below. At $T_P \approx T_A$, essentially no Ni dissolution or liquid dilution occurs since C_L = 99 wt% Cu (i.e., negligible Ni solubility in the liquid phase). As DSC results have quantitatively shown, this results in a decreased initial liquid fraction ($W_{Ao} < C_O$). Figure 4-16*c* illustrates how this diminished liquid fraction via solid-sate interdiffusion results in an enlarged, solid-state sintered Ni particle in comparison to its original size (i.e., $a_{Bss} > a_{Bi}$). EDS results have also shown that the liquid rapidly ($\leq$ 1 minute) obtains a uniform, saturated compositon at C_L due to high diffusivity rates within the liquid phase.

For the case where $T_P > T_A$, in Figure 4-16*d* (e.g., 1140°C) dissolution and melting of the outer regions of the Ni particle serve to decrease the Ni particle size to a_{Bo} at the beginning of the isothermal segment. As evidenced by DSC results, this serves to recover some of the liquid lost because a portion of the solid-state interdiffused regions (labelled 'SS'), having solute contents above the new solidus C_S (i.e., > 86 wt% Cu at 1140°C), now melt as they are non-equilibrium phases at $T_P > T_A$. This recovered liquid phase is illustrated by the liquid region surrounding the diminished 'SS' region and inside the heavy dashed line of Figure 4-16*d*. This heavy dashed line represents the previous 1090°C interface at a_{Bss}. Also, the increased solubility of Ni in the liquid phase, as indicated by the new equilibrium liquidus composition (C_L = 92 wt% Cu at 1140°C) leads to dissolution of the Ni particles and dilution of the liquid to a lower C_L. The interfacial solid surface concentration of the Ni particles is reduced from $C_S \approx$ 99 wt% Cu at 1090 °C to the new solidus concentration of 86 wt% Cu at 1140°C. The solute profile in the particles is altered accordingly and resembles those measured by EDS in specimens shortly after melting.

With hold time at the process temperature of 1140°C, isothermal solidification takes place by the movement of the solid-liquid interface outward and the growth of the Ni particle (see Figure 4-16*e*). DSC data show that there is as a measurable decrease in the liquid fraction with increasing hold time. As the *ex situ* EDS analysis of Figure 4-14 indicates, the isothermal solidification process creates a Cu-rich solid shell surrounding the original Ni particle (see the

solid region labelled as 'iso.' in Figure 4-16*e)* having compositions near C_S with very little long range diffusion into the particle core. The growth of this relatively saturated peripheral region, which has small compositional gradients resulting in low diffusion mass transfer rates, explains the slower solidification kinetics at long hold times (Figure 4-11). Grain growth, overlapping unit cells, and the developing Kirkendall pore structure are also factors that will decrease mass transfer and diffusional solidification rates. Finally when all of the liquid is removed from the sample (Figure 4-16*f*) the solid-liquid interface is no longer present and the composition of the Cu-rich outer region will drop below C_s since it is no longer constrained by local equilibrium with the liquid. As depicted in Figure 4-16*f* (and evidenced by the EDS results of Figure 4-14) even at this stage the center of the Ni particle only contains a few wt% Cu. Homogenization within the solid-solution structure serves to gradually decrease concentration gradients with increasing hold time. At $t = \infty$ the sintered specimen will obtain a uniform composition determined by the bulk mixture composition (see the dashed line at C_O in Figure 4-16*f*).

4.3.2. Isothermal Solidification Rates

Further examination of Figure 4-11 reveals that isothermal solidification rate comparisons at both temperatures are difficult to make based on the slopes of the W_A curves. Although TLPS at higher temperatures clearly generated greater W_{Ao} and required greater removal times, it is difficult to ascertain if the rate of liquid removal is faster at 1140°C - as might be expected from increased diffusivities. It is important to note that there are multiple reinforcing and opposing factors that affect the rate of isothermal solidification at different T_P. Increased diffusivities at higher T_P will tend to increase solidification rates. Also, the decreased base metal particle size as a result of dissolution processes will increase the Ni particle surface area/volume ratio and decrease diffusion depths – causing increased rates.

Solubility effects at higher T_P will tend to decrease isothermal solidification rates. The decreased Cu solubility limit within the solid base metal at higher T_P (i.e., the interfacial boundary condition at C_S*)* will decrease solidification rates due to the reduced magnitude of concentration gradients within the solid phase. Also, the decreased C_S and C_L solubilities at higher T_P result in a decreased partition coefficient ($k = C_S/C_L$) across the solid/liquid interface

vs. $k = 1$ at T_A. The increased composition difference between the liquid and solid requires more solute diffusion away from the interface for it to progress into the liquid. As such, the partition coefficient may play a significant role in determining solidification kinetics since EDS data suggest that this is an interface-controlled process (vs. long range solid-state solute diffusion away from the interface). Finally, accelerated grain growth at higher T_P will decrease the amount of grain boundaries present, which offer a high diffusivity pathway for the solute. This may also decrease mass transfer rates within the solid and reduce the solidification rate.

This complex interaction of temperature dependent processes explains the varying curvature of W_A plots in Figure 4-11, where all plots show a decreasing slope, or solidification rate, with increasing time. For a given sample type, the W_A curvatures and slopes appear to be similar at a given time. Comparisons are therefore difficult due to the varying rates and the fact that the curves are offset on the ordinate axis due to different initial liquid fractions. The diffusion-based model developed in Section 6.2 will discuss important temperature-dependent effects such as diffusivity and solubility limits in more detail. However, the most notable and initially counterintuitive effect of increased T_P in the presented DSC data is that longer net isothermal solidification times are required (t_C). This is attributed to the increased initial liquid fraction formed as a result of dissolution, which assists densification. These are important practical attributes for TLPS brazing applications, which favour shorter processing times at T_P.

4.3.3. Sample Type and Liquid Distribution Effects

The DSC results plotted in Figure 4-11, which are also tabulated in Table 4-5, can be used to evaluate the effects of liquid distribution caused by the different A and B preparation techniques. Both layered/pressed data sets in Table 4-5 required much more time to completely solidify the liquid phase when compared to the mixed/loose counterparts despite the fact that lower initial liquid fractions were measured for Type A specimens. This is likely due to the fact that, although the Ni-Cu distribution is more segregated in the layered/pressed compacts (which limits interdiffusion, increasing W_{Ao}), green pressing counteracts this effect by significantly increasing the deformed contact area between the powders. This increases solid-state interdiffusion during heat-up and reduces initial liquid fractions relative to Type B mixtures at both temperatures. At increasing hold times, the rate of isothermal solidification

slows significantly in layered/pressed Type A specimens due to the less homogeneous liquid distribution around a densely compacted Ni particle network (as clearly exhibited in Figure 4-12*a*). As the isothermal process continues, the layered/pressed and mixed/loose curves progressively deviate/separate. After approximately 30 minutes, the layered/pressed samples now contain almost 50 wt% more liquid in comparison (Table 4-5). This difference becomes more pronounced at long hold times, where layered/pressed samples required over an additional hour for complete isothermal solidification at both temperatures - indicating a slower net isothermal solidification process.

In summary, pressing may explain the somewhat smaller initial liquid fractions, but the increased inhomogeneity in the layered/pressed samples explains the prolonged solidification times required. Relative to the pressed Type A samples, distribution of the liquid and particle rearrangement are less restricted in the loose Type B mixtures. The less uniformly distributed liquid formations in Type A samples creates certain liquid-deficient areas that will solidify rapidly due to a relative abundance of adjacent Ni particles (as found by the rapid solidification observed at short hold times). Conversely, larger liquid 'pools' found in peripheral areas of the specimen (Figure 4-12*a*) will require much more time to be removed by solute diffusion into the few adjacent base metal particles. This effect is amplified by green pressing since flow and uniform redistribution of the liquid is inhibited by the pressed and sintered Ni skeleton. These observations can be made at both temperatures studied, where slow, prolonged solidification is particularly evident at long hold times.

4.3.4. Ni Particle Size Effects

A final isothermal solidification DSC study was conducted for Type B mixtures TLP sintered at 1140°C to investigate the effect of base metal (Ni) particle sizes on TLPS. Mixture compositions of C_O = 65 wt% Cu were prepared using the Cu powder and the three different Ni particle sizes shown in Table 3-1. Figure 4-17 shows DSC results for the liquid fraction remaining as a function of hold time at 1140°C. Mixtures containing smaller Ni particles initially formed much less liquid (effectively no liquid in the 3.39 μm case) and isothermal solidification required less time to reach completion. The rate of solidification seems to be faster in the a_{Bi} = 57.51 μm data relative to the coarse Ni mixtures (a_{Bi} = 80.50 μm).

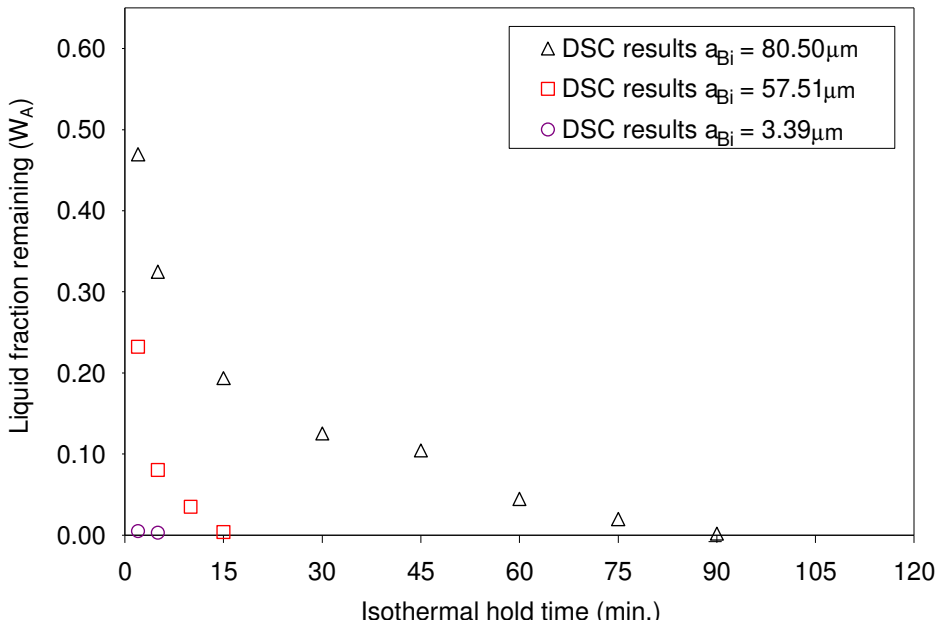

Figure 4-17: DSC results showing the fraction of liquid remaining after interrupted isothermal holds at 1140°C for 65 wt% Cu Type B mixtures prepared using three different Ni particle sizes.

Comparison of the data in Figure 4-17 shows that interdiffusion and solidification rates are significantly affected by changes in a_{Bi}. Other TLPS studies on Pb-Sn [11,28] and Al-Zn [26] powder systems have also shown the TLPS kinetics is highly sensitive to base metal particle size. If we recall from Section 2.1, this is attributed to the fact that interdiffusion during sintering is a highly surface/interface area dependent process [2]. Crank's equations for solute penetration into spherical particles [47], as well as Corbin's diffusion-based TLPS model [25], show that the rate of solute uptake is a function of Dt/a_B^2.

Since smaller base metal particles have higher surface area/volume ratios, they provide lower diffusion depths and a higher total inter-particle contact surface area for a given mixture composition C_O (i.e. more fine Ni particles for the same mass fraction Ni). These factors both accelerate the interdiffusion process during the initial heat-up segment (effectively decreasing the initial liquid fraction formed) as well as during the isothermal solidification process (causing accelerated freeze-off and isothermal solidification). The DSC data in Figure 4-17 clearly demonstrates these effects, where low a_B cause significantly reduced W_{Ao} and rapid isothermal solidification.

4.4. Summary

It was found that DSC is a valuable tool for quantitatively examining liquid formation and removal during athermal segments in TLPS sintering cycles, especially when combined with microscopy techniques. Metallographic analysis alone would not allow the determination of liquid fractions in TLP sintered specimens due to the variation of numerous particles, and most importantly because isomorphous systems do not exhibit an interface in the solid-state. Archimedes density measurements and microscopy results showed that braze densities above 95% were achieved with Cu concentrations of 55 wt% or higher. Full densification did not occur due to observed large trapped gas pores, residual starting Ni powder pores, and Kirkendall pores generated from unequal diffusivities.

Unlike previous DSC studies with low temperature eutectic powder systems with limited solubility, it was found that solid-state interdiffusion during the heat-up segment and dissolution at $T_P > T_A$ significantly affect the amount of liquid initially formed and its removal in the Cu-Ni system. For 65 wt% Cu loose powder mixtures (Type B), complete isothermal solidification of the liquid at a processing temperature of 1140°C occurred in approximately 90 minutes. However, solidification of the liquid phase for identical braze mixtures sintered at 1090°C occurred in significantly less time - 45 minutes. This can be explained by the observed increase in liquid fractions formed at higher processing temperatures (due to the dissolution of Ni), which effectively counteracts the increased diffusivities at these temperatures and requires more time to isothermally solidify. Pressed/layered brazes (Type A) required much more time for complete solidification due to inhomogeneous liquid distributions. The increase in the post-processed melting point of this braze composition was in excess of 80°C upon reheating.

TLP sintered at 1140°C using three different particles sizes revealed that fine base metal Ni particles cause high degrees of solid-state interdiffusion during heat-up, small initial liquid fractions, and accelerated liquid removal rates due to high surface area/volume ratios. *Ex situ* metallographic analysis of post-sintered specimens via SEM and EDS indicates that isothermal liquid solidification occurs by limited long-range Cu diffusion within the Ni particles, which grow epitaxially by the transient progression of the solid/liquid interface at compositions given by the liquidus and solidus (C_S/C_L). Since the DSC technique only quantifies the liquid fraction remaining, it is difficult to confirm this isothermal solidification mechanism without actual *in situ* interdiffusion data collected during the isothermal hold at T_P.

5. Neutron Diffraction Experiments

Thermal neutrons are a highly penetrating non-destructive material probe with significant potential for elucidating the transient aspects of TLPS via *in situ* structural evolution measurements from large specimens throughout the sintering cycle. In this way it has the potential to add unique information that compliments DSC and metallographic techniques. The aim of this work was to study Ni-Cu TLPS kinetics under similar conditions to DSC experiments, and determine the effectiveness of the ND technique for gathering *in situ* interdiffusion and phase transition information.

Prior to attempting long isothermal TLP sintering experiments, it was necessary to perform preliminary experiments to better understand the results obtained as well as the capabilities of the C2 diffractometer and the ancillary equipment at the CNBC Chalk River Labs. Table 5-1 provides a description of the ND experiments conducted at the CNBC that will be discussed below. The maximum duration of the isothermal segments was determined by the beam time available at the CNBC NRU reactor for each experiment.

Table 5-1: List of ND experiments

Sample no.	Powder mass (g)	C_O (wt%Cu)	Atmos-phere	R_h (°C/min.)	T_P (°C)	Experiment type	Description
1	2.498	64.8	N_2	N/A	27	preliminary	Room temperature ND pattern characterization
2	2.522	100.0	N_2	40	1112	preliminary	Cu melting characterization (30 min. hold atT_P)
3	2.140	64.0	N_2	40	1200	preliminary	Non-interacting powders w/ Al_2O_3 barrier
4	2.515	65.2	N_2	40	1080	SSS	630 minute hold at T_P
5	2.523	65.0	N_2	40	1091	TLPS	1040 minute hold at T_P
6	2.529	65.3	N_2	10	1128	TLPS	900 minute hold at T_P
7	2.495	65.0	N_3	40	1162	TLPS	10 minute hold at T_P
8	2.490	64.8	N_2	40	1194	TLPS	30 minute hold at T_P
9	2.502	65.0	N_2	40	1178	TLPS	720 minute hold at T_P

5.1. Results and Analysis of Preliminary Experiments

5.1.1. ND Pattern Assessment and Powder Characterization (Sample 1)

Figure 5-1 presents a neutron diffraction pattern collected during 1 minute from sample 1 (C_O = 65wt% Cu) at room temperature. A Rietveld profile fit calculated via GSAS for Al_2O_3, Ni, and Cu phases is also shown. The difference between the observed pattern and the calculated profile is shown along with the fit quality residual terms (R). The calculated powder phase fraction of Cu is also provided, which coincides well with the prepared mixture composition (C_O).

Figure 5-2 presents a similar plot, but for five sequential 1-minute diffraction patterns that were summed to give a 5-minute pattern (i.e., a 5-minute sum interval). A large 2θ scan range (20-110°), which is larger than the typical 80° range, was used in this experiment. This was done in order to initially evaluate diffraction peaks at high angles and determine if this was needed for all experiments. The full ND patterns in Figure 5-1 and Figure 5-2 were found to show no significant Ta, V, Mo, W, or Al peaks arising from the furnace, thermocouple, or sample environment materials. The predicted peak locations and profiles for Ni, Cu and Al_2O_3 were found to account for all measured peaks and provide a good fit to the experimental patterns.

By comparing Figure 5-1 and Figure 5-2, the 5-minute pattern is clearly shown to provide improved data due to a visibly better peak/background intensity ratio and a smoother background signal (note the lower noise variation in the difference plots). The low neutron counts collected during short 1-minute scans are not sufficient to form strong peaks that facilitate quality GSAS fits with low R values. This explains the improved residual fit terms (wR_p and R_p) and C_O calculation with 5 minute scan durations. However, both experimental patterns provide distinct Ni, Cu and Al_2O_3 peaks, include no unknown peaks, and provide reasonable GSAS fit parameters considering the short scan time and low neutron counts. This illustrates that ND data can be obtained on the C2 diffractometer at scan intervals as low as 1 minute and still allow the identification of individual peaks and phases. Signal quality can be improved by summing 5 successive patterns, thereby decreasing the time resolution to 5 minutes.

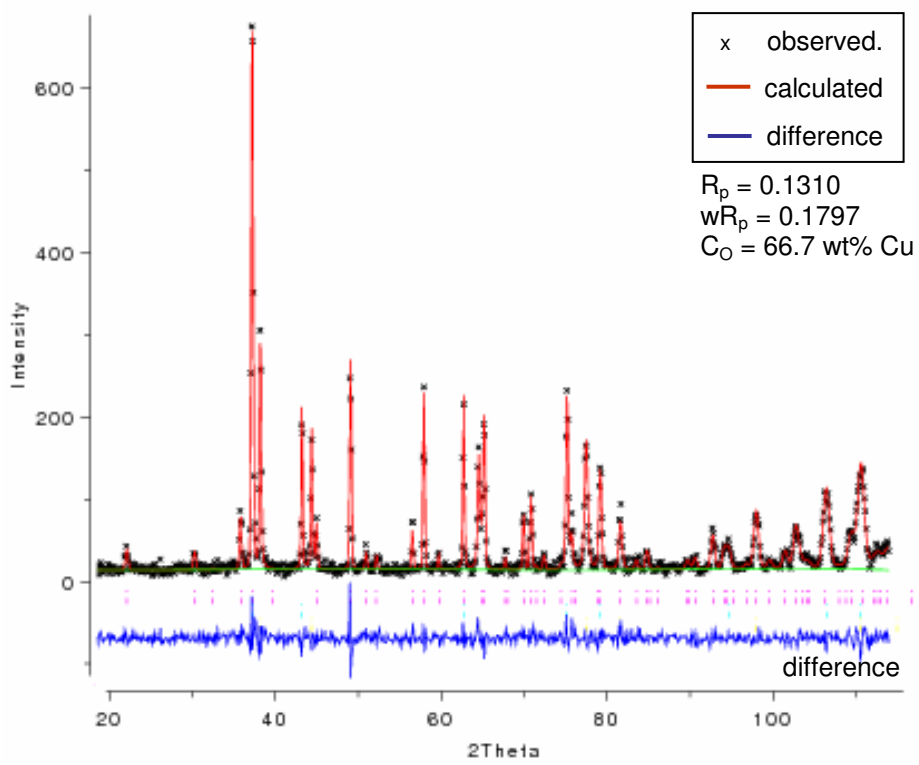

Figure 5-1: ND pattern (1-minute) and GSAS Rietveld fit of a 65 wt% Cu mixture (sample 1).

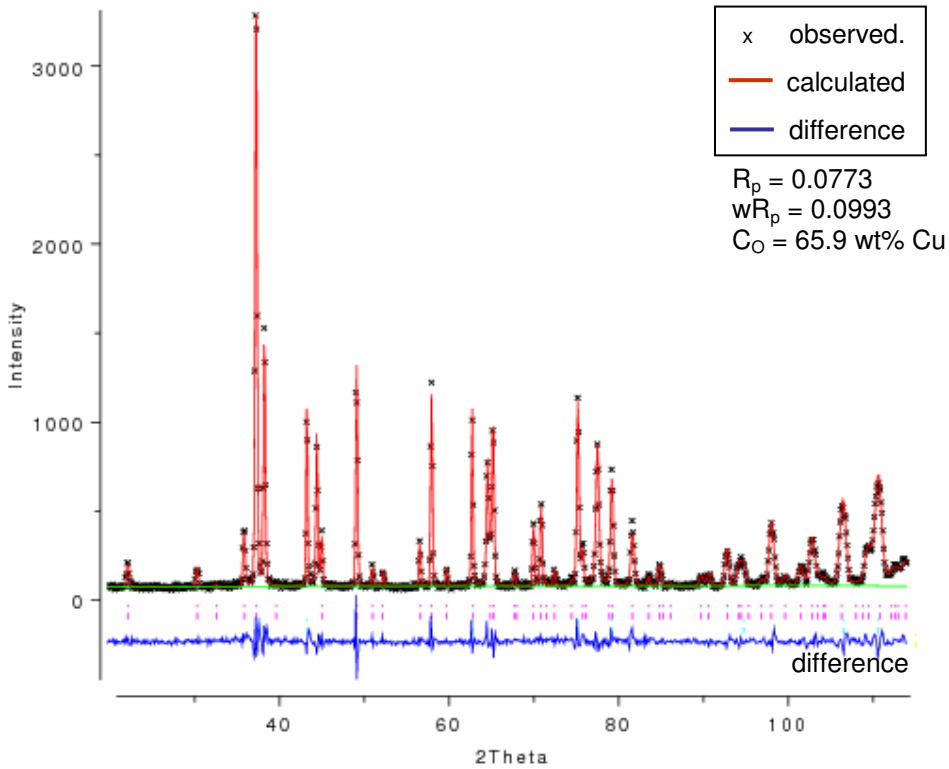

Figure 5-2: ND pattern (5-minute sum) and GSAS Rietveld fit of a 65wt% Cu mixture (sample 1).

Table 5-2 and Table 5-3 show the calculated lattice parameters for Al_2O_3 and Ni/Cu respectively. Table 5-2 shows that the calculated Al_2O_3 lattice parameters for both ND patterns agree well with the high-accuracy XRD measurements described in Section 3.1 as well as literature values [103]. The estimated standard deviations *(σ)* for each lattice parameter are also lower with the 5-minute scan fit. The 5-minute scan provides a more accurate measurement due to improved signal quality and statistics (as indicated by the observed-calculated difference curves in both figures). Both GSAS fits indicated that zero correction parameters ($\delta\theta$) of 0.0465° in 2θ were necessary to align the patterns and correct for sample displacement (as described in Section 2.11.7). This zero correction was typical of that required for past experiments on the C2 diffractometer [107] and ensuing TLPS experiments in this study.

Table 5-3 shows the calculated Ni and Cu powder lattice parameters as well as literature values for a_{Cu} [111] and a_{Ni} [112]. These results are considered to be within the expected range of experimental errors for this type of rapid ND measurement. In the case of Al_2O_3 (Table 5-2), the derived *a* and *c* lattice parameter measurements for the 5-minute ND data and Bruker XRD data are within 0.00560Å and 0.02155Å respectively (or 0.1177% and 0.1658%).

Table 5-2: Comparison of Al_2O_3 lattice parameters calculated by GSAS for XRD and ND data.

	Alumina lattice parameters				Residual terms	
Data Source	**a (Å)**	**σ_a (A)**	**c (Å)**	**σ_c (A)**	**wRp**	**Rp**
C2 ND - 1 minute	4.76586	0.00039	13.01517	0.00014	0.1797	0.1310
C2 ND - 5 minute	4.76592	0.00022	13.01627	0.00080	0.0993	0.0773
Bruker XRD	4.76032	0.00005	12.99472	0.00020	0.1035	0.0758
Lutterotti *et al*	4.76050		12.99560			

Table 5-3: Ni and Cu lattice parameters calculated by GSAS for ND data.

	Cu lattice		Ni lattice		Residual terms	
Data Source	**a (Å)**	**σ_a (A)**	**a (Å)**	**σ_a (A)**	**wRp**	**Rp**
C2 ND - 1 minute	3.62017	0.00027	3.52869	0.00030	0.1797	0.1310
C2 ND - 5 minute	3.62037	0.00015	3.52878	0.00017	0.0993	0.0773
Srinavasa *et al*	3.62465					
Swanson *et al*			3.52380			

The expanded 2θ scale in Figure 5-3 presents peaks of interest which are labelled within the 40-80°. The presence of many distinct Ni and Cu peaks in the 40-80° range revealed that collecting 80° scans (20-100°), would be sufficient for further *in situ* studies. Important

peaks have been labelled according to the *hkl* Miller indices of the corresponding crystallographic planes and phases which generated them. All other peaks are identified by tick marks for each phase at the bottom of the figure. For reference, Table 5-4 lists the room temperature 2θ positions for all the Cu and Ni peaks formed at angles below 100°.

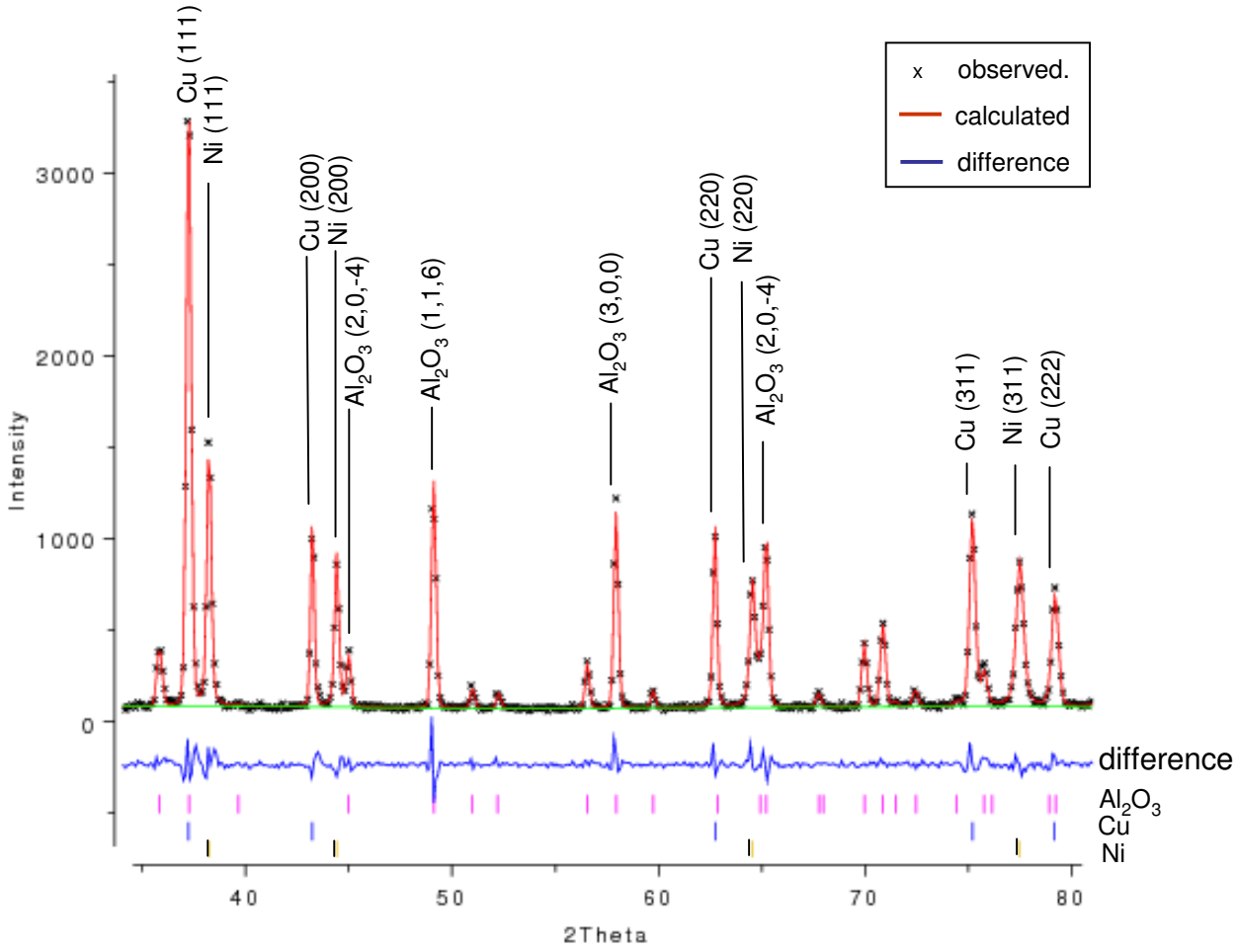

Figure 5-3: Peak identification for Ni, Cu and Al_2O_3 reflections for sample 1 (5-minute sum).

Table 5-4: Cu and Ni neutron diffraction peak locations at room temperature (λ = 1.33069Å)

Cu		Ni	
2θ (°)	***hkl* peak**	**2θ (°)**	***hkl* peak**
37.23	111	38.23	111
42.24	200	44.42	200
62.74	220	64.56	220
75.20	311	77.51	311
79.17	222	81.65	222
94.71	400	97.99	400

The numerous reflection tick marks at the bottom Figure 5-3 clearly show that Al_2O_3 generates many peaks - arising from its HCP structure. Alternatively, Ni and Cu generate fewer peaks that appear at similar angles - both having FCC patterns. Inevitably, many of the Ni/Cu FCC and Al_2O_3 peaks overlap. For further *in situ* experiments it was important to identify Ni and Cu peaks which could be used for clearly interpreting Ni-Cu interdiffusion and phase transformations (Cu melting/solidification). Al_2O_3 peaks facilitating thermal expansion calculation and temperature verification were also required. The list below describes important criteria used in this selection process:

- High intensity reflections should be used whenever possible to provide strong, sharp peaks that are more easily distinguished from the background. As indicated in Figure 5-1 and Figure 5-2, lower angle peaks appear somewhat sharper and more intense, whereas peaks above 100° appear much broader. This is due to increased instrumental broadening, a weaker diffraction signal, and the presence of many more overlapping high-index Al_2O_3 peaks at high angles.
- Overlapping peaks should be avoided since this complicates the determination of a given peak's location. Overlapping also alters a peaks measured profile and width, which are important for interpreting interdiffusion/alloying in the case of Ni and Cu.
- Peak shifting due to thermal expansion throughout the temperature program must be considered since this may affect how peaks overlap at different temperatures. As the lattice of each phase thermally expands with increasing temperature, peaks will shift to lower angles as per Bragg's law (i.e., $d_{hkl} = \lambda/2\sin\theta$). Since each phase has a different coefficient of thermal expansion (CTE), it is expected that the respective peaks will shift by varying degrees.
- Peaks having simple *hkl* indices (e.g., 200, 300) facilitate the calculation and tracking of lattice parameter thermal expansion (see Section 2.11.2). This is a convenient consideration, particularly for Al_2O_3, since numerous patterns were collected at different temperatures throughout the temperature programs.

- As in Rudman's solid-state sintering XRD study [84], a set of Ni and Cu peaks having the same *hkl* Miller indices should be used to evaluate interdiffusion/alloying effects This is important since substitutional diffusion will cause the d-spacing of different *hkl* reflections to change differently for each type of plane. As such, the 2θ reflections for each *hkl* plane will shift and broaden in a different manner.
- The set of Ni and Cu peaks chosen must not be separated by alumina peaks since this will overlap with the Ni-Cu alloy region that will form during TLPS. Since Ni and Cu can form isomorphous alloys, the entire 2θ region separating two similar Ni and Cu *hkl* peaks will begin to participate in Bragg diffraction as interdiffusion/alloying takes place.

Figure 5-3 shows that the Cu(111) and Ni(220) peak significantly overlap with Al_2O_3 peaks, thus complicating the analysis of the (110) and (220) reflections. Furthermore, the (222) and (311) peaks were not chosen due to the increased broadening at higher 2θ angles and the fact that they are separated by Al_2O_3 peaks. Considering the above criteria, the (200) reflections were chosen for Ni/Cu interdiffusion analysis. These reflections are sufficiently intense and, as will be further shown in the ensuing sections, are least affected by overlapping peaks throughout the high temperature programs. The Ni (200) peak overlaps the Al_2O_3(20-4) peak at 44.99°, yet this peak is small and the degree of overlap is less than other candidate peaks. Upon heating, these peaks diverge due to the larger CTE value of Ni. Also, the Al_2O_3(20-4) peak does not separate the (200) Ni and Cu reflections. The Al_2O_3 (300) peaks were chosen for temperature verifications since they do not overlap other peaks and have simple *h00*-type Miller indices that facilitate lattice parameter expansion calculations (as per Equation(2-66)).

5.1.2. Cu Melting and Thermal Expansion (sample 2)

Figure 5-4 presents the recorded thermocouple temperatures during this experiment (sample 2 in Table 5-1), which was performed to observe the melting behaviour of a pure Cu powder sample within the C2 furnace. The sample was initially held at 177°C (T_C = 450°K)

for 30 minutes and then linearly heated at 39.2°C/min. past the melting point of Cu and isothermally held at T_C = 1115°C prior to rapid cooling.

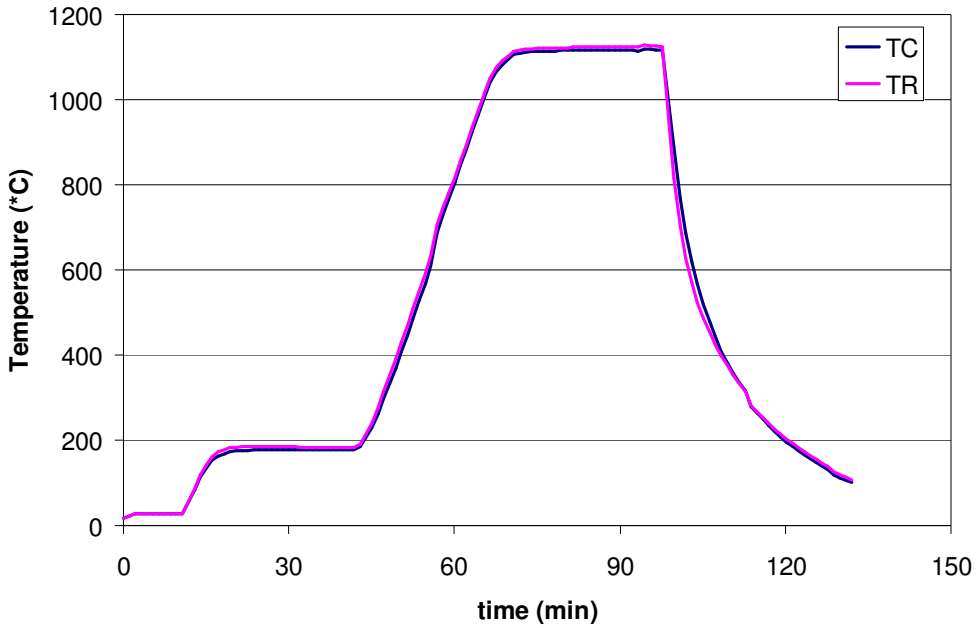

Figure 5-4: Thermocouple temperature history of sample 2 (pure Cu, 123 data sets)

Figure 5-5 presents a 2D film plot of 123 diffraction profiles collected at 1 minute intervals during heating of the pure Cu powder. This film plot can provide a clear view of the evolution of many peaks as they evolve during the experiment at 1 minute intervals. Data sets are sequentially plotted along the y-axis, providing the best time resolution possible over a large 2θ range. The corresponding temperature segment regimes and observed thermal phenomena are described on the right.

Figure 5-6*a* and Figure 5-6*b* show 3D plots of the same patterns in the region of the Cu(200) peaks to expose the Cu melting event (1-minute and 5-minute data respectively). Such 3D plots provide a somewhat more intuitive view of the evolving patterns since the peak profiles and relative intensity changes are visible in a third dimension. However, when more than approximately ~150 patterns are collected, 3D plots become somewhat difficult to interpret, particularly for noisy 1-minute data and larger 2θ ranges with many peaks. In comparison, Figure 5-6 presents a 3D plot for patterns summed over 5 minute time intervals where the individual 1-minute patterns were summed in sequential groups of 5 to give 24 5-

minute patterns. This summed 3D presentation provides improved patterns which have sharper peaks and smoother backgrounds, but time resolution is limited to 5 minutes.

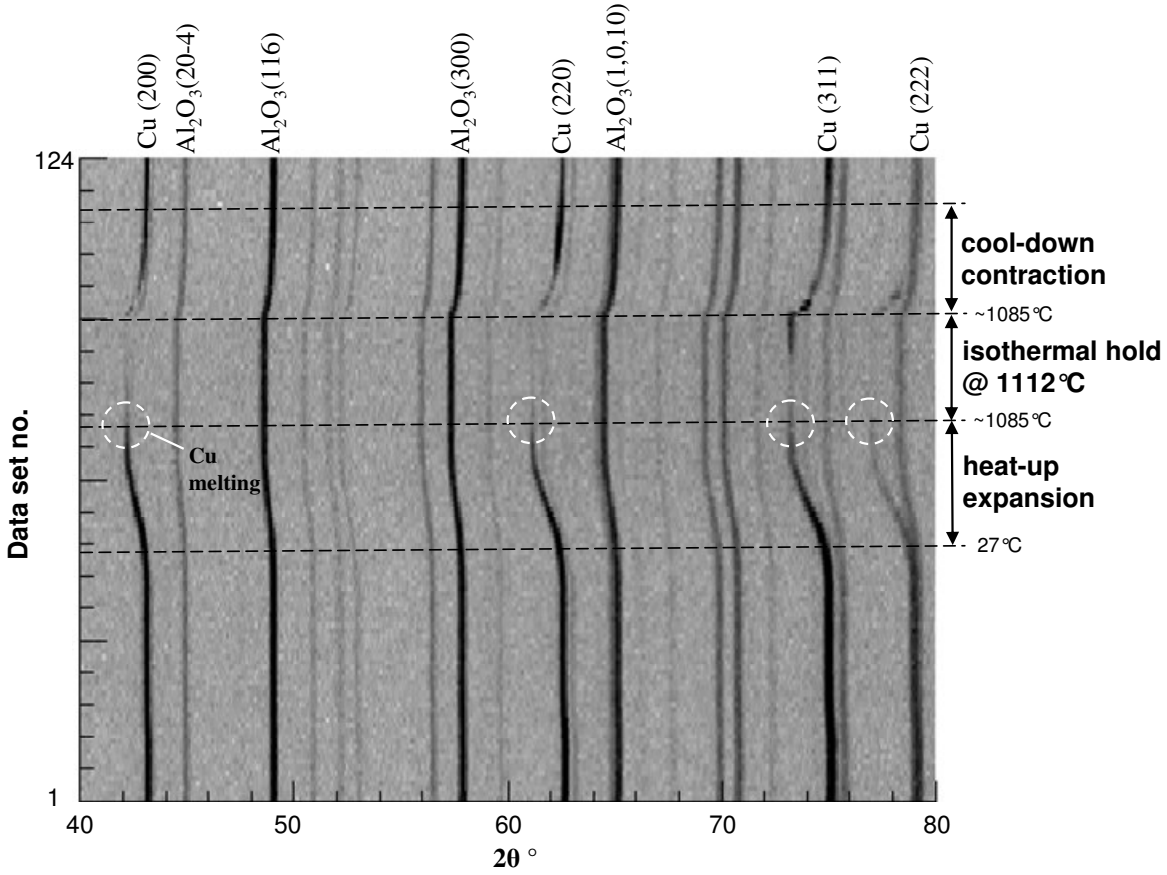

Figure 5-5: 2D film plot of 1-minute diffraction pattern evolution during melting of Cu powder (sample 2).

Figure 5-5 shows the thermal expansion of the various peaks as they shift to lower angles during the heat-up segment. The magnitude of peak shifting is greater in the case of Cu since it has a significantly greater CTE than Al_2O_3, which is typical of ceramic and metallic materials. Once the sample reaches the melting point of Cu, the (200), (300), (222), and (311) peaks visibly decrease in intensity until they are no longer present. Upon cooling the Cu peaks re-appear in the diffraction pattern as Cu solidifies. However, the Cu(311) peak appears to form before the other peaks become visible during freezing. This may be due to directional solidification of the melt, which can generate textured polycrystalline materials having a preferred (311) orientation. The fact that the (311) peak forms even prior to cooling, as measured by the primary thermocouple, is not completely understood. This may also be due to temperature gradients or instability within the hot zone, as well as directional solidification in a

preferred (311) direction at the very bottom of the crucible, which is the coldest region of the specimen.

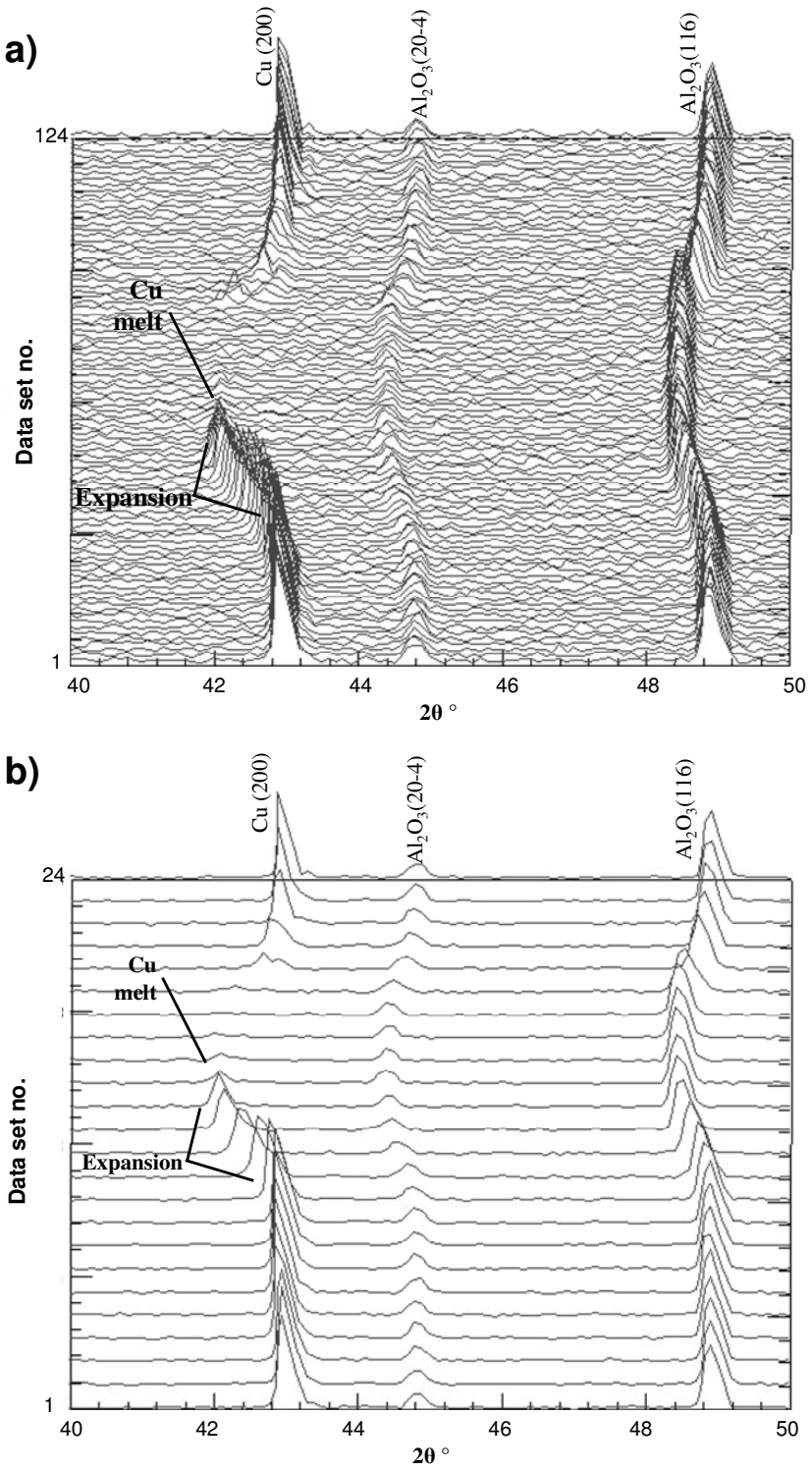

Figure 5-6: 3D plot of diffraction pattern evolution during melting of Cu powder at a) 1 minute intervals, and b) 5 minute intervals.

.

Figure 5-5 and Figure 5-6 illustrate the thermal expansion and melting behaviour of sample 2 well. However, detailed analysis of peak locations and important temperatures requires a 2D presentation method where small changes in the diffraction pattern profiles can be detected, measured, and directly compared. Figure 5-7 presents a waterfall plot where specific temperature-resolved ND patterns are plotted on the same ordinate axis. The corresponding control thermocouple temperature (T_C) and data set number are shown for each pattern. Patterns were selected at ~200°C temperature intervals during the heating segment to show the thermal expansion shifts of the Cu and Al_2O_3 peaks.

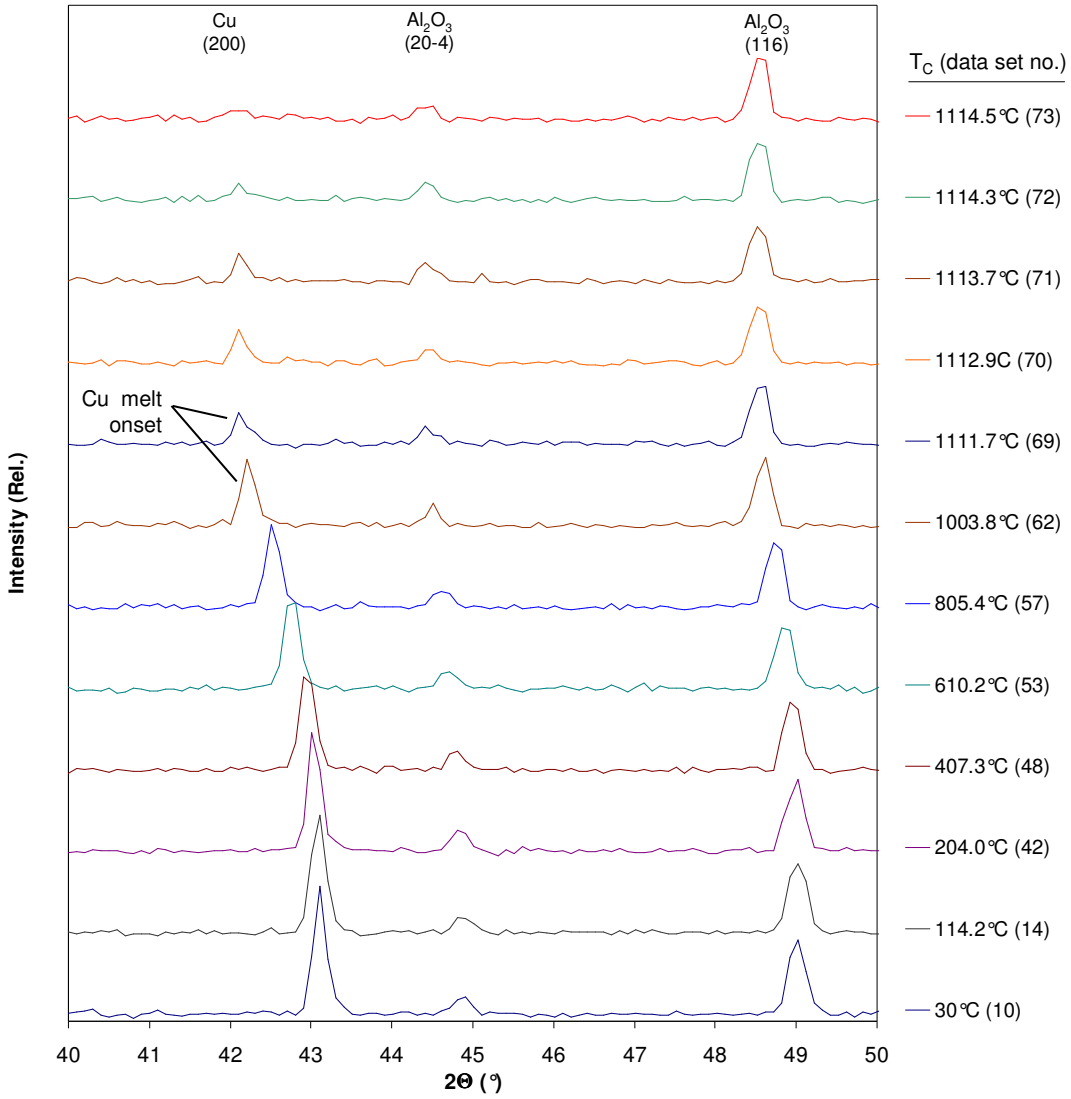

Figure 5-7: ND patterns collected *in situ* at 1 minute intervals during the 40°C /min heating segment of a 100 wt% Cu powder mixture (sample 2).

As the sample temperature approaches the melting point of Cu the (200) peaks begin to broaden and decrease in intensity as expected from the temperature factor and temperature gradients. Once T_C reaches 1111.7°C (data set no. 69), thermal peak shifting ceases and there is an abrupt decrease in the (200) peak intensity. This behaviour is indicative of the onset of Cu melting, which should theoretically occur at 1085°C. One the Cu powder reaches 1085°C, it is no longer stable in the solid state, and therefore further thermal expansion of the lattice (i.e., peak shifting) is not possible, and instead peak diffraction intensity expectedly decreases. This ND data indicates that the melting process is takes place over a certain temperature and time range under these experimental conditions. Since the melting of Cu material once it reaches 1085°C is know to be quite rapid (< 1s [5]), this time period is principally due to temperature gradients and lag within the sample relative to the thermocouple outside the canister. It is expected that some time is required for the sample temperature to equilibrate as well.

The patterns following the detected onset of melting (i.e., data sets 69-73, T_C =1111.7-1114.5°C) indicate that approximately 4-5 minutes is required to equilibrate the sample and cause complete Cu melting throughout the whole crucible length (i.e., completely remove the (200) peaks). The observed melting point (T_C = 1117°C vs. T_m = 1085°C) indicates that there is a radial temperature gradient between the control thermocouple sensor and the sample and that it may have a transient characteristic during athermal segments (as expected based on the sensor position in Figure 3-17). In the sample temperature range near the actual melting point of Cu (1085°C), this temperature difference is approximately 26.7°C since the onset of melting is measured at T_C = 1111.7°C (data set no. 69).

Axial temperature gradients along the length of the cylindrical sample may also contribute to experimental error. As a result of these gradients, the measured temperature is higher than the actual sample temperature and the latter lags behind the more responsive T_C readings as more time is required for the sample to equilibrate. This reinforces the importance for internal standards (i.e., using the Cu melting event itself and Al_2O_3 thermal expansion) to verify the extent of these errors. Based on the Cu melting event, a simple 26.7°C correction can be applied at the melting point of Cu. This error can be determined for each experiment but will only be relevant at 1085°C. A simple method where the magnitude of this error is assumed to linearly extrapolate from zero at room temperature to the measured value at

1085°C could also be used. However, it was decided to further investigate these errors by evaluating the thermal expansion behaviour of Al_2O_3 and Cu prior to melting.

Table 5-5 and Table 5-6 show the 2θ locations of the Cu and Al_2O_3 peaks (measured at FMHW using Powder3D) and corresponding thermocouple temperatures for the patterns shown in Figure 5-7. Equation (2-65) was used to determine the Cu lattice parameter (a) using three different peaks (111, 200, and 220) for each pattern. The three calculated values for a (i.e., a_{111}, a_{200}, *and* a_{220}) were then used to calculate the degree of thermal expansion ($\Delta a/a_o\%$) according to each peak. These values were then averaged ($\Delta a/a_{o,\,avg.}$) to verify the accuracy of the calculation method. The Al_2O_3 a-axis lattice parameter was similarly calculated using the (300) peaks and Equation (2-66). Figure 5-8 and Figure 5-9 plot these data versus the measured control thermocouple temperature (T_C). Both figures include expected thermal expansion predictions based on the extensive data obtained from Touloukian *et al* (Equations (2-74), (2-75), and (2-76)) [81, 82].

Table 5-5: Measured Cu peak locations and calculated thermal expansion values (sample 2)

Set	Temp.	(111) Peak			(200) Peak			(220) Peak			$(\Delta a/a_o)_{avg}$	
no.	T_C (°C)	(2θ °)	a_{111} (Å)	$\Delta a/a_o$ %	(2θ °)	a_{200} (Å)	$\Delta a/a_o$ %	(2θ °)	a_{220} (Å)	$\Delta a/a_o$ %	$\Delta a/a_o$ %	σ (%)
2	22.0	37.05	3.6271	0.00	43.06	3.6260	0.00	62.63	3.6208	0.00	0.00	0.000
10	27.0	37.05	3.6271	0.00	43.06	3.6260	0.00	62.63	3.6208	0.00	0.00	0.000
14	114.2	37.04	3.6281	0.03	43.05	3.6268	0.02	62.62	3.6213	0.01	0.02	0.006
42	204.0	37.00	3.6319	0.13	43.01	3.6300	0.11	62.52	3.6265	0.16	0.13	0.024
45	297.0	36.98	3.6338	0.18	42.98	3.6324	0.18	62.48	3.6286	0.22	0.19	0.021
48	407.3	36.94	3.6376	0.29	42.92	3.6372	0.31	62.39	3.6333	0.35	0.31	0.029
51	527.4	36.88	3.6433	0.44	42.82	3.6453	0.53	62.24	3.6412	0.56	0.51	0.062
53	610.2	36.82	3.6490	0.60	42.73	3.6527	0.74	62.11	3.6480	0.75	0.70	0.082
55	726.6	36.68	3.6625	0.97	42.61	3.6625	1.01	61.93	3.6576	1.02	1.00	0.022
57	805.4	36.56	3.6741	1.29	42.50	3.6715	1.26	61.75	3.6672	1.28	1.28	0.019
60	924.3	36.42	3.6877	1.67	42.33	3.6856	1.64	61.49	3.6812	1.67	1.66	0.015
62	1003.8	36.32	3.6975	1.94	42.23	3.6939	1.87	61.34	3.6893	1.89	1.90	0.035
69	1111.7	36.22	3.7074	2.21	42.09	3.7056	2.20	61.10	3.7024	2.25	2.22	0.029
73	1114.3	N/A - melt			N/A - melt			N/A - melt			N/A	

Table 5-6: Measured Al_2O_3 peak locations and calculated thermal expansion values (sample 2)

Set no.	Temp. T_C (°C)	(300) Peak (2θ °)	a_{300} (Å)	$\Delta a/a_o$ %
2	22.0	57.86	4.76458	0.00
10	27.0	57.86	4.76458	0.00
14	114.2	57.85	4.76534	0.02
42	204.0	57.82	4.76759	0.06
45	297.0	57.80	4.7691	0.09
48	407.3	57.76	4.77212	0.16
51	527.4	57.71	4.7759	0.24
53	610.2	57.66	4.77968	0.32
55	726.6	57.58	4.78575	0.44
57	805.4	57.52	4.79032	0.54
60	924.3	57.44	4.79642	0.67
62	1003.8	57.38	4.80101	0.76
69	1111.7	57.30	4.80714	0.89
73	1114.3	57.29	4.80791	0.91

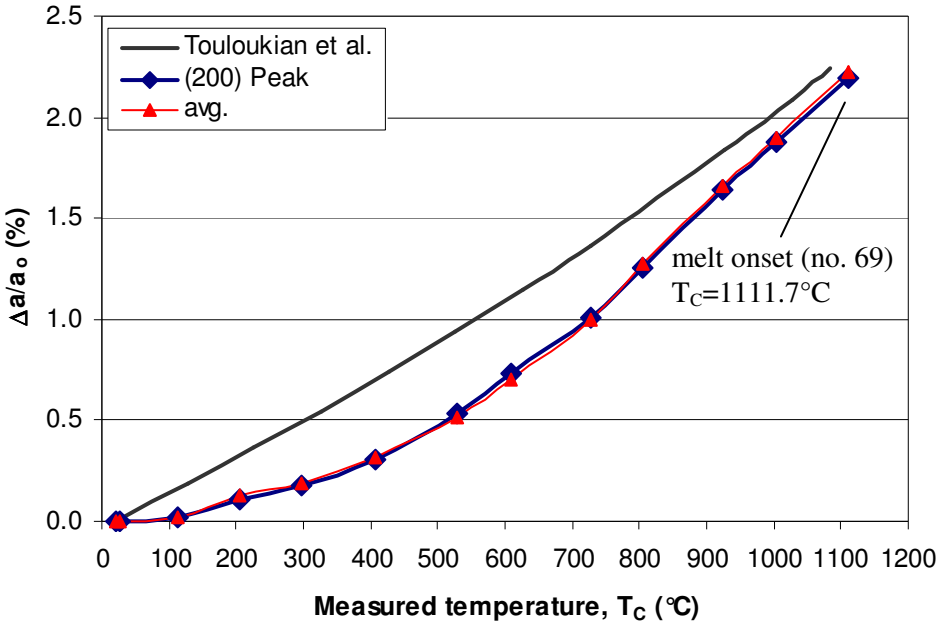

Figure 5-8: Thermal expansion of Cu lattice versus measured sample 2 temperature

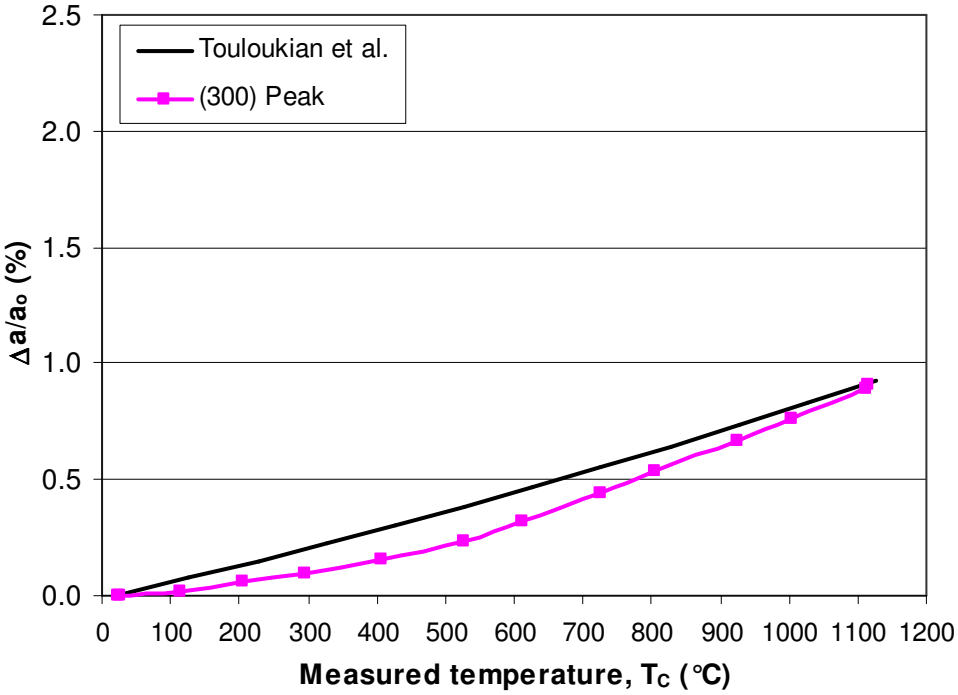

Figure 5-9: Thermal expansion of Al_2O_3 lattice (a-axis) versus measured sample 2 temperature.

Figure 5-8 illustrates Cu thermal expansion measurements based on the (200) peaks alone as well as the averaged value of the (111), (200), and (220) peaks. Both methods yield similar results - where the maximum standard deviation between a and $\Delta a/a_o$ values for any temperature were 0.0041Å and 0.082% $\Delta a/a_o$ respectively (see Table 5-5). Therefore, to simplify calculations, the Cu (200) peak will be used for future calculations since this peak has already been selected for interdiffusion analysis as per Section 5.1.1. Figure 5-8 clearly shows that the measured Cu thermal expansion behaviour deviates from expected Touloukian *et al* values as the thermocouple temperature increases. This may be due to the axial temperature gradient discussed above (i.e., 26.7°C thermocouple overestimation at the Cu melting event). If the sample temperature is overestimated by the thermocouples, plotting thermal expansion vs. T_C will inevitably show low expansion values. However, this deviation is at a maximum in the 400-500°C range and then significantly decreases up to the melting point of Cu, where the deviation can be explained by the 26.7°C T_C error (i.e., the curve is shifted to the right). The large deviation at intermediate temperatures may be due to transient furnace effects which cause the sample temperature to significantly lag behind the exterior thermocouple temperature. Convective cooling of the crucible bottom by the incoming purge gas may cause

this lag/gradient. As the heat transfer rate from the surrounding tantalum heating elements increases to achieve higher program temperatures, the convective cooling effect of the purge gas will have a diminishing impact on the sample temperature since the N_2 flow rate was kept constant during all experiments (5 cm^3/min). In other words, the increasing heat input of the heating elements gradually overcomes the cooling effect of the constant gas flow.

Temperature deviations are inevitable in the current furnace configuration, but fortunately they are at a minimum (~26.7°C) at the temperature range of interest (i.e., above the melting point of Cu). This may be partially due to the furnace controller, which gradually decreases the heating rate at high temperatures approaching the isothermal segment set point, which decreases temperature gradients between the thermocouple and the lagging sample temperature. However, the above observations reinforce the importance of verifying the thermocouple temperatures with the temperatures indicated by the Al_2O_3 diffraction peaks. When plotted versus T_C, the measured Al_2O_3 a-axis expansion (see Figure 5-9) shows the same behaviour as that of Cu shown in Figure 5-8. However, the magnitude of the deviation from the Touloukian data is less significant, particularly at the melting point of Cu (i.e., data set 69, T_C = 1111.7°C). This is likely due to the closer proximity of the Al_2O_3 crucible to the thermocouple location as well as its lower CTE value. Comparatively, the Cu specimen is more insulated from the thermocouple by the alumina crucible, which has a low thermal conductivity typical of ceramics.

As discussed in Section 2.11.5, Equation (2-76) can be used to calculate the Al_2O_3 temperature based on the measured thermal expansion of the Al_2O_3 internal standard. The calculated temperature based on Al_2O_3 diffraction peaks will be referred to as T_a, and should not be confused with the melting point of the additive phase Cu (referred to as T_A in previous sections). The Cu peaks can not be used for this purpose since Cu is not an inert phase during TLPS experiments.

MathCad was used to solve Equation (2-76) for the actual Al_2O_3 temperature (T_a) of each data set in Table 5-6. Using the XRD Al_2O_3 data as an accurate lattice parameter (a_O, denominator) and (300) peak position calibration at room temperature, the ND 2θ patterns were corrected for sample displacement by -0.0557° during the short room temperature segment at 27°C.

Table 5-7 shows the calculated Al_2O_3 temperatures and the thermocouple temperatures for the patterns previously tabulated in Table 5-5 and Table 5-6. T_a is significantly lower than the thermocouple temperature for most of the heat-up segment, but this difference decreases to only a few degrees at the peak isothermal temperature. This supports the previous hypothesis that the thermocouple overestimates the lagging sample temperature during the heat-up segment, yet less so approaching the isothermal segment. The calculated temperature of data set no. 69 (T_a = 1091°C), which is the pattern where the Cu melt onset was first detected, is much closer to the actual Cu melting temperature (1085°C). The 6°C overestimation is likely due to diffraction signal quality and the fact that Al_2O_3 is closer to the thermocouple and therefore hotter than the sample.

Figure 5-10 and Figure 5-11 re-plot the thermal expansion data for Cu and Al_2O_3 respectively, versus the thermocouple temperature (T_C) and the actual Al_2O_3 temperature (T_a) on the abscissa. In the case of Cu, T_a clearly provides a better estimation of the actual specimen temperature than T_C. As for the Al_2O_3 expansion plot, since the T_a values are calculated from the Touloukian *et al* expansion equations, the measured lattice expansions now coincide directly with the literature data.

Table 5-7: Comparison of measured thermocouple temperatures and calculated temperatures for sample 2.

Data set	Temp.		(300) Peak		
no.	T_C (°C)	T_a (°C)	(2θ °)	a_{300} (Å)	$\Delta a/a_o$ %
10	27.0	27.0	57.92	4.7604	0.01
14	114.2	50.6	57.91	4.7611	0.02
42	204.0	119.6	57.88	4.7634	0.07
45	297.0	164.3	57.86	4.7649	0.10
48	407.3	250.9	57.82	4.7679	0.16
51	527.4	354.8	57.77	4.7717	0.24
53	610.2	454.5	57.72	4.7755	0.32
55	726.6	607.1	57.64	4.7815	0.45
57	805.4	717.0	57.58	4.7861	0.55
60	924.3	858.0	57.50	4.7922	0.67
62	1003.8	961.0	57.44	4.7967	0.77
69	1111.7	1091.0	57.36	4.8029	0.90
73	1114.3	1112.0	57.35	4.8036	0.91

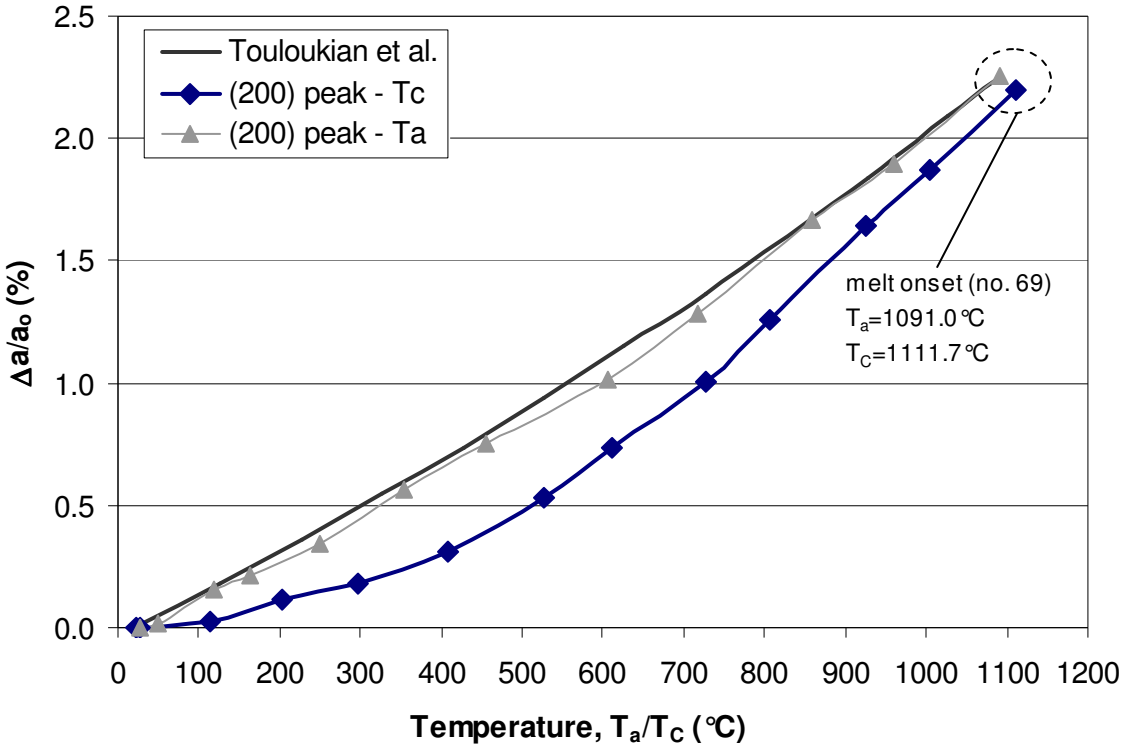

Figure 5-10: Thermal expansion of Cu lattice (a-axis) versus measured (T_C) and calculated (T_a) temperatures.

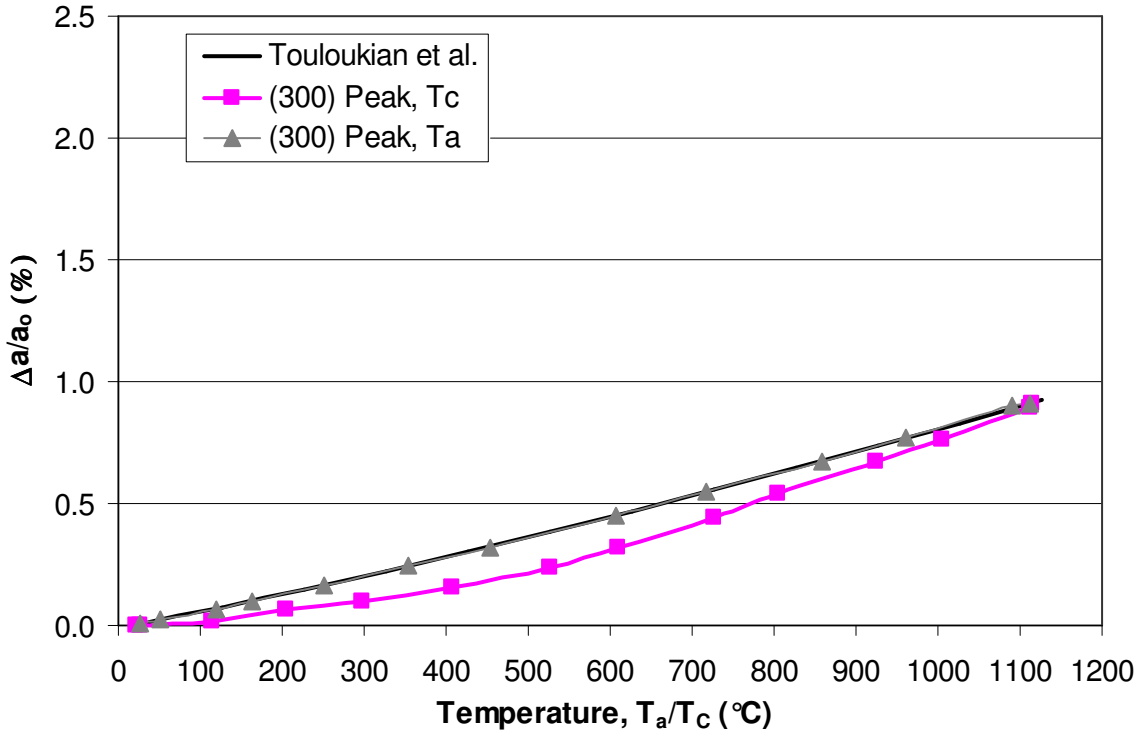

Figure 5-11: Thermal expansion of Al_2O_3 lattice (a-axis) versus measured (T_C) and calculated (T_a) temperatures.

This analysis reveals that the Cu melting event is a very good indication of the actual sample temperature, but this only provides a temperature reference at 1085°C. Al_2O_3 (300) peak tracking indicates that the diffraction peaks of the Al_2O_3 crucible can provide a suitable internal temperature standard which is more accurate than the thermocouple data, particularly during athermal segments. All diffraction pattern plots following this section will now cite corrected temperatures derived from the Al_2O_3 lattice expansion (T_a).

Temperature calculation method: Table 5-8 provides the expected lattice expansion behaviour of the Al_2O_3 internal standard at 100°C increments. Values at all intermediate temperatures can also be readily calculated. The high accuracy Al_2O_3 lattice parameter measurement obtained via XRD at 24.0°C (discussed in Section 3.1) provides the lattice parameter reference at this temperature (i.e., a = 4.760318Å). The expected thermal expansions ($\Delta a/a_o$%) were calculated using the Touloukian *et al* data at temperatures ranging from 20°C-1200°C. The 20°C lattice parameter serves as the denominator in the $\Delta a/a_o$% calculations via Equation (2-76) since 20°C (293K) is the room temperature reference point where $\Delta a/a_o$ = 0% in Touloukian's equations. The expected peak locations could then be calculated from the thermally-expanded a values at each temperature. The expected Bragg diffraction angle for the (300) peak is also shown for neutron beam data (λ = 1.33069Å).

Table 5-8: Expected expansion of Al_2O_3 internal standard in ND experiments (λ = 1.33069Å).

		Expected expansion		
Temp (°K)	**Temp (°C)**	**Δa/ao %**	**a(A)**	**2θ(300)**
293.0	**20.0**	**0.0000**	**4.76013**	**57.919**
297.0	**24.0**	**0.0035**	**4.76030**	**57.917**
300.0	27.0	0.0055	4.76040	57.916
373.0	100.0	0.0550	4.76275	57.884
473.0	200.0	0.1260	4.76613	57.839
573.0	300.0	0.2005	4.76968	57.792
673.0	400.0	0.2783	4.77338	57.743
773.0	500.0	0.3593	4.77724	57.692
873.0	600.0	0.4433	4.78124	57.640
973.0	700.0	0.5301	4.78537	57.585
1073.0	800.0	0.6196	4.78963	57.529
1173.0	900.0	0.7115	4.79400	57.472
1273.0	1000.0	0.8058	4.79849	57.413
1358.0	1085.0	0.8877	4.80239	57.362
1373.0	1100.0	0.9022	4.80308	57.353
1413.0	1140.0	0.9414	4.80495	57.329
1473.0	1200.0	1.00067	4.80777	57.292

In order to determine the alumina temperature from Equation (2-76), measured experimental thermal shifts/expansions were required (Δa), but we first needed an accurate and consistent a_o value for $\Delta a/a_o\%$ calculations. The predicted (300) peak location at 27°C is included in Table 5-8 since this is the temperature of the initial isothermal hold segments appended at the beginning of the temperature programs (as shown in Figure 3-18). Once stabilized at 27°C, the thermocouple temperature reading was assumed to accurately estimate the actual specimen temperature. This is a reasonable assumption since there should be no temperature gradients at room temperature prior to heating above this temperature regime. As such, the purpose of this segment was to obtain stable room temperature diffraction patterns which could be compared to the expected Al_2O_3 27°C peak locations for each sample/experiment.

The expected 2θ locations for the (300) peak at 27°C, as well as those in the temperature range shown in Table 5-8, assume no diffractometer misalignment or sample displacement, which cause 2θ deviations in practice. Since sample displacement is difficult to avoid experimentally, small 2θ deviations were encountered in the experimental ND patterns as previously discussed with respect to GSAS fits. The extent of 2θ deviation, or misalignment ($\delta\theta$), was determined by the difference between the expected (300) peak location at 27°C (Table 5-8) and the measured FWHM (300) peak location of the stabilized patterns collected at T_C = 27°C for each experiment. These $\delta\theta$ deviations were found to vary from 0.0159° to 0.0557°- this particular experiment (sample 2) having the largest sample displacement.

This deviation value was then used to re-align the experimental patterns in 2θ such that all experiments had accurate and consistent Al_2O_3 peak positions at 27°C. The corrected Al_2O_3 peak locations at 27°C could then serve as reference points for temperature and 2θ calibration via the internal standard's thermal expansion and peak shifting at higher temperatures. This $\delta\theta$ correction was applied at all temperatures since it was assumed that the sample displacements caused during set-up did not change during sintering. The magnitude of these 2θ corrections is typical of ND measurements on the C2 instrument and the manual dial gauge system used to limit the sample displacements [107]. Furthermore, these 2θ deviation corrections had a negligible effect on the magnitude of the peak shifts ($\Delta\theta$) and Δa values measured since lattice expansion is primarily affected by the magnitude of peak *shifts* (i.e. the

change in θ), and not the precise 2θ location of each peak, which are shifted equally by the $\delta\theta$ correction.

From the corrected 27°C data, the reference a_o value at 20°C (293K) could then be determined via Touloukian's equations. This value would serve as the numerator for further $\Delta a/a_o\%$ ratios determined for the diffraction patterns at different temperatures – each having shifted peaks and therefore expanded lattice parameters (Δa). Temperature determination was achieved by solving Equation (2-76) for T using the $\Delta a/a_o\%$ ratio for each pattern – giving T_a.

5.1.3. Non-interacting Cu + Ni Experiment (Sample 3)

A final preliminary experiment was conducted (i.e., sample 3) in order to evaluate the evolution of ND patterns for a specimen containing Cu and Ni as well as to further evaluate furnace temperature gradients at temperatures up to 1200°C. Figure 5-12 shows the sample and thermocouple set-up and Figure 5-13 shows the recorded thermocouple temperatures during the experiment.

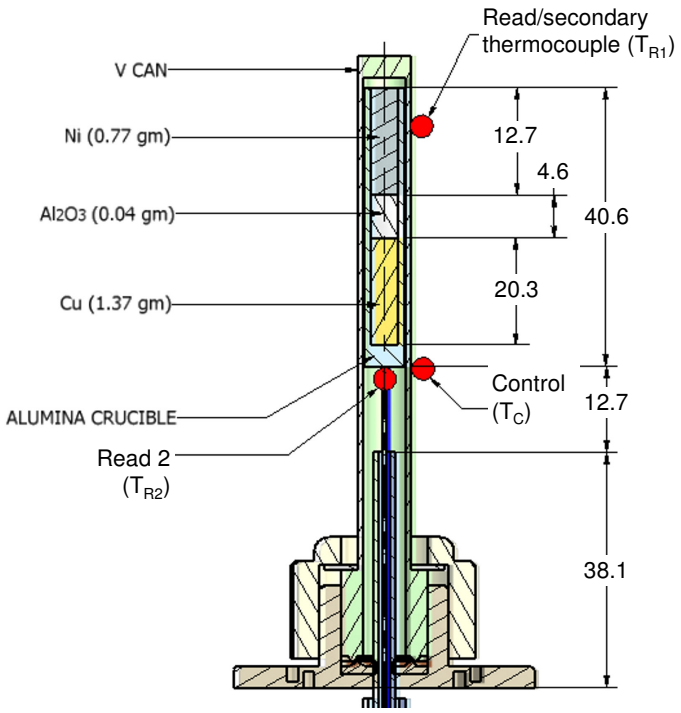

Figure 5-12: 2D section of sample environment and thermocouple placement for sample 3.

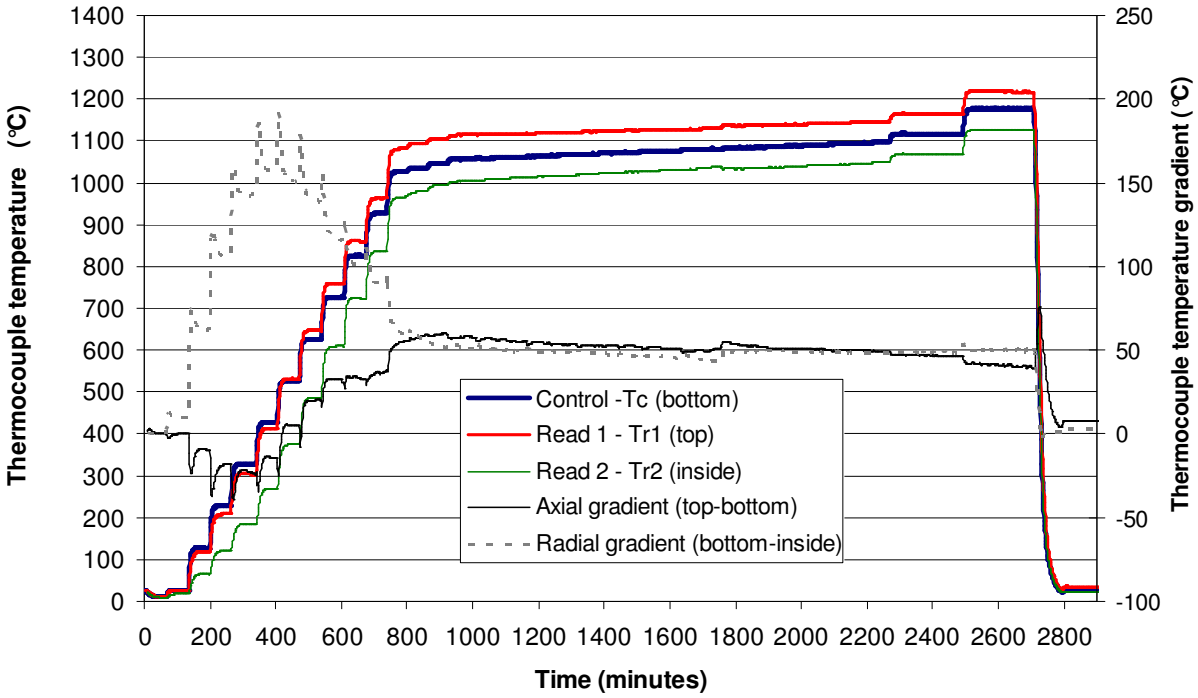

Figure 5-13: Measured thermocouple temperature history of sample 3.

A much slower, step-wise heating profile was used which consisted of 1 hour hold segments/steps at increasing temperatures - extending the experiment duration to over 3000 minutes (2800 data sets). This was done to allow the lagging internal temperatures to equilibrate during the 1 hour segments and allow the evaluation of steady-state axial and radial temperature gradients. Ni powder was included in the crucible such that the Cu content was 64.0 wt% Cu. However, the Ni and Cu powders were separated by an Al_2O_3 powder barrier in this case (as shown by Figure 5-12) to prevent interactions between the two elemental powders at high temperatures. This experiment would provide baseline ND patterns for Cu melting and thermal expansions up to 1200°C without peak shifting and broadening effects from interdiffusion, which is expected in the upcoming TLPS experiments.

Figure 5-12 also illustrates the different thermocouple configuration used in this experiment. In order to investigate axial temperature gradients along the length of the V canister, thermocouples were positioned at the top and bottom relative to the crucible (measuring the control, T_C, and secondary read temperature T_{R1}). The control thermocouple was placed on the V canister outer wall near the bottom of the crucible in order to control the furnace temperature based on the lower temperature region of the sample. This would ensure

that T_C measures a minimum sample temperature – indicating the last region to melt at 1085°C for example. A third thermocouple (i.e., a second read thermocouple, T_{R2}) was passed through the purge gas line and placed inside the canister under the crucible to measure radial temperature gradients with respect to T_C. The locations of the thermocouples are indicated with respect to the furnace base (in mm). Figure 5-13 shows the recorded thermocouple temperatures during the experiment. The axial ($T_{R1} - T_C$, or top-bottom) and radial ($T_C - T_{R2}$, or bottom-inside) temperature gradients are also plotted on the secondary y-axis.

These data show that the top thermocouple readings (T_{R1}) are higher than the bottom thermocouple readings (T_C) at elevated temperatures due to the conductive cooling effects of the furnace base. As expected, the inner thermocouple readings (T_{R2}) are also lower than both T_{R1} and T_C due to convective cooling by the incoming purge gas. These reading may be exceptionally low due to the fact that the thermocouple is placed directly in the gas line whereas the powder specimen is isolated by the thick crucible. The spiky temperature gradient plots indicate transient effects during heat-up at 100°C step increments up to T_C = 1027°C. Both gradient plots below T_C = 1027°C show that some time is required for temperature equilibration at the new temperature step. This supports the previous observations of lagging specimen temperatures with respect to the external thermocouples (discussed in Section 5.1.2). Once T_C reaches 1027°C, smaller temperature increments were used between the 1 hour hold segments (i.e., 10°C followed by 2°C) to ensure the accurate measurement of the Cu melting event (i.e., a quasi-steady state measurement).

As will be shown via the ND data, Cu peaks were removed at T_C = 1055.1°C. This is lower than the Cu melting point and also lower than the observed melt onset temperature of sample 2 (T_C = 1111.7°C, Section 5.1.2) since the sample temperature does not lag T_C as much during such slow step-wise heat-up in this case. The underestimation of the melting temperature in this case is thought to be due to the low measurement location of T_C on the V canister, which is a conductive material. It is lower than the bottom of the crucible and closer to the water-cooled base than in sample 2 (see Figure 5-12). At these near steady-state temperatures the axial and radial temperature gradients have stabilized to approximately 50°C. This axial gradient agrees well with the 26.7°C temperature deviation measured at the onset of Cu melting in Sample 2 (Section 5.1.2). T_C was measured at the mid-height of the sample (vs. top and bottom of the crucible in sample 3) and provided an average measurement in that case.

As an approximation, if we subtract half of the measured axial gradient (i.e., 50°C/2 from sample 3) to the measured melt onset for sample 2 (T_C = 1111.7°C at mid-height), we get 1086.7°C at the bottom region of the crucible.

So, to summarize based on the observation of Cu peak removal and measured temperature gradients, it appears that T_C may overestimate the inner sample temperature by up to 26.7°C during athermal segments approaching melting (i.e., 40°C/min in sample 2 and future samples). This overestimation arises from the fact that the thermocouple can not be placed directly within the sample and must be place on the canister wall, closer to the furnace heating element. These measurements do not directly indicate inner sample temperatures, but they do provide an estimation of the average temperature at the canister's mid-height position, where the axial temperature gradient is approximately less than 50°C from top to bottom (or T_C ±25°C in the worst case). It is expected that the magnitude of the actual temperature gradient in the sample is less significant due to the insulating effects of the crucible and the fact that the thermocouple measurements spanned a longer canister length than the crucible in sample 3. The canister is also more conductive and is directly attached to the water-cooled base. In any case, this experiment has provided an indication of the temperature gradients present at the isothermal temperatures of interest. This type of data was not previously available for the C2 furnace.

Once the Cu melting event had been identified at T_C = 1055.1°C, two final isothermal hold segments were appended at the end of the high portion of the temperature program to collect data at T_C ~1140°C and 1200°C. The above discussion is useful for better understanding the transient thermal behaviour of the furnace and thermocouple measurement system, but further characterization of this instrument is outside the scope of the current study. The evolution of measured ND patterns is of primary interest since this experiment can provide quasi steady-state information about the melting event as well as the Ni peaks at 1140°C and 1200°C with interdiffusion interactions with Cu. As previously shown, the temperatures indicated by the thermal expansion of the Al_2O_3 internal standard (T_a) were used to provide a better indication of the inner sample temperature. Although more complicated and time consuming for such large data arrays, this approach provides more reliable data that is more representative of the actual sample temperature.

It is important to note that T_a provides an estimate of the average crucible temperature over its entire volume since it generates the Al_2O_3 peaks used for temperature determination. It is a reasonable assumption that the measured thermocouple gradient of 50°C (from top to bottom) is still applicable as a worst case estimation of sample temperature variations near T_P (i.e., temperatures are accurate within T_a ±25°C in the worst case). Figure 5-13 indicates this axial gradient is fairly stable during isothermal segments in the high temperature regime of the experiment, and slightly decreases near 1200°C. Summing of sequential ND patterns during athermal segments (i.e., 5-minute sums during 40°C/min furnace heating), will cause some additional broadening in the measured Al_2O_3 (300) peaks. However, the center of the summed peak may provide a reasonable estimation of the average sample temperature at the midpoint of the 5-minute span.

Figure 5-14 shows a film plot of the 40-70° 2θ region for 1-minute ND patterns collect throughout the entire 3000 minute experiment (i.e., 2800 ND data sets). Sets of Cu/Ni peaks are identified and the remaining peaks are from the Al_2O_3 crucible.

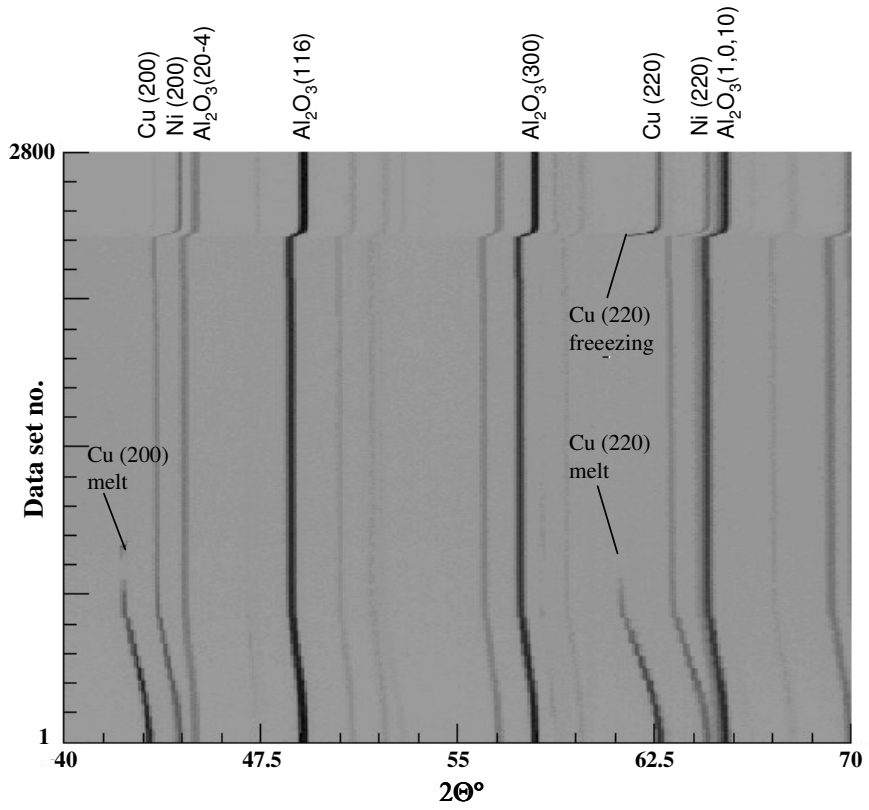

Figure 5-14: Film plot of 1-minute ND patterns collected *in situ* for a Ni-65wt%Cu non-interacting powder mixture. The mixture was slowly heated to 1096°C, isothermally held at 1145°C, and 1196°C, and then cooled to room temperature.

This plot clearly shows the gradual thermal expansion of each phase during the slow, step-wise heating segment at 100°C intervals. The Cu peaks are removed from the pattern due to Cu melting at an onset of T_a = 1079°C, which is in much better agreement with the Cu meting point T_A. Between 1079°C and approximately 1200°C, the remaining Ni and Al_2O_3 peaks shift moderately to lower angles as these phases continue to expand. Upon cooling, only Cu(220) peaks reappear in the diffraction pattern (indicating textured, directional solidification of the liquid) and these peaks shift to higher angles as all phases thermally contract.

Figure 5-15 presents a temperature-resolved waterfall plot of 5-minute diffraction patterns collected at key temperatures in the experiment, where peak intensities and shapes are more easily observed.

The calculated Al_2O_3 temperatures (T_a) are shown for each pattern (see right hand legend) as well as a brief description of the phenomenological observations made at that particular point. The Cu peak intensities are clearly seen to be reduced at 1079°C. Upon cooling, only Cu(220) peaks are first found to reappear at 859°C, which would indicate that undercooling was required to freeze the liquid. Both Figure 5-14 and Figure 5-15 show that no changes in the Ni peak intensities and widths are visible aside from temperature effects, indicating that no interdiffusion took place between Ni and Cu. This was later confirmed when the sample was examined and the solidified Cu liquid was found to be completely separated from the sintered Ni powders by the Al_2O_3 barrier.

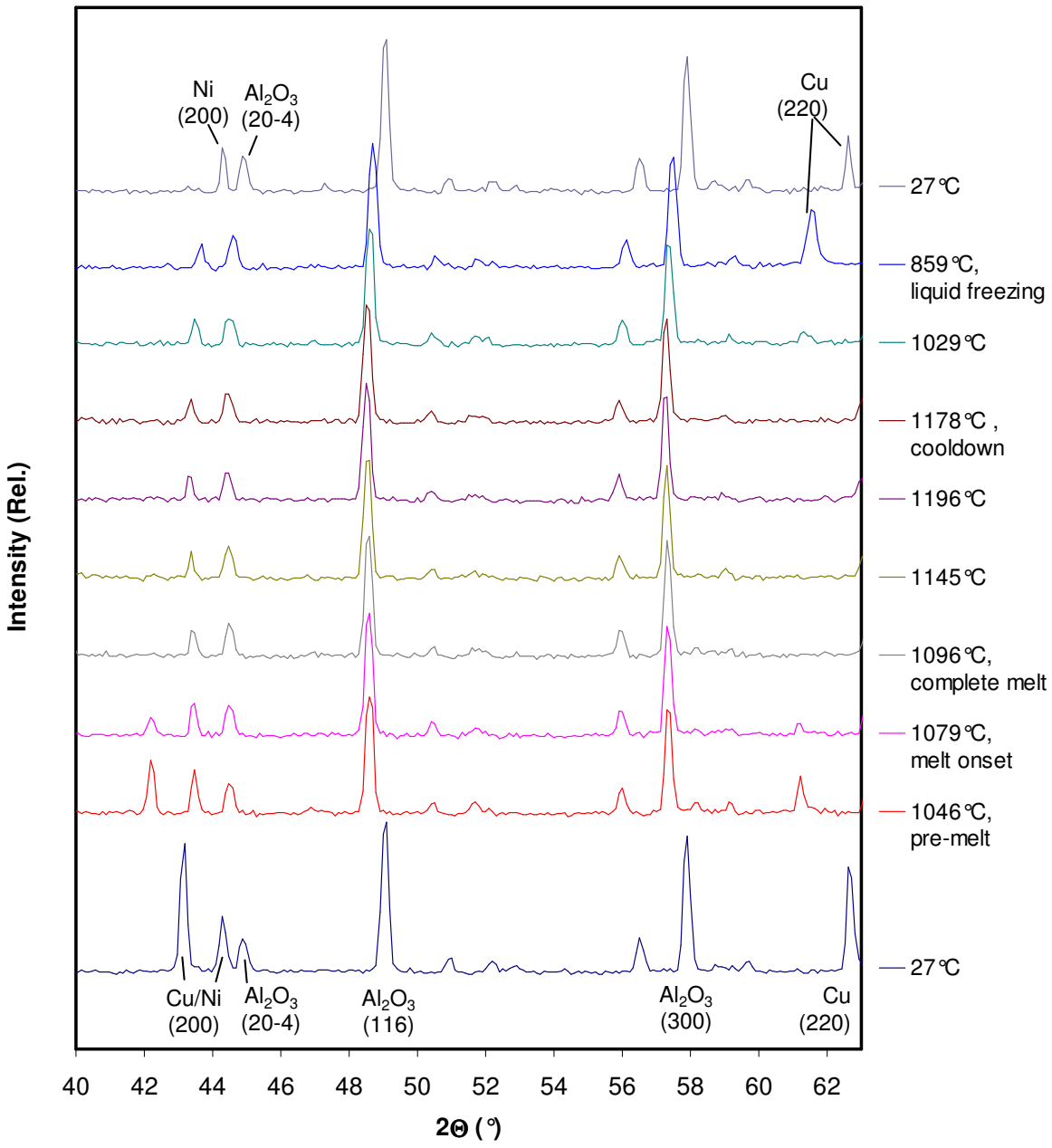

Figure 5-15: 5-minute ND patterns collected *in situ* for a Ni-65wt%Cu non-interacting powder mixture (sample 3). The Ni and Cu powders were separated by an alumina barrier. The mixture was slowly heated to 1096°C, isothermally held at 1145°C, and 1196°C, and cooled to 27°C.

5.2. Cu-Ni TLPS Experiments

5.2.1. Results

This section will present ND data collected *in situ* for samples 4-9 (described in Table 5-1), which consisted of elemental Ni and Cu powder mixtures (65wt% Cu) that were transient liquid phase sintered at different temperatures. An alumina powder barrier was not used in these experiments, thus allowing interdiffusion to take place. The film plots included here provide a good visualization of the gradual diffraction pattern evolution during sintering at 1 minute intervals throughout each experiment.

As shown in Figure 5-16, these plots span the 40-50° 2θ range, where Ni and Cu (200) peaks are visible as well as the Al_2O_3(116) peaks, which provide a visual thermal expansion reference for temperature changes. In other words, Al_2O_3(116) peak shifts and stabilizations visually indicate athermal and isothermal temperature segments respectively. The thermocouple temperature histories of each sample are shown in Appendix A for reference. The calculated temperatures from the Al_2O_3 internal standard (T_a, as discussed in Section 5.1.2) were used to determine the collection temperature of diffraction patterns. T_a will be used to refer to sample temperatures (vs. thermocouple measurements T_C) unless otherwise noted. The large array of ND patterns presented in these film plots provides a good initial characterization of the general TLP sintering behaviour of each specimen. A more detailed analysis will follow in Section 5.3.1.

The first film plot for sample 4 (Figure 5-16) shows the initial (200) peak locations at 27°C, which are stable for the first few data sets. Upon heat-up to T_a = 1080°C, all peaks gradually shift to lower angles. Once the peak temperature is reach the Cu peaks do not appear to be completely removed as in the pure Cu specimen previously discussed in Section 5.1.2 (sample 2). It is important to remember the axial temperature gradients observed on the conductive canister wall in sample 3 (i.e., 50°C, or T_a ±25°C). However, T_a = 1080°C is probably somewhat higher than the sample temperature inside the crucible since the powders are further from the heat source and canister wall. Therefore, it is expected that the actual temperature gradient within the sample is < ±25°C, but a portion of the sample near the top was likely above 1085°C and partially melted. The Cu (200) peaks appear to shift to moderately

higher angles at the end of heat-up (i.e., the area identified by a dashed circle). This may indicate partial melting of the specimen, which would leave behind some pure Cu regions as well as solid-state alloyed regions having Cu rich compositions. Conversely, the Ni(200) peaks do not appear to shift as abruptly, since Ni can not melt at these temperatures and Cu diffusion has not likely penetrated the Ni particles to an appreciable degree.

Successive diffraction patterns show inward shifting of Cu and Ni peaks concomitantly with increasing diffraction intensity from the 2θ region separating the two peaks (i.e., the alloy region). This trend continues as Ni-Cu interdiffusion causes the gradual formation of a broad, alloyed diffraction peak/range. This broad peak gradually becomes more refined due to the apparently slow homogenization of the alloy. Prior to cooling, the intensity distribution across the broad peak indicates a Cu-rich solid-solution, which is expected since the mixture initially contained 65wt% Cu. Upon cooling, all peaks shift to higher angles due to thermal contraction. To summarize these observations, it is likely that mixed TLPS/SSS occurred in this specimen since the peak temperature was 1080°C and certain regions may easily have melted due to the temperature gradients in this furnace. Further analysis and comparison of this pattern evolution to other samples heated at higher temperatures will be useful.

Figure 5-17 presents the diffraction pattern evolution during sintering of sample 5. Starting room temperature data were not collected in this case due to furnace control issues (see Appendix A). Upon heat-up to the isothermal segment starting at T_a = 1091°C, the same abrupt inward Cu(200) peak shifting is observed after the thermal expansion shift is complete. However, in this case the magnitude of the Cu(200) inward shift is increased. This can be explained by the fact that at these higher temperatures, most or all of the pure Cu has melted - leaving behind solid-state alloyed regions which are still Cu rich, yet less so than sample 4.

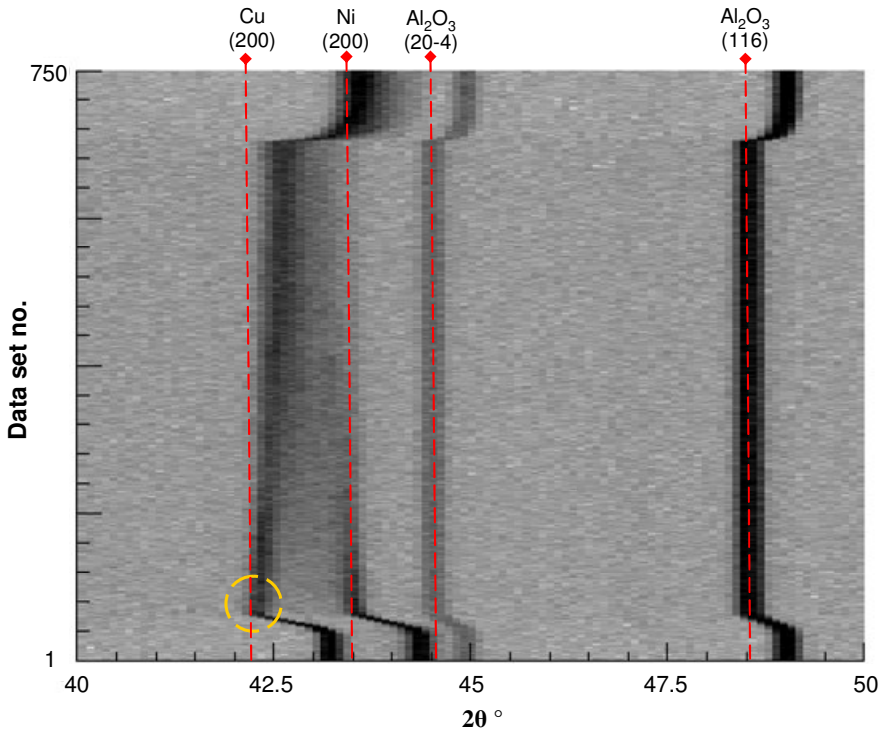

Figure 5-16: Film plot of *in situ* diffraction pattern evolution collected at 1 minute intervals during TLPS of a Ni-65wt% Cu powder mixtures heated to T_a = 1080°C for 630 min. (sample 4)

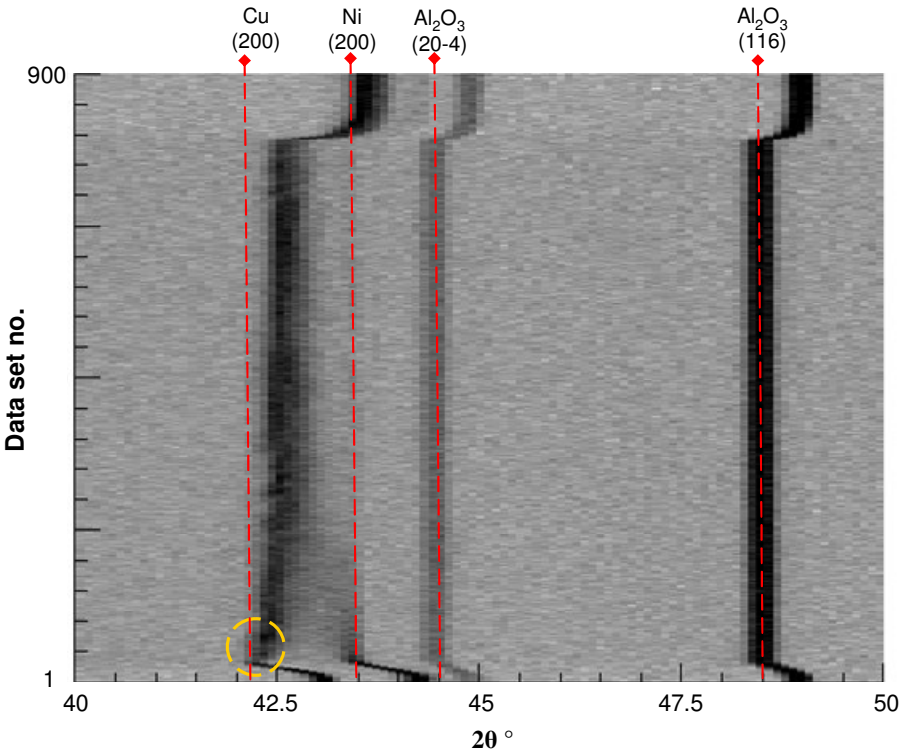

Figure 5-17: Film plot of *in situ* diffraction pattern evolution collected at 1 minute intervals during TLPS of a Ni-65wt% Cu powder mixtures heated to T_a = 1091°C for 1040min. (Sample 5).

The increased Cu peak shift of sample 5 at the Cu melting event is likely due to the decreased solid solubility (C_S) of Cu in Ni-Cu alloy at higher temperatures. As shown by the phase diagram in Figure 2-10, the maximum Cu content of Ni-Cu solid solutions decreases at higher temperatures, which would cause such alloy peaks to shift to higher angles. Another significant difference with respect to the film plot of sample 4 in Figure 5-16, is that homogenization of the solid-solution appears to be much more rapid. This supports the previous suggestion that the low peak temperature of sample 4 likely caused very little melting and therefore slower solid-state sintering mechanisms dominated the interdiffusion kinetics. The enhanced liquid formation due to the higher temperatures of sample 5 would cause a more uniform liquid Cu distribution, where TLP sintering mechanisms can homogenize the alloy more rapidly.

Figure 5-18 presents a film plot for sample 6, which was heated to T_a = 1128°C at 10°C/minute and held for 900 minutes. Cooling segment data were not collected in this experiment and a gap of 63 minutes of ND data could not be collected during the isothermal sintering segment due to reactor power fluctuations, as explained in Appendix A. Upon heat-up to the isothermal segment, the Cu melting event is even more evident. In this case the Cu(200) peak almost appears to be completely removed. This indicates complete Cu melting as well as melting of solid-state alloyed regions having Cu-rich compositions above C_S. The residual Cu-rich solid-solution peak in this case (hereafter referred to as the C_S(200) peak), does not reappear in the diffraction patterns until a few data sets after melting, and it has similarly shifted to a higher angle. This Cu-rich C_S peak grows in width and intensity rapidly as the elemental Ni (200) peak intensity decreases due to Cu diffusion in the Ni particles. This particular ND pattern evolution provides useful information for understanding the isothermal solidification mechanism in TLPS. The growth of C_S (200) peaks (which corresponds to solid-solution regions having compositions near C_S) indicates the increasing proportion of Cu-rich regions within the specimen during the isothermal segment. This supports previous DSC and metallographic data, which indicated that the liquid isothermally solidifies by the growth of a Cu-rich layer on the Ni particles.

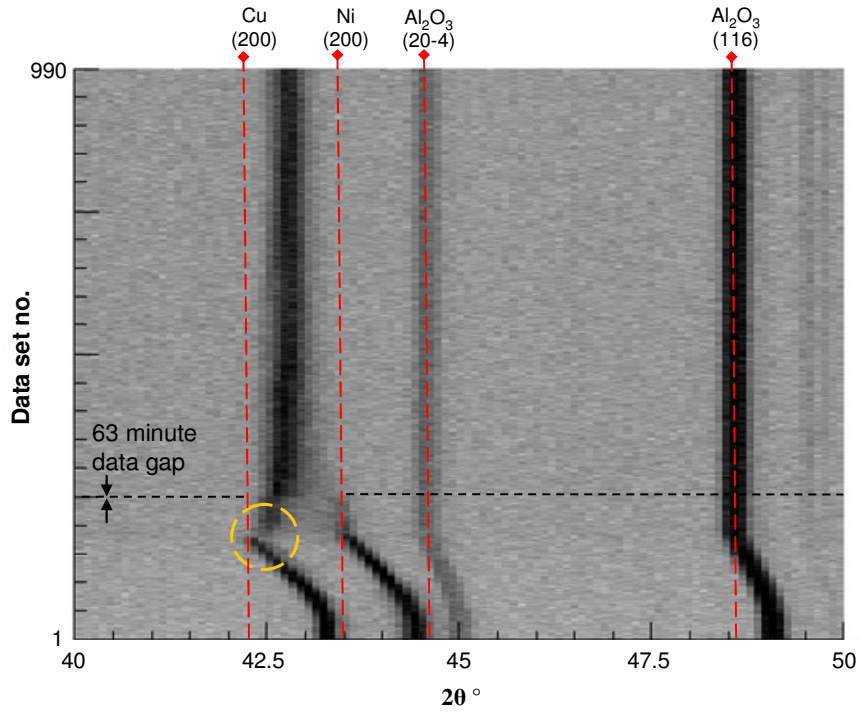

Figure 5-18: Film plot of *in situ* diffraction pattern evolution collected at 1 minute intervals during TLPS of a Ni-65wt% Cu powder mixtures heated to T_a = 1128°C for 900min. (Sample 6).

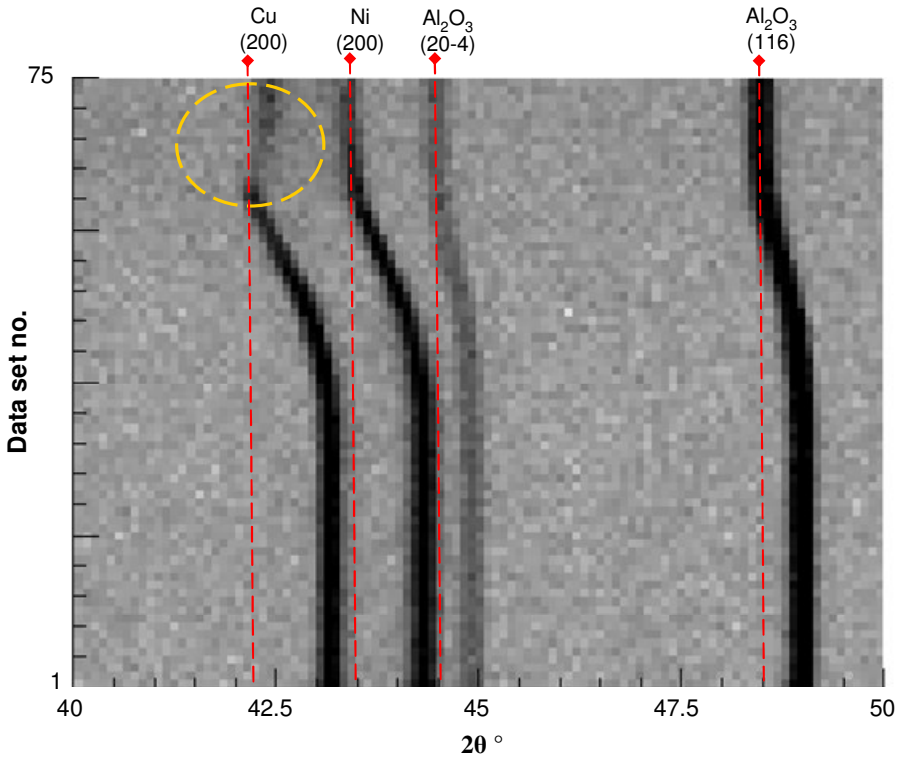

Figure 5-19: Film plot of *in situ* diffraction pattern evolution collected at 1 minute intervals during TLPS of a Ni-65wt% Cu powder mixtures heated to T_a = 1162°C for 15min. (Sample 7).

Figure 5-19 presents a film plot for sample 7, which was heated to T_a = 1162°C at 40°C/minute and held for only 15 minutes. The purpose of this experiment was to provide a comparison to sample 6 for the heat-up segment data (i.e. 10°C/minute vs. 40°C/minute) over a short collection time (i.e., only 75 data sets). This film plot displays an expanded y-axis due to the fewer data sets available for inclusion from rapid heating. The ND pattern evolution exhibits Cu melting behaviour and C_S growth that are similar to Sample 6. A more detailed comparison of individual diffraction patterns will follow in Section 5.3.1.

Figure 5-20 presents a film plot for sample 8, which was heated to T_a = 1194°C at 40°C/minute and held for only 30 minutes. The film plot in Figure 5-21 includes a larger 2θ range to observe other peaks above 50° for this sample. The purpose of this experiment was to obtain high temperature TLPS data near 1200°C. A short hold segment was used to interrupt the isothermal solidification process and investigate freezing of the remaining liquid after 30 minutes (i.e., athermal solidification).

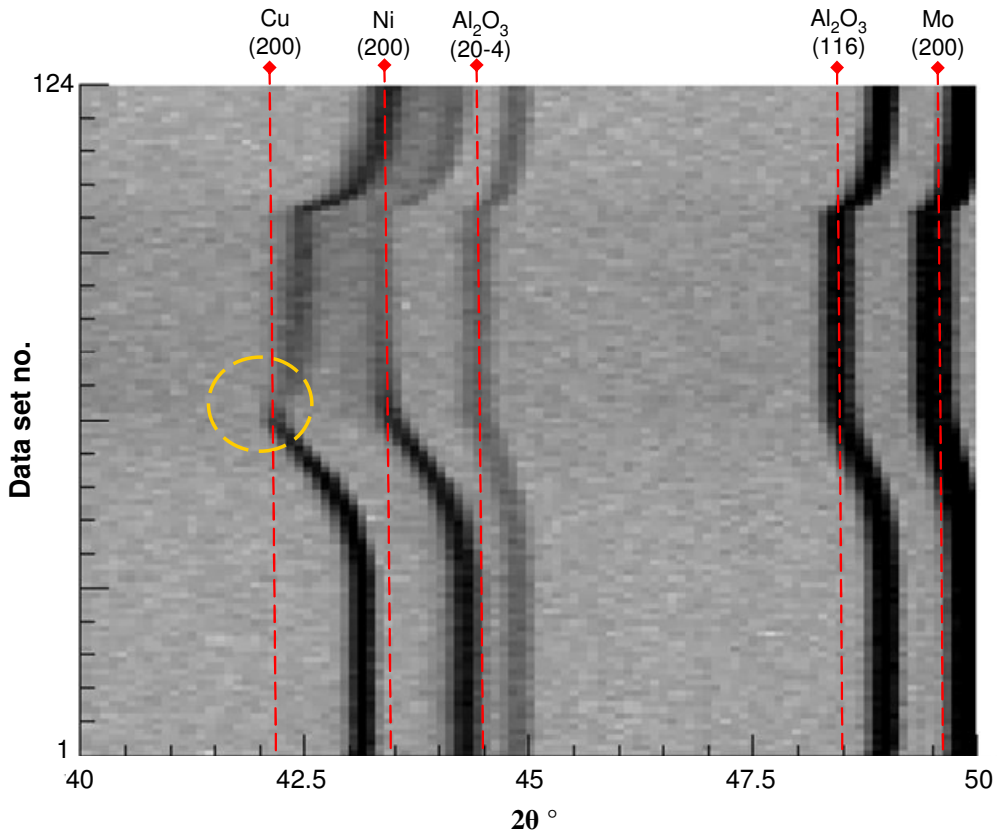

Figure 5-20: Film plot of *in situ* diffraction pattern evolution collected at 1 minute intervals during TLPS of a Ni-65wt% Cu powder mixtures heated to T_a = 1178°C for 30min. (Sample 8).

Additional peaks are present in these diffraction patterns for the duration of the experiment (~50° and 62° for example). These peaks originate from the different canister material (i.e., Mo vs. V) used for the last two experiments (samples 8 and 9). Due to a shortage of vanadium canisters at the CNBC Chalk River Labs, molybdenum canisters were used [113]. Both V and Mo have similar BCC structures, but V is favourable since it is more neutron transparent and will contribute less strongly to the measured diffraction pattern. This is because V has a much lower coherent neutron scattering amplitude, which is typically described by its coherent scattering length b (b_V = -0.3824x10^{-15}m *vs.* b_{Mo} = 6.715x10^{-15}m) [114]. As such, Mo scattering may result in relatively decreased diffraction intensity from the other phases in these two experiments.

The remaining Ni, Cu and Al_2O_3 peaks in Figure 5-20 and Figure 5-21 show similar trends to the previous samples. In this case the Cu melting event is quite evident and the C_S peak shift is large due to the relatively high sintering temperature of this experiment. Upon cooling after 30 minutes, the C_S(200) peak appears to grow in width and intensity, indicating that the remaining Cu-rich liquid has solidified at similar compositions. Closer examination of the C_S(220) peak upon cooling in the larger scale film plot of Figure 5-21, shows that this process is more pronounced for the (220) reflection than the (200) reflection (see top right area of film plot). This type of preferred orientation was also observed during Cu liquid freezing in sample 3 (Figure 5-14). Directional solidification in a preferred (220) orientation may be due to temperature gradients within the specimen. Further investigation of the athermal solidification behaviour is not included in this document.

Figure 5-22 presents a film plot for sample 9, which was heated to T_a = 1178-1194°C at 40°C/minute and held for a significantly longer time than sample 8 (720 minutes). The purpose of this experiment, which was heated to similar temperatures, was to study the full TLPS process at high temperatures until a fairly homogeneous alloy is formed. Additional Mo peaks are also present in these patterns due to the molybdenum canister. The evolution of Ni and Cu (200) reflections is similar to that observed in previous specimens, but in this case the melting event and inward shift of the C_S peak are very evident. Interdiffusion during the isothermal segment causes a sharp solid-solution peak to gradually form – indicating that the specimen compositon is quite homogeneous.

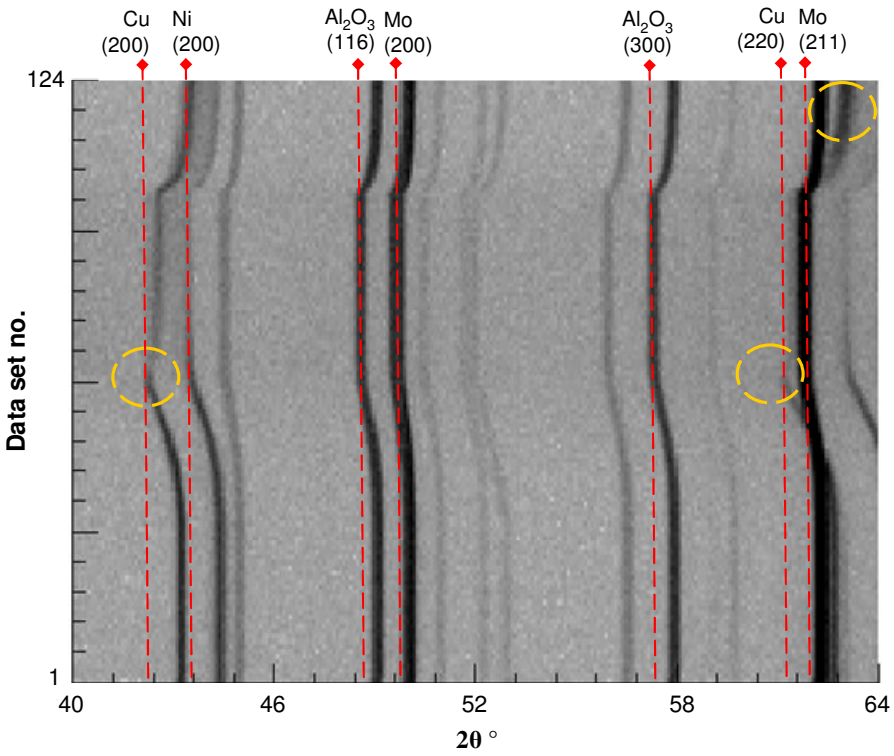

Figure 5-21: Film plot of *in situ* diffraction pattern evolution collected at 1 minute intervals during TLPS of a Ni-65wt% Cu powder mixtures heated to T_a = 1178°C for 30 min. (Sample 8).

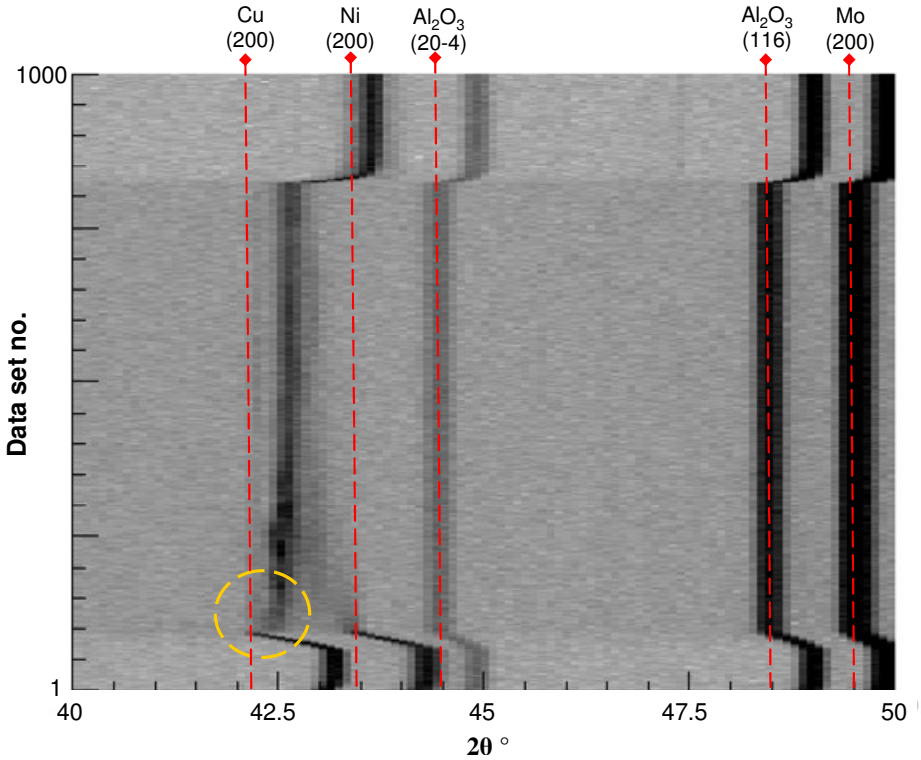

Figure 5-22: Film plot of *in situ* diffraction pattern evolution collected at 1 minute intervals during TLPS of a Ni-65wt% Cu powder mixtures heated to T_a = 1178°C for 720 min. (Sample 9).

To summarize, these film plots have provided a good visual interpretation of the *in situ* diffraction pattern evolution throughout the full sintering cycle at 1 minute intervals. The general melting and interdiffusion behaviour occurring during sintering cycles of varying peak temperature have been initially characterized. The melting event is characterized by an abrupt decrease in the pure Cu(200) reflection intensity and an immediate peak shift to slightly alloyed compositions/angles (referred to as the C_S peak). Melting is most evident in samples heated to higher temperatures due to a larger C_S peak shift and a greater reduction of the Cu diffraction intensity. This process is less evident in the data collected for sample 4 and sample 5, which were heated to 1080°C and 1091°C respectively. As such, these samples likely formed less liquid, if any in the 1080°C case.

After the melting event, growth of the Cu-rich C_S(200) peak appears to be rapid. This indicates that a Cu-rich solid-solution is forming during the isothermal segment. The concomitant decrease and broadening of the pure Ni peak is relatively slow. Throughout this process there is a gradual diffraction intensity increase across the solid-solution 2θ range at intermediate angles, indicating that interdiffusion is taking place. At long hold times a more refined solid-solution peak is formed, which is indicative of a more homogeneous sintered alloy.

5.3. Discussion

5.3.1. Solid-state Sintering Stage

Figure 5-23 presents a waterfall plot of 5-minute diffraction patterns collected during the 10°C/minute heat-up segment of sample 6. This presentation format for less noisy 5-minute patterns facilitates the interpretation and analysis of peak intensities, shapes and locations as they evolve along the y-axis. The 27°C pattern collected at the beginning of the experiment is shown at the bottom. Patterns were selected at approximately 200°C intervals and plotted up to the peak isothermal temperature (1128°C as shown in the legend). The temperatures assigned to each pattern (T_a) were determined by the degree of thermal expansion of the Al_2O_3 crucible internal as per the method described in Section 5.1.2. The intense Al_2O_3(116) peaks included in the 40-50° 2θ range also provide a visual indication of thermal expansion and

temperature changes without interaction effects. Vertical dashed lines have also been included for visual reference (positioned at the Cu, Ni, and Al_2O_3 peak centers at melt onset) and interpretation of peak shifting and broadening effects.

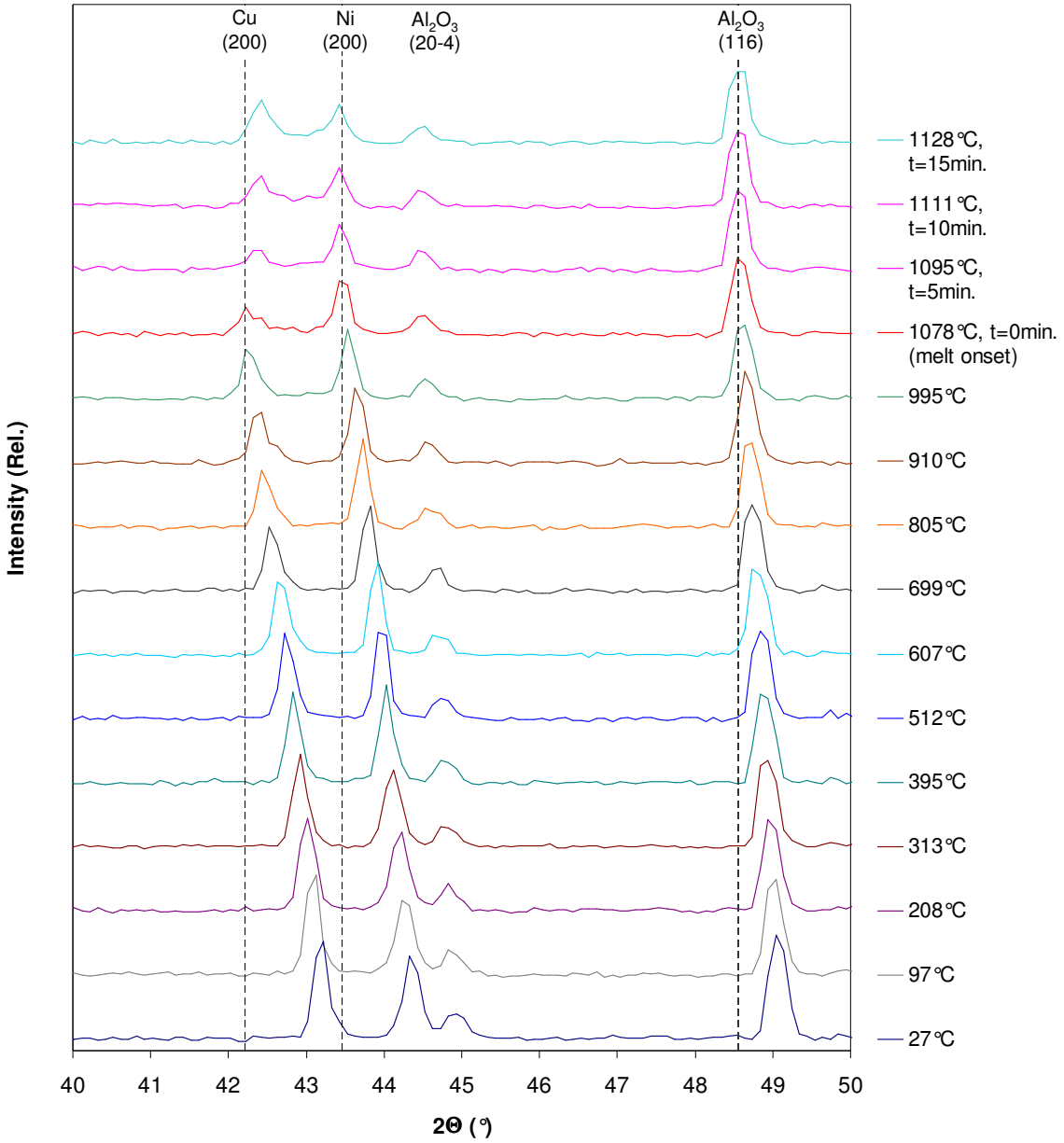

Figure 5-23: 5-minute ND patterns collected *in situ* during the 10°C /min heat-up segment of a Ni-65wt% Cu powder mixture (sample 6).

Figure 5-23 shows that all peaks shift to lower angles and moderately decrease in maximum intensity during heat-up due to thermal expansion and temperature effects discussed in Section 2.11.5. Furthermore, the Ni(200) peak separates from the small Al_2O_3(20-4) peak,

which overlaps it at room temperature, due to the relatively low thermal expansion of alumina. At T_a = 1078°C, the onset of Cu melting is detected by an abrupt decrease in Cu(200) peak intensity. This is in reasonable agreement with the theoretical melting point of Cu (1085°C). It is important to note that the melting of Cu at precisely 1085°C is difficult to capture with 5-minute diffraction patterns. As observed in Section 5.1.2 (1-minute data sets Figure 5-7), the melting event from top to bottom of the sample spans a 4-5 minute period due to temperature gradients and thermal lag retarding the temperature equilibration of the inner sample. Therefore, the summation of five sequential 1-minute patterns by ATRANS results in summed patterns with decreased time/temperature resolution. It is therefore expected that the T_a values determined from the smoother, more intense 5-minute patterns will not exactly coincide with the melting point of Cu. The summed 5-minute peak provides an average peak position over the summation period.

The ensuing diffraction patterns are at 5 minute intervals following the onset of Cu melting. The post-melt time of each pattern is shown in the legend. At this point the alumina peaks have essentially stabilized as the furnace controller approaches the peak temperature (1128°C). The dashed vertical lines, which are positioned at the center of Ni, Cu, and Al_2O_3 peaks after the onset of Cu melting, serve as useful reference points for 2θ shifts. As shown in Figure 5-10 and Figure 5-11, the thermal expansions indicated from the shifted Cu (200), and Al_2O_3 (300) peak positions at the onset of melting are in good agreement with calculated expansions from Touloukian *et al* data.

At 1078°C, the onset of melting is shown by a significantly decreased intensity on the left side of the Cu (200) reflection, corresponding to the pure Cu regions of the specimen. A small residual shoulder peak is also apparent on the right hand side of this diminished Cu (200) reflection. This shoulder corresponds to the inward-shifted residual C_S peaks which are apparent after melting in the film plot for this sample (see Figure 5-18). This diffraction signal may be a remnant of the pre-melt alloyed peak and originate from solid-state sintered inter-particle regions of the specimen having slightly alloyed compositions near C_S. The previous peaks before the onset of melting (i.e., 995°C, 910°C, etc.) also appear to be asymmetrical and exhibit this broadened right-hand shoulder. Again, this can be explained by increasing Ni-Cu interdiffusion at higher temperatures, which causes alloyed compositions to form at inter-

particle necks during the heat-up segment. As observed by Delhez *et al* and Rudman during solid-state sintering, this caused asymmetric peak broadening on the appropriate side of the elemental Cu(200) reflection. At 1095°C, past the melting point of Cu, only the alloyed C_S peak/shoulder remains since these regions do not appear to completely melt. Within the 15 minute period following melting these C_S peaks have already grown significantly.

Figure 5-24 presents a waterfall plot of 5-minute diffraction patterns collected during TLP sintering of sample 7. In this case a faster heating rate was used during the heat-up segment (40°C/minute vs. 10°C/minute) up to T_a = 1162°C and fewer diffraction patterns could therefore be collected during this segment using the same data collection intervals. 5-minute diffraction patterns were only available for the intervals shown (i.e., 27-1162°C). The evolution of peaks in these data indicates the same solid-state sintering and melting behaviour as sample 6. However, in this case the peak shapes change more abruptly due to the larger temperature increments and the expanded ordinate axis due to the fewer patterns being plotted. For a proper comparative analysis of the heating rate effect, diffraction patterns collected at similar temperatures prior to melting should be plotted together.

Before comparing peak profiles, it is worth noting the effects of transient temperature gradients and interdiffusion effects during higher heating rate athermal segments, since both can contribute to peak broadening. As shown in Section 5.1.3, temperature gradients across the sample can be significant below approximately 1000°C, and these are likely amplified at higher heating rates. Furthermore, the temperature difference across 5 summed data sets (i.e., 5 minutes) is also increased with high rates. Both of these effects will increase peak broadening in patterns collected sequentially during athermal segments with higher heating rates. However, as shown in Section 5.1.3 as well as the temperature histories in Appendix A, when the furnace and sample slowly approach the peak temperatures of interest (i.e., above ~1000°C), the heating rate significantly decreases and these broadening effects are minimized.

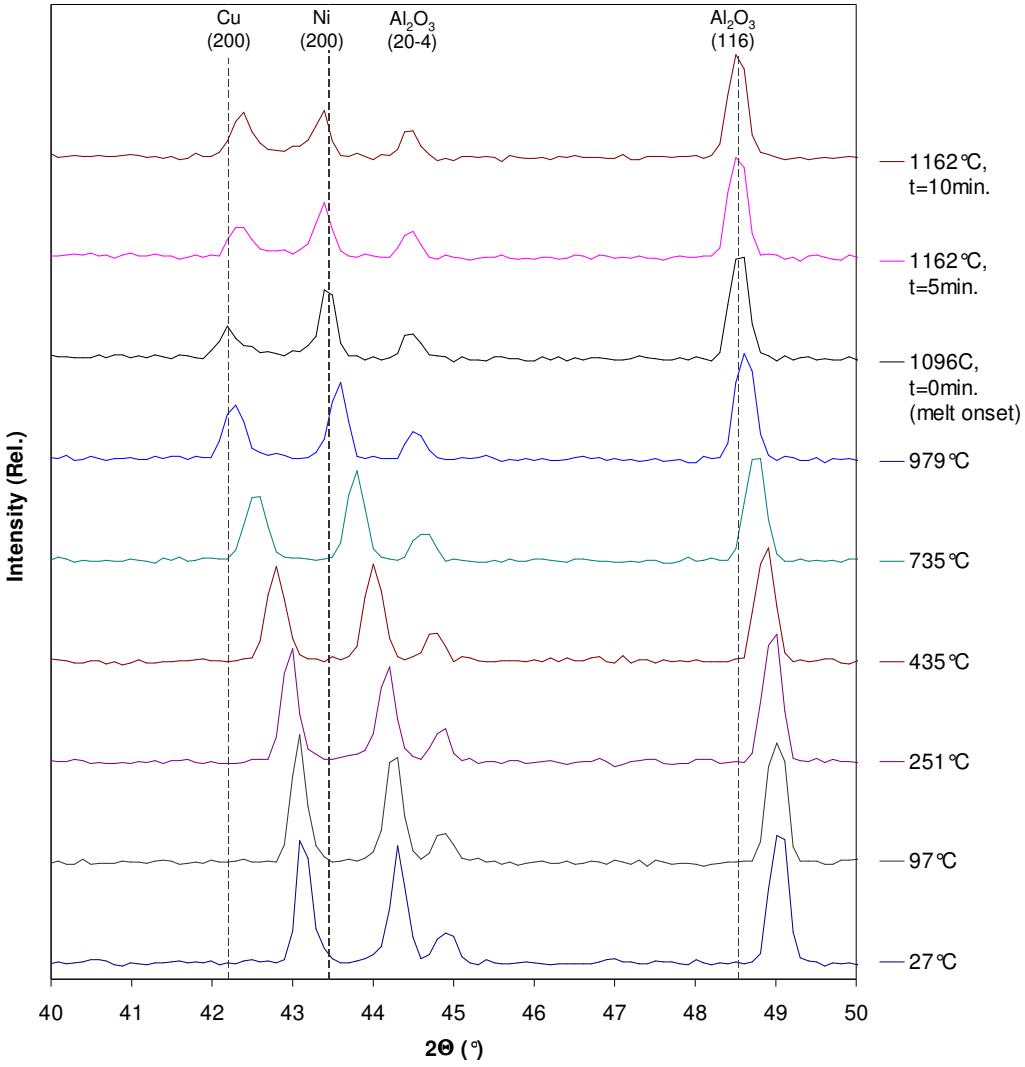

Figure 5-24: 5-minute ND patterns collected *in situ* during the 40°C /min heating segment of a Ni-65wt% Cu powder mixture (sample 7).

In any case, the calculated Al_2O_3 temperatures provide a good estimate of the mean sample temperature. Therefore, it was decided to compare diffraction patterns at similar temperatures collected immediately prior to melting for samples 5 and 6 in order to interpret the effect of interdiffusion on peak profiles at the end of the heat-up segment for 40°C/minute and 10°C/minute heating rates (see the expanded scale and superimposed patterns Figure 5-25). A pre-melt diffraction pattern for the non-interacting Ni-Cu specimen (sample 3) is also included as a reference.

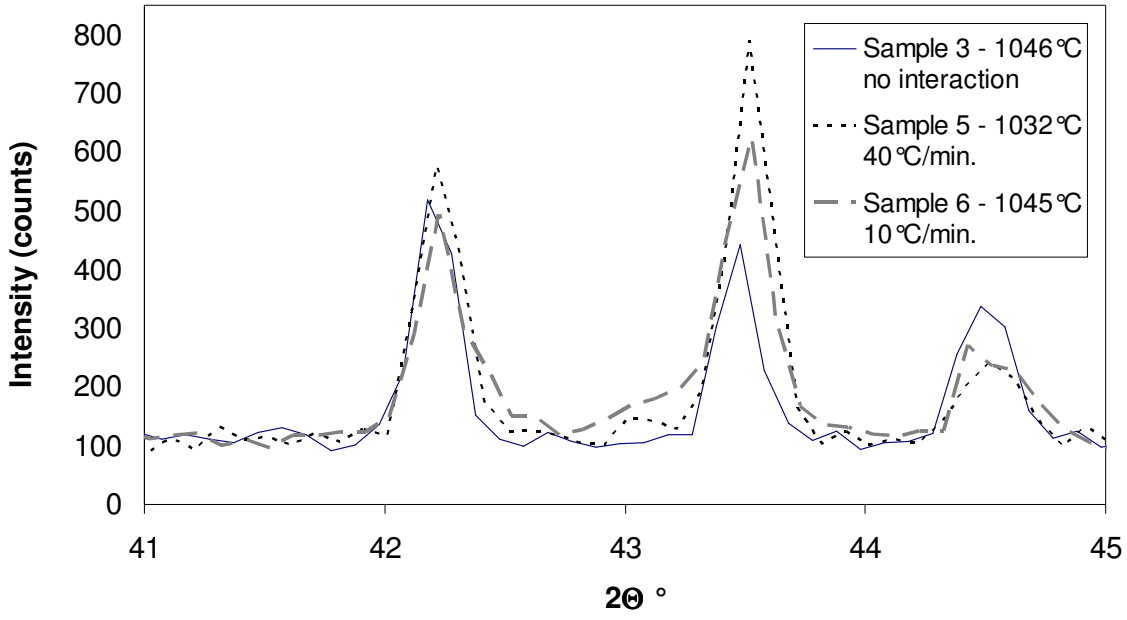

Figure 5-25: Comparison of peak profiles for diffraction patterns collected immediately prior to melting in sample heated at 40°C/minute and 10°C/minute. The diffraction pattern of a non-interacting specimen (sample 3) is also included.

The peak intensities in the diffraction pattern of sample 3 are lower due to the lower powder content in this sample (particularly Ni) to accommodate the Al_2O_3 barrier (see Figure 5-12 and Table 5-1). These data are included to serve as a baseline comparison where no compositional broadening from Ni-Cu interdiffusion occurred. This allows us to better determine the effects, if any, of solid-state interdiffusion on ND patterns as a function of the heating rates investigated. Both the 10°C/minute and 40°C/minute Cu and Ni peaks show moderately increased asymmetric broadening and diffraction intensities in the intermediate solid-solution 2θ range compared to the non-interacting sample data. Solid-solution diffraction intensities in the intermediate alloy range appear moderately greater in the 10°C/minute sample, as might be expected since greater degrees of interdiffusion can occur during slow heating to similar temperatures. However, the magnitude of the intensity difference across this 2θ range is only moderately greater than the background/baseline variance and therefore it may not be significant.

Another possible reason for the low alloy intensities is that the degree of interdiffusion permitted to occur by the end of the heat-up segments may be too low to be detectable in both

cases and therefore difficult to measurably differentiate with this technique using short scan times. The total nominal elapsed times during heat-up are approximately 25 minutes and 100 minutes for heating rates of 40°C/minute and 10°C/minute respectively from 27°C to ~1027°C. It must also be considered that diffusivity rates increase exponentially with temperature, thus only a portion of the heat-up time significantly causes interdiffusion. As such, these short durations and the low average temperature (~500°C) may not allow for degrees of interdiffusion that are measurable with this technique. The neutron diffraction profiles in Figure 5-25 are comparable to Rudman's XRD patterns after heat-up plus a 5 minute hold at 780°C and cool-down (see Figure 2-34). This data also shows minimal diffraction occurring at intermediate alloy angles.

Sample 4 in the current study, which was initially heated just below the melting point of Cu (T_a = 1080°C), can provide insight into solid-state sintering behaviour at long hold times via the ND technique. The film plot in Figure 5-16 shows that sample 4 resulted in slow interdiffusion kinetics when compared to the other specimens TLP sintered at higher temperatures well above the Cu melting point. This is shown by the relatively slow generation of diffraction at intermediate alloy compositions. The initial peak temperature (1080°C) and the small amount of pure Cu melting indicated by the film plot in Figure 5-16 indicate that mixed SSS and TLPS may have taken place in this experiment. The slow interdiffusion rates indicated in the film plot suggest that SSS was dominant.

Figure 5-26 presents a waterfall plot of 5-minute diffraction patterns collected at increasing times during the isothermal segment of sample 4. The isothermal segment began at 1080°C (at t = 0 minutes) and drifted to 1096°C after 180 minutes, where any minimal liquid formation would have already solidified. The room temperature diffraction patterns for the pre- and post-sintered specimen can also be easily compared at the bottom of the figure. The patterns at 893°C and 1080°C do not show the evident Cu(200) peak intensity decrease and C_S shift typically observed during the melting event (as in Figure 5-23 and Figure 5-24). This indicates that little melting has occurred and solid-state sintering is likely the primary metallurgical process throughout the sintering cycle. As such, the Cu phase is not as uniformly distributed relative to TLPS conditions. This causes limited Ni-Cu contact, which significantly restricts Ni-Cu interdiffusion and slows the rate of homogenization [2]. This observation further indicates that the magnitude of the actual temperature gradient within the

powder sample is lower than that measured along the length of the canister wall (see Section 5.1.3). The sample's temperature variation is likely less than T_a ±25°C, and may be as low as ±5°C if indeed melting did not occur in this sample. Again, this can be attributed to the insulating, non-conductive characteristics of the alumina crucible, which, unlike the vanadium canister, is not directly connected to the water-cooled base of the furnace. The elemental Cu peak does not abruptly decrease in intensity or shift at the beginning of the isothermal stage, as observed in Rudman's XRD solid-state sintering studies [84,85]. As hold time increases both elemental Ni and Cu peaks broaden until one broad peak forms after approximately 180 minutes. This broad peak appears to occupy the entire alloy region ranging from pure Cu to pure Ni. At the end of the isothermal segment (780 minutes) the alloy peak is more refined due to continued homogenization. When compared to the width of the initial pure Cu and Ni peaks in the pre-sintered specimen; however, the post-sintered alloy still appears to contain significant compositional gradients since the alloyed peak width extends to the initial Cu to Ni angles. This indicates that more time would be necessary to fully homogenize the alloy under these conditions. It is worth noting that the centroid of the alloy peak approximates the predicted location for a homogeneous 65 wt%Cu alloy shown by the intermediate dashed line at C_O. This diffraction angle is simply calculated from the elemental peak locations using Vegard's law as per Equation (2-78).

According to the XRD study by Delhez *et al*, approximately 260 minutes were required to achieve 90% homogenization during solid-state sintering at 1000°C, as determined by relative peak positions [86]. Delhez used different, yet similar mixture compositions (70 wt% Cu) and powders size ratios. However, compaction and the use of much finer powders in Delhez's study ($\varnothing_{Ni}$ = 35μm, $\varnothing_{Cu}$ = 14μm) will significantly increase Ni-Cu contact and accelerate the interdiffusion process compared to the coarse loose powder specimens used in this study (see Table 3-1) [2]. Crank's equations for solute uptake by spherical particles [47], as well as TLPS models [25], show that the homogenization rate of solid particles is related to Dt/a^2, since smaller particles provide much greater surface areas and decreased diffusion distances.

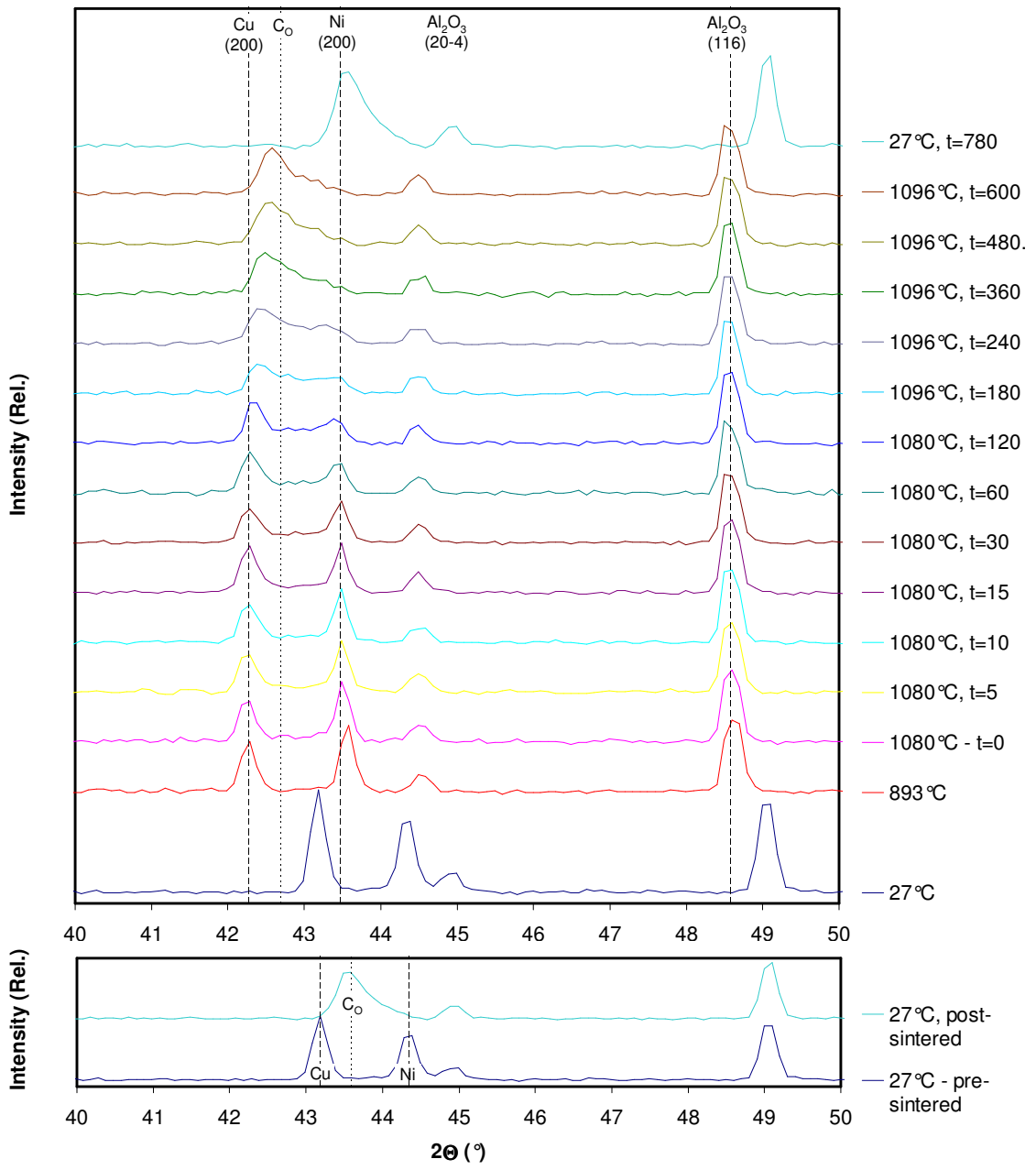

Figure 5-26: 5-minute ND patterns collected *in situ* during the isothermal segment of a solid-state sintered Ni-65wt%Cu powder mixture (sample 4).

5.3.2. Isothermal Solidification Stage

In this section, specimens that were heated to temperatures past the melting point of Cu and isothermally held to undergo transient liquid phase sintering will be analyzed (i.e., samples 5-9). These experiments constitute the primary focus of this study. Figure 5-27 presents ND

patterns collected during the isothermal segment of sample 5, which was heated to T_a = 1091-1123°C at 40°C/minute and isothermally held for over 1040 minutes before cooling to room temperature. The onset of melting (i.e., post-melt time t = 0 minutes) was first detected in the 5-minute diffraction pattern collected at 1072°C. The next pattern at 1091°C clearly shows the diminished Cu peak, which has already shifted to C_S compositions. This peak grows in the successive diffraction patterns as the pure Ni peak diminishes from Cu diffusion into the Ni particles.

At approximately 15 minutes this C_S peak is larger than the Ni peak, which indicates a significant fraction of the specimen now consists of a Cu-rich solid-solution. After 30-60 minutes at 1091°C, which is approximately the time where DSC results indicate that the liquid has been completely isothermally solidified (i.e., t_c = 45minutes), the C_S peak is significantly larger than the Ni peak and it has begun shifting to higher angles. This may be indicative of complete removal of the liquid, which constrains the surface composition of the growing solid-solution phase at C_S due to local equilibrium at the interface. Once the liquid has been removed this constraint is no longer active since the solid-liquid interface does not exist.

During the remainder of the isothermal segment the solid-solution peak becomes more refined as homogenization takes place. This process appears to be slow following liquid removal (~180-1040 minutes), which is indicative of slower solid-state sintering processes as observed with sample 4 in Figure 5-26. After the long isothermal sintering step and cooling to room temperature, the pattern collected at 20°C clearly shows a single alloy peak that is larger than either of the initial pure Cu and Ni peaks – indicating a fairly homogeneous alloy. Pre-sintered room temperature data could not be collected for this experiment due to furnace difficulties on start-up (see Appendix A).

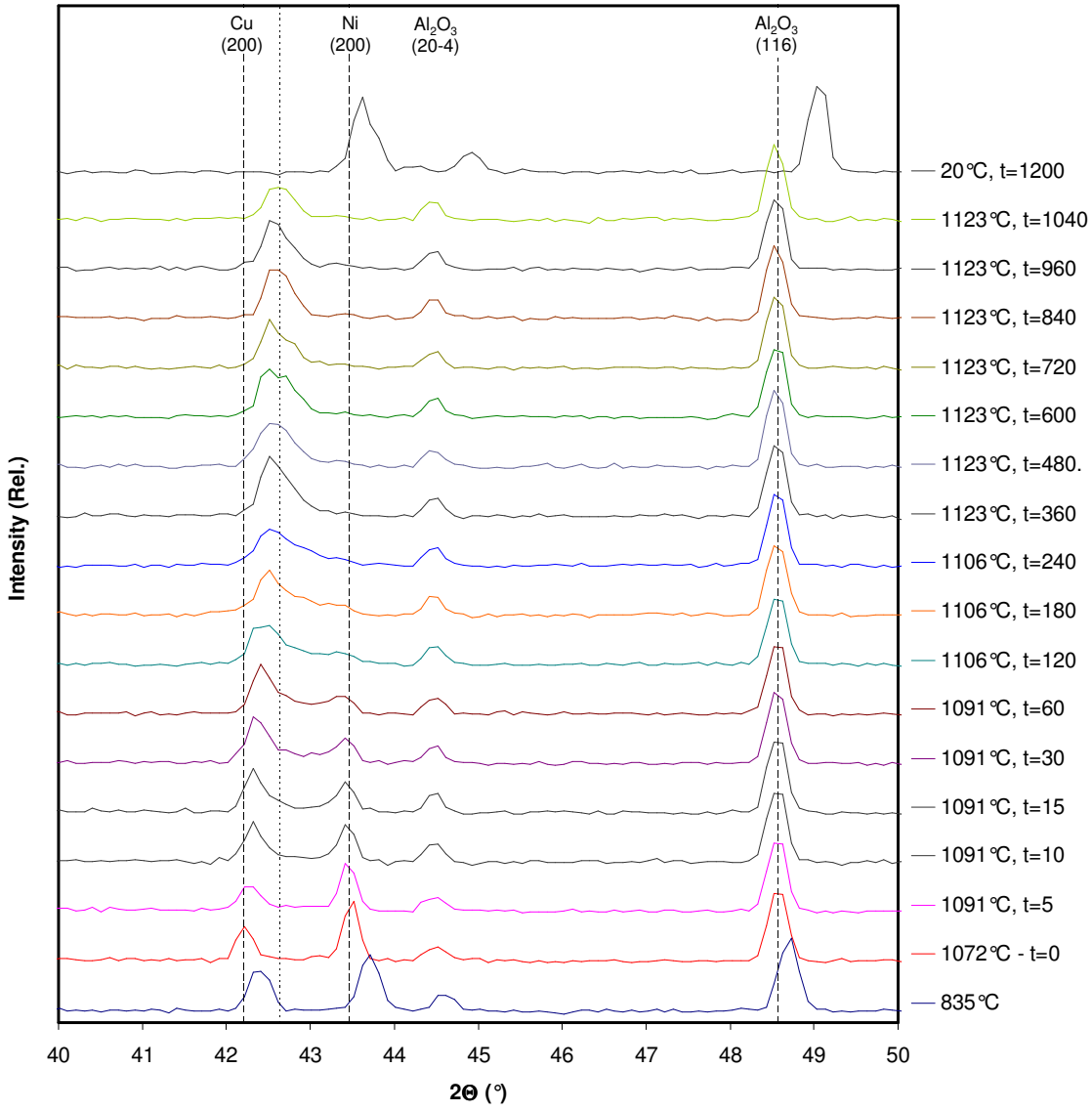

Figure 5-27: 5-minute ND patterns collected *in situ* during the isothermal solidification stage of a Ni-65wt%Cu powder mixture sintered at 1091-1123°C (sample 5).

Figure 5-28 presents ND patterns collected during the isothermal segment of sample 6, which was heated to T_a = 1128°C at 10°C/minute and isothermally held for over 900 minutes before cooling to room temperature. The onset of melting was first detected in the 5-minute diffraction pattern collected at 1078°C. The remaining C_S peak is more shifted than in sample 4 due to the increased sintering temperature (i.e. 1128°C vs. 1091°C). The post-melt shift is minimal in the 1091°C experiment since the maximum solubility of Cu in the solid-solution is very high near the melting point of Cu. As shown in the Ni-Cu phase diagram in Figure 2-10, the value of C_S approaches of pure Cu at temperatures nearing 1085°C.

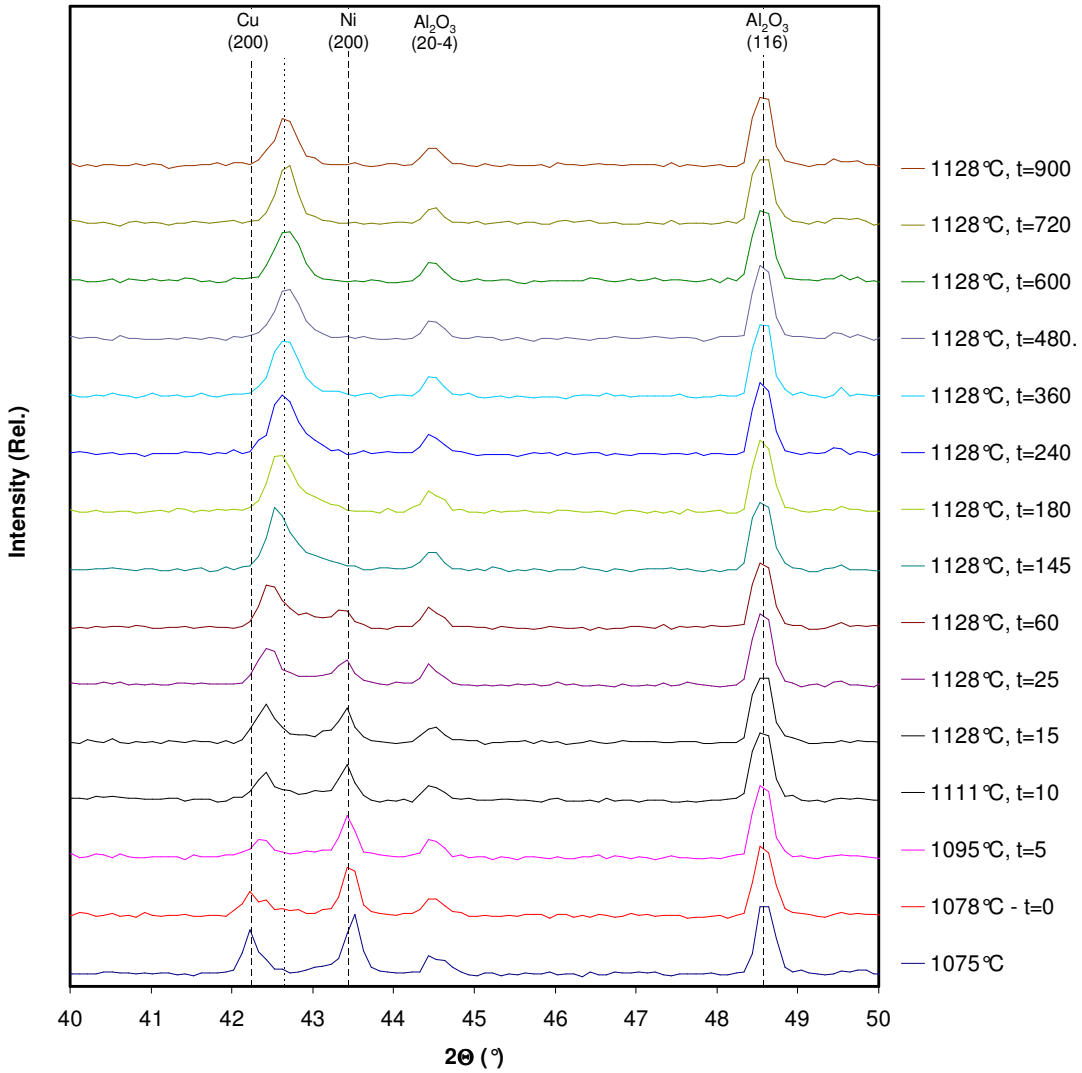

Figure 5-28: 5-minute ND patterns collected *in situ* during the isothermal solidification stage of a Ni-65wt%Cu powder mixture sintered at 1128°C (sample 6).

Sample 7 was heated to 1162°C at 40°C/minute and held for only 10 minutes before the experiment was terminated. Therefore, insufficient isothermal data are available to justify another plot. However, Figure 5-24, which was presented in Section 5.3.1, contains the 5-minute ND patterns collected during the short isothermal hold segment of sample 7 and should be referred to for isothermal segment analysis. This sample was aimed at investigating the solid-state sintering effects during the heat-up segment only. However, the three post-melt diffraction patterns included in Figure 5-24 clearly show the melting event that was detected in the diffraction pattern collected at 1096°C. The C_S peak shift and initial growth exhibited are typical of previous observations.

Figure 5-29 presents ND patterns collected during the isothermal segment of sample 8, which was heated to T_a = 1194°C at 40°C/minute and isothermally held for 30 minutes before cooling to room temperature. As discussed in Section 5.2.1, Mo peaks originating form the canister wall are present at approximately 50°. These peaks do not overlap with the Ni, Cu, and Al_2O_3 peaks of interest in the 40-50° 2θ range plotted. The onset of melting was first detected in the 5-minute diffraction pattern collected at T_a = 1112°C since the heating rate was still close to 40°C/minute at this point. This likely caused a greater temperature gradient between the Al_2O_3 internal temperature standard and the sample at the melting point of Cu, resulting in an overestimation of the melting point. In other words, since the peak program temperature is significantly higher than the Cu melting point in this particular experiment, the typical slow approach to the isothermal set point began at a later temperature with respect to the specimens sintered at lower temperatures.

Once melting has been detected at T_a = 1112°C, the residual C_S peak shifts by a similar degree to that observed in sample 6 (Figure 5-28). Due to the increased sintering temperature of sample 8 (i.e. 1194°C vs. 1128°C), the phase diagram clearly shows that C_S decreases, which would cause compositional shifting of C_S peaks to higher angles at higher temperatures. However, the continued thermal expansion of this stable solid-solution at C_S will cause thermal peak shifting in the opposite direction (i.e., to lower angles). A detailed comparison of C_S peak shifts at the various sintering temperatures will follow in Section 5.3.3.

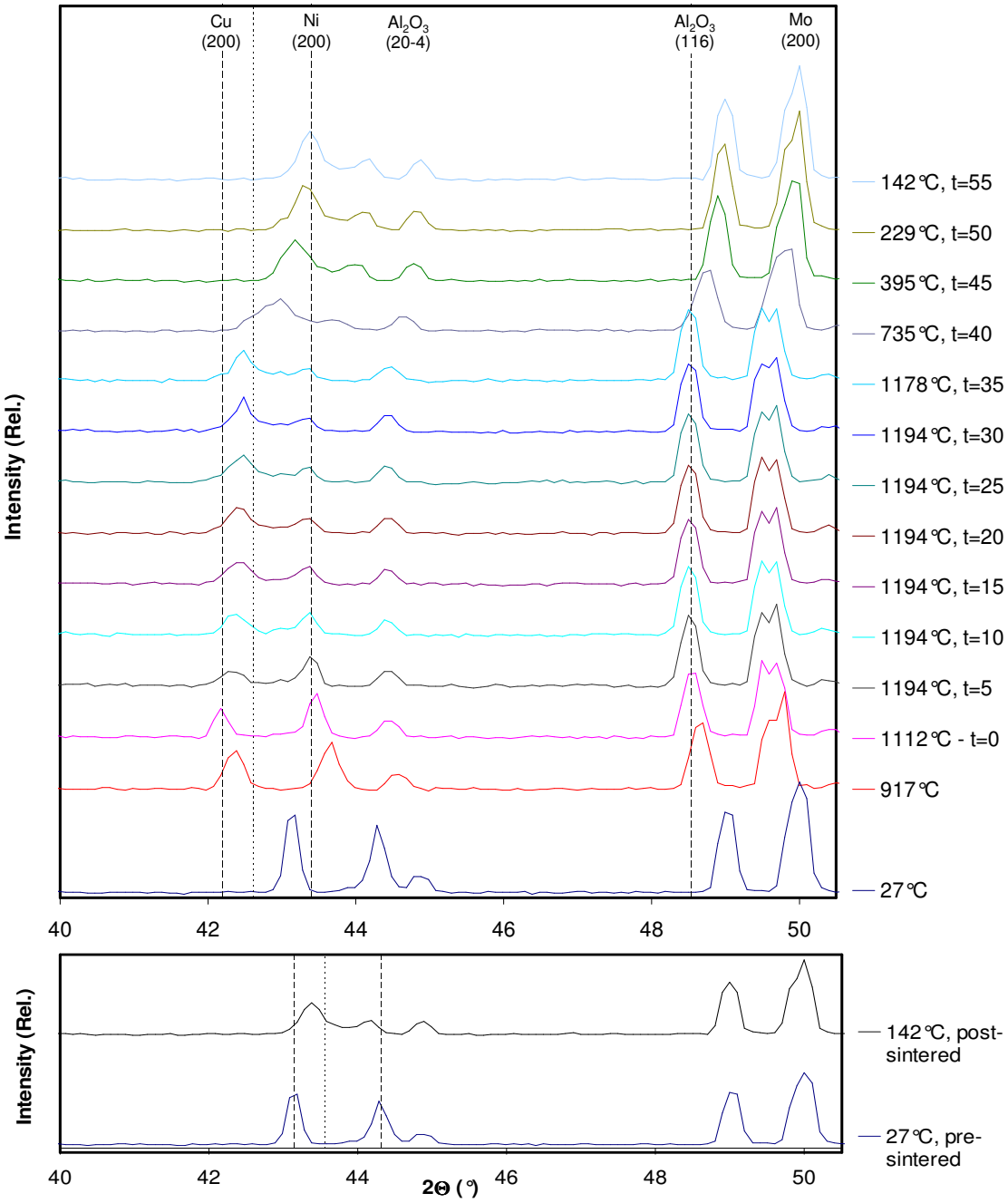

Figure 5-29: 5-minute ND patterns collected *in situ* during the isothermal solidification stage of a Ni-65wt%Cu powder mixture sintered at 1194°C for 30 minutes (sample 8).

The diffraction patterns after the melting event in Figure 5-29, which are separated by 5 minute intervals, show similar behaviour to the other experiments. At the end of the 30 minute isothermal segment (which corresponds to a 35 minute post-melt time), the C_S peak is significantly more intense than the Ni peak, which still remains. Upon cooling the Cu(200)

peak grows – indicating athermal solidification/freezing of the remaining liquid. This observation was also made for the Cu(220) peak in this sample's film plot (Figure 5-20).

At room temperature (see bottom of Figure 5-29) a broad, bi-modal intensity distribution is present in the 2θ alloy range – indicating a very heterogeneous Cu distribution in the post-sintered alloy. Since most of the peak area appears to be Cu-rich (extending to pure Cu), this further indicates that some Cu-rich liquid (having compositions near C_L) was still present at the end of the short isothermal segment. Based on experimental DSC results for 65wt% Cu mixtures TLP sintered at 1090°C and 1140°C and the analytical model developed in this study, it is expected that incomplete isothermal solidification of the liquid occurs after 30 minutes at ~1200°C.

Figure 5-30 presents ND patterns collected during a much longer isothermal segment for sample 9, which was heated to similar temperatures (T_a = 1178-1194°C). This data illustrates similar melting behaviour and the growth of the initial C_S peak. Data at longer post-melt times shows the gradual transition from a bi-modal C_S/Ni intensity distribution to a single, broad alloy peak. After some time the alloy peak becomes sharper due to increased homogenization generating a uniform composition distribution. The final peak position (at t = 720 minutes) is in good agreement with that predicted for a homogeneous 65wt% Cu solid solution (as per Equation (2-78)). As previously discussed, the additional peaks found at 50° originate from the Mo sample canisters used for only this experiment and sample 8.

Now that the isothermal evolution of the time/temperature-resolved diffraction patterns collected for each specimen have been interpreted as a function of post-melt time at the respective calibrated temperatures, it is appropriate to analyze the implications of this behaviour with respect to the important metallurgical processes in TLPS. After the melting event, growth of the Cu-rich C_S(200) peak appears to be rapid. This indicates that a Cu-rich solid-solution is rapidly forming during the isothermal segment. This is in agreement with the SEM/EDS analysis of DSC specimens sintered at 1090°C and 1140°C (Section 4.1.5), where isothermal solidification would leave behind a Cu-rich layer (having a composition near C_S) surrounding the still solute-deficient Ni particles.

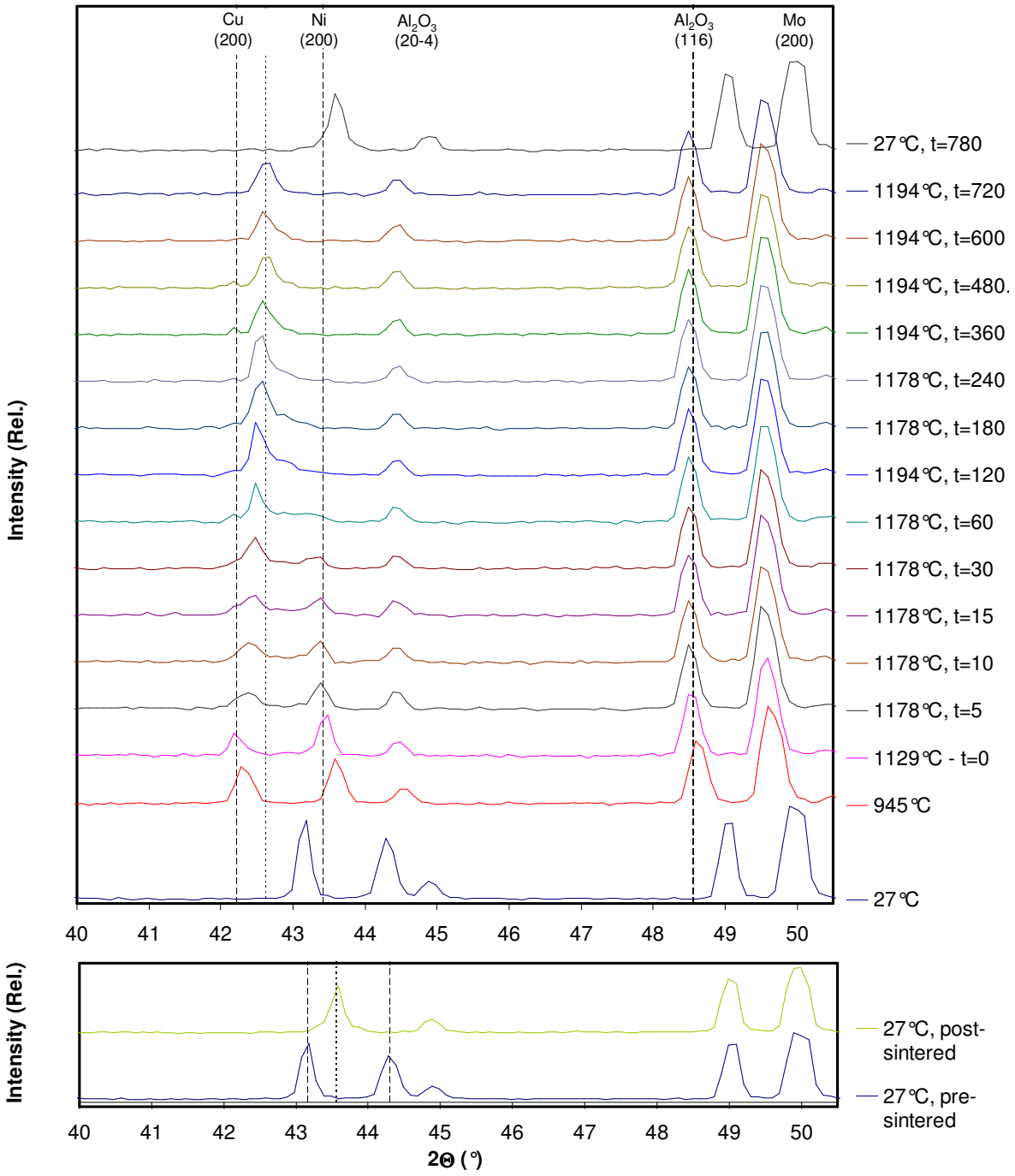

Figure 5-30: 5-minute ND patterns collected *in situ* during the isothermal solidification stage of a Ni-65wt%Cu powder mixture sintered at 1178-1194°C for 780 minutes (sample 9).

ND patterns at short hold times demonstrate a bi-modal intensity distribution (i.e., two peaks at C_S and Ni), indicative of the significant compositional gradients between the Ni particle core and the isothermally solidifying Cu-rich layer. The C_S peak grows rapidly following the melting event. Comparatively, the rate of Ni peak broadening and intensity

reduction is relatively slow. This is an indication that the rate of Cu penetration deeply into the Ni particles is relatively slow vs. the growth of the C_S region, both of which contribute to liquid removal. This is also in agreement with the previous SEM/EDS results where large compositional gradients were measured for interrupted experiments. Cu-deficient Ni particle cores were still present at the end of the isothermal solidification process at 1090°C and 1140°C (see the 45 and 75 minute curves in Figure 4-14*c* and *d*).

Therefore, this *in situ* neutron diffraction data supports the hypothesis that isothermal liquid solidification in TLP sintered Ni and Cu powders occurs by the epitaxial growth of a Cu-rich layer at C_S and limited long range diffusion into the Ni particles. Furthermore, the rapid growth of the C_S peak indicates that this process is rapid following the liquid formation and redistribution. This is in agreement with the fast rate of liquid removal measured by DSC at short hold times (i.e., the rapid initial decrease in the measured liquid fraction, W_A in Figure 4-11). This initial behaviour has also been observed in TLPS DSC studies of other alloy systems [11,25,28]. This can be explained by the fact that once liquation of Cu occurs, it can rapidly redistribute uniformly around surrounding Ni particles. This rapid redistribution throughout the mixture results in the Cu-rich liquid encountering a large 'virgin' Ni surface area, which will quickly alloy and solidify a portion of the redistributing liquid. This is evidenced in DSC traces by the small exothermic peak typically found immediately following melting (see in Figure 4-2 and Figure 4-3). This rapid, diffusional re-solidification of the redistributing liquid is sometimes referred to as 'freeze-off' [27].

Interdiffusion within the solid-solution particles during the isothermal segment is evidenced by the gradual increase in diffraction intensity at intermediate alloy angles. Prior to complete isothermal solidification of the liquid, a bi-modal intensity distribution is still expected - as observed by SEM/EDS analysis of DSC specimens sintered at 1090°C and 1140°C. Once the liquid phase in no longer present, the interface is no longer compositionally constrained at C_S and C_L compositions. Therefore, it is expected that diffraction intensities should not longer increase at compositions/angles near C_S. However, the measured diffraction intensity distribution should still be fairly bi-modal at this point depending on the sintering temperature. Ongoing interdiffusion within the now fully solid alloy serves to homogenize the material. Accordingly, this refines the intensity distribution of the ND peak profile – gradually forming a single peak centering around the predicted location for a homogeneous 65wt% Cu

alloy. Samples held for a sufficient time clearly showed the formation of a refined single peak. The location of this post-sintered peak was in good agreement with that predicted for the bulk alloy composition, C_O.

Solute penetration into the Ni particle cores does contribute to the removal of liquid as well as epitaxial growth at C_S. It is expected that this contribution is more signification at higher temperatures where C_S approaches C_O. The approximate time for the very gradual transition from a double- to single-peak profile (i.e., the removal of the Ni peak) during the homogenization process is difficult to determine from the experimental diffraction patterns. It is believed that the liquid may have long been removed at this point. Nevertheless, this transition can still provide an indication of process kinetics at different temperatures and the point where a sample definitely contains no liquid. This analysis will be discussed in Section 5.3.3.

5.3.3. Temperature Effects

The diffraction pattern evolution illustrated in the waterfall plots shown in Section 5.3.2 for the individual specimens helped elucidate the isothermal solidification process during TLPS. It is clear that the formation of a transient liquid complicates the process and ND pattern interpretation relative to Rudman's XRD studies of solid-state sintering. It was found that samples 5-9 exhibited similar sintering behaviour characteristic of TLPS, yet differentiating observations were a result of the different peak process temperatures. In order to evaluate the effects of isothermal sintering temperature on the evolution of neutron diffraction data sets, which can provide valuable insight on TLPS process kinetics, it is useful to directly compare diffraction patterns from the different samples at common post-melt times.

Before doing so, it is important to review the expected effects of sintering temperature on the TLPS process as well as the diffraction patterns. Table 5-9 shows a list of important counteracting effects of temperature on metallurgical processes in TLPS as well as their expected effects on diffraction profiles at the melting event. The corresponding effects on the amount of liquid formed and process kinetics, as represented by the rate of ND pattern evolution, are also indicated.

Table 5-9: Summary of expected temperature effects on TLPS (↑ T_P)

	Metallurgical process	Effect on diffraction profile at t_o	Kinetics/ evolution	Liquid fraction
1	Thermal expansion	All peaks shift to lower 2θ		
2	Decreased solid solubility (C_S)	C_S(200) peak shifts to higher 2θ	↓	
		Reduction of intermediate 2θ alloy range Δθ	↓	↑
3	Decreased liquid solubility (C_L)	Dissolution of Ni --> Ni peak reduction	↑	↑
4	Melting of SSS alloyed regions	More evident Cu(200) melting event and smaller residual C_s peak area		↑
5	Increased diffusivity	Accelerated evolution	↑	

Factor 1 states that as the temperature increases, thermal expansion causes all peaks to shift to lower angles. The decreasing solid solubility limit of Cu within the Ni-Cu solid-solution (C_S) at higher temperatures (factor 2) has many counteracting effects on the initial conditions of the isothermal segment as well as the rate of solidification. As C_S decreases with increasing temperature, the residual C_S peak, which grows after melting, will shift to higher angles and this will decrease the intermediate 2θ range separating the Ni peak from the Cu-rich peak. This effectively decreases the compositional range within the Ni particles since the surface is now constrained to a lower Cu content. Decreased compositional gradients will result in decreased mass transfer rates as per Fick's 1st law (Equation (2-6)) and thus slow isothermal solidification kinetics.

As indicated by DSC and SEM/EDS results, Factors 3 and 4 significantly affect the amount of liquid formed, its duration, as well as the rate of its removal. Decreased Cu solubility in the liquid, $C_{L,}$ (or increased Ni solubility) causes an increased liquid fraction via dissolution of Ni particles, which should cause a decrease in Ni peak intensity upon melting. However, the decreased Ni particle size as a result of dissolution is expected to increase process kinetics and the rate of ND pattern evolution. Factor 4, which is related to factor 2 by the decreasing C_S value, results in the melt-back of Cu-rich solid-state alloyed regions at the Ni surface since these compositions are no longer stable at temperatures above 1085°C. This results in a more evident melting event at higher temperatures due smaller residual C_S peaks immediately after melting. The increased liquation from this melt-back process increases the liquid fraction as well as its duration.

Figure 5-31 compares diffraction patterns collected at the onset of melting (t = 0 minutes) for various specimens. All peak positions are similar due to the temperature

proximity of all samples to the Cu melting point. The diffraction profile of sample 4, which was solid-state sintered just below the melting point of Cu (i.e., 1080°C), is included for relative comparisons between SSS and TLP sintered specimens. The initial 1080°C Ni and Cu peak positions are indicated by dashed vertical lines as a visual reference for pre-melt peak shifting and profile changes at later times in upcoming figures. The predicted peak position for a homogeneous 65wt% Cu alloy is also shown. Another practical use of the 1080°C SSS pattern is that the total area under the profile across the entire solid-solution 2θ range represents a fully solid specimen. It is worth noting that sample 6 was heated to 1128°C at a slower heating rate than the other samples (10°C/minute vs. 40°C/minute) and therefore may exhibit greater degrees of interdiffusion. However, as shown in the expanded plot in Figure 5-25, this effect does not appear significant relative to the gross diffraction profile changes observed during the isothermal sintering segment.

Figure 5-31 shows that at the onset of melting, the Cu peaks have significantly diminished in intensity relative the respective Ni peaks as well as the Cu peak for the solid-state sintered sample at 1080°C. This observation, and the post-melt C_S peak shifts are a strong indication of melting. In the case of sample 6, the residual C_S shoulder is visible in the diffraction pattern. At high sintering temperatures, the diminished Cu/C_s peaks are somewhat shifted to lower angles due to additional thermal expansion as melting occurs over a ~4-5 minute period (see Section 5.1.1)

Five minutes after the onset of melting (Figure 5-32) all patterns show the typical small, residual C_S peaks, which are stable and begin to grow rapidly. These have all shifted to higher angles due to compositional shifting, yet less so at the higher temperatures due to the counteracting thermal expansion effect, which is most apparent at 1178°C and 1194°C. At this point all C_S peaks are still significantly smaller than the Ni peaks. Relative to the onset of melting data (Figure 5-31) and the reference SSS 1080°C pattern, the Ni peaks also show decreased intensities at higher temperatures – indicative of Ni dissolution effects and increased liquid fractions also indicated by DSC.

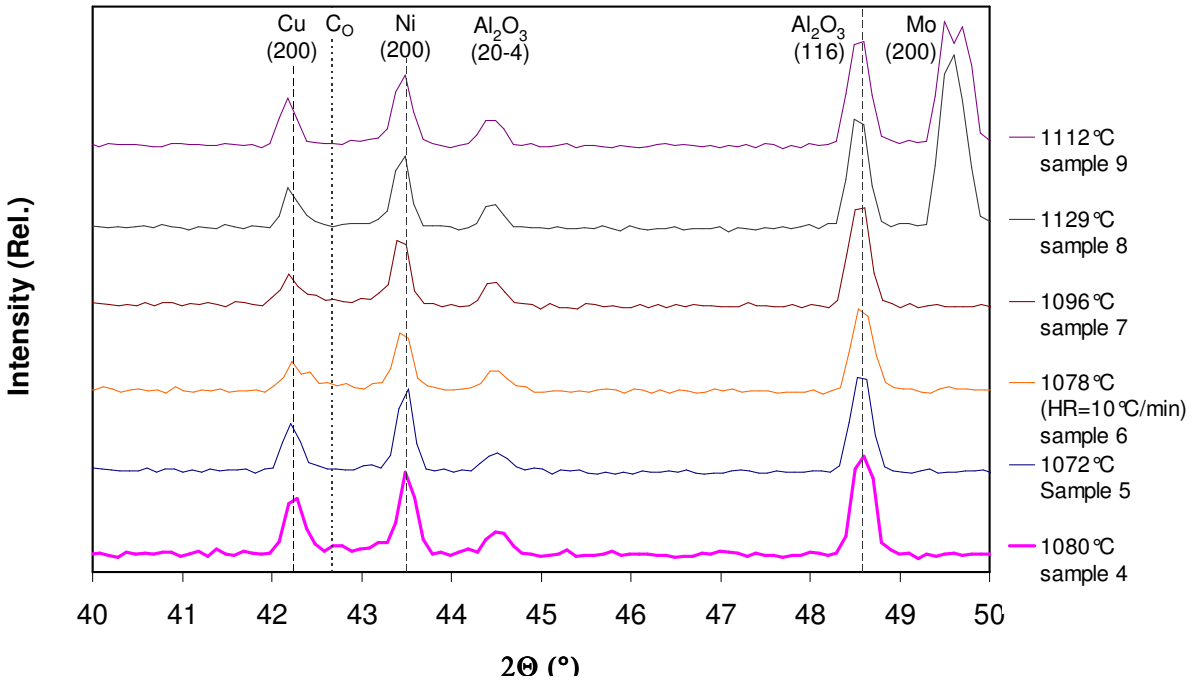

Figure 5-31: ND patterns collected at the onset of melting (t = 0 minutes) for Ni-56wt%Cu powder mixtures isothermally held at different process temperatures.

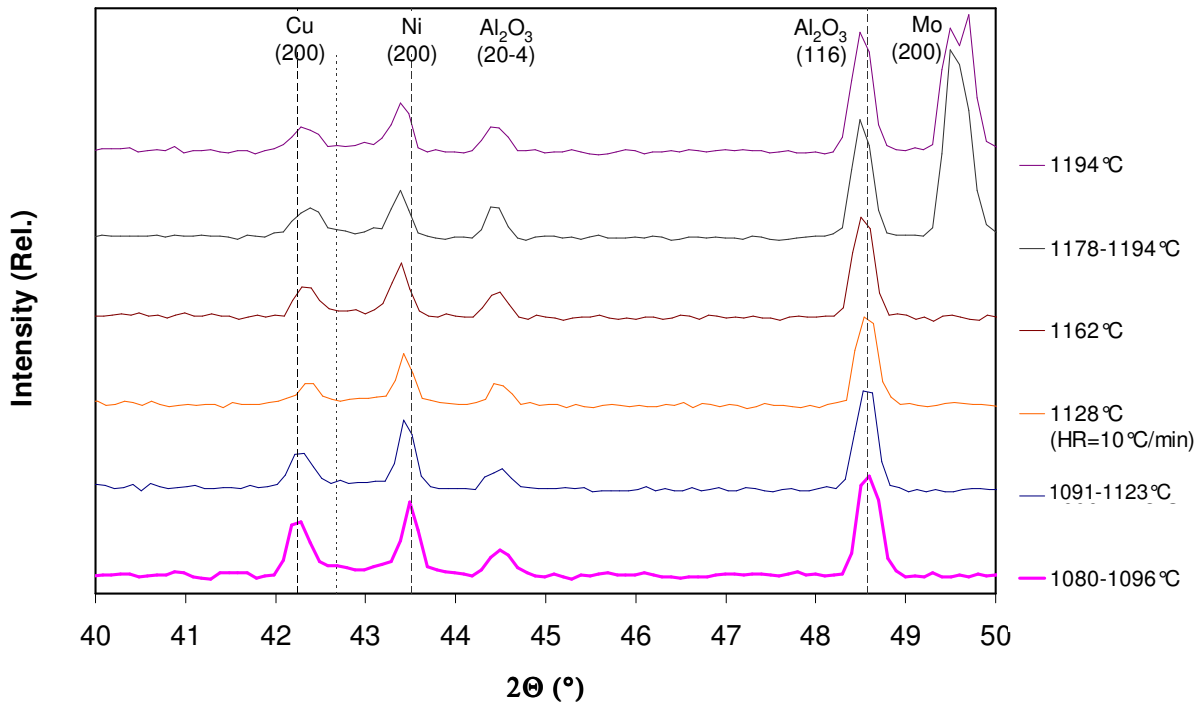

Figure 5-32: ND patterns collected 5 minutes after the melting event for Ni-56wt%Cu powder mixtures isothermally held at different process temperatures.

In order to gain confidence in this interpretation of the melting behaviour and post-melt profile evolution, it is appropriate to confirm the identity of the C_S peak. Figure 5-33 shows the traced Ni, Cu, and C_S peak positions measured at FWHM for all specimens near the melting event. The shifting peak positions of each sample are plotted according to their respective processing temperature (T_P) on the y-axis. This presentation format is somewhat similar to a film plot, but this data summarizes the melting behaviour of all specimens as they are heated to their respective T_P – from just below to well above the melting event. See the traces connecting the t = 0, 5, and 10, minute data between experiments to observe the effect of increasing T_P from sample to sample (or temperature to temperature).

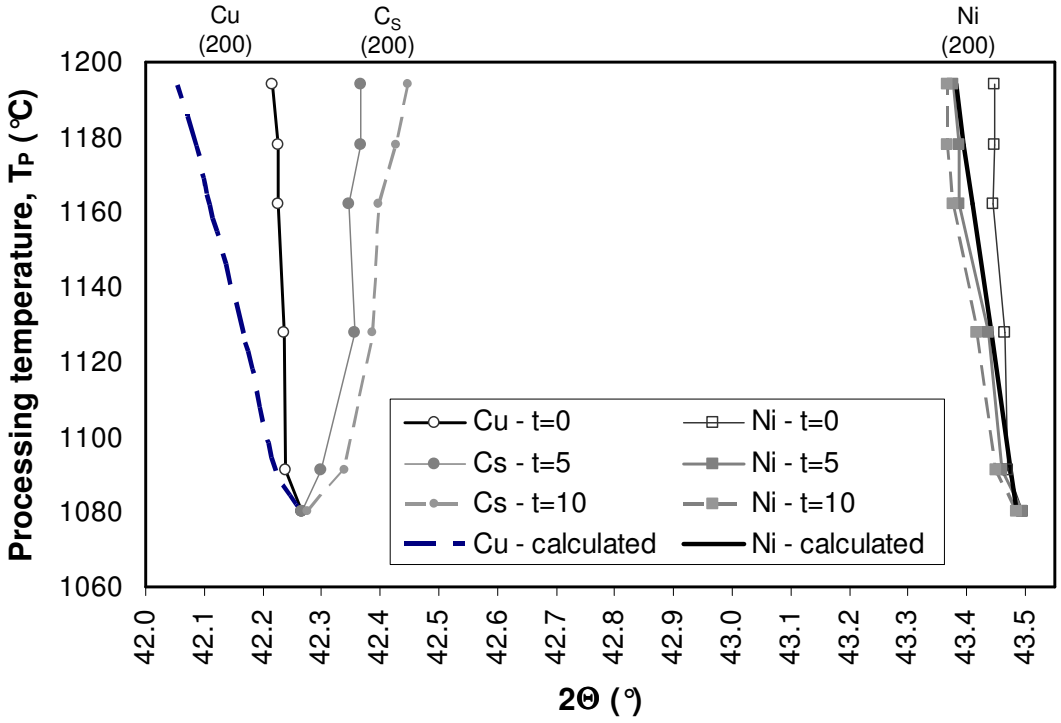

Figure 5-33: Cu, Ni, and C_S peak positions at t = 0 minutes (onset of melting), 5 minutes, and 10 minutes for samples 4-9 (i.e., 1080-1094°C).

The fairly stable peak positions of the solid-state sintered specimen are plotted at 1080°C as a non-melting reference. The position of these peaks is seen to shift insignificantly during the first 0-10 minutes at 1080°C due the absence of melting and negligible interdiffusion. At the onset of melting (t = 0 minutes for samples heated above 1085°C), the Ni peaks were all observed at similar angles due to their temperature proximity to 1085°C. Accordingly, the solid-stated sintered Ni peak at 1080°C is at a moderately higher angle due to slightly less

thermal peak shifting. The diminished pure Cu peaks at t = 0 minutes all have similar positions as well due to their proximity at melt onset.

At t = 5 minutes, the Ni peaks have progressively shifted to slightly lower angles due to thermal expansion. The calculated thermal expansion of Ni from Touloukian *et al* data is also included for comparison [81]. Conversely, the Cu peaks exhibit a very different behaviour since they shift to higher angles in the opposite direction of thermal expansion. This is because the pure Cu peaks melt and leave behind residual C_S peaks that have compositionally shifted in the opposite direction due to alloying (i.e., opposing thermal expansion shifts to lower angles). The calculated theoretical peak positions of a pure Cu lattice due to thermal expansion past the Cu melting point have also been plotted to illustrate the superimposed thermal and compositional shifting effects listed in Table 5-9 (i.e., factors 1 and 2). These values were calculated by extrapolating Touloukian's thermal expansion expression for Cu (see Equation (2-74)), which does not significantly change in curvature above 1085°C (see Figure 2-32). In this temperature range the solid Cu lattice is unstable and will melt, but these data nevertheless serve to illustrate the relatively large thermal expansion trend of the Cu lattice above 1085°C, if it were stable of course. Comparison of the extrapolated pure Cu expansion and the experimentally observed C_S peaks shows a large divergence, particularly at high temperatures. As such, the melting event in TLPS clearly has a distinct effect which is distinguishable in the evolution of neutron diffraction patterns.

After 10 minutes following the onset of melting, the Ni peaks have almost stabilized, yet the C_S peak centroids continue to shift somewhat due to rapid asymmetric growth at greater angles. The rapid growth of this peak provides a strong indication of the isothermal solidification mechanism (i.e., epitaxial growth at C_S compositions). To further elucidate the isothermal solidification process, the relative peak positions shown in Figure 5-33 can be used to determine the approximate composition of the isothermally solidifying material from which the growing C_S diffraction peaks originate.

The measured Ni, Cu, and C_S peak positions (θ_{Ni}, θ_{Cu}, θ_{Cs}) were substituted in Equation (2-78) and then solved for the alloy composition - in this case C_S (in wt.% Cu). Figure 5-34 shows how this calculation does not agree well with the expected C_S composition traced by the linear solidus line of the superimposed Ni-Cu phase diagram. This is due to the fact that the

last measured positions of the pure Cu peak were used at the onset of melting (i.e., θ_{Cu} at $t = 0$ minutes in Figure 5-33). These peak positions at $t = 0$ do not incorporate the thermal expansion effects as the sample reaches T_P shortly after melt onset. Unfortunately pure Cu peaks are not physically possible at T_P above the Cu melting point. However, the C_S calculation can be corrected to account for the theoretical expansion of pure Cu at the appropriate temperatures by using the calculated (θ_{Cu}) values plotted in Figure 5-33. Figure 5-34 shows that this correction shows improved agreement with the Ni-Cu solidus. However, at lower temperatures the calculated C_S values appear to be too deficient in Cu (or too rich in Ni). This may be due to the assumed theoretical Cu expansion above 1085°C, where extrapolation of Touloukian's equation may not provide a sufficient correction. Conversely, it is possible that the full samples have not yet reached their respective process temperatures as determined by the Al_2O_3 temperatures (T_a) and the plotted temperatures are somewhat too low.

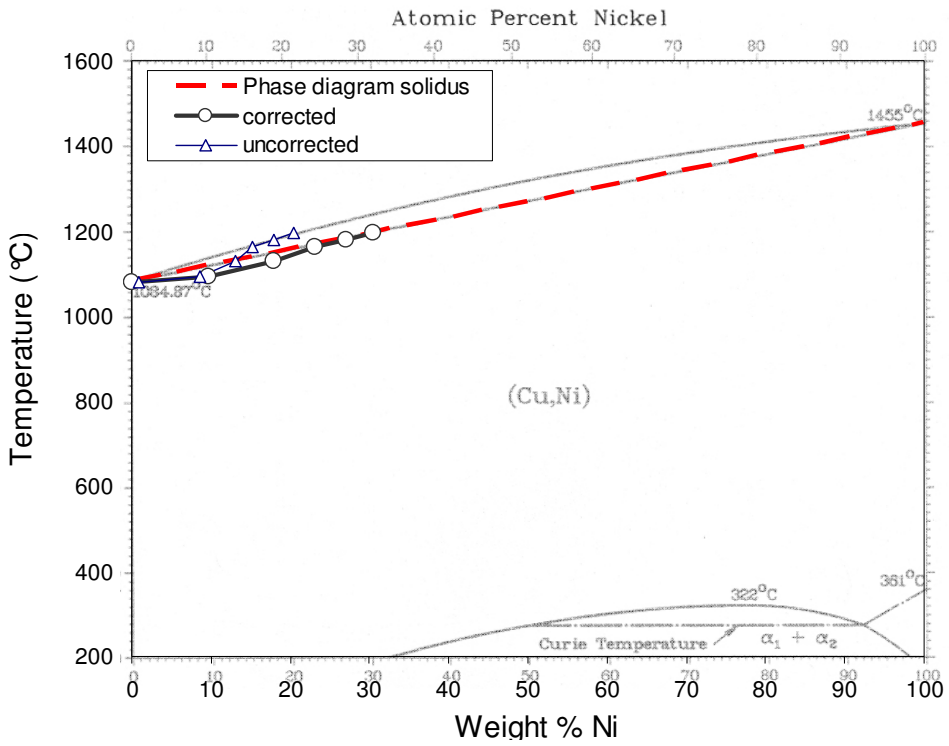

Figure 5-34: Calculated C_S peak compositions compared to the expected Ni-Cu solidus line. Note: this plot is superimposed over the Ni-Cu phase diagram.

Nevertheless, this data provides a strong indication that the isothermally solidifying phase responsible for abrupt peak growth has a composition that can be approximated by the

solidus (C_S). This further indicates that isothermal solidification of the liquid phase in Ni-Cu TLPS occurs by epitaxial growth of a Cu-rich phase surrounding Ni particles.

Figure 5-35 presents ND patterns collected 15 minutes after the melting event. In comparison to the t = 5 minute data in Figure 5-32, all ND patterns show that the C_S peaks are growing rapidly. This observation is made more evident by observing the growth of C_S peaks after 5 and 15 minutes relative to the Ni peaks at all TLP sintering temperatures. This rapid intensity increase is indicative of rapid initial isothermal solidification of the liquid at Cu-rich solid-solution compositions. At 1090°C and 1128°C for example, both patterns show C_S peaks that are noticeably larger than the Ni peaks at this point. Dashed baselines have been added to interpret peak sizes relative to the background signal. The growth of the area under these C_S peaks must be a result of an increase in the amount of diffracting solid material in the specimen having this composition. This can only occur by isothermal solidification of the liquid at C_S since the process temperature is stable.

Furthermore, the total area under the diffraction profile spanning the entire alloy range (i.e., the area between the diffraction profile and the horizontal dashed line from θ_{Cs} to θ_{Ni}) provides an indication of the total amount of diffracting solid present at that time. Conversely, since all samples had very similar total masses, this also indicates how much liquid must be present. Larger diffraction profile areas indicate more solid is present and therefore less liquid. For example, after 15 minutes (Figure 5-35) the area of the entire solid-solution range observed at lower temperatures is noticeably greater than that at higher temperatures. This is primarily due to the enlarged C_S peaks and the less dissolved Ni peaks at lower temperatures - indicating that there is more solid, or less liquid, present. Also, similar, yet somewhat greater diffraction intensities are visible between the C_S and Ni peaks at higher temperatures – indicative of greater degrees of interdiffusion while still maintaining a very bi-modal solute distribution. This is in agreement with metallographic and DSC data (Figure 4-11) where less liquid was still present after a 15 minute isothermal hold at 1090°C (W_A = 7 wt% liquid) than 1140°C (W_A = 19 wt% liquid).

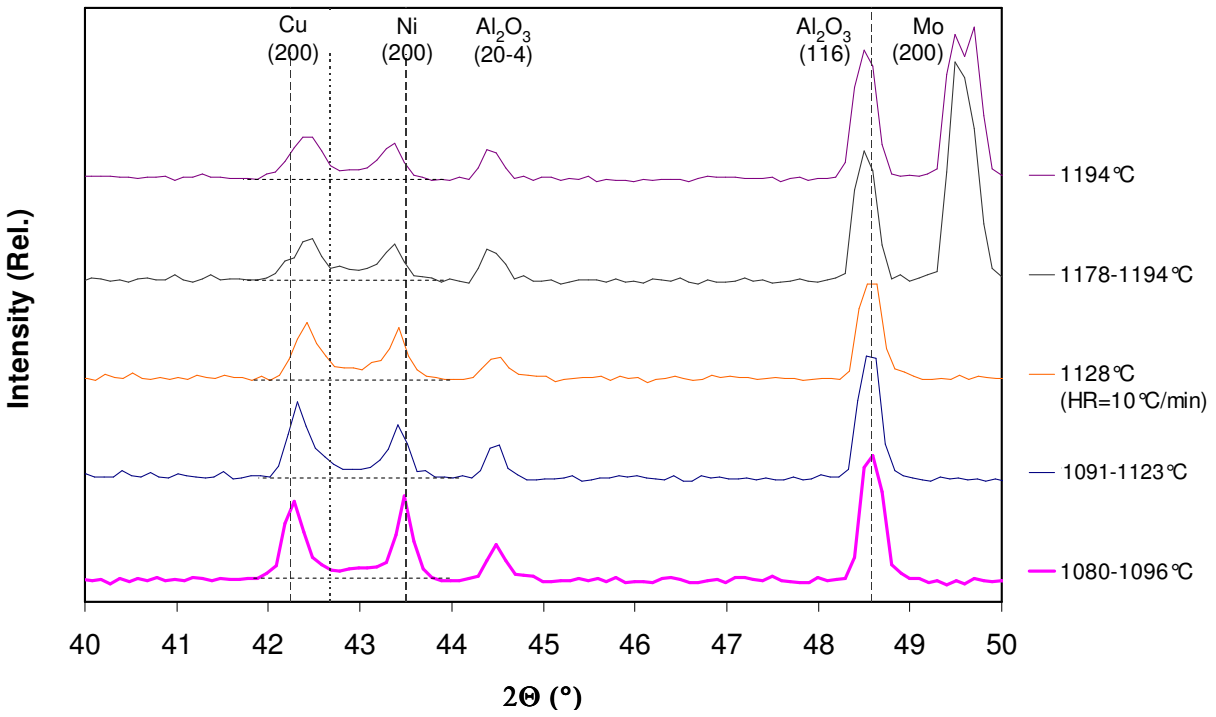

Figure 5-35: ND patterns collected 15 minutes after the melting event for Ni-56wt%Cu powder mixtures isothermally held at different process temperatures.

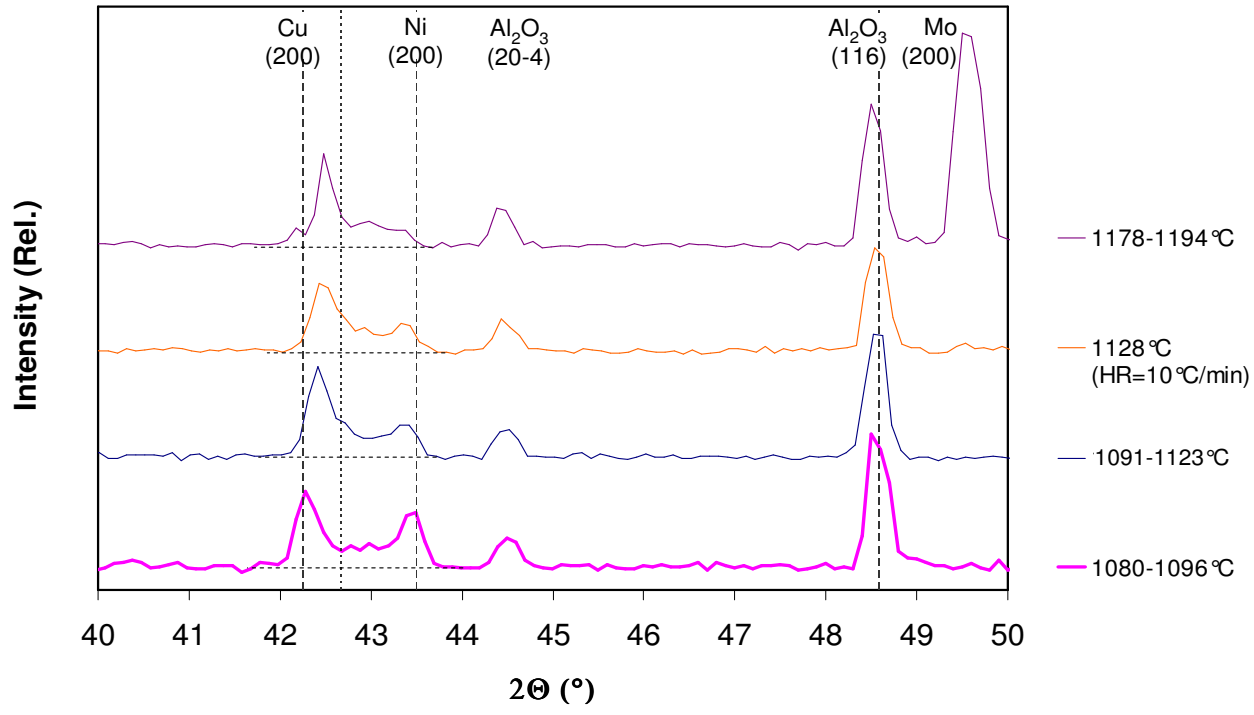

Figure 5-36: ND patterns collected 60 minutes after the melting event for Ni-56wt%Cu powder mixtures isothermally held at different process temperatures.

After 60 minutes (Figure 5-36) the diffraction patterns have significantly evolved. The diffraction profiles at higher temperatures demonstrate less of a bi-modal intensity distribution. For example, the specimen sintered at 1178-1194°C shows a single-peak profile whereas the other patterns still have broad double-peak profiles. As such, there appears to be very little pure Ni left in the sample sintered at 1178-1194°C, indicating significant interdiffusion and solute penetration into the Ni particles.

This can be explained by increased diffusivities as well as dissolution at higher temperatures (see C_S and diffusivity factors described in Table 5-9). Ni dissolution at higher T_P generates smaller Ni particles (i.e., smaller diffusion depths) with lower maximum solute solubilities at the surface ($\downarrow C_S$, factor 2 in Table 5-9). At higher temperatures, this reduces the compositional range which can exist within the solid-solution (i.e., 0-C_S wt% Cu). This correspondingly refines/narrows the 2θ range that can participate in diffraction and therefore refines the alloy peak width. Furthermore, diffusivities are significantly increased with rising temperatures, thus accelerating interdiffusion. Both solubility and diffusivity effects contribute to accelerated saturation by Cu and the more rapid formation of a single, more homogeneous peak. Figure 5-36 also shows that all samples exhibit a significant increase in diffraction intensity at intermediate alloy angles relative to Figure 5-35 (t = 15 minutes) due to increased interdiffusion and the formation of alloyed surface regions with shallower concentration gradients. At 1178°C, it is worth noting that there is a small peak present at very Cu-rich angles. This is may be due to noise in the collected diffraction pattern from instrumental broadening effects and the low collection times. As shown in Figure 5-30, this small peak is not always present and may very well be due to low signal quality. It is also possible that during the initial set-up of this sample within the furnace, some Cu powder was displaced outside of the crucible near the cooler bottom regions on the sample environment, yet still within the beam.

Evidently, the TLPS process is significantly affected by increasing T_P since the partially dissolved Ni particles are now smaller at this elevated temperature (factor 3 in Table 5-9) and more rapidly penetrated and saturated by the increased diffusivity of Cu solute atoms (factor 5). Consequently, more liquid is formed at these temperatures (due to factors 3 and 4). This liquid is removed by epitaxial solidification at a lower C_S (or higher 2θ angle), and solute

penetration deeper into the Ni core – accelerating the formation of a single peak profile. Therefore, the smaller Ni particles must achieve a higher degree of saturation and homogenization to absorb the increased amount of Cu-rich liquid. However, it is difficult to determine the amount of liquid remaining based on ND patterns since this is an amorphous phase which does not contribute to diffraction. Its metallurgical effects on the solid phase that is present - ranging from the Ni particle core to the growing C_S region- must therefore be carefully interpreted, particularly when attempting to determine complex temperature effects from diffuse peak areas. This complexity reinforces the importance of quantitative DSC data to determine liquid fractions, which can then be correlated to the evolving diffraction patterns. This combination provides a much improved understanding of the isothermal solidification process during TLP sintering and its kinetics

DSC data indicates that there should no longer be any liquid present after 60 minutes at 1090°C and only 2 wt% liquid at 1140°C. This marginal difference is also exhibited by the similarity of the 1091°C and 1128°C diffraction patterns, which both have total areas comparable to the solid-state sintered 1080°C specimen, which is fully solid at this point. Based on DSC data at 1140°C, which indicated that 2 wt% liquid was still present at this point, it is expected that liquid is still present in the ND specimen sintered at 1178°C. The diffraction pattern for this sample appears to support this point, since the intensity distribution shows a smaller total area than the other specimens.

This complex behaviour is even more evident after 180 minutes (Figure 5-37). At this point, the SSS sample at 1080°C still exhibits a bi-modal intensity distribution, indicative of much slower interdiffusion and homogenization rates in the solid state. Also, at 1080°C the maximal C_S value (i.e., C_S = 100wt% Cu) allows diffraction over the broadest 2θ range. After 180 minutes all specimens likely contained no liquid based on DSC data - including the 1178°C specimen. Accordingly, the 1178°C diffraction pattern illustrates that a greater degree of homogenization within the solid phase has been achieved – primarily due to a low C_S value, smaller dissolved Ni particles, and increased diffusivity.

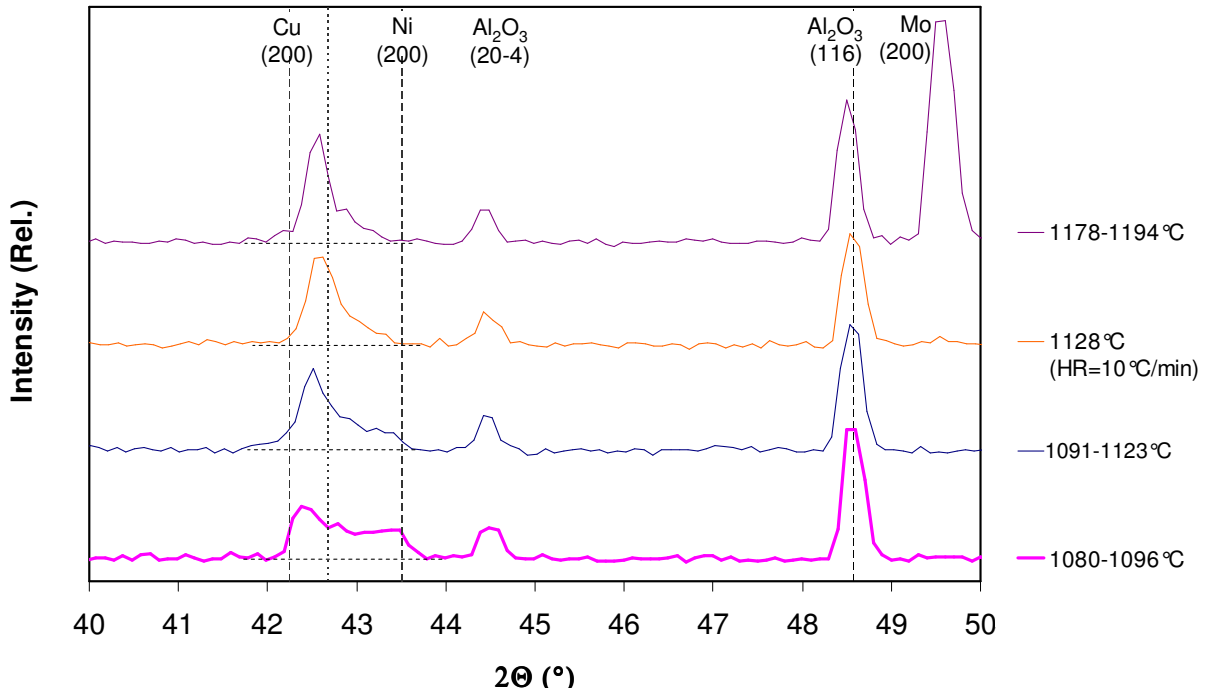

Figure 5-37: ND patterns collected 180 minutes after the melting event for Ni-56wt%Cu powder mixtures isothermally held at different process temperatures.

After 600 minutes (10 hours), all patterns indicate that fairly homogenous compositions were obtained within the sintered alloys (see Figure 5-38). The degree of homogenization appears to be greater at higher temperature due to the more refined alloy compositions and peak widths exhibited. The solid-state sintered specimen shows a relatively broad peak illustrating the slower interdiffusion process during SSS relative to TLPS.

The center of each peak is in good agreement with the predicted location for a 65wt% Cu alloy as per Equation (2-78), but the peaks still appear to be somewhat asymmetric. This in part is due to low neutron counts within the rapid 5-minute scans, but also due to remaining compositional gradients within the sample. The small Ni peak in the 1091°C profile indicates that there may still be a small amount of Ni-rich material at the particle cores. Conversely, the peak profile of the 1178-1194°C specimen is noticeably sharper than the other peaks, indicating a more homogeneous composition and a high degree of interdiffusion. Again, the increased homogeneity indicated by the sharper, less bi-modal, peaks at high temperatures is due to increased diffusivities and narrower compositional ranges (i.e., 0-C_S wt% Cu) from decreasing solid solubility.

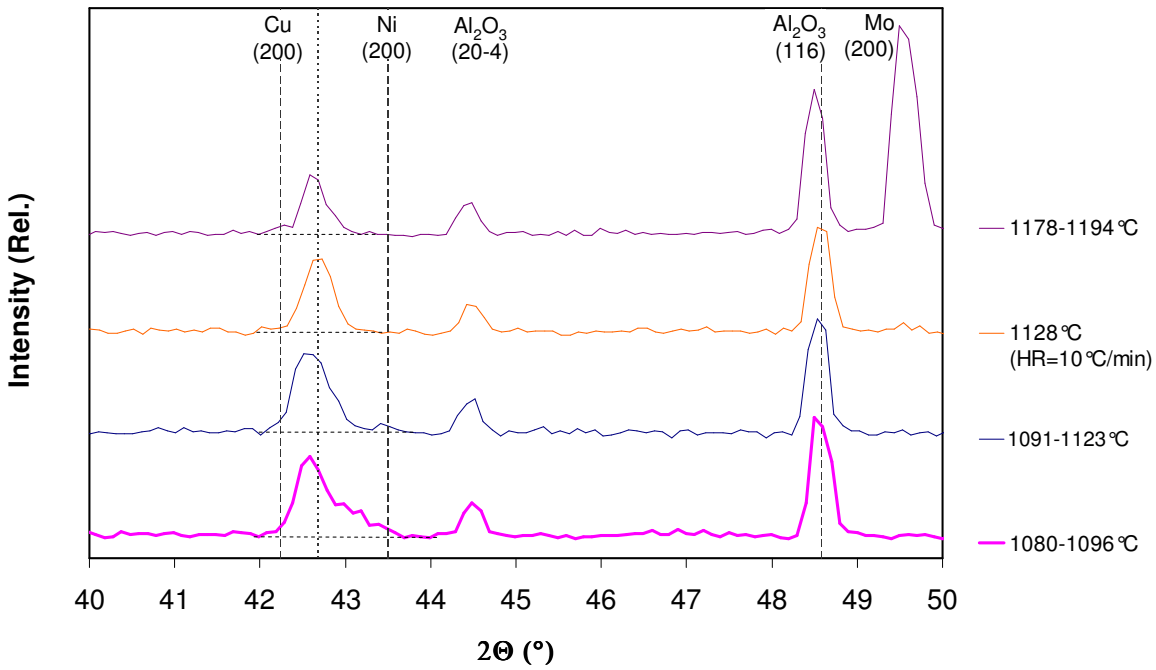

Figure 5-38: ND patterns collected 600 minutes after the melting event for Ni-56wt%Cu powder mixtures isothermally held at different process temperatures.

It is interesting to note that the total area of the 1178°C alloy peak appears to be somewhat lower than that of the other specimens. This may be due to a small amount of persistent liquid because of the proximity of the sample temperature to the solidus temperature for a 65wt% alloy (T_S ~ 1210°C). Unavoidable temperature gradients within the current C2 furnace configuration (see Section 5.1.2 and Section 5.1.3), may result in a portion of the specimen near the top of the crucible to be above the solidus and partially liquated.

Examination of the film plot for this specimen (Figure 5-22 and Figure 5-39) does not immediately indicate the freezing of a persistent Cu-rich liquid since no *additional* Cu peaks are visible upon cool-down. However, solidification of the liquid may be more subtle and occur at compositions along the shifting solidus line during cool-down - generating a typical cored structure [1]. This will cause the solidifying liquid to have compositional gradients (vs. a Cu-rich composition distinctly from the isothermally solidified solid).

If there was indeed some persistent liquid remaining at T_P, this cored solidification effect will cause the freezing liquid to simply broaden and intensify the pre-existing, isothermally-solidified/homogenized peaks during cool-down. This will therefore make the identification of persistent liquid freezing difficult. Close examination of the expanded cool-down region of

Figure 5-39 does indicate that the intensity and width of the isothermally alloyed (200) peak do increase after cool-down. Metallographic analysis (Section5.4) will provide additional information to assess liquid persistence and density.

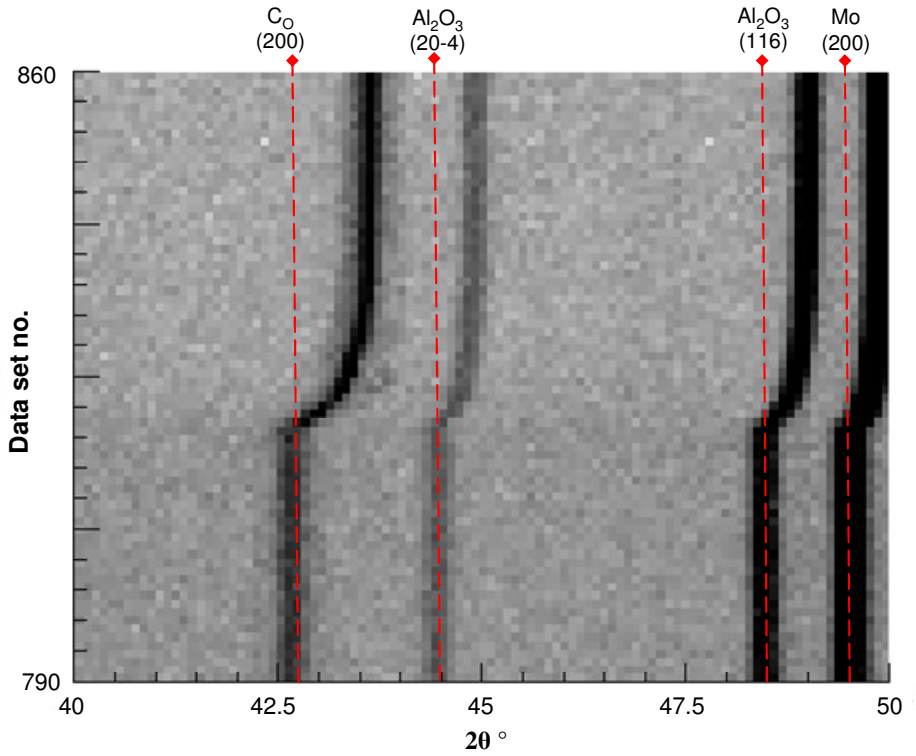

Figure 5-39: Film plot of *in situ* diffraction pattern evolution collected at 1 minute intervals near the end of TLPS and during cool-down of Sample 9.

5.4. Metallographic Analysis

Figure 5-40 to Figure 5-44 show mosaic images of entire specimens that were each assembled from multiple SEM BSE micrographs. The left side of the sample corresponds to the top of the crucible and the right hand side of the sample corresponds to the region at the bottom (i.e., the coldest part of the crucible).

The solid-state sintered 1080°C specimen (Figure 5-40) shows good shape retention due to the absence of liquid during the process. Individual particles are still distinguishable at the bottom, or right hand side. The degree of consolidation is low and the sample is denser at the top. This density gradient is likely due to axial temperature gradients in the furnace – causing

enhanced densification at the top region of the sample, possibly from higher temperatures or a small liquid formation. This sample also contains a significant amount of fine pores additional to the interparticle areas. As observed in DSC specimens (Figure 4-12), these have formed due to unequal Ni and Cu diffusivities ($D_{Cu} > D_{Ni}$) as a significant degree of unbalanced interdiffusion accrues over the long hold period – referred to as Kirkendall effect porosity [43, 39, 45].

The next samples sintered at 1090°C and 1128°C (for 1040 and 900 minutes respectively) show increased consolidation levels in most areas due to the formation of a liquid phase; but large pores are visible. These large pores may be due to uneven liquid redistribution and trapped gasses as found in DSC specimens after melting. This may also be due to the initial powder distribution prior to sintering. However, the extensive porosity exhibited in Figure 5-40 to Figure 5-44 indicates that Kirkendall pore nucleation and excessive growth during these very long hold segments accounts for the significant pore formation observed. This is most apparent when comparing all samples sintered for long hold times (i.e., samples 4-7 and 9) to sample 8, which was sintered for only 30 minutes. This specimen shows that much less Kirkendall porosity had time to develop at this point.

The higher-temperature specimens in Figure 5-40 to Figure 5-44 appear to be relatively denser than specimens TLP sintered at 1080°C and 1090°C. For example, the sample sintered at 1194°C for 30 minutes shows the highest degree of densification due to the higher liquid fraction formed, as indicated by the poor shape retention. This liquid appears to have spread uniformly and consolidated the entire specimen. A small amount of trapped-gas porosity is visible. Kirkendall pores have not had sufficient time to form in this case since much lower degrees of interdiffusion have occurred relative to the other TLP specimens sintered for much longer times (720-1040 minutes). In comparison, sample 9, which was sintered at a similar temperature for a much longer time (720 minutes at 1178°C), shows increased porosity levels. This sample particularly shows the effects of increased temperature at the top of the sample due to increased density and poor shape retention from increased melting. This is consistent with the lower post-melt diffraction signals in the ND profile for this sample (Figure 5-38).

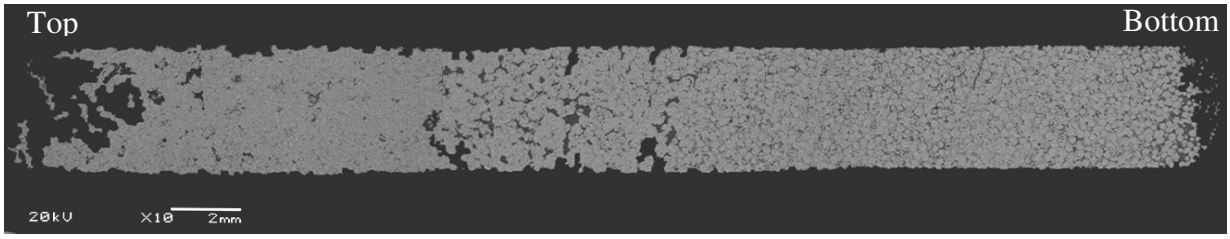

Figure 5-40: BSE micrograph of post-sintered sample 4 (630 minutes at 1080°C).

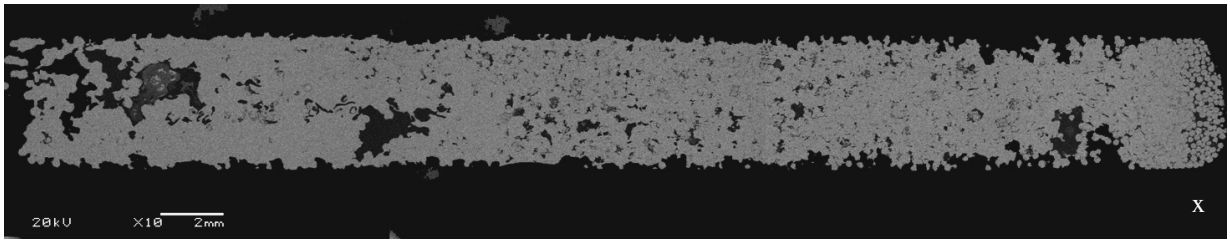

Figure 5-41: BSE micrograph of post-sintered sample 5 (1040 minutes at 1090°C).

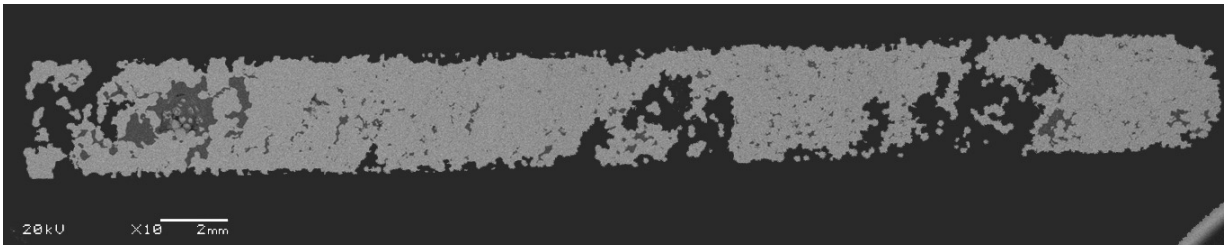

Figure 5-42: BSE micrograph of post-sintered sample 6 (900 minutes at 1128°C).

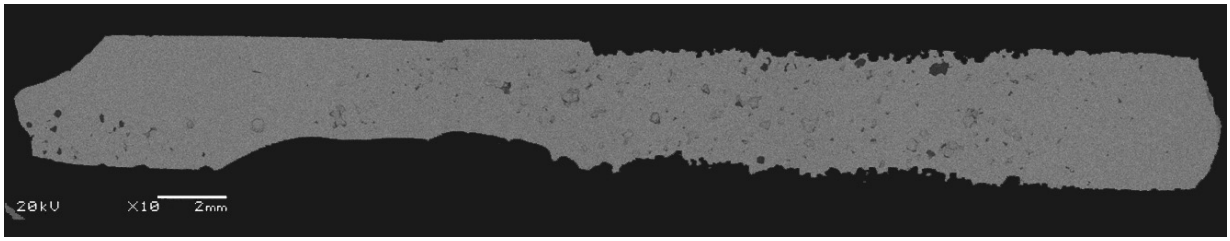

Figure 5-43: BSE micrograph of post-sintered sample 8 (30 minutes at 1194°C).

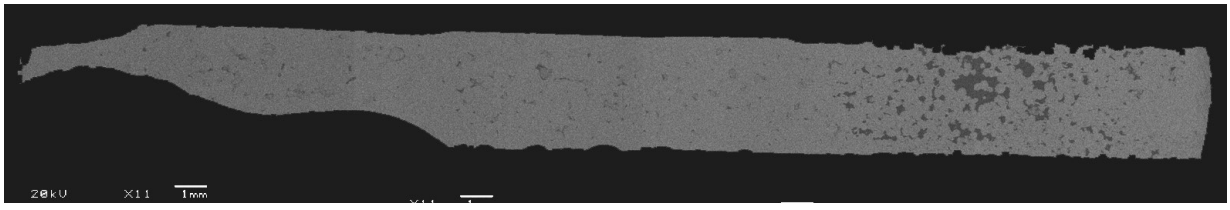

Figure 5-44: BSE micrograph of post-sintered sample 9 (720 minutes at 1178°C).

Figure 5-45 shows high magnification images of the top and bottom regions of sample 4 as well as EDS line scans (labeled for Ni and Cu) showing the compositional gradients present. These BSE images show moderate compositional contrast between the darker Ni-rich regions (labeled as '*a*') and lighter Cu-rich regions as well as a fine distribution of Kirkendall pores in the previous Cu-rich regions. The EDS lines cans more clearly show that the bottom region contains distinguishable Ni and Cu particles which exhibit a low degree of sintering and consolidation. As such, significant compositional gradients are shown by the line scans for Ni and Cu. The center of the Ni particle (point *a*) was found to consist of 19.33 wt% u whereas the peripheral Cu region (*b*) was found to be composed of 88.03 wt% Cu. This is consistent with the ND pattern for this sample (Figure 5-26), which still indicates a broad alloyed peak and a significant fraction of Cu-rich and Ni-rich material on either side of the bulk composition (65 wt% Cu).

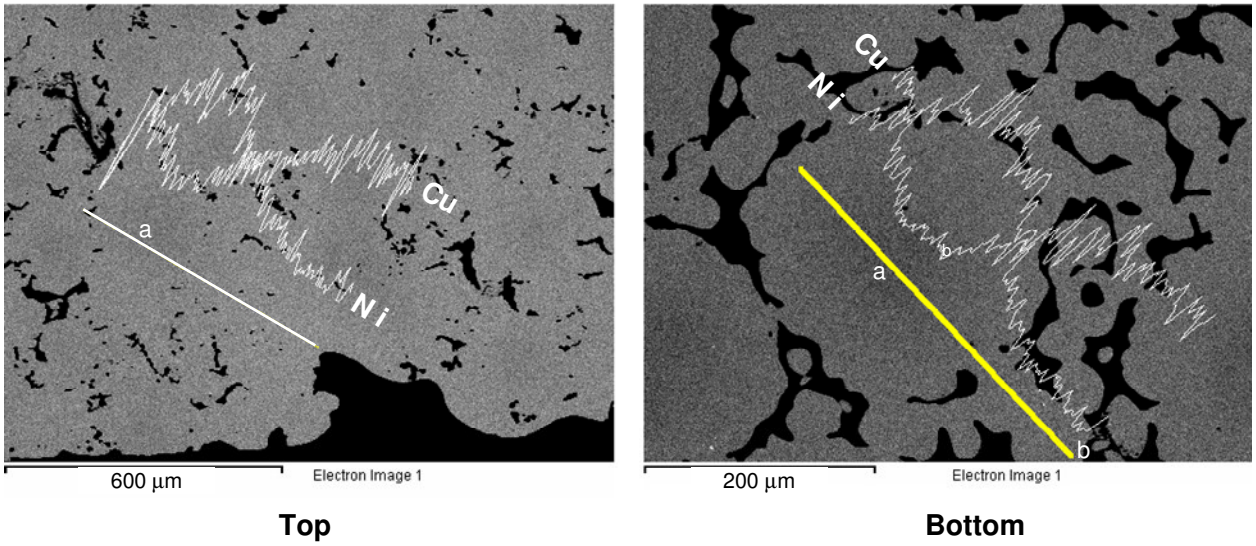

Figure 5-45: EDS line scans showing compositional gradients within the top and bottom regions of the solid-state sintered specimen (sample 4, 630 minutes at 1080°C).

EDS analysis of large regions (~ 4mmX6mm) more representative of the bulk sample at lower magnifications revealed that the bulk composition was 63.50 wt% Cu, which is reasonably close to the as-mixed Cu-Ni ratio (i.e., 65wt% Cu). A network of pores surrounding each Ni core is visible in the top micrograph. This is attributed to Kirkendall effect porosity, which has nucleated at the Ni-Cu necks where interdiffusion rates and the Ni-Cu mass-flux imbalance are greatest [39, 45].

The TLP sintered sample at 1090°C (sample 5 in Figure 5-41) was also found to have a bulk /average composition of 64.49 wt% Cu. However, in this case the presence of the liquid appears to have significantly increased the degree of interdiffusion and homogenization throughout the remainder of the specimen. EDS line scans for Ni and Cu in Figure 5-46 show small compositional gradients in the high magnification region where a remnant Ni particle is still visible. Compositions at *a* and *b* were found to be 62.43 wt% Cu and 66.95 wt% Cu respectively, indicating a high degree of interdiffusion.

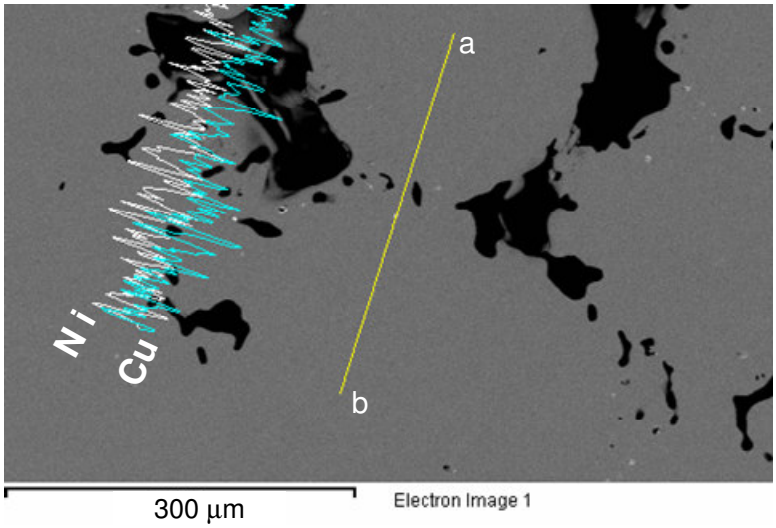

Figure 5-46: BSE image and EDS line scans showing compositional gradients within the bottom region of the TLP sintered specimen (sample 5, 1040 minutes at 1090°C).

Figure 5-47 shows low and high magnification BSE images for sample 8, which was sintered at 1194°C for only 30 minutes. Due to the short duration of the liquid and low degrees of interdiffusion, dark Ni particles are still distinguishable from the Cu matrix. EDS line scans show that very little Cu has penetrated to the Ni core and that the compositon of the liquid appears to be uniform. The Ni core (point *a*) was measured to consist of 100wt% Ni whereas the solidified liquid composition varied from 85.66-87.26 wt% Cu (across *b*). This large compositional divergence between the liquid and solid regions is in agreement with the very bi-model ND profile exhibited for this sample at the end of the isothermal sintering segment (Figure 5-29). The ND profile after 30 minutes at T_P indicates that there is still a significant pure Ni peak present and an even larger C_S peak that has grown due to isothermal solidification of the liquid phase, which is at C_L. This very bi-modal profile is maintained during cooling

down to 142°C, where the experiment and data collection was terminated abruptly due to a reactor power fluctuation (see Appendix A for details).

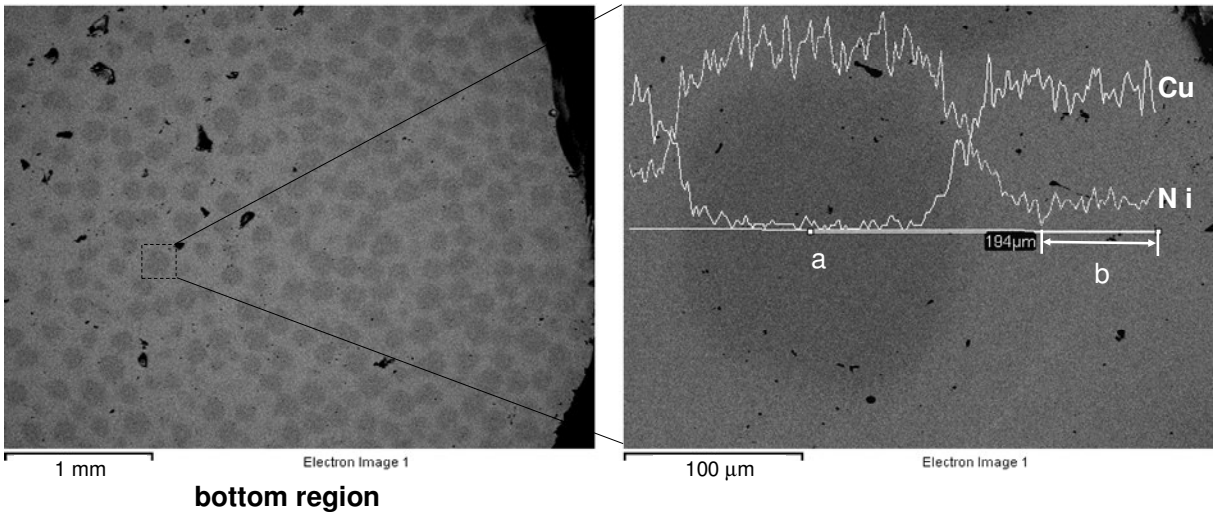

Figure 5-47: BSE image and EDS line scans showing compositional gradients within the bottom region of the TLP sintered specimen (sample 8, 30 minutes at 1194°C).

The BSE images for sample 9 (Figure 5-44, and Figure 5-48 below) show that Ni particles are no longer distinguishable after sintering for 720 minutes at similar elevated temperatures. The development of many Kirkendall-type pores surrounding previous Ni particles is apparent. An EDS line scan shows a fairly uniform Cu composition throughout this region near the bottom of the sample). Composition varied from 45.61-49.58wt% Cu from point *a* to *b* – indicating that this may be a region that initially contained an agglomeration of Ni particles. Other regions near the top of the specimen were found to also have uniform compositions, but ranging from 62.02-66.83 wt% Cu in this case. Again this indicates high levels of local homogenization from extensive interdiffusion, but some macroscopic segregation remains. This may be due to initial powder distribution inhomogeneity, liquid distribution inhomogeneity, and the axial temperature gradient along the sample, which affects solubility compositions (C_S andC_L).

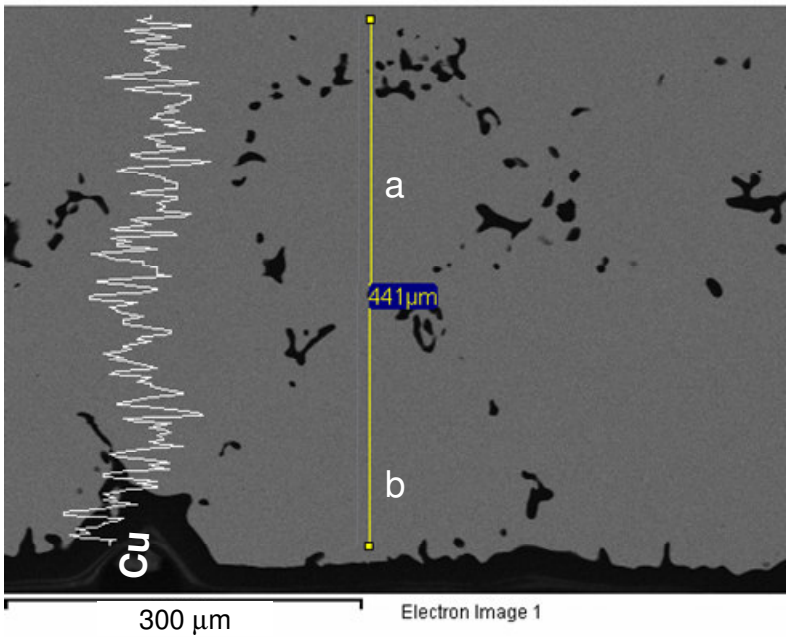

Figure 5-48: BSE image and EDS line scans showing compositional gradients within the bottom region of the TLP sintered specimen (sample 9, 720 minutes at 1178-1194°C).

5.5. Summary

The results show the ND technique is very useful for examining interdiffusion during sintering of larger powder mixtures *in situ*. The film plots and waterfall plots of the evolving ND patterns in the regions of the (200) FCC peaks for Ni and Cu clearly show that TLPS exhibits characteristic sintering behaviour that is easily distinguishable from that observed by Rudman during SSS XRD studies. The melting event in TLPS experiments is a particularly distinguishable characteristic. Also, post-melt peak evolution analysis served to identify the isothermal solidification mechanism. A gradual interdiffusion process was typically exhibited in all experiments such that the original Cu and Ni peaks eventually form a broad single peak, which refines during the isothermal stage due to homogenization. The evolution of ND patterns clearly distinguishes between the solid-state sintering and transient liquid phase sintering processes. In SSS, interdiffusion is much slower and the generation of a homogeneous alloy composition with a single peak at C_O is significantly delayed.

In comparison, the ND pattern evolution for TLPS samples heated above the melting point of Cu showed a clear melting event. Melting was characterized by the removal of pure Cu peaks, which leave behind solute rich peaks originating from alloy regions having

compositions near the solidus for the given T_P (C_S). After melting, the evolution of ND patterns clearly shows a rapid increase in C_S peak intensity, confirming that the isothermal solidification process occurs by the growth of solute-rich regions at C_S. This further supports *ex situ* metallographic evidence obtained from SEM/EDS analysis of DSC samples, which showed that isothermal solidification left behind a solute-rich layer (having compositions near C_S) surrounding the original Ni particle.

As the isothermal processing temperature was increased in the ND experiments, the location of the isothermally solidifying C_S peaks was shifted to higher 2θ angles (vs. lower angles due to thermal expansion), thus indicating lower Cu compositions. This was coincident with the C_S variation expected from the Ni-Cu phase diagram, further confirming the identity of the phase that is isothermally solidifying and which is responsible for the liquid removal rates quantified by DSC.

Temperature gradients within the C2 diffractometer furnace reinforced the importance of using the Al_2O_3 peaks (originating for the corundum sample crucibles) as an inert temperature reference. The measured gradients, which are due to the thermocouple sensor locations as well as actual temperature gradients within the furnace, indicate sample temperature variations of $\leq$ 50°C within the canister. The temperatures calculated from the Al_2O_3 peaks are considered to provide a better estimate of the actual mean sample temperature due to the sample/crucible proximity and since thermal expansion data were more reliable and in closer agreement with thermocouple data at the stabilized temperatures of interest (i.e., T_P). However, future work should investigate placing a temperature sensor within the sample environment/crucible itself as well as revising the furnace design to attempt to reduce temperature gradients.

Also, an investigation of other available neutron facilities with higher neutron fluxes should be considered to determine if higher signal strengths can achieve improved time/temperature resolution. ND profiles with greater neutron counts and less noise (i.e., a greater signal/noise or peak/background ratios) would also facilitate a more detailed quantitative analysis of *in situ* data using programs like GSAS. However, special consideration is necessary for the very broad diffraction profiles that develop from the single-phase alloy region that isothermally solidifies containing significant compositional gradients.

Metallographic analysis of the ND samples showed that all samples held for long isothermal sintering times to near full homogenization showed significant levels of Kirkendall porosity. In comparison, the sample held near 1200°C for only 30 minutes showed significant levels of consolidation and very little Kirkendall effect porosity. These results indicate that, from a practical brazing perspective, the Ni-Cu filler metal should only be held at T_P long enough to cause complete liquid removal. Otherwise, the effects of the developing Kirkendall pore structure will negatively affect mechanical properties. Therefore, the determination of the isothermal solidification time from quantitative experimental data or an appropriate TLPS model becomes even more important is the case of isomorphous systems susceptible to the Kirkendall effect.

6. TLPS Modelling in Isomorphous Systems

Since Corbin's simplified analytical model was developed specifically for TLPS problems and showed good agreement with low temperature eutectic powder systems, it will be used as a basis for developing a TLPS model for high temperature binary isomorphous systems. Ni-Cu DSC results presented in Section 4 for loose/mixed (type B) Cu-Ni powder mixtures will be used for comparisons to the developed model. This sample type best approximates the uniform powder distribution condition assumed in concentric sphere models. The inhomogeneous powder distributions in the layered/pressed (type A) DSC specimens are not as suitable for model comparisons, which assume uniform concentric sphere distributions.

The numerical models developed by Larrson and Karlsson [48,49] and Puckert *et al* [5], both assume concentric sphere geometry and share some similarities with Corbin's model. However, predictions are not directly relevant to this liquid-rich TLPS problem since transient liquid fractions are not predicted. Puckert's model predicts solute profiles that are used to determine the location of melting. The predicted melt formations are in the form of small, inter-particle liquid bridges, which deviate from the uniform concentric-sphere model that is applicable in this study. Also, the effects of solid-state interdiffusion during heat-up and dissolution on the melting event itself are not considered. Further development and coupling of Larrson and Karlsson's one-phase [48] and two-phase [49] concentric sphere models could provide numerical solutions for interdiffusion during heat-up and isothermal solidification for $T_P > T_A$. The ease by which concentration-dependence can be incorporated for each element along concentration profiles is a significant benefit. However, the transition from a one-phase diffusion problem to a two-phase problem after melting would have to be carefully considered (i.e., numerically modelling liquid melting/formation, dissolution, and re-solidification).

The numerical models by Puckert *et al* and Larsson and Karlsson will be referred to in this work due to some of the similar assumptions and initial conditions used. However, the development of a numerical scheme is outside the scope of the current study. Since Corbin's analytical model was developed specifically for liquid-rich TLPS problems and showed good agreement with low temperature eutectic powder systems, it will be used as a basis for

developing a TLPS model for high temperature binary isomorphous systems. The applicability of this simple, diffusion-based analytical approach will be evaluated relative to the quantitative DSC data obtained experimentally.

6.1. Limitations and Implications of the Simplified Model

Corbin's modelling technique does not account for the effects of solid-state interdiffusion during the heating stage since Equation (2-26) implies that no solute is present in the base metal particles at the beginning of isothermal solidification. In high-solubility systems such as Ni-Cu, where these effects are significant [2,11], this assumption will cause overestimations of the initial liquid fraction formed and overestimated solidification times to remove this liquid. Also, this will cause an overestimation of the rates of isothermal solidification because base metal particles are assumed to have no solute content at hold time $t = 0$. This also implies that the base metal particles are smaller than if solid-state sintering had taken place. Realistically, in systems exhibiting significant solid-solubility, solid-state sintering will cause a certain degree of base metal solute saturation prior to the isothermal solidification stage and this will tend to decrease diffusion kinetics.

Base metal dissolution for cases when $T_P > T_A$ is also not accounted for in the prior model since predictions are restricted to the melting point of the eutectic additive powder (i.e., $T_P = T_A = T_E$). This will cause an underestimation of the initial liquid fraction and an overestimation of the base metal particle size during isothermal solidification – both having significant effects on isothermal solidification kinetics. Therefore, isothermal solidification kinetics predictions using this model are not applicable for cases where both constituents exhibit high solubility and when the processing temperature exceeds T_A.

6.2. Model Development

It was determined to not use the negligible solid-state interdiffusion assumption used in the simplified model (Equation (2-26)) since it has been shown in the previous two chapters that high solubility systems such as Cu-Ni interdiffuse significantly during heat-up. Thus the governing equation for isothermal solidification kinetics becomes:

$$W_A = \left(C_O - (M_t/M_f)C_S\right)/C_L \quad \textbf{(6-1)}$$

As a result, this equation is not normalized by the initial liquid fraction, W_{Ao}, and will predict the actual liquid fraction present at a given isothermal hold time. However, a method for predicting the influence of solid-state interdiffusion on the initial liquid fraction at a hold time $t = 0$ must be developed. As will be discussed, the effects of solid-sate interdiffusion during the heat-up segment can be accounted for by considering non-zero M_t/M_f values at the onset of melting (i.e., some solute uptake exists at the start of the isothermal stage). Solute uptake and concentration profiles will be calculated using Crank's solutions to Fick's second law as per Equations (2-19) and (2-23).

Equation (6-1) now accounts for the changing maximum solute solubility (C_L) within the liquid at different temperatures. Consequently, the decreasing C_L value at increasing temperatures $T_p > T_A$ will cause increases in W_A and account for some B particle dissolution and dilution of the increased liquid phase A. The other resultant effects of dissolution (i.e., decreased base metal particle size and solute uptake reduction) will be considered in a later section. Table 6-1 lists a summary of input and modelled parameters that will be discussed in more detail below.

The concentric sphere model used to describe Corbin's model (Figure 2-13) is still used as the basic unit cell for predictions in the current model. The additive phase (A) is assumed to uniformly surround the base metal (B) particles and the initial phase fraction of A is given by the bulk solute composition of the mixture (C_O, in wt% A). The detailed evolution of this unit cell as observed from metallographic analysis of Ni-Cu TLPS specimens is better understood in reference to Figure 6-1. In this figure, the evolution of concentration profiles and phase fractions is better illustrated from: a) the starting powders, b) solid-state interdiffusion during heat-up ($T < T_A$), melting, and isothermal solidification at c) T_A or d) $T_P > T_A$.

Table 6-1: List of parameters and nomenclature

Input parameters	Description	Values used
D_{ol}, Q_l	lattice diffusion parameters	D_{ol} = 5.7E-05 m^2/s[1] Q_l = 258300 J/mol[1]
D_{ob}, Q_b	boundary diffusion parameters	D_{ob} = 1.1E-04 m^2/s[51] Q_b = 124700 J/mol[51]
$\widetilde{D}$	concentration-dependent lattice interdiffusion parameter	composition dep. (from [50])
d	base metal particle grain size	meas.experimentally (6.4-9.5μm)
δ	effective grain boundary width	0.5 nm[31]
T_P	isothermal processing temperature	1085, 1140, 1200°C
a_{Bi}	initial base metal particle size (avg. radius)	3.4-80.5 μm
C_O	powder mixture solute content	65 wt% solute
C_L	solute solubility in liquid at Tp	ref. phase diagram
C_S	solute solubility in solid particle at Tp	ref. phase diagram
R_h	heating rate during heat-up segment	1-200°C/min.
t_o	heat-up segment time up to T_A	= $(T_A-T_{room})/R_h$

Modeled Parameters	Description
M_t/M_f	fractional solute uptake by base metal at t
W_{Ao}	initial liquid fraction of A formed at melt onset (t = 0)
W_A	liquid fraction of A present at t
a_B	base metal B particle size at t
t_{ss}	equivalent iso. segment time required to absorb M_{ss}/M_f solute uptake during heat-up segment
t_c	time required for complete isothermal solidification of the liquid phase

As metallographic results of this study indicate (Section 4.1.3), the concentric sphere model is a good representation of the solid/liquid couple and a reasonable representation of the solid/solid couple during the heat-up segment. While it is a simplification of the 3-D geometry of the contact between additive and base metal particles, other studies [5,44,84] have indicated that surface diffusion is rapid enough that a continuous layer and supply of solute from the additive phase develops around the base metal powder very early in the sintering process. For these reasons

the unit cell of Figure 6-1*a* is considered to be a reasonable representation of the interdiffusion stage particularly for the case where the A powder comprises a significant fraction of the mixture and is smaller in size than the B phase. In this case the A phase forms a matrix in which the B particles are suspended. In addition, this unit cell greatly simplifies the complex powder mixture geometry. Accordingly, the concentric sphere model is adopted by most modelling studies for SSS and LPS of powders [5,25,48,49].

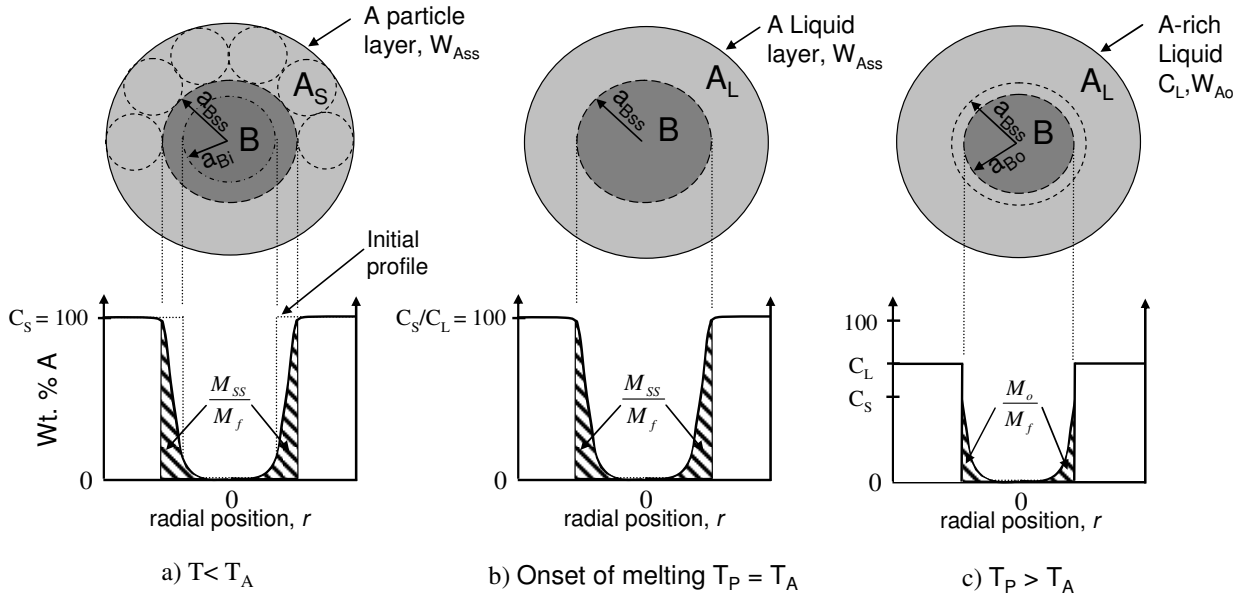

Figure 6-1: Unit cells showing particle size and solute distribution at different times- note nomenclature regions for W_A and a_B at key points in the sintering process: a) completion of the solid state interdiffusion/sintering process b) initial melting and isothermal solidification at $T_P = T_A$ (i.e., with no dissolution), and c) including dissolution due to heating above T_A.

Figure 6-1*b* and Figure 6-1*c* illustrate the initial conditions of the isothermal stage modelled in the unit cell after melting at T_A and at $T_P > T_A$. Figure 6-2 illustrates a more detailed conceptual view of the solid/liquid interface during these different stages of the process to better understand the solute profile and particle size evolution.

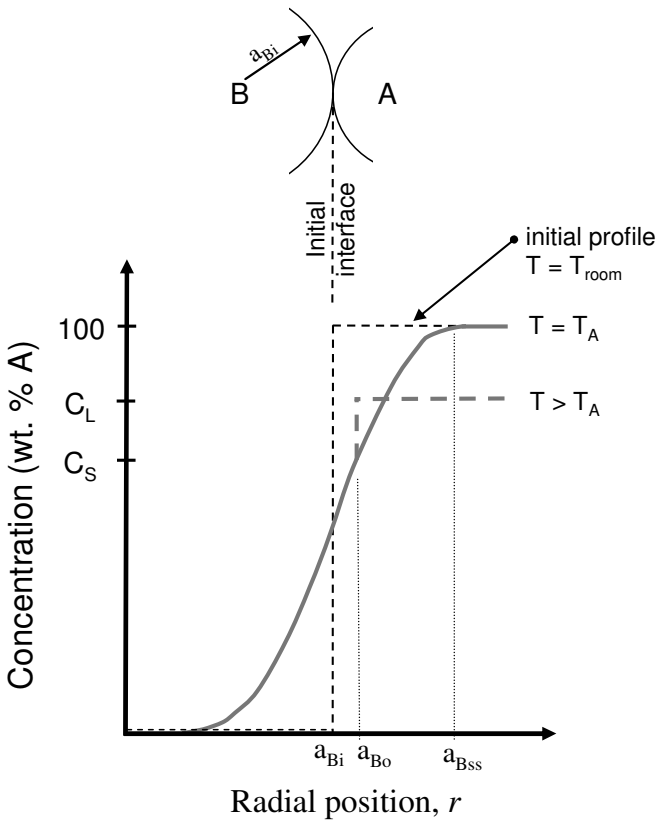

Figure 6-2: Simplified schematic of the solid/liquid A/B interface during solid-state interdiffusion and dissolution processes.

Figure 6-2 shows a B/A diffusion couple at the initial interface of two contacting particles for the case of an isomorphous system. The initial base metal particle size of the starting B powder is given by a_{Bi} and marks the location of the original interface formed prior to heating and interdiffusion. Initially, a square solute profile exists that consists of pure B and pure A (represented by the broken line). The typical solute compositional profile that develops in the solid-state during heat-up to T_A is shown by the solid black curve. Once T_A is reached, pure A, un-alloyed regions (i.e., 100wt% A) will melt. The newly formed solid/liquid interface (represented by the vertical dotted line) now separates the A and B phases at a radial position of $r = a_{Bss}$. At T_A, only pure A will melt to the right of the interface $(r \geq a_{Bss})$. Consequently, solid-state interdiffusion up to T_A results in an effective solid particle size increase as well as a decrease in the initial liquid fraction formed to a value of $W_{Ass} < C_O$, where C_O is the initial weight fraction of additive powder and therefore the amount of liquid formed in the absence of interdiffusion. If T_P increases further past T_A, a gradual dissolution of the B phase takes place since B solubility in the liquid phase increases (or A solubility C_L decreases) with increasing

T_P. This is accompanied by the melt-back of non-equilibrium A-rich regions along the solute profile that have solute contents greater than C_S (dashed grey curve past $r \geq a_{Bo}$). Rapid diffusion of B in the liquid generates a uniform composition distribution within this phase. This dissolution process causes an increase in the liquid fraction formed to a value of $W_{Ao} > W_{Ass}$ and a concomitant regression of the solid/liquid interface, causing the solid particle radius to decrease to a_{Bo}.

The liquid fraction and particle size after solid-state interdiffusion during heat-up (W_{Ass} and a_{Bss} respectively*)* must be determined to account for solid-state interdiffusion and provide accurate initial conditions for the isothermal solidification stage if it takes place at T_A. In addition, values W_{Ao} and a_{Bo} must be determined to further account for dissolution following solid-state sintering and to provide accurate initial conditions for the isothermal solidification stage if it takes place at a process temperature $T_P > T_A$. Table 6-2 lists these variables as they evolve immediately following the melting event. In a case where no dissolution takes place (i.e., isothermal solidification occurs at $T_P = T_A$*),* then $W_{Ao} = W_{Ass}$, and $a_{Bo} = a_{Bss}$. Solute uptake terms from Table 6-2 (M_{ss}/M_f and M_o/M_f*)* will be defined below.

Table 6-2: Values of model parameters following solid-state sintering and dissolution

time	Processing temperature (T_P)	Solute uptake by B particles (M_t/M_f)	Liquid fraction formed (W_A)	B particle size (a_B)
SS sintering complete (onset of melting)	T_A	M_{ss}/M_f	W_{Ass}	a_{Bss}
Dissolution complete (iso. solidification start)	$T > T_A$	M_o/M_f $= X_r(M_{ss}/M_f)$	W_{Ao}	a_{Bo}

6.3. Solid-state interdiffusion

The heating rate used in the heat-up stage (R_H), the original B particle size (a_{Bi}*)*, and the diffusivities (D) of the constituents will influence the gradient of the solute profile obtained and the extent of interdiffusion during solid state sintering. This will influence the degree of solid particle growth and liquid phase reduction from solid-state interdiffusion. Heating past T_A will counteract these effects by dissolution and melt-back of the B particles. The degree of dissolution is primarily determined by T_P and R_H. The interdiffusion and dissolution process

described in Figure 6-2 will occur at every A-B contact point throughout the 3-D powder mixture.

Below the melting point of pure A, we are interested primarily in how much of the additive phase remains in pure form, (i.e., 100 % solute) since this will determine how much liquid is initially formed at T_A. Consequently, prior to melting $C_A = C_L = 1$ and Equation (2-24) simplifies to give;

$$W_{Ass} = C_O - [C_B W_B]_{ss} \tag{6-2}$$

where the initial liquid fraction formed W_{Ass} is equal to the initial amount of pure A added to the system (i.e., C_O) minus the amount of solute A taken up by the base metal particle B (i.e., $[C_B W_B]_{ss}$) due to solid-state interdiffusion during the heating stage. This equation can be used to predict the weight fraction of liquid that will form initially at T_A as a result of solid-state interdiffusion, providing an expression for $[C_B W_B]_{ss}$ can be developed.

Crank's analytical solution of Fick's second law of diffusion for spherical particle and constant diffusivity under the conditions shown in Figure 6-1*a* can be used to determine the solute profile developed during the heat-up segment (Equation (2-19)) and solute uptake within the spherical particle M_t/M_f (Equation (2-23)). Figure 6-1*a* and Figure 6-1*b* depict the unit cell geometry and applicable solute profiles that develop in a Crank solution. In this case the particle is considered to be defined by a region where $0 < C_B < 1$ and the surface concentration of the particle is fixed at $C_S = C_A = 1$. Inherent in the assumption of a constant $C_S = 1$ is that there is an unlimited supply of additive phase A, which is suitable for large A weight fractions and fast heating rates.

Fractional solute uptake due to solid-state interdiffusion can then be expressed as follows to obtain $[C_B W_B]_{ss}$:

$$M_{ss} / M_f = [C_B W_B]_{ss} / [C_B W_B]_f \tag{6-3}$$

where C_{Bf} is the average final composition of phase B at $t = \infty$, W_{Bf} is the weight fraction of phase B at $t = \infty$, and $C_{Bf}W_{Bf}$ is the solute content of phase B at $t = \infty$. In the Crank solution, $t = \infty$ corresponds to the time where the spherical particle is completely saturated with solute. In a TLPS problem, Crank's solution is truncated at the point in time where, finally, all the solute available has been taken up and only the base metal phase remains (i.e., $W_{Bf} = 1$). Only when $C_O =$

C_S will the full solution for M_t/M_f be used in the isothermal solidification solution. For the case of the solid-state interdiffusion problem illustrated in Figure 6-1*a*, $C_S = C_{Bf} = 1$, $W_{Bf} = 1$ and substitution of Equation (6) into (3) gives;

$$W_{Ass} = C_O - M_{ss}/M_f \tag{6-4}$$

As predicted by mass conservation arguments and as shown in Figure 6-1 and Figure 6-2, solute uptake by the base metal particle is accompanied by a gradual particle growth (i.e., assuming that the particle is defined by the region where $C_s < 1$). Corbin's previous study [25] has indicated that, for short times and small solute uptakes during rapid heating, accounting for particle growth has only a small effect on model predictions. Therefore a fixed, initial particle size was assumed for the solid-state sintering/interdiffusion calculation in the current study. A stepwise solution technique was not employed for this short heat-up segment.

It was decided to approximate the heat-up segment by representing this stage with an equivalent isothermal stage (one where the average diffusivity was effectively the same), since Crank's equations are for isothermal conditions. A similar approach has been used by Puckert *et al* to account for the temperature dependence of D in discrete stages [5]. The average diffusivity of an equivalent isothermal heating stage can be obtained by calculating the arithmetic average of the apparent diffusivity, $\bar{D}_{app}$, during heating from room temperature (T_O) to T_A;

$$\bar{D}_{app} = \frac{\int_{T_o}^{T_A} D_{app}(T)\,dT}{(T_A - T_o)}$$

$$\text{or,} \quad \bar{D}_{app} = \frac{\int_{T_o}^{T_A} \left(D_l(T) + \frac{\delta}{d} D_b(T)\right) dT}{(T_A - T_o)} \tag{6-5}$$

Where D_l and D_b are lattice and grain boundary diffusion coefficients in the effective, or apparent diffusivity (D_{app}) (see Section 2.9). The contribution of the grain boundaries, which have thickness δ [31], to the interdiffusion process is determined by the particle grain size d, which can be measured microscopically and controls the amount of grain boundary diffusion pathways within the powder. This approach of using an apparent, diffusivity (D_{app}) is commonly used to account for complex grain boundary contributions in analytical models

[11,31,53]. This approach will be elaborated upon with respect to isothermal solidification predictions in Section 6.6.1. Using the average apparent diffusivity for the heat-up segment, $\bar{D}_{app}$, solid-state interdiffusion was accounted for by Crank's solution for solute uptake under the conditions of the unit cell shown in Figure 6-1*a*. Figure 6-1*b* illustrates the concentration profile developed in the particle at the end of the heating stage, when T_A is reached and pure A regions have melted. Solute uptake from solid-state sintering (M_{ss}/M_f) was then calculated using (Equation (2-23)). The time allowed for solute uptake during heat-up in stage I, t_o, is determined by the heating rate used (R_H) and T_A. When the powder mixture reaches T_A, melting of the pure A regions will take place and the amount of liquid formed as a result of solid-state diffusion (i.e., W_{Ass} in Figure 6-1*b*) can be determined by substituting the value for M_{ss}/M_f in Equation (6-4).

Once this liquid forms, subsequent isothermal solidification predictions at $T_P = T_A$ (i.e., without dissolution) require: 1) the new particle size at T_A, and 2) a method capable of taking into account the gradual particle growth during isothermal solidification. This is because the isothermal stage lasts much longer than the heating stage, involves significant solute uptake by the base metal, and therefore significant changes in particle size. In this work we adopted a previous approach [25], which developed an expression for particle growth based on solute mass conservation between the solid and liquid phases (i.e., in the current case between the pure A and B phases at T_A). This expression takes the following form;

$$a_{Bss} = a_{Bi}\left(W_{Bss}/W_{Bi}\right)^{\frac{1}{3}}$$
$$\text{or, } a_{Bss} = a_{Bi}\left[\left(1-W_{Ass}\right)\Big/\left(1-C_O\right)\right]^{\frac{1}{3}} \qquad \textbf{(6-6)}$$

where a_{Bi} and W_{Bi} and a_{Bss} and W_{Bss} are the base metal particle size and weight fraction initially and after heating to T_A respectively. The mean value of a_{Bi} can be measured in the as-received powders and W_{Bi} is simply the weight fraction of B powder in the initial bulk powder mixture, which is given by (1- C_O). Substituting these values into Equation (6-6) gives the new particle size after initial heating to T_A (i.e., a_{Bss}) from knowledge of W_{Ass} calculated from Equation (6-4).

The effects of particle size on the initial liquid fraction formed and processing times required for complete isothermal solidification are important attributes from a brazing

perspective [2]. These effects can be studied with the current analytical model. Predictions from Equation (6-4) and (6-6) for W_{Ass} and a_{Bss} are plotted in Figure 6-3 as a function of the initial base metal particle size. Growth from a_{Bi} to a_{Bss} is expressed as normalized volumetric growth, $(a_{Bss}{}^3 - a_{Bi}{}^3)/a_{Bi}{}^3$. For ease of interpretation the parameters used in this calculation were based on the Cu-Ni system, however the model is applicable to any binary isomorphous system. Model input values are listed in Table 6-2 as well as in the figure captions. The value of $\bar{D}_{app}$ given in the caption of Figure 6-3 was determined from Equation (6-5), where D_l includes a grain boundary diffusion contribution within a dilute Ni alloy. Section 6.6.1 will elaborate on diffusivity effects.

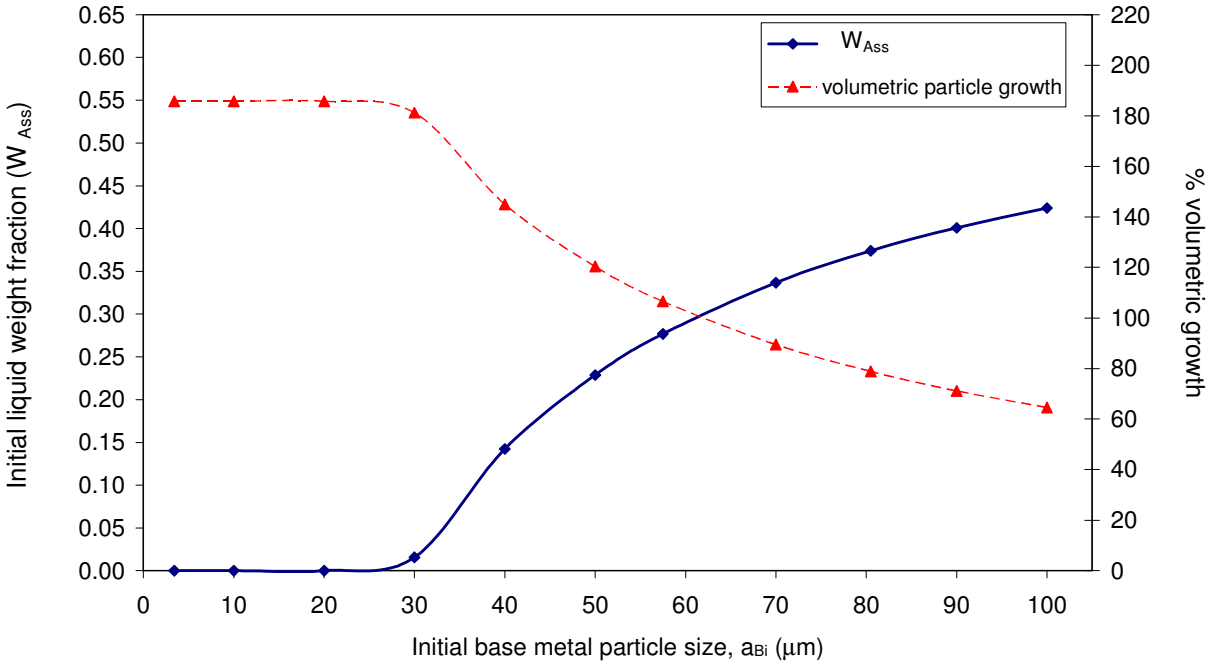

Figure 6-3: Predictions of initial liquid formations and volumetric growth of various initial base metal particle sizes (a_{Bi}). Conditions: R_H = 40°/min., $T_P = T_A$ = 1085°C, C_O = 65wt%Cu, $\bar{D}_{app}$ = 4.7671x10^{-14}m^2/s

These predictions show that smaller base metal particle sizes undergo greater volumetric expansion as a result of solid-state sintering during heat-up. This generates smaller initial liquid formations at T_A. It is worth noting that under these conditions, particle sizes less than approximately 30 µm cause complete removal of the 100 wt% A regions due to extensive solid-state interdiffusion. This is indicated by the prediction of no liquid formation, which

makes TLPS impossible and would lead to poor densification in the powder compact during sintering. This prediction is consistent with experimental DSC results shown in Figure 4-17. For Cu-Ni powder mixtures with 65 wt% Cu, effectively no liquid was formed for a Ni particle size of 3.4 μm, while some liquid was formed for particle sizes of 57.5 μm. This prediction technique, which assumes complete B coverage by A in the heat-up segment via the concentric sphere model, likely causes some overestimation of coverage/interparticle contact and interdiffusion between the powders, especially at low temperatures, thus causing predictions tending to overestimate M_{ss}/M_f and underestimate W_{Ass}. Relaxation of the full coverage assumption implied by the concentric sphere model may be achieved by limiting the predicted interparticle contact prior to melting via a fractional contact factor, which could be inserted into Equation (2-23). This factor would assume values from 0 to 1 for scenarios of no contact and full B particle coverage by A respectively, thus reducing M_{ss}/M_f uptake during this stage. At this point this modification does not appear necessary.

In all cases where $a_{Bi} < 30$ μm in Figure 6-3, similar volumetric expansions are shown. This is due to the fact that, as shown in Equation (6-6), when W_{Ass} approaches zero all of the solute is taken up by the base metal powder. In the limit, each particle will grow in volume representing a constant value due to complete uptake of the solute available (i.e., $a_{Bss}/a_{Bi} = [1/(1-C_O)]^{1/3}$).

Also of practical interest, is the effect of the heating rate (R_H) used to attain the desired processing temperature during stage I. Figure 6-4 shows model predictions that illustrate the relationship between W_{Ass} and R_H for different particle sizes. These predictions show that:

1. For a given initial particle size, faster heating rates generate greater initial liquid formations by reducing the time for solid-state interdiffusion.
2. At very high heating rates, many of the predictions become asymptotic to $W_{Ass} = C_O = 0.65$ as the effects/duration of solid-state interdiffusion become negligible.
3. Smaller particle sizes require higher heating rates to generate any liquid formation (i.e., $W_{Ass} > 0$). For example in the 30 μm prediction a $R_H > 40$°/min is required to form a liquid phase at T_A. The 3.4 μm prediction shows that heating rates in excess of 200° C/min. would be required to form liquid at 1085°C.

These predictions show that the model is capable of identifying the heating rate necessary to form a desired liquid fraction (or any liquid at all) for a given particle size and vice versa.

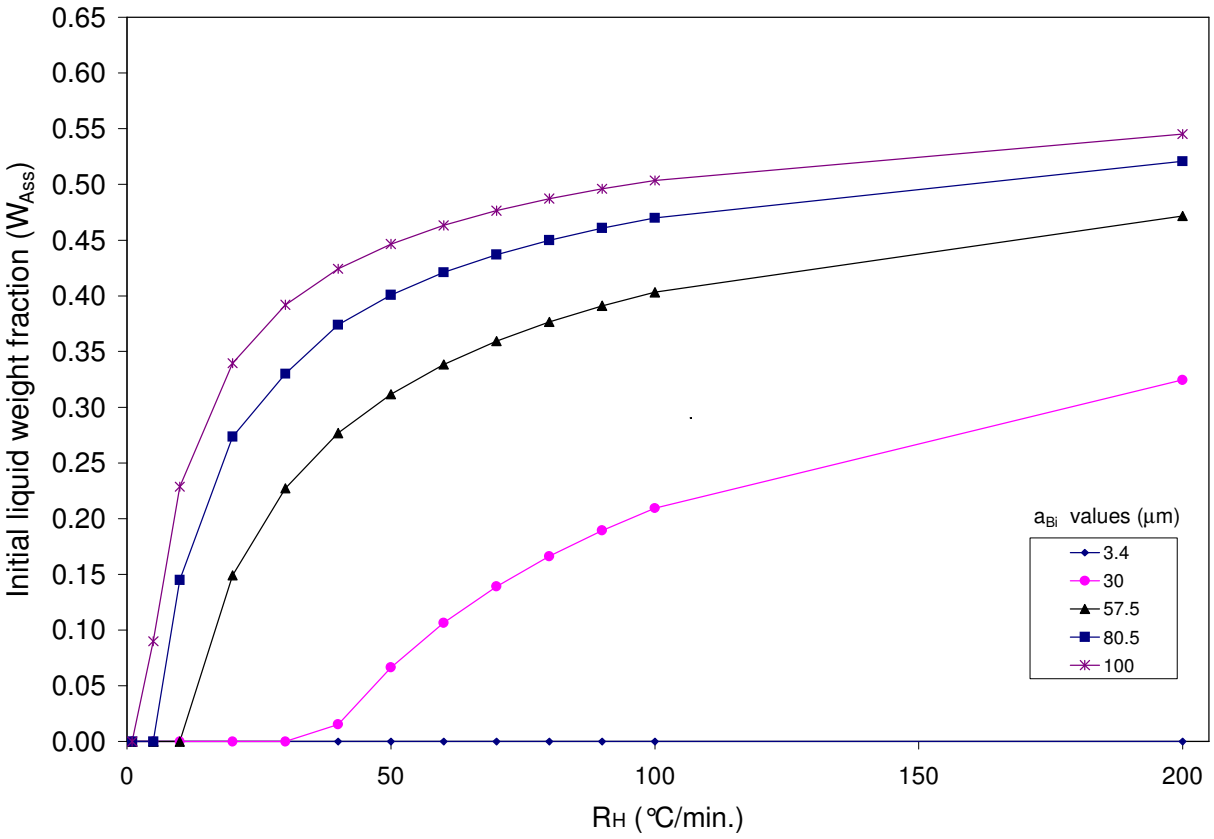

Figure 6-4: Predictions of initial liquid formations (W_{Ass}) for various particle sizes and heating rates during stage I (R_H). $T_P = T_A = 1085°C$, $C_O = 65wt\%Cu$, $\bar{D}_{app} = 4.7671x10^{-14}\ m^2/s$.

6.4. Isothermal Solidification Predictions at T_A

With the liquid fraction (W_{Ass}) and particle size (a_{Bss}) after the heat-up segment known, it is now possible to predict the rate of liquid removal by isothermal solidification at T_A. Again we adopt the approach previously used by Corbin [25], which calculates the liquid fraction present at increments of isothermal solidification time by a stepwise procedure where [M_t/M_f] is calculated by Equation (2-23) and W_A is now calculated by Equation (6-1). The particle size a_B is then updated by Equation (6-6) for the next calculation sequence after some incremental increase in time t. The stepwise solution technique used is shown in Figure 6-5. Initial

conditions used in this calculation are shown in the figure and represent the state immediately following heating to T_A.

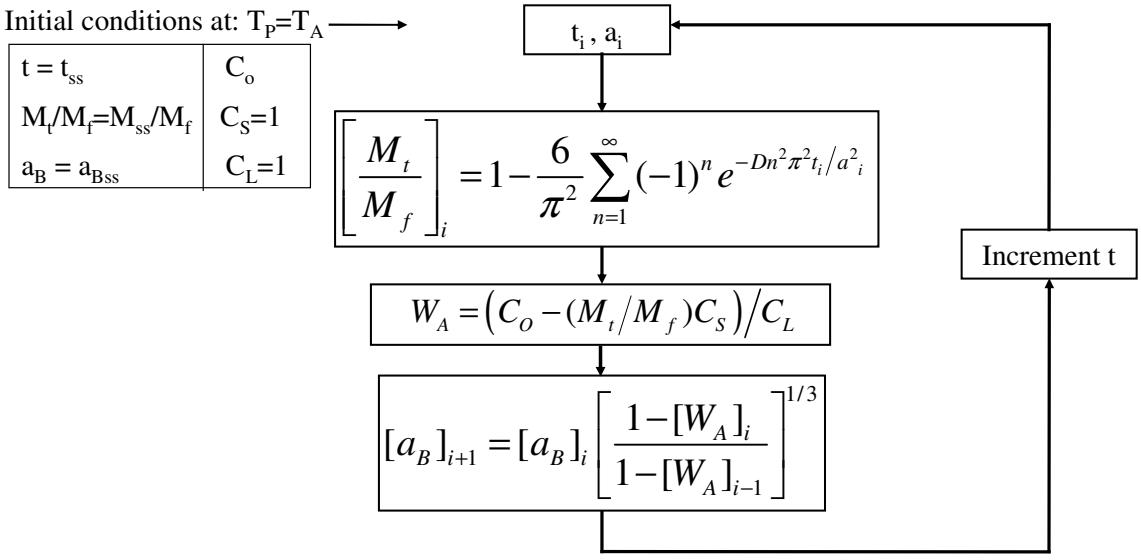

Figure 6-5: Stepwise solution technique for isothermal solidifications predictions at $T_P = T_A$.

In order to properly account for the solute uptake from the heating stage, the M_{ss}/M_f term cannot be simply inserted as a non-zero solute uptake initial condition in the stepwise solution at isothermal hold time $t = 0$. The solid curve in Figure 6-6 presents a typical solute uptake solution during the isothermal stage. Superimposing an amount of uptake at $t = 0$, say $M_{ss}/M_f = 0.4$ for example (as shown in Figure 6-6, point '*c'),* would artificially shift the M_t/M_f solution and cause solute uptake predictions to start at 0.4. This method will give the correct initial solute uptake at $t = 0$, but will overestimate the ensuing isothermal solidification rate (i.e., dashed curve '*c'* to '*d'*) since solute uptake will initially occur at the same rate regardless of prior pre-saturation. To properly account for the partial pre-saturation of the base metal particles due to M_{ss}/M_f, it is necessary to start the M_t/M_f solution at an equivalent time (i.e., t_{ss} or point '*a'* in Figure 6-6). This is equivalent to assuming that the solid-state solute uptake prior to t_{ss} occurred under the isothermal solidification conditions depicted in Figure 6-1*b*. In this case, the proper initial solute uptake is accounted for as well as the slower kinetics of isothermal solidification caused by the "pre-saturation" of the base metal particle due to solid-sate interdiffusion (i.e., curve "*a*" to "*b*).

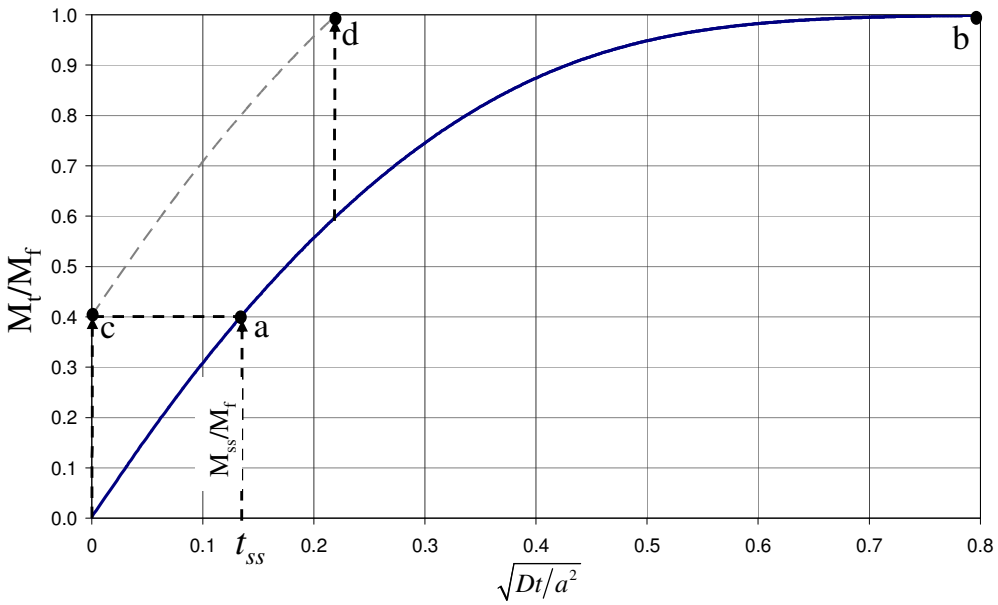

Figure 6-6: Fractional solute uptake (M_t/M_f) predictions of base metal particles during isothermal solidification.

The value of t_{ss} can be determined by solving Equation (2-23) for the time variable by using the known M_{ss}/M_f, and a_{Bss} values and the remaining parameters of the isothermal solidification stage. This approach essentially solves for the time it would have taken for the base metal particles to absorb M_{ss}/M_f of solute, which was absorbed during the heat-up stage, but under the conditions of the isothermal solidification stage at T_A. The remaining solute is then absorbed by solute uptake during the isothermal stage, which is determined by M_t/M_f solutions starting at t_{ss}. Thus, the M_t/M_f calculation must be started at t_{ss} for the beginning of the isothermal solidification stage as indicated in Figure 6-5. However, by convention predictions for the isothermal solidification of phase A will always be plotted starting at the beginning of the isothermal hold at T_P (i.e., hold time $t = 0$ once T_P is reached). The t_{ss} term is only relevant to the solute uptake solution to account for the non-zero M_t/M_f condition.

Figure 6-7 illustrates two isothermal solidification and particle growth predictions at $T_P = T_A$ for two situations; 1) where solid-state interdiffusion is neglected and, 2) where it is accounted for by the method above. The case neglecting solid-state interdiffusion ($M_{ss}/M_f = 0$) results in a larger initial liquid fraction that is equal to C_O and a smaller initial particles size, since no solute has been absorbed in the solid state prior to melting. These particles must therefore undergo a greater degree of growth to completely isothermally solidify the liquid. It

is important to note that accounting for interdiffusion leads to less rapid isothermal solidification kinetics (indicated by a shallower slope) compared to no interdiffusion. This is due to the fact that interdiffusion results in larger initial base metal particles that are pre-saturated with solute.

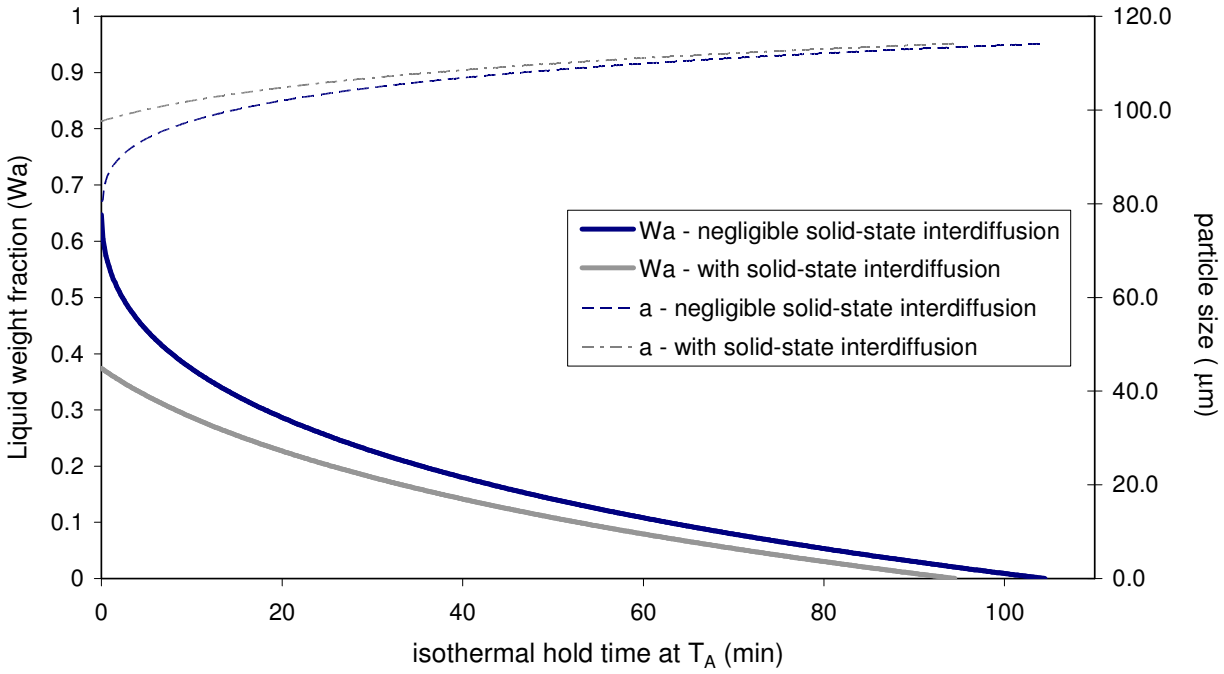

Figure 6-7: Solid-state interdiffusion effects on the rate of isothermal solidification for Cu-Ni powder mixtures under these conditions: R_H = 40°C/min., T_P = 1085°C, C_O = 65 wt% Cu, a_{Bi} = 80.5µm, D_{app} = 1.2517x10^{-13} m^2/s.

Despite slower kinetic conditions, the predictions including solid-state interdiffusion indicate a slightly shorter time required for complete isothermal solidification. This shorter, yet similar, solidification time in both cases was also noted by Larsson and Karlsson when comparing interdiffusion results from numerical models for a 1-phase (solid-solid) and 2-phase (solid/liquid) concentric sphere diffusion couples for an arbitrary alloy system [48,49]. This is due to a compromise between initial liquid fraction, particle size, and solute concentration profile (i.e., "pre-saturation) effects on predicted isothermal solidification kinetics in TLPS. The larger particles and shallower solute composition gradients created by solid-state interdiffusion result in slower solidification kinetics in the early stages of solidification. However, this is compensated for by the lower initial liquid fraction formed (W_{Ass}), which seems to be the dominant factor leading to shorter isothermal completion times.

Figure 6-8 shows the corresponding times required to complete the isothermal solidification of the liquid phase when taking into account solid state interdiffusion as a function of initial base metal particle size. These predictions clearly indicate that smaller a_{Bi} values generate smaller initial liquid formations (W_{Ass}), which thus require less time for removal by isothermal solidification. The presence of solid-state interdiffusion shortens isothermal solidification times required compared to no interdiffusion and this affect becomes more significant at smaller base metal particle sizes.

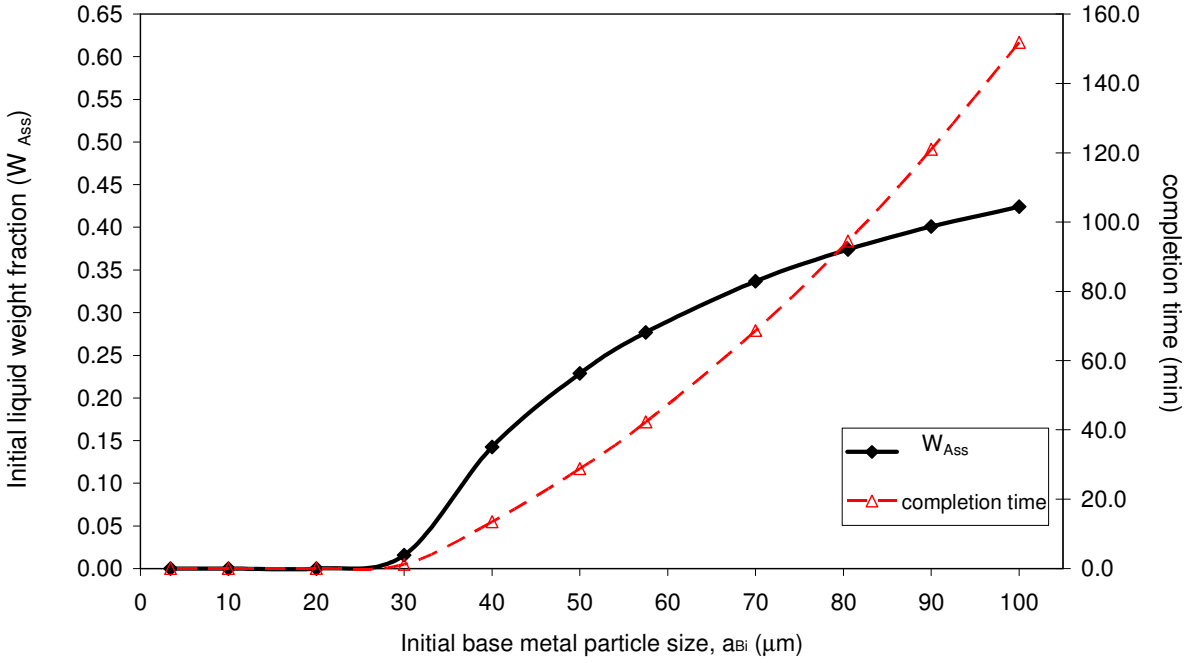

Figure 6-8: Initial liquid formations (W_{Ass}) and time required for complete liquid removal for various initial base metal particle sizes (a_{Bi}). Conditions: 40°/min., $T_P = T_A = 1085$°C, $C_O =$ 65wt%Cu, $D_{app} = 1.2517 \times 10^{-13}$ m^2/s.

6.5. Dissolution and Melt-Back Considerations for $T_P > T_A$.

For the case where $T_P > T_A$, dissolution and melting of the outer alloyed regions of the B particle with a solute content above C_S must be accounted for. As depicted in Figure 6-1*c* and Figure 6-2, the dissolution process increases the liquid fraction to W_{Ao} and decreases the particle size to a_{Bo}. The increase in the solubility of element B in the liquid due to the new equilibrium liquidus composition C_L leads to dissolution of B particles and melting of non-equilibrium alloyed regions. The surface concentration of the B particles is also reduced from $C_S = 1$ to the new solidus concentration at T_P and the solute profile in the particles is altered

accordingly. It is important to note that this process also causes a reduction in the solute uptake content from M_{ss}/M_f to M_o/M_f within the now partially dissolved B particle.

In the current model, B dissolution due to liquid solubility is accounted for by fact that C_L now < 1 (in Equation (6-1) and Figure 6-5). Melt-back of unstable alloyed regions is quantified by determining the concentration profile in the B particles and identifying the non-equilibrium regions. This was accomplished by solving Equation (2-19) using Mathcad. Heating from T_A to T_P was then assumed to occur very rapidly, or instantaneously. In this way the solute concentration profile in the particle below the new C_S is unchanged from that developed during heating to T_A (i.e., Figure 6-1*b*). This calculated solute profile is illustrated in Figure 6-9, where the radial concentration profile C after solid-state interdiffusion is plotted versus the normalized particle radius, (r/a_B) for the time required to reach T_A (t_o). Regions having solute contents greater than C_S will melt back once T_P is reached. This description is supported by ND results, where post-melt C_S peaks were shifted to higher 2θ angles above T_A. The approximate location of the solid-liquid interface at T_P (i.e., where melt-back would stop) is determined by the location where the concentration in the solute profile is C_S (shown by the line at p_1). Regions to the right of this line will melt and cause the amount of solute contained within the particle to decrease.

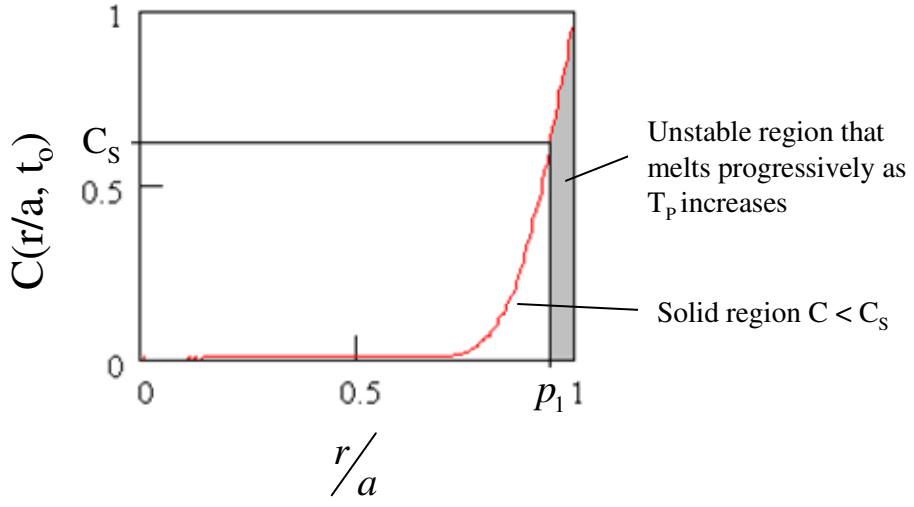

Figure 6-9: Concentration profile inside the base metal particles once T_A is reached. Regions with $C > C_S$ (grey region) will melt back progressively as T_P increases.

The amount of solute lost by the particle is represented by the area under the curve that lies to the right of the dashed line at p_1. If we let $p = r/a$, the magnitude of this area can be

obtained by integrating C from $p = p_1$ to $p = 1$. Thus, the fraction of solute remaining inside the particle (defined as X_r) can be obtained by;

$$X_r = \left(\int_0^1 C(p,t_O) \cdot dp - \int_{P_1}^1 C(p,t_O) \cdot dp \right) \Big/ \int_0^1 C(p,t_O) \cdot dp \qquad \textbf{(6-7)}$$

X_r can then be used to determine the fraction of solute uptake remaining inside the particles immediately after dissolution and melt-back at T_P by;

$$M_o / M_f = X_r (M_{ss} / M_f) \qquad \textbf{(6-8)}$$

where M_o/M_f is the fractional solute uptake present after dissolution and partial melt-back of the base metal particles, which initially contained M_{ss}/M_f at T_A. In the case where $T_P = T_A$, no melt back of the solute profile will occur ($X_r = 1$) and Equation (6-8) correctly indicates that in this case $M_o/M_f = M_{ss}/M_f$. An expression for the liquid fraction formed after dissolution can be obtained in a similar manner to that described in Equations (6-1) and (6-4). The primary difference being that C_S and C_L no longer equal unity but have the values < 1 according to the phase diagram solidus and liquidus. Therefore the relevant equation becomes;

$$W_{Ao} = \left(C_O - (M_o / M_f) C_S \right) \Big/ C_L \qquad \textbf{(6-9)}$$

where M_o/M_f is determined from Equation (6-8). The corresponding change in particle size from a_{Bss} to a_{Bo} at T_P can similarly be obtained by conservations of mass;

$$a_{Bo} = a_{Bss} \left(W_{Bo} / W_{Bss} \right)^{\frac{1}{3}}$$
$$\text{or, } a_{Bo} = a_{Bss} \left[(1 - W_{Ao}) \Big/ (1 - W_{Ass}) \right]^{\frac{1}{3}} \qquad \textbf{(6-10)}$$

Using these new initial conditions for cases where $T_P > T_A$, the stepwise solution of Figure 6-5 can then be used to calculate the rate of isothermal solidification for a case involving dissolution. Figure 6-10 illustrates isothermal solidification predictions of a Cu-Ni TLPS system (C_O = 65 wt% Cu) for three different processing temperatures; 1) $T_P = T_A$ = 1085°C (i.e., no dissolution and melt back); 2) T_P = 1140°C; and 3) T_P = 1200°C. W_A and a_B predictions are shown for each case. The initial liquid fraction predicted at $t = 0$ is greatest in the 1200°C case, which is consistent with significant base metal dissolution and melt back.

Accordingly, this case has the smallest initial particle size, but it must grow by a greater degree to completely isothermally solidify the liquid. Both the 1085°C and 1140°C cases have initial liquid fractions $W_{Ao} < C_O$, which indicates that base metal dissolution is not sufficient to recover the liquid lost due to solid-state interdiffusion. Conversely W_{Ao} at 1200°C is slightly greater than C_O.

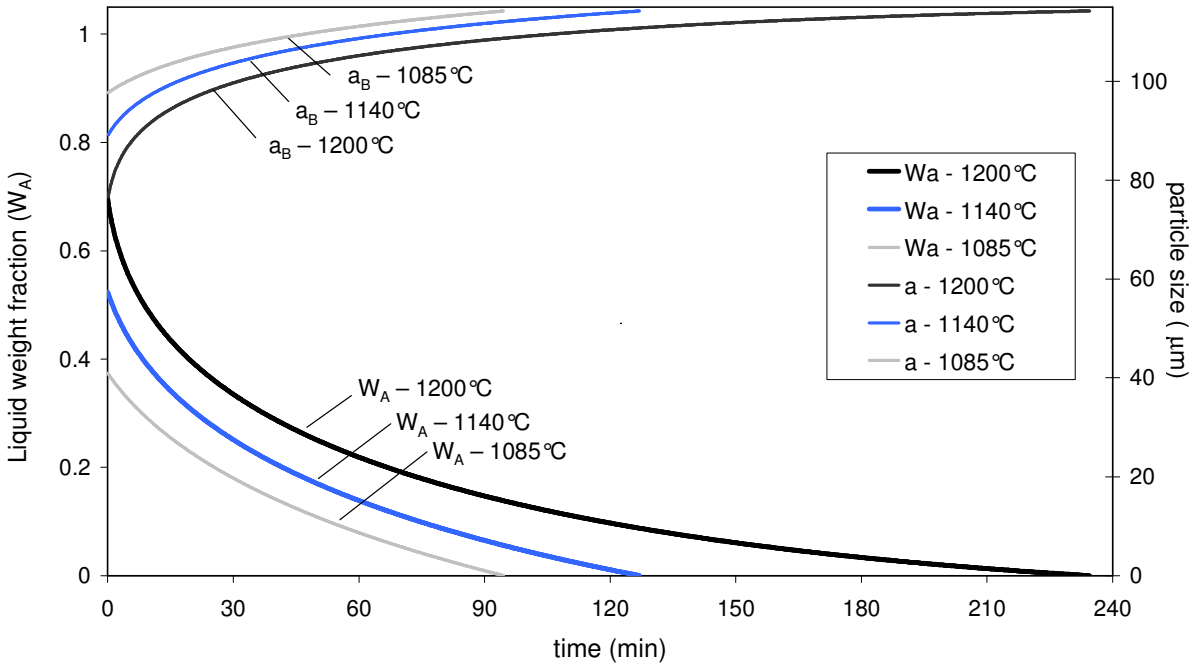

Figure 6-10: T_P effects on the rate of isothermal solidification for Cu-Ni powders under conditions: R_H = 40°/min., C_O = 65 wt% Cu, a_{Bi} = 80.5µm, T_P = 1085°C (D_{app} = 1.2517 x10^{-13} m^2/s), T_P = 1140°C (D_{app} = 1.5835 x10^{-13} m^2/s), T_P = 1200°C (D_{app} = 2.1978 x10^{-13} m^2/s).

A somewhat surprising result is that the time for complete removal of the liquid phase is longer at higher temperatures, as observed with DSC results for TLPS sintered specimens at 1090°C and 1140°C. This is in agreement with DSC analysis results (Section 4.1.5) and supports the previous hypothesis that the net effect of having an increased liquid fraction from dissolution seems to dominate the kinetic effects of increased diffusivity and decreased particle size at higher T_P, where both would be expected to decrease solidification times. Rather, process completion times increase at higher T_P.

6.6. Comparison of Model to Experimental Results

Figure 6-11 shows a comparison for experimental DSC data collected for loose/mixed powder mixtures (Type B) and model predictions for $T_P = T_A = 1085°C$ and $T_P = 1140°C$. Experimental DSC data for Type A (layered/pressed) specimens was not used to model comparisons due to the fact that the very inhomogeneous, pressed macrostructure deviates significantly from the TLPS model assumptions and concentric sphere geometry. The included model predictions in Figure 6-11 are as shown in Figure 6-10. Poor agreement with the experimental data is primarily due to underestimated solidification kinetics.

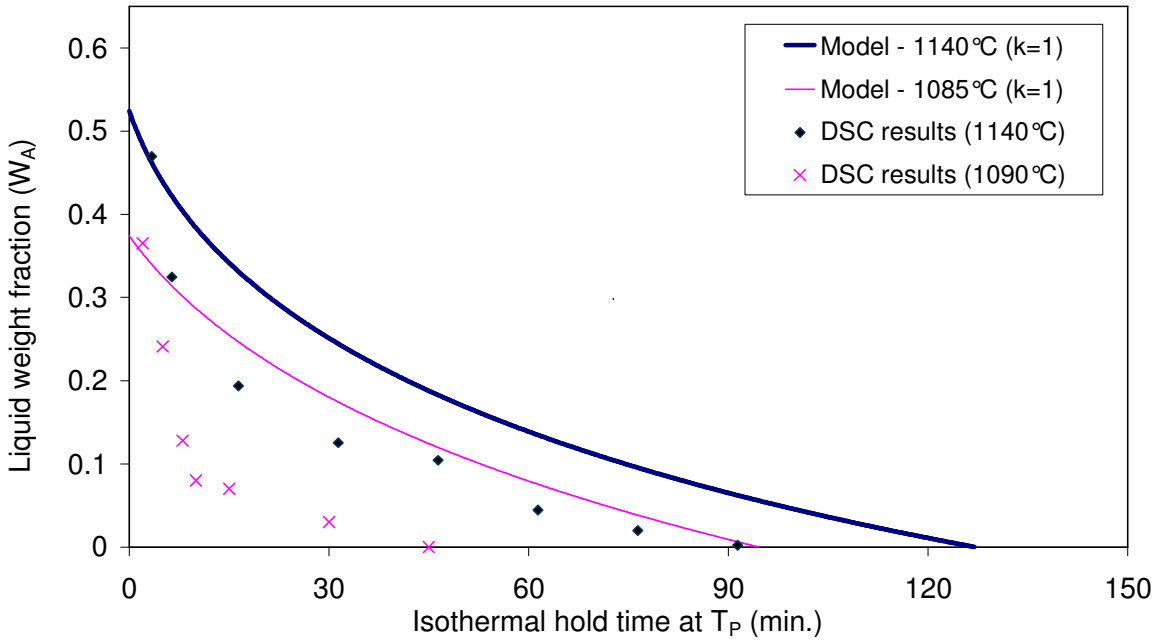

Figure 6-11: Comparison of Type B experimental DSC data and model predictions for liquid fraction remaining as a function of hold time. Model conditions: R_H = 40°/min., C_O = 65wt%Cu, a_{Bi}=80.5 µm, T_P=1085°C (k = 1, D_{app} = 1.2517x10^{-13} m^2/s), T_P=1140°C (k = 1, D_{app} = 1.5835 x10^{-13} m^2/s).

6.6.1. Diffusivity Effects

A key model parameter which strongly affects process kinetics for a given experimental system is the relevant diffusivity value. The work of Fisher and Rudman [44] and Puckert *et al* [5] indicates that, in solid-state and liquid-phase sintering of Cu-Ni powder mixtures, grain boundary diffusion is an important diffusion mechanism. Therefore, predictions should incorporate grain boundary diffusivity (D_b) to account for the enhanced mass transport from these less restricted high-diffusivity paths. In Corbin's model [25], predictions using apparent

diffusivity values, which incorporate grain boundary diffusivity, generated good agreement to DSC results for the Pb-Sn system [13].

In the current model an apparent diffusivity (D_{app}) is used as per Equation (6-5), which includes the contributions of both lattice and grain boundary diffusion, as discussed in Section 2.9.1 [31,53].

$$D_{app} = D_l + k\frac{\delta}{d}D_b$$
$$\text{or, } D_{app} = D_l\left[1 + k\left(\frac{\delta D_b}{dD_l}\right)\right] \quad \textbf{(6-11)}$$

where D_l is the lattice diffusivity of solute A (i.e., Cu) in base metal B (i.e., Ni), D_b is the grain boundary diffusivity of solute in base metal, δ is the grain boundary width taken to be 0.5 nm [31]), d the average base metal grain size (6.2 μm < d < 9.5μm, measured via optical microscopy), and k is a factor determining the relative contribution of the grain boundaries to the mass transport process [53]. Schwarz *et al* state that 0.5< k < 1.5 depending on the grain boundary orientation, alloy system, and other complex grain boundary effects discussed in Section 2.9.1 (i.e., DIR, DIGM) [53]. The temperature dependence of D_{app} is accounted for by the Arrhenius expressions for D_l and D_b. The values of D_o and Q for lattice and grain boundary diffusion are given in Table 6-2 as well as all other important input values. Model predictions presented thus far have incorporated a k value of unity.

Elevated k values increase the apparent solute diffusivity by increasing the relative contribution of grain boundary diffusion. This can be rationalized by the cases where grain boundaries can be preferentially oriented normal to the B particle surfaces and processes such as grain boundary grooving [55], diffusion induced recrystallization (DIR) [56,58,59], and diffusion induced grain boundary migration (DIGM) [56], act to increase boundary effectiveness for solute transport. These grain boundary phenomena are difficult to model due to their complex geometry and transient nature. Furthermore, the rough surface morphology of the Ni powders (see Figure 3-2*b*) will also increase liquid penetration through cracks and enhance solute transport within the Ni particles via more grain boundaries. In the case of such complex powder mixtures, the k parameter may provide an effective means of estimating these effects. Figure 6-12 shows model predictions for k = 1.5.

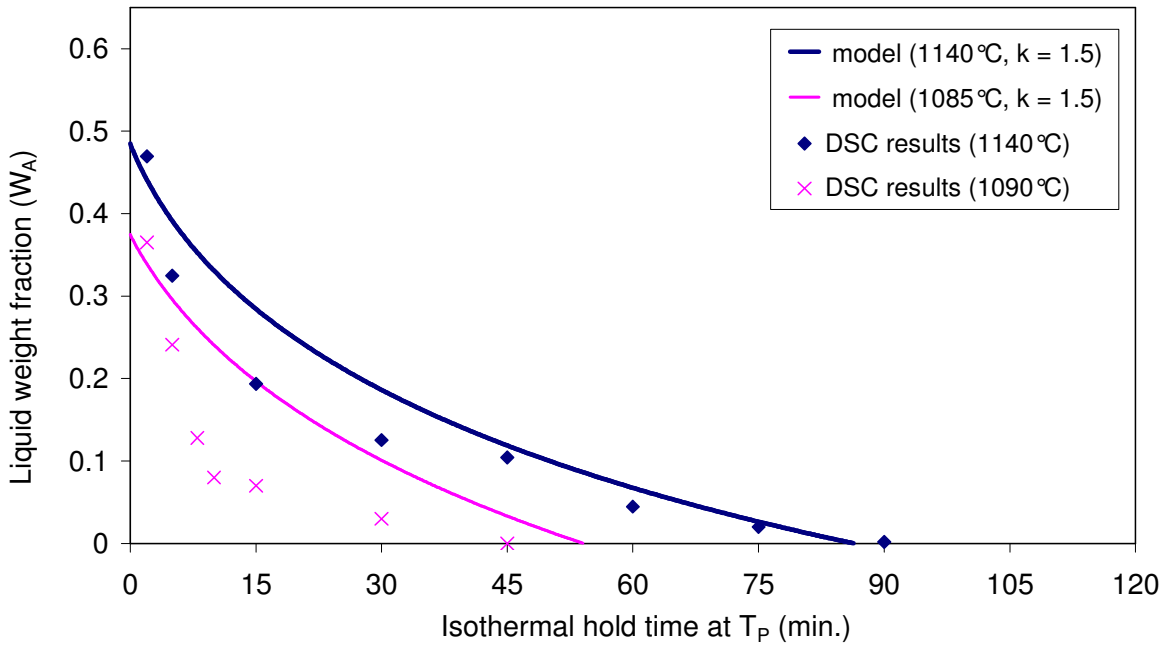

Figure 6-12: Comparison of Type B experimental DSC data and model predictions that account for grain boundary diffusions via apparent diffusivity (D_{app}). The liquid fraction remaining W_A is plotted as a function of hold time. Model conditions: R_H = 40°/min., C_O = 65wt%Cu, a_{Bi}=80.5 µm, T_P=1085°C (k = 1.5, D_{app} = 2.1888x10^{-13} m^2/s), T_P = 1140°C (k = 1.5, D_{app} = 2.2948x10^{-13} m^2/s).

Agreement between the model and experimental data is improved at 1140°C when using a k factor of 1.5, suggesting a strong grain boundary contribution to the effective diffusivity of Cu diffusing in Ni. The rate of liquid removal seems underestimated at short hold time. Model/experiment agreement is not good at 1085°C. This is partly due to the fact that the DSC experiments could not be carried out at 1085°C but required some over-heating to 1090°C. However, even at 1085°C the total time for solidification predicted by the model is close to the experimental value. The model also correctly predicts the overall trend of decreasing initial liquid fraction and time for isothermal solidification at the lower sintering temperature. The data indicates that better model/experimental agreement might be obtained with higher diffusivity values, or at k >1.5. This indicates that greater grain boundary contributions might be present at 1090°C relative to 1140°C. This is likely since mass transport processes with lower activation energies, such as grain boundary diffusion (relative to lattice diffusion), become relatively more significant at lower process temperatures [31]. However, it is worth noting that: 1) Cu penetration within the grain boundaries was not experimentally observed during SEM/EDS analysis; and 2) Porter and Easterling suggest that the grain boundary

mechanism becomes dominant *below* homologous temperatures of 0.74-0.8T_m, above which lattice diffusion is dominant [31]. Puckert *et al* [5] and others [44,51] have however observed or measured grain boundary diffusion/penetration in the Ni-Cu system. This mechanism is surely a contributor to the solute transport process during TLPS, but its significance to the overall solute transport process is difficult to verify, particularly since the base metal grain size d is increasing during the isothermal stage due to grain growth at such elevated temperatures

Closer examination of Figure 6-12 shows that both predicted W_A plots exhibit less curvature than the DSC data, particularly at 1090°C. This will be explained by the inhomogeneity effects discussed in Section 6.6.2. The remaining discrepancy that does exist between the model and experimental data is primarily due to the difficulty in determining an appropriate diffusivity value. This is true for Corbin's simplified model [11,25] and diffusion-based models in general. For example, literature data for D_{app} and D_b is very limited for most systems, including Ni-Cu [51]. The complex powder size distribution and morphology are also difficult to account for in the model and these deviations from the ideal concentric sphere model act to increase process kinetics in experimental results.

In addition, an important simplification made in the model is the use of constant intrinsic diffusivity which does not account for concentration effects. Rather, as called for by most analytical models, the dilute alloy assumption is made, where the diffusivity of A in pure B is used for the heat-up and isothermal segments. This assumption is valid at short times, but becomes less valid as appreciable levels of interdiffusion accumulate. This is particularly the case in this TLPS problem for high solubility systems. If we consider the square EDS concentration profiles (Figure 4-14) and ND experimental results (see C_S peak growth in Figure 5-34), liquid removal occurs by the growth of a Cu-rich layer at the periphery the base metal particles and minimal long range diffusion into the Ni core. As such, the diffusing Cu atoms encounter a non-dilute Ni base metal particle once across the solid/liquid interface. Solute atoms must then diffuse through a solute rich layer having compositions closer to pure Cu than pure, or dilute Ni (i.e., C_S values are closer to pure Cu at 1090°C and 1140°C).

Concentration Dependence

Figure 2-18 previously showed the significant variation of D_{Cu} and D_{Ni} as a function of alloy composition at 1000°C [31]. This figure illustrates how diffusivity is highly concentration dependent in the Cu-Ni alloy system and diffusivity values increase as the Cu content increases. Thus, the current model will tend to underestimate solidification kinetics, particularly at longer times where the isothermally solidified layer at C_S has grown to an appreciable thickness. It may be that incorporating the concentration dependence of diffusion into the model will lead to a better prediction of the experimental results. However, the significant geometrical and arithmetic issues involved in calculating solute uptake by a base metal particle with varying diffusivity across the evolving solute profile is beyond the scope of the simplified analytical approach intended in this work. A full treatment would likely necessitate a numerical modelling technique. Furthermore, the concentration dependence of boundary diffusion (D_b) is not known.

An alternative approach that can be readily implemented in this analytical technique is the use of constant diffusivity values for in a non-dilute base metal particle. In substitutional alloys, such as Ni-Cu, the concentration dependence of diffusivity is accounted for by an interdiffusion coefficient ($\widetilde{D}$) that accounts for both A and B diffusing species in A-B alloys [31]:

$$\widetilde{D} = X_{Ni} D_{Cu} + X_{Cu} D_{Ni} \qquad \textbf{(6-12)}$$

Where X_{Ni} and X_{Cu} and are the Ni and Cu fractional concentrations in the alloy, D_{Cu} is the diffusivity of Cu in Ni and D_{Ni} is the diffusivity of Ni in Cu (both at a specific alloy composition). As previously shown in Figure 2-18, the expression for $\widetilde{D}$ simply states that the interdiffusion process in Ni-Cu couples is dominated by Cu diffusivity in dilute Ni alloys whereas the opposite occurs in dilute Cu alloys. Since experimental data indicate that the peripheral base metal region is solute rich (having compositions $\leq C_S$), diffusivity values through an A-rich alloy should be investigated. Interdiffusion coefficient data for lattice diffusivity over a range of temperatures and alloy compositions were obtained from [50]. Figure 6-13 presents these data in a typical semi-log plot, which has been extrapolated to 1140°C (i.e., the left most side of each trend line). This plot clearly shows how diffusivity

values increase significantly with increasing temperature as well as Cu content. Diffusivity data for Cu-rich alloy compositions near C_S at 1085°C (i.e., 100wt% Cu) and 1140°C (i.e., 86wt% Cu) are included. The diffusivity data for the 86wt% line were obtained by linear interpolation between the 80 and 90 wt% Cu data.

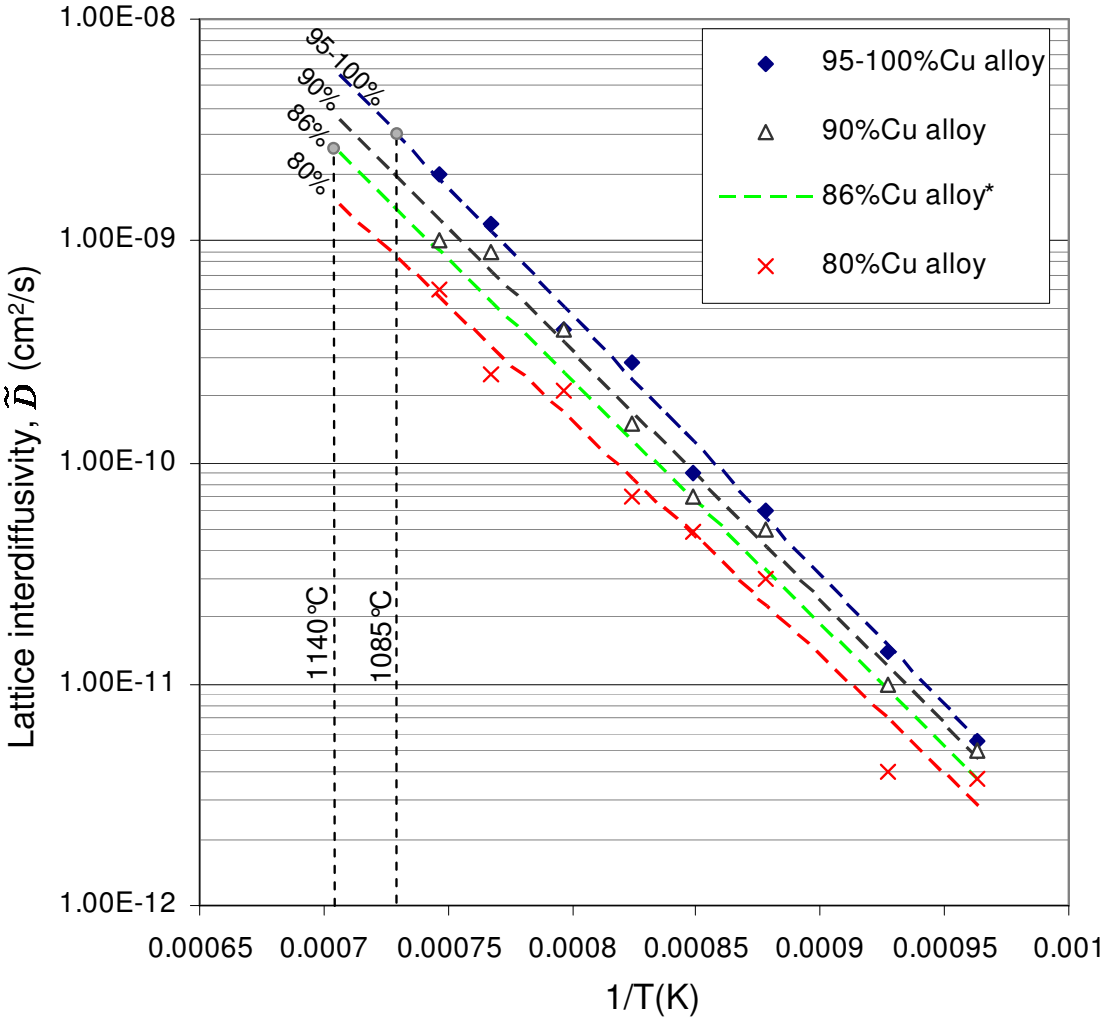

Figure 6-13: Interdiffusion coefficient values as a function of temperature for various Ni-Cu alloy compositions [50].

The above diffusivity data are only for interdiffusion through the Ni-Cu lattice and does not include a grain boundary contribution. As such, the above $\widetilde{D}$ values can substitute the dilute lattice diffusivity (D_l) in Equation (6-11) for the calculation of a concentration dependent apparent diffusivity ($\widetilde{D}_{app}$).

$$\widetilde{D}_{app} = \widetilde{D}_l + k\frac{\delta}{d}D_b$$
$$\text{or, } \widetilde{D}_{app} = \widetilde{D}_l\left[1 + k\left(\frac{\delta D_b}{d\widetilde{D}_l}\right)\right] \quad \textbf{(6-13)}$$

However, the concentration dependence of grain boundary diffusivity (D_b) is not known and information for Ni-Cu alloys is limited in the literature. As such, grain boundary contributions were not considered for initial predictions (i.e., $k = 0$). However, the D_b for dilute Ni alloys from Grabovetskaya *et al* may provide a reasonable, yet conservative, estimate of the grain boundary contribution [51].

Figure 6-14 presents DSC data as well as model predictions generated using constant $\widetilde{D}$ and $k = 0$ for the 1085°C case (i.e., $\widetilde{D}_{app} = \widetilde{D}$ in a C_S = 100wt% Cu layer) and the 1140°C case (i.e., $\widetilde{D}_{app} = \widetilde{D}$ through a C_S = 86 wt% Cu alloy layer). It is important to note that the increased temperature and decreased Cu content in the 1140°C case have opposing effects on diffusivity. As such, both the 1085°C and 1140°C employ similar diffusivities (see points in Figure 6-13) that are both higher than lattice diffusivity through a dilute Ni alloy. Figure 6-14 shows that in both cases, the predicted solidification kinetics are more rapid relative to the dilute alloy cases in Figure 6-11 (k = 1) and similar to Figure 6-12 ($k = 1.5$). Again, this occurs since diffusivity values increase significantly for these predicted Cu-rich alloys. These predictions agree reasonably well with experimental data but the solidification kinetics appear to be underestimate – particularly at intermediate times at 1085°C. Essentially, the predictions do not have the same degree of curvature as the experimental W_A curves, which exhibit a more pronounced concave curvature due to a transition from initially very rapid liquid removal, to much diminished removal rates near the end of the process.

If we now account for an intermediate grain boundary contribution by letting k = 1 and using the D_b data from Grabovetskaya *et al,* Figure 6-15 shows that the predicted solidification rate increases noticeably. However, in this case the solidification rate is overestimated at long times and underestimated the completion time at 1085°C and 1140°C. Again, we see that the predicted W_A traces have insufficient curvature relative to the experimental data. This type of curvature discrepancy can be explained by powder mixture inhomogeneity effects in Section 6.6.2.

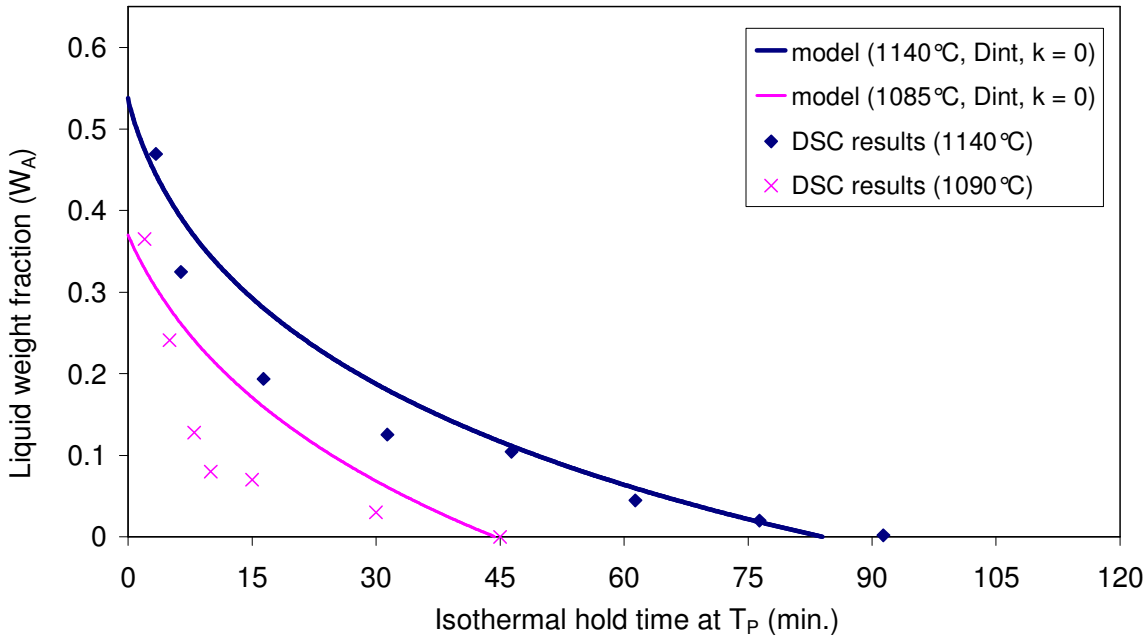

Figure 6-14: Comparison of Type B experimental DSC data and model predictions using concentration dependent diffusivities. The liquid fraction remaining W_A is plotted as a function of hold time. Model conditions: R_H = 40°/min., C_O = 65wt%Cu, a_{Bi}=80.5 µm, T_P = 1085°C (k = 0, $\widetilde{D}_{app}$ = 2.6593 x^{-13} m^2/s), T_P = 1140°C (k = 0, $\widetilde{D}_{app}$ = 2.4647x10^{-13} m^2/s).

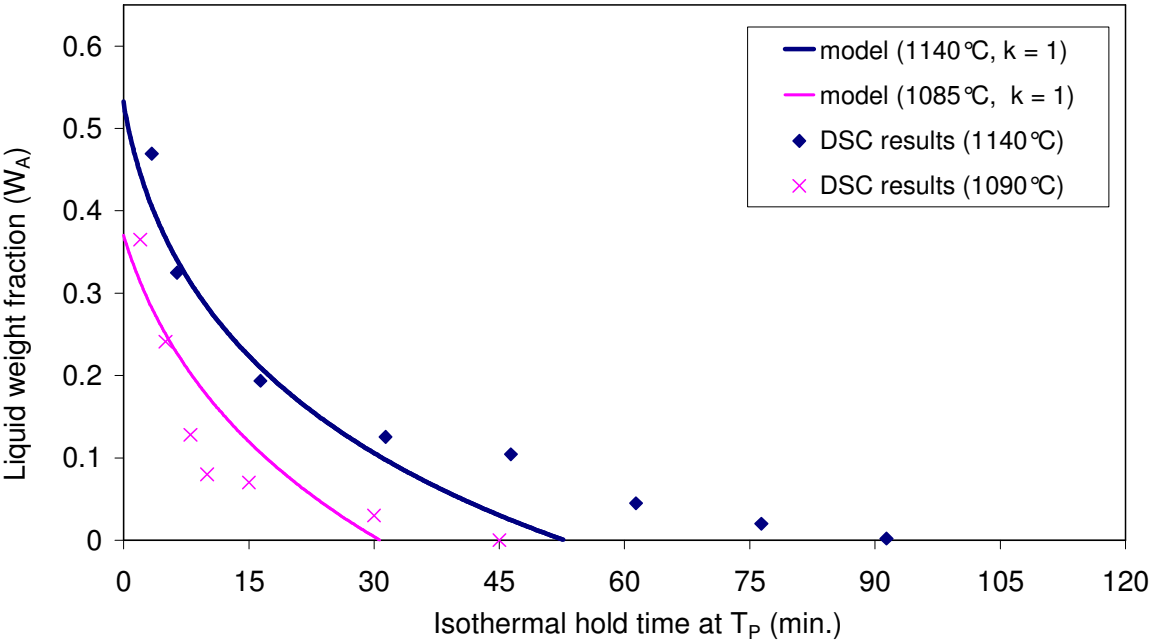

Figure 6-15: Comparison of Type B experimental DSC data and model predictions using concentration- dependent diffusivities. The liquid fraction remaining W_A is plotted as a function of hold time. Model conditions: R_H = 40°/min., C_O = 65wt%Cu, a_{Bi}=80.5 µm, T_P = 1085°C (k = 1, $\widetilde{D}_{app}$ = 3.6504 x^{-13} m^2/s), T_P = 1140°C (k = 0, $\widetilde{D}_{app}$ = 3.9198x10^{-13} m^2/s).

6.6.2. Mixture Inhomogeneity Effects

The underestimated curvature of model predictions in Figure 6-14 and Figure 6-15, particularly for the 1090°C data, can be explained by the fact that the idealized concentric sphere model (which assumes uniformly distributed representative unit cells) does not account for certain inhomogeneity effects such as powder size/morphology variations and non-uniform powder mixture distribution effects. Powder size and morphology inhomogeneity, which are expected in PM materials, will cause variations in solidifications rates throughout a given mixture. This will affect the curvature of the experimental data plots relative to the idealized concentric sphere model. For example, B particles that are smaller than the average a_B value within experimental mixtures will cause rapid isothermal solidification at short times while larger particles will retard the process, particularly at longer hold times. Similarly, if powder mixture distribution inhomogeneity is significant, this will also introduce increased curvature to the experimental W_A data. For example, if relatively solute rich regions exist within the sample where the Cu content is somewhat above the average bulk composition C_O, these regions will require more time to isothermally solidify due to the relative scarcity of Ni particles. Similarly, solute deficient regions will isothermally solidify more rapidly. Both of these inhomogeneity effects for non-uniform B particle sizes and solute distributions will introduce increased curvature in the experimental W_A plots. Increased solidification rates will be evident at the beginning of the process whereas retarded solidification kinetics will be found near the end.

Mixture inhomogeneity can be accounted for by considering a model that consists of N *sub*-unit cells, each having a different solute content, such that the average solute content of all unit cells is equal to that of the desired bulk mixture composition C_O.

$$C_{avg} = \frac{C_1 + C_2 + ...C_N}{N} = C_O \qquad \textbf{(6-14)}$$

The contribution of each unit cell to the level of solute uptake (M_t/M_f) or liquid fraction (W_A) at a given time can then be obtained by summing each cell's contribution and dividing by N. As a first approximation of this effect, two unit cells were considered, each having solute contents deviating by ±5 wt% Cu from the bulk mixture composition (i.e., C_1 = 0.60, C_2 = 0.70, giving C_O = 0.65 wt%Cu), which is reasonable based on ND and metallographic analysis

of experimental powder mixtures. Figure 6-16 presents predictions for these bi-modal concentric sphere unit cell distributions. A line break was added to both predicted curves to clearly show where the solute deficient unit cell (C_1) has completely solidified and the solute rich cell (C_2) continues to slowly remove the remaining liquid at a reduced rate near the end of the isothermal solidification process. The incorporation of more sub-unit cells with increased N, while maintaining C_O = 65 wt% Cu and the ± 5 wt% Cu total variance, would smoothen the predicted curve at the line breaks, where a given sub-unit cell has reached completion.

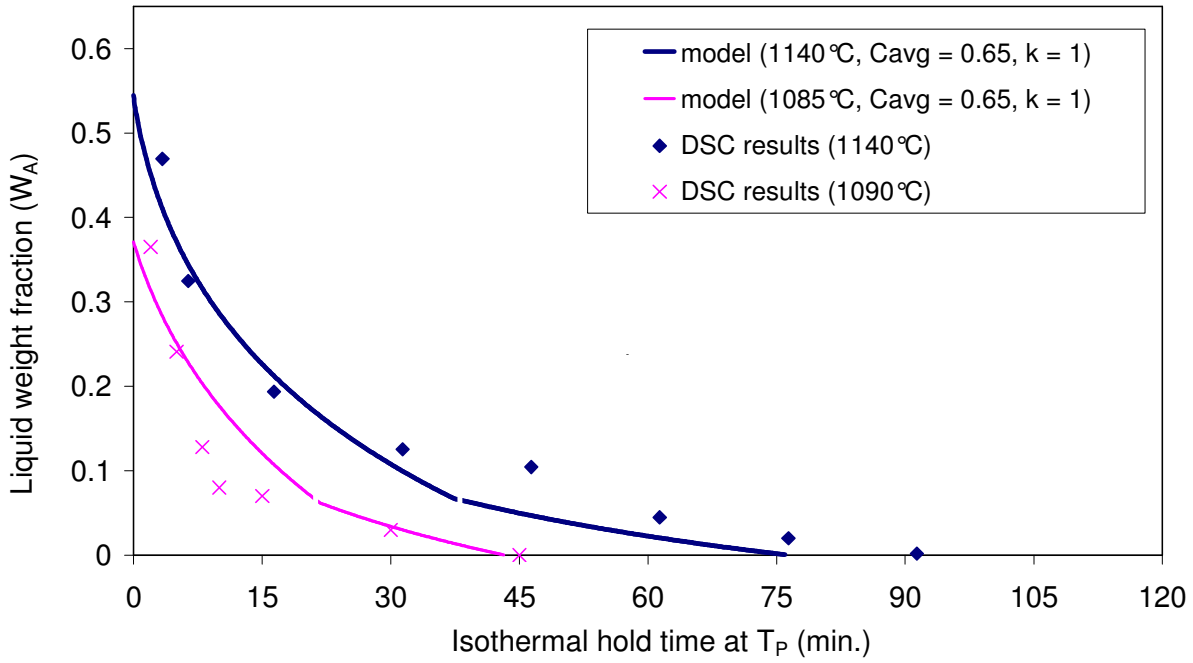

Figure 6-16: Comparison of Type B experimental DSC data and model predictions for an inhomogeneous A distribution. Liquid fraction remaining is plotted as a function of hold time. Model conditions: R_H = 40°/min., C_O = (60+70)/2 = 65 wt% Cu, a_{Bi}=80.5 µm, T_P = 1085°C (k = 1, $\widetilde{D}_{app}$ = 3.6504 x^{-13} m^2/s), T_P = 1140°C (k = 1, $\widetilde{D}_{app}$ = 3.9198x10^{-13} m^2/s).

Figure 6-16 shows that this modelling approach improves agreement with the experimental data at both temperatures and indicates that the DSC samples may have had compositional variations of ± 5 wt% Cu from one region of the mixture to the other. This degree of variance is expected in loose powder mixtures, particularly where there is a large size difference between the A and B powders and segregation can occur. As shown in Table 3-1, this powder combination (i.e., coarsest Ni powder and Cu powder) constituted the largest particle size difference tested.

More curvature is present in the 1090°C experimental data and this results in worse agreement at this temperature, particularly in the 10 minute region. This is likely due to the increased particle distribution and shape inhomogeneity in the experimental mixtures after melting at 1090°C vs. 1140°C. Inhomogeneity effects are amplified at lower processing temperatures since the smaller initial liquid fractions that form can re-arrange the mixtures to a lesser degree. At elevated temperatures, such as 1140°C, the increased liquid fraction from B dissolution can create a more uniform B particle distribution (and thus A distribution). Furthermore, dissolution of the Ni particles also serves to melt back and round out the outer Ni regions near the original rough surface (see Figure 4-13), which deviated from the idealized concentric sphere model. These effects might explain the improved agreement at 1140°C, where the round concentric sphere assumptions are more valid in comparison to 1090°C. Ni powders with smoother spherical surfaces should be obtained or produced for future DSC experiments to allow improved comparisons to the idealized model conditions.

6.6.3. Particle Size Effects

Figure 6-17 shows predicted isothermal solidification rates as well as experimental results for various Ni particle sizes and a fixed Cu particle size at 1140°C. The model predictions incorporated interdiffusion data ($\widetilde{D}_{app}$) and grain boundary effects ($k = 1$) as per the last predictions shown in the previous section.

DSC results indicate that virtually no liquid formed in samples using the finest Ni powder (a_{Bi} = 3.39 μm). The samples prepared with larger Ni particles had greater initial liquid formations and slower rates of isothermal solidification. This illustrates that smaller a_{Bi} values result in faster interdiffusion and isothermal solidification kinetics. Smaller liquid fractions are obtained with smaller base metal particle sizes due to greater levels of solute uptake in the solid-state during heat-up. Smaller particles provide a greater total base metal surface area for solid-state sintering and interdiffusion - resulting in larger M_o/M_f values and decreased W_{Ao}. The same concept of increased surface area/volume explains why greater isothermal solidification rates are obtained with smaller particles (i.e., the slope of the W_A data becomes steeper with smaller a_{Bi} values). These trends are in agreement with predictions by the TLPS model.

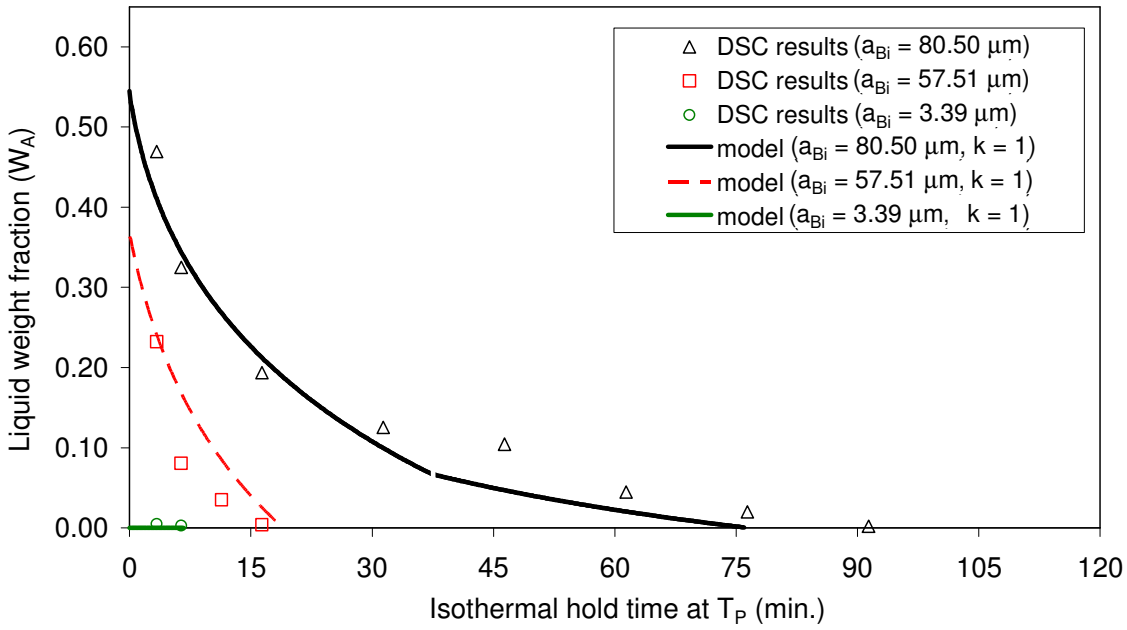

Figure 6-17: Comparison of Type B experimental DSC data and model predictions for different initial particles sizes (a_{Bi}). Liquid fraction remaining is plotted as a function of hold time. Model conditions: R_H = 40°/min., C_O = 65 wt% Cu, 1140°C (k = 1, $\widetilde{D}_{app}$ = 3.9198x10^{-13} m^2/s). The prediction for a_{Bi}=80.5 µm includes mixture inhomogeneity effects (C_O = (60+70)/2 = 65 wt%) to account for particle segregation between the coarse Ni powder and finer Cu solute powder.

The model accurately predicts that no liquid forms at a_{Bi} = 3.39 µm (i.e., the prediction lies on the abscissa in Figure 6-17). For the a_{Bi} = 57.51 µm case, the model under-predicts the solidification rate. This may be due to an underestimated grain boundary or different B particle size/morphology distribution effects. Also, the incorporation of some $k > 1$, or concentration dependent D_b data (if it were available), would increase the effective diffusivity and increase the solidification rate. For the a_{Bi} = 80.50 µm data, model/experimental agreement is good. As discussed in Section 6.6.2, when segregation effects of this powder combination are considered (by $C_{avg} = C_O$ = (60+70)/2 = 65 wt% Cu), the curvature of the W_A prediction increases and improves agreement near process completion. This mixture inhomogeneity arises from the increased relative size difference between the coarsest Ni powder and finer Cu powder in this combination, causing smaller Cu particles to segregate and generate non-uniform solute distributions. This type of inhomogeneity adjustment does not seem to be necessary with powder mixtures using the medium and fine Ni powders. Due to the

smaller relative size difference with the Cu powder, segregation was not observed in these powder mixtures.

6.7. Summary

A simple analytical model was developed based on Corbin's TLPS model to predict the impact that solid-state interdiffusion and dissolution have on liquid formation and its duration during TLPS for isomorphous systems. The model predicts that solid-state interdiffusion and base metal dissolution have significant effects on the initial liquid fraction formed (W_{Ao}) and initial particle size (a_{Bo}) at the beginning of the isothermal solidification process at T_P. Solid-state alloying decreased W_{Ao} and increased a_{Bo}. Initial liquid formations were found to increase with increases in a_{Bi} and R_H by decreasing the extent of solid-state sintering and interdiffusion during heat-up.

In cases where $T_P > T_A$, base metal dissolution counteracted the effects of solid-state sintering and caused W_{Ao} to increase and a_{Bo} to decrease. Both of these phenomena were also important in predicting the kinetics of isothermal solidification since changes in W_{Ao} and a_{Bo} significantly influence the rate and duration of the isothermal solidification stage. The model predicted that longer times are required to isothermally solidify the greater amounts of liquid formed at higher temperatures (due to dissolution). These trends agree with experimental DSC results for Ni-65wt%Cu mixtures sintered at 1090°C and 1140°C.

Model/experimental agreement for isothermal solidification rates critically depends on the diffusivity values used. Liquid removal predictions underestimate kinetics when only lattice diffusion through dilute base metal particles is considered. When enhanced apparent diffusivities (D_{app}) are considered that incorporate grain boundary contributions within dilute Ni, agreement is significantly improved for k = 1.5. However, the solidification kinetics and the curvature of the W_A removal curves are still underestimated, particularly at 1085°C. Metallographic and ND analyses have shown that isothermal solidification occurs by the growth of a Cu-rich layer at the base metal particle periphery. If the dilute base metal assumption is dismissed on this basis, and the enhanced concentration dependent diffusivities within Cu-rich base metal regions are utilized (via interdiffusion coefficients, $\widetilde{D}$ from literature), the predicted isothermal solidification process is accelerated. This significantly

improves agreement for the majority of the isothermal solidification process at 1085°C and 1140°C, with some overestimation of the kinetics at long hold times causing shorter completion times. It is proposed that some combination of grain boundary diffusion (i.e., $k \sim 1$) and lattice interdiffusion through Cu-rich alloy regions will most accurately predict the effective mass-transport process and solidification kinetics. A brief study of the model's sensitivity to diffusivity values (using physically-based values from literature for different mechanisms and compositions) has shown that apparent diffusivities of 3.6504×10^{-13} m^2/s at 1085°C (in ~100 wt % Cu) and 3.9198×10^{-13} m^2/s at 1140°C (in 86 wt% Cu) provide the best agreement between the model and experimental results.

The incorporation of multiple sub-unit cells to account for possible powder segregation effects accurately predicts the increased curvature and retarded removal rates exhibited by the DSC data near the end of the process. This type of adjustment is applicable to A/B powder mixtures with large particle size differences that have a higher tendency to segregate (i.e., mixtures utilizing the coarsest Ni powder). Isothermal solidification predictions for three different particle sizes showed good agreement with DSC experimental; however, predictions seem to underestimate the rate of liquid removal for $a_{Bi} = 57.51$ μm.

This model highlights the importance of the diffusivity values used for predictions. In PM materials, the complex base metal surface and particle morphology, grain boundary orientation and growth, and the concentration-dependence of diffusivity in Ni-Cu alloys make it difficult to determine accurate diffusivity values. This is exacerbated by the lack of relevant net or effective diffusivity data in literature. Nonetheless, it is believed that this model elucidates the isothermal solidification process in high-solubility systems such as Ni-Cu, where the effects of solid-state interdiffusion and dissolution are significant.

7. Conclusions

In brief, the stated objectives of this study were:

- Develop and characterize an experimental sample preparation technique for fluxless Ni-Cu powder systems that exhibit TLPS characteristics (i.e., melt formation, isothermal solidification, and variable melting point behaviour).
- Develop an experimental DSC technique to quantify the amount of liquid formed and the rate of its removal.
- Identify, and study the effects of key process parameters on the TLPS process (i.e., sample preparation techniques, T_P, and powder particle size).
- Investigate the use of *in situ* neutron powder diffraction techniques to study interdiffusion *during* the isothermal processes in TLPS. This was aimed at elucidating the isothermal solidification mechanism.
- Modification and refinement of a diffusion-based analytical model (initially developed for low-temperature TLPS solders) [25] to verify its applicability to higher temperature isomorphous systems.

7.1. Differential Scanning Calorimetry Results

It was found that DSC is a valuable tool for quantitatively examining liquid formation and removal during athermal segments in TLP sintering cycles, especially when combined with microscopy techniques. Metallographic analysis alone would not allow the determination of liquid fractions in TLP sintered specimens due to the variation of numerous particles, and most importantly because the isomorphous sintered alloys did not exhibit an interface in the solid-state.

- It was found that increased Cu contents caused increased liquid fractions and post-melt densities in Type A samples (layered/pressed). Archimedes density measurements and microscopy results showed that densities above 95% were achieved shortly after melting with Cu concentrations of 55 wt% or higher. Type B mixtures (mixed/loose)

formed more liquid than Type A for the same compositions due to decreased inter-particle contact since green-pressing was not employed with this preparation technique. However, post-melt sintered densities were typically 5% lower than Type A mixtures for the 65 wt% Cu composition studied. Type A mixtures achieved higher densities than Type B mixtures due to the higher starting green densities from pressing. However, green pressing increased interparticle contact and heat-up interdiffusion, resulting in suppressed liquid fractions (~5 wt% less liquid). Full densification did not occur using either preparation technique or sintering temperature (1090°C or 1140°C) due to observed trapped gas pores, residual starting Ni powder pores, and Kirkendall pores generated from unequal diffusivities.

- Unlike previous quantitative DSC studies by Corbin *et al* [10,11,13,25] on low-temperature eutectic powder systems with limited solubility, it was found that solid-state interdiffusion during the heat-up segment and dissolution at $T_P > T_A$ significantly affect the amount of liquid initially formed and its removal in the Cu-Ni system. This is due to the unlimited solubilities and high interdiffusion rates characteristic of isomorphous systems. When using 40°C/min. heat-up rates in both Type A and B preparation techniques, it was found that the initial liquid fraction (W_{Ao}) was significantly less than the initial bulk Cu content of the mixtures (i.e., $W_{Ao} < C_O$). This is primarily due to solid-state interdiffusion between contacting Ni and Cu particles during heat-up, thereby suppressing Cu liquation once $T \geq T_A$.
- 65 wt% Cu loose powder mixtures (Type A and B), were used for investigating isothermal solidification kinetics. In both Type A and B mixtures, it was found that significantly more time was required for complete liquid removal at 1140°C vs. 1090°C. For layered/pressed Type A mixtures, complete removal occurred in between 160 and 240 minutes at 1140°C. At 1090°C, complete removal of the liquid phase required 150 minutes, and significantly less liquid was remained at a given time during the process. For loose/mixed Type B mixtures, complete isothermal solidification required 90 minutes at 1140°C and 45 minutes at 1090°C under identical conditions. The increased sintering times required for liquid removal at 1140°C can be explained by the observed increase in initial liquid fractions (W_{Ao}) formed at higher processing

temperatures due to the dissolution of Ni. This effectively counteracts the increased diffusivities at these temperatures, and thus more time is required to completely isothermally solidify the increased liquid content.

- The green-pressed brazes (Type A) required much more time for complete isothermal solidification due to the inhomogeneous liquid distributions caused by layering the initial powders. This generated liquid-rich peripheral areas, or pools, surrounding the pressed Ni skeleton that required extended sintering times for removal. The increase in the post-processed melting point of this braze composition was in excess of 80°C upon reheating.
- A similar isothermal solidification DSC study for Type B mixtures TLP sintered at 1140°C using three different particles sizes revealed that fine base metal Ni particles cause high degrees of solid-state interdiffusion during heat-up, small initial liquid fractions, and accelerated liquid removal rates due to high surface area/volume ratios.
- *Ex situ* metallographic analysis of post-sintered specimens via SEM and EDS indicates that isothermal liquid solidification and cool-down leaves behind Ni-rich cores surrounded by Cu-rich matrix regions having compositions near the solidus composition (C_S). Due to the lack of a remnant solid-liquid interface and difficulties in obtaining macroscopically representative data from individual particle micrographs, it is difficult to distinguish between athermally frozen liquid areas from isothermally solidified areas. However, the square solute profiles measured in solidified brazes (i.e., very sharp gradients separating Cu deficient cores and uniform Cu-rich regions at C_S) does suggest that isothermal solidification occurs by limited long-range Cu diffusion within the Ni particles. This indicates that a solute rich solid solution layer grows epitaxially around Ni by the transient progression of the solid/liquid interface at compositions given by the liquidus and solidus (C_S/C_L). Since the DSC technique only quantifies the liquid fraction during athermal segments, it is difficult to confirm this isothermal solidification mechanism without actual *in situ* interdiffusion data collected during the isothermal hold at T_P.

7.2. Neutron Diffraction Results

This investigation has shown that the ND technique is very useful for examining interdiffusion during sintering of larger powder mixtures *in situ*. The film plots and waterfall plots of the evolving ND patterns in the 2θ region of the (200) FCC peaks for Ni and Cu were useful in characterizing melting and interdiffusion phenomena. Also, the observed post-melt ND profile evolution clearly identifies the isothermal solidification mechanism.

- If we disregard the melting event and interdiffusion kinetics for a moment, all samples generally displayed similar (200) FCC peak evolution behaviour. During extended isothermal hold segments at T_P, the measured diffraction intensity gradually increases at intermediate 2θ angles separating the original Cu and Ni peaks - indicative of the gradual interdiffusion process between Ni and Cu exhibited by all specimens. Eventually, the initially bi-modal Cu-Ni diffraction profile formed a broad single peak, which refines during extended isothermal sintering due to interdiffusion - causing homogenization. The evolution of ND patterns can be used to clearly distinguish between the solid-state and transient liquid phase sintering process variants (i.e., SSS vs. TLPS). In solid-state sintered specimens (as studied by Rudman), interdiffusion is much slower and the generation of a homogeneous alloy composition with a single peak at C_O is significantly delayed relative to TLP sintered specimens.

- In comparison, the ND pattern evolution for TLP sintered samples heated above the melting point of Cu showed a clear melting event which deviates from typical SSS behaviour. Melting was characterized by the removal of pure Cu peaks, which leave behind solute rich peaks originating from alloy regions having compositions near the solidus for the given T_P (i.e., C_S). After melting, the ensuing evolution of ND patterns clearly shows a rapid increase in C_S peak intensity relative to the stable Ni peaks, indicating the growth of Cu-rich rich material having compositions at C_S. Also, the intensity of the Ni peaks is seen to decrease with increasing T_P due to dissolution. This *in situ* data confirms that the isothermal solidification process occurs by the growth of solute-rich regions at C_S. This further supports *ex situ* metallographic evidence obtained from SEM/EDS analysis of DSC samples, which suggested that the liquid

phase isothermally solidified by interfacial motion and epitaxial growth of a solute-rich layer (having compositions near C_S) surrounding the original Ni particle.

- As the isothermal processing temperature was increased in the ND experiments, the location of the isothermally solidifying C_S peaks shifted to higher 2θ angles (vs. lower angles due to thermal expansion), thus indicating lower Cu compositions. This was in agreement with the C_S variation expected from the solidus line of Ni-Cu phase diagram - further confirming the identity of the phase that is isothermally solidifying and which is responsible for the liquid removal rates quantified by DSC.
- Temperature gradients within the C2 diffractometer furnace reinforced the importance of using the Al_2O_3 peaks (originating for the inert corundum sample crucibles) as an internal standard for temperature reference. The measured temperature gradients, which are due to the thermocouple sensor locations (i.e., outside the sample canister) as well as actual temperature gradients within the furnace due to its design, indicate sample temperature variations of $\leq 50°C$ within the canister. These observed gradients were unavoidable in the current C2 furnace configuration. The temperatures calculated from the Al_2O_3 peaks are considered to provide a better estimation of the actual mean sample temperature due to the sample/crucible proximity and since thermal expansion data was more reliable and than the thermocouple data at the stabilized temperatures of interest (i.e., T_P). The different isothermal sintering temperatures (as measured by calibrated Al_2O_3 temperatures and thermocouple data) indicate that the average sample temperatures were sufficiently different to rationalize the distinct sintering behaviour of each specimen.
- Metallographic analysis of the ND samples showed that all samples held for long isothermal sintering times to near full homogenization showed significant levels of Kirkendall porosity. In comparison, the sample held near 1200°C for only 30 minutes showed significant levels of consolidation and very little Kirkendall effect porosity. These results indicate that, from a practical brazing perspective, the Ni-Cu filler metal should only be held at T_P long enough to cause complete liquid removal. Otherwise, the effects of the developing Kirkendall pore structure will negatively affect mechanical properties. Therefore, the determination of the isothermal solidification

time from quantitative experimental data or an appropriate TLPS model becomes even more important is the case of isomorphous systems susceptible to the Kirkendall effect.

7.3. Modelling Results

A simple analytical model was developed based on Corbin's TLPS model to predict the impact that solid-state interdiffusion and dissolution have on liquid formation and its duration during TLPS for isomorphous systems. The model predicts that solid-state interdiffusion and base metal dissolution have significant effects on the initial liquid fraction formed (W_{Ao}) and initial particle size (a_{Bo}) at the beginning of the isothermal solidification process at T_P.

- Solid-state interdiffusion predictions during heat-up (using Crank's solute uptake model) suppressed liquid formations at T_A (i.e., decreased W_{Ao}) and increased the solid-state alloyed B particle size (a_{Bo}). Initial liquid formations were found to increase with increases in a_{Bi} and R_H by decreasing the extent of solid-state sintering and interdiffusion during heat-up.
- In cases where $T_P > T_A$, base metal dissolution counteracted the effects of solid-state sintering and caused W_{Ao} to increase and a_{Bo} to decrease. Both of these phenomena were also important in predicting the kinetics of isothermal solidification since changes in W_{Ao} and a_{Bo} significantly influence the rate and duration of the isothermal solidification stage. The model predicted that longer times are required to isothermally solidify the greater amounts of liquid formed at higher temperatures (due to dissolution). These results agree with experimental DSC results for a Ni-65wt%Cu TLPS mixtures sintered at 1090°C and 1140°C.
- Model/experimental agreement for isothermal solidification rates critically depends on the diffusivity values used. Liquid removal predictions underestimate kinetics when only lattice diffusion through dilute base metal particles is considered. When enhanced apparent diffusivities (D_{app}) are considered that incorporate grain boundary contributions within dilute Ni, agreement is significantly improved for k = 1.5. However, the solidification kinetics and the curvature of the W_A removal curves are still underestimated, particularly at 1085°C.

- Metallographic, DSC, and ND results have shown that after the solid-liquid interface has been established, isothermal solidification proceeds via the epitaxial growth of a Cu-rich layer surrounding the Ni particles. If the dilute base metal assumption is dismissed on this basis, and the enhanced concentration dependent diffusivities within Cu-rich base metal regions are utilized (via interdiffusion coefficients, $\widetilde{D}$ from literature), the predicted isothermal solidification process is accelerated. This significantly improves agreement for the majority of the isothermal solidification process at 1085°C and 1140°C, with some overestimation of the kinetics at long hold times causing shorter completion times. It is proposed that some combination of grain boundary diffusion (i.e., $k \sim 1$) and lattice interdiffusion through Cu-rich alloy regions will most accurately predict the effective mass-transport process and solidification kinetics using this analytical model. A brief study of the model's sensitivity to diffusivity values, using physically-based values from literature for different mechanisms and compositions, has shown that apparent diffusivities of 3.6504×10^{-13} m^2/s at 1085°C (in ~100 wt % Cu) and 3.9198×10^{-13} m^2/s at 1140°C (in 86 wt% Cu) provide the best agreement between the model and experimental results.
- The incorporation of inhomogeneity effects in the model (e.g., powder and liquid distribution) by using multiple unit cells generates $W_A(t)$ predictions with decreasing solidification rates at longer times. The predicted $W_A(t)$ curves have increased curvature and retarded removal rates near the end of the process, as exhibited by the DSC data. These predictions attempt to capture the effects of liquid rich areas/pools and how they will retard the liquid removal process, especially at longer times. This type of multi-cell model is applicable to A/B powder mixtures with large particle size differences that have a higher tendency to segregate (i.e., mixtures utilizing the coarsest Ni powder).
- Isothermal solidification predictions for three different particle sizes showed good agreement with DSC experimental data using $\widetilde{D}$ and $k = 1$. However, predictions seem to underestimate the rate of liquid removal for $a_{Bi} = 57.51$ μm.

In summary, this model shows that predictions are highly sensitive to the diffusivity values used and highlights the importance of the mass transport mechanisms considered for predictions. In PM materials, particle morphology, grain boundary orientation and growth, and the concentration-dependence of diffusivity make it difficult to determine accurate diffusivity values. This is worsened by the lack of relevant net or effective diffusivity data in literature. Furthermore, the complex base metal surface and particle morphology in particulate materials will affect solidification kinetics with respect to the idealized concentric sphere model. These considerations as well as the process' sensitivity to numerous inter-related variables (e.g., sintering temperature, T_P), make TLPS a complex process to model. Nonetheless, it is believed that this diffusion-based analytical model elucidates the isothermal solidification process in isomorphous systems, where the effects of solid-state interdiffusion and dissolution are significant.

7.4. Recommendations and Future Work

In order to minimize baseline shifting in DSC traces, lower heating rates should be investigated. Although this will suppress liquid formation, it may be possible to simply reduce the heating rate by appending a small athermal segment near the melting and solidification events as in [96]. A parametric study of various heating rates could also be used to validate model predictions and determine processing windows that will form sufficient liquid amounts and consolidation levels. Current work is also aimed at investigating TLP bonding of Ni and Cu foils. Preliminary DSC and larger-scale vacuum furnace experiments have shown that stacked Cu/Ni/Cu foil interlayers (of 25-50 μm thickness) exhibit TLPS characteristics within a reasonable time frame. This approach can provide an alternative geometry that can be used for bonding flat surfaces.

As for ND experiments, further quantitative analysis of alloy phase fractions (using programs like GSAS) and quantification of the degree of interdiffusion (based on Rudman's XRD technique [85]) should be investigated. The broad alloy peaks (i.e., ranging from pure Cu to pure Ni) and weak signal quality from short scan durations will require special consideration for accurate results. An applicable program allowing batch-mode analysis of large ND data set arrays will also be important for evolutionary results. Also, temperature

measurements using external thermocouples attached to the outer diameter of the vanadium sample canister were found to provide lagging, non-representative estimations of the inner sample temperature indicated by the Al_2O_3 peaks – particularly during athermal segments. Potential improvements for future work, should consider placing a temperature sensor within the sample environment or crucible itself to obtain direct inner sample temperature data. Also, revising the furnace design to reduce temperature gradients and general faults is an issue also under consideration at the CNBC labs.

Also, an investigation of other available neutron facilities with higher neutron fluxes should be performed to determine if higher signal strengths and/or time resolution can be obtained. Rapidly acquired ND profiles with greater neutron counts would be less noisy (i.e., have a greater signal/noise or peak/background ratio) and would facilitate a more detailed quantitative analysis of *in situ* data using programs like GSAS. In such experiments, quantitative phase fraction and phase composition data could be calculated from ND profiles as a function of sintering time – further elucidating TLPS kinetics.

For future modelling efforts (analytical or numerical), the determination of the dominant diffusion mechanism(s) and effective diffusivity data for similar experimental powder conditions should be considered. This should be done using idealized diffusion couple and powder couples, preferentially at T_P above the melting point of Cu. The numerical modelling approach developed by Larrson and Karlsson [48,49], may also be worth investigating since numerical techniques facilitate the incorporation of concentration dependent diffusivities for each element along solute profiles. However, this model, as well as Crank's model for solute uptake [47], does not predict solute concentration profiles with an inflection point at the original interface. When considering the experimental Cu concentration profiles in the study, these predicted profiles have overestimated concentration gradients near the interface and may therefore lead to overestimate TLPS kinetics.

As an extension of this study, the mechanical properties of these TLP sintered mixtures should be investigated in the context of a VMP braze filler metal. Preliminary tests should attempt to determine bulk properties as well as their evolution during different points in the TLPS cycle (i.e., during isothermal solidification, completion, and homogenization). The effects of the developing Kirkendall pore structure will be an important consideration as well

because increasing void fractions will diminish joint strength, yet increased homogenization to intermediate compositions will increase alloy strength in the Ni-Cu system [1]. As such, there may be an optimal sintering time, and this should exceed the time required for liquid removal in order to exploit VMP characteristics. Further mechanical testing should be performed on actual TLPS braze joints using standard brazement procedures and qualification procedures based on AWS/ANSI standard B2.2-91 outlined in [94].

Appendix A: ND TLPS Experiment Temperature Histories

- Samples were sintered at varying hold time durations due to beam time availability at the CNBC-CRL.
- Thermocouple measurements (T_C and T_R) appear to be consistent during sintering due to the proximity of the two sensors (see Figure 5-12). In the case of sample 4, the secondary thermocouple was found to abruptly fail near the end of the isothermal segment and record incorrect temperatures. This data was disregarded.
- Missing data gaps are apparent in the temperature vs. elapsed time plots for some samples. This was due to unavoidable NRU reactor fault and power flections during the experiments. These fluctuations caused a decrease in the incident neutron beam flux and resulted in prolonged or even delayed collection times for each data set since each data set required that a certain total neutron count was required per diffraction pattern acquisition (described in Section 3.3.5). In sample 5 for example, over 1300 minutes were necessary to collect 1080 patterns. This issue is not critical since the sample was maintained at the prescribed temperature by the separate furnace control system during the reactor power fluctuation. Furthermore, the elapsed time, which is the important experiment variable (vs. data set number); can be calculated from the data set time stamps.
- In some cases 27°C hold segments could not be appended at the beginning or end of an experiment due to difficulties with the furnace control system. This issue is still being investigated by NRC staff at the Chalk River Labs.

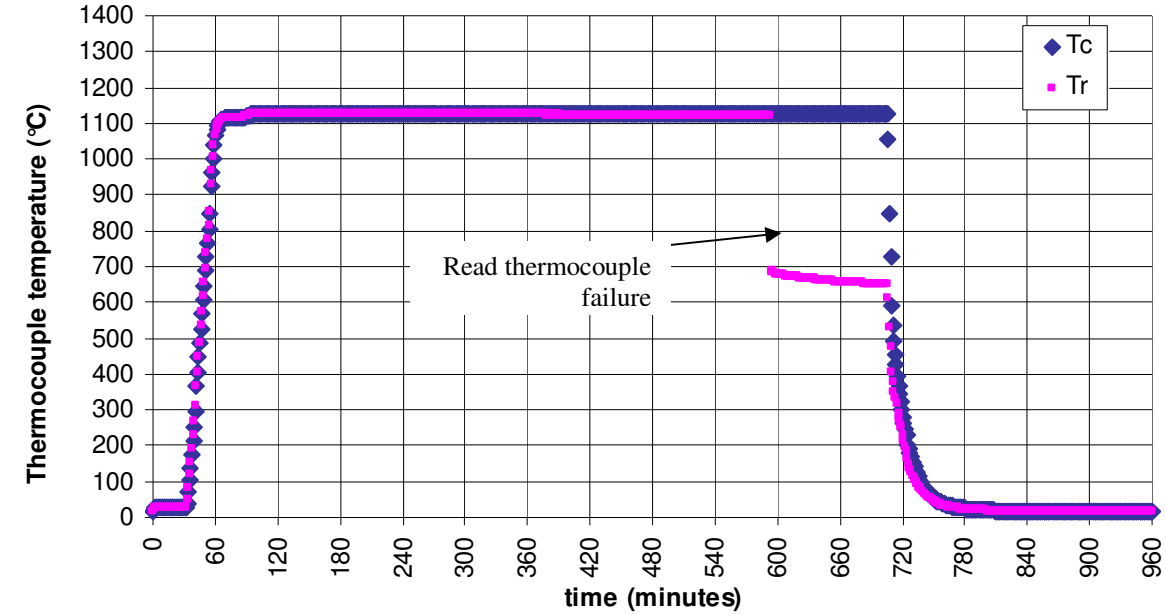

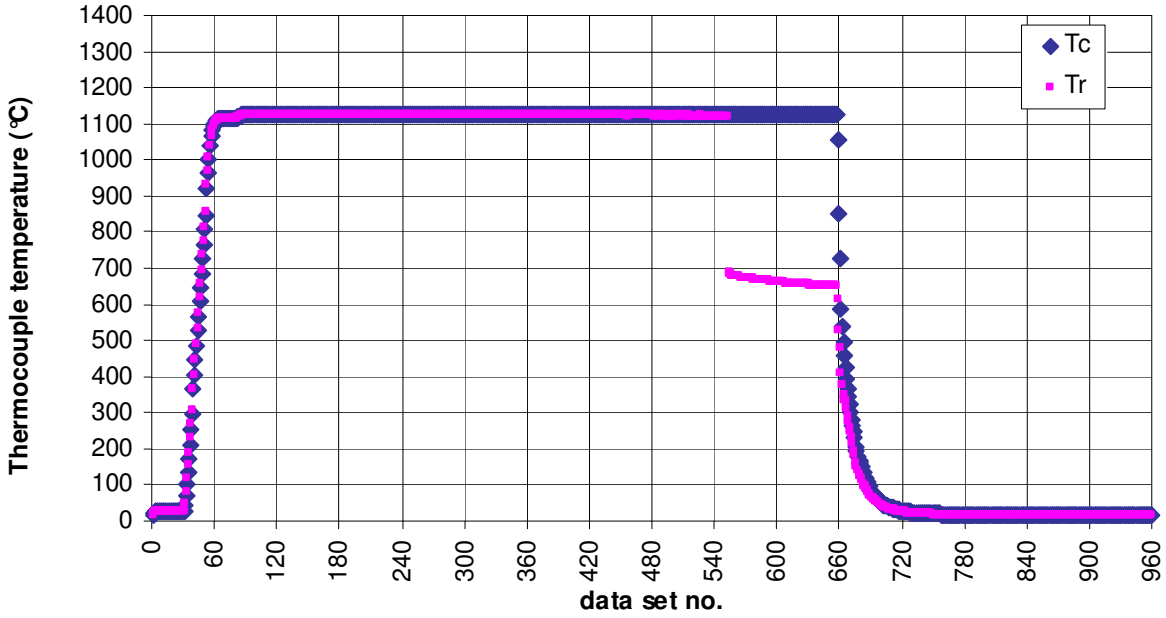

Appendix A - Figure 1: Thermocouple temperature history (vs. elapsed time and data set no.) collected via ATRANS for Sample 4 (N57907).

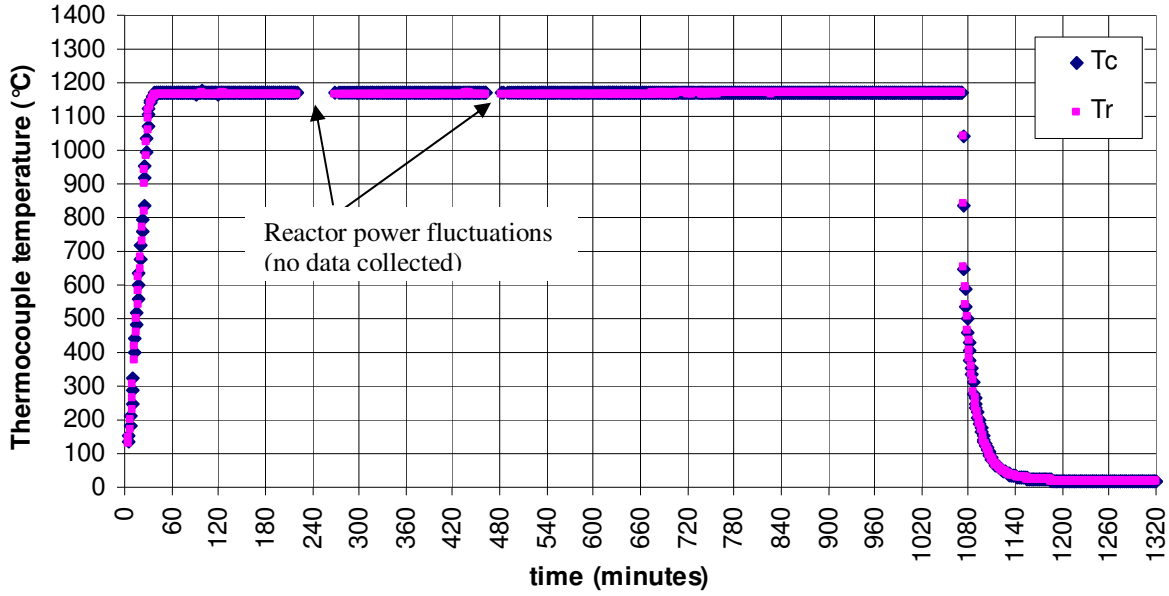

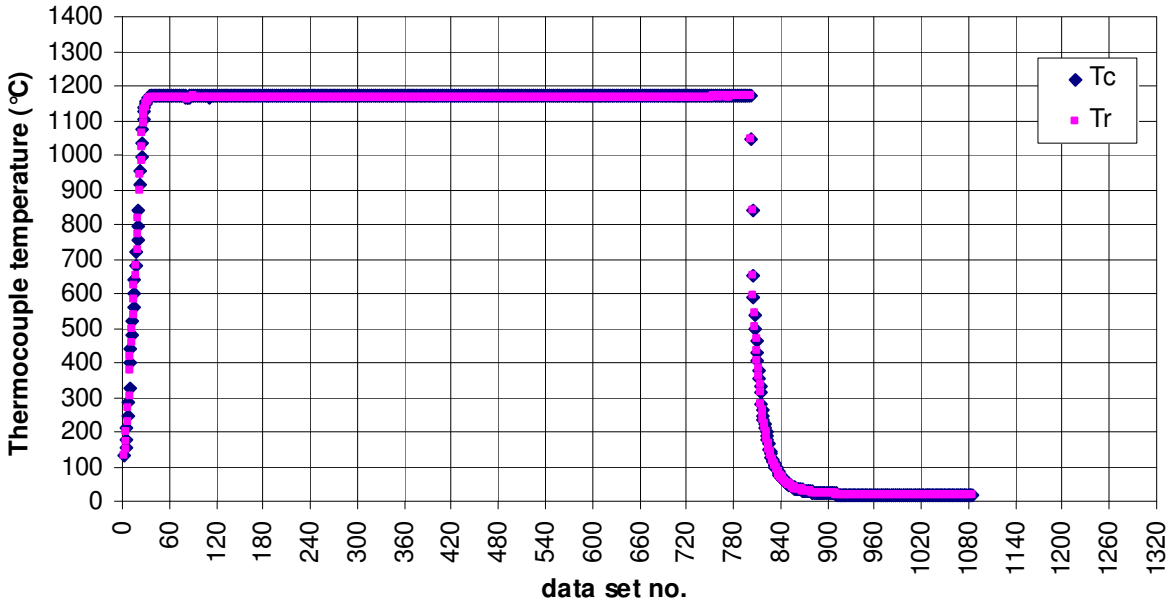

Appendix A - Figure 2: Thermocouple temperature history (vs. elapsed time and data set no.) collected via ATRANS for Sample 5 (N57912).

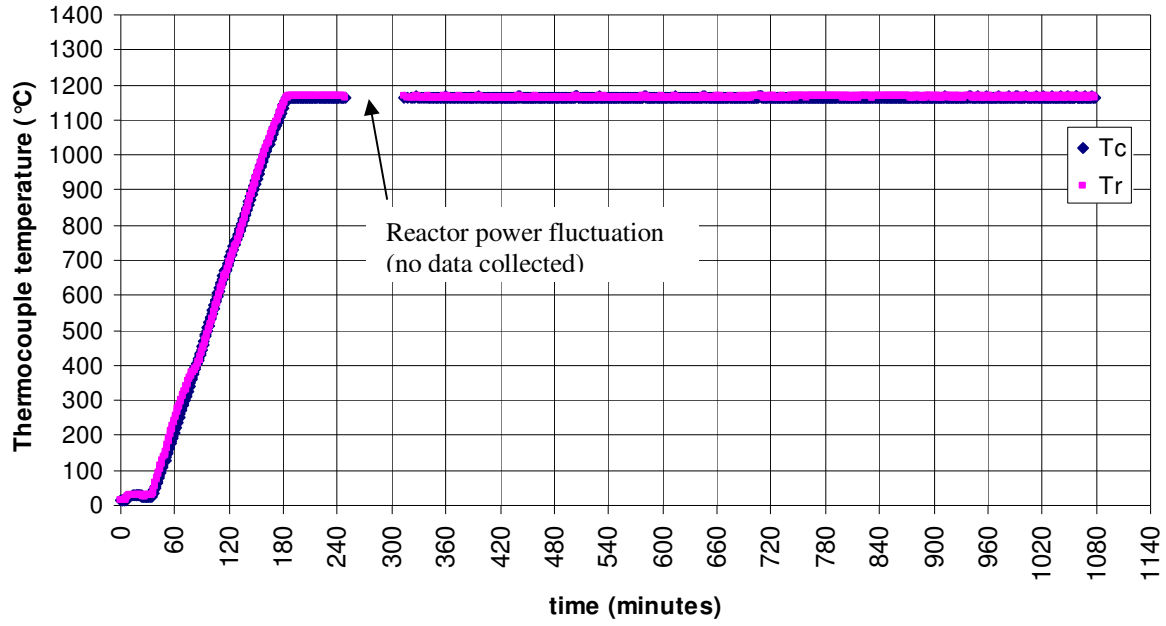

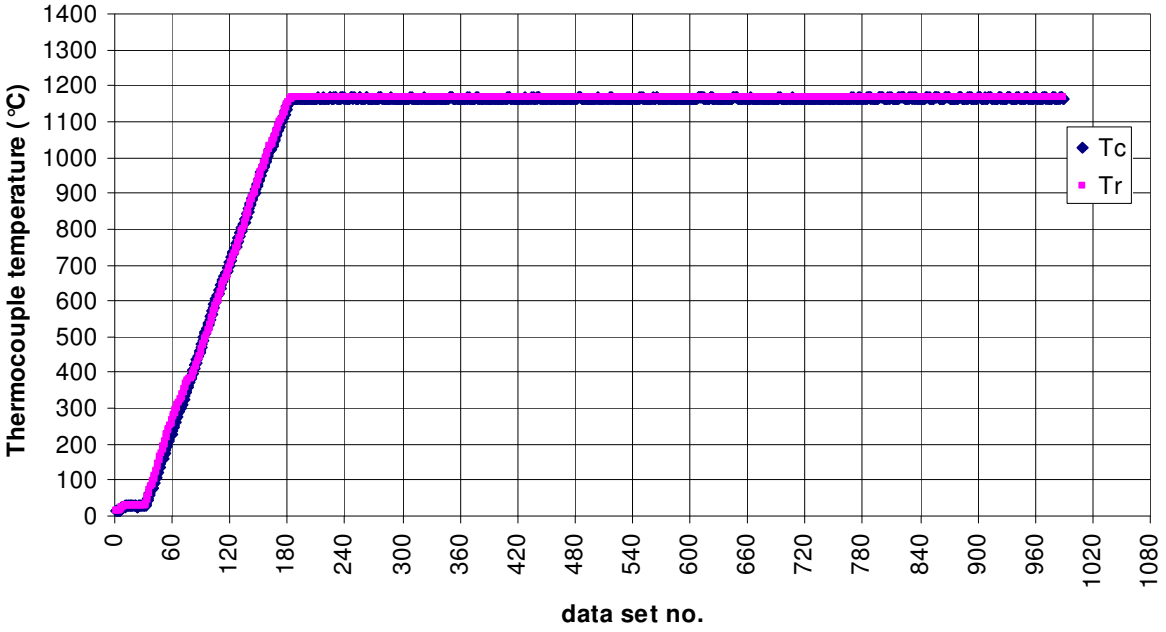

Appendix A - Figure 3: Thermocouple temperature history (vs. elapsed time and data set no.) collected via ATRANS for Sample 6 (N57905).

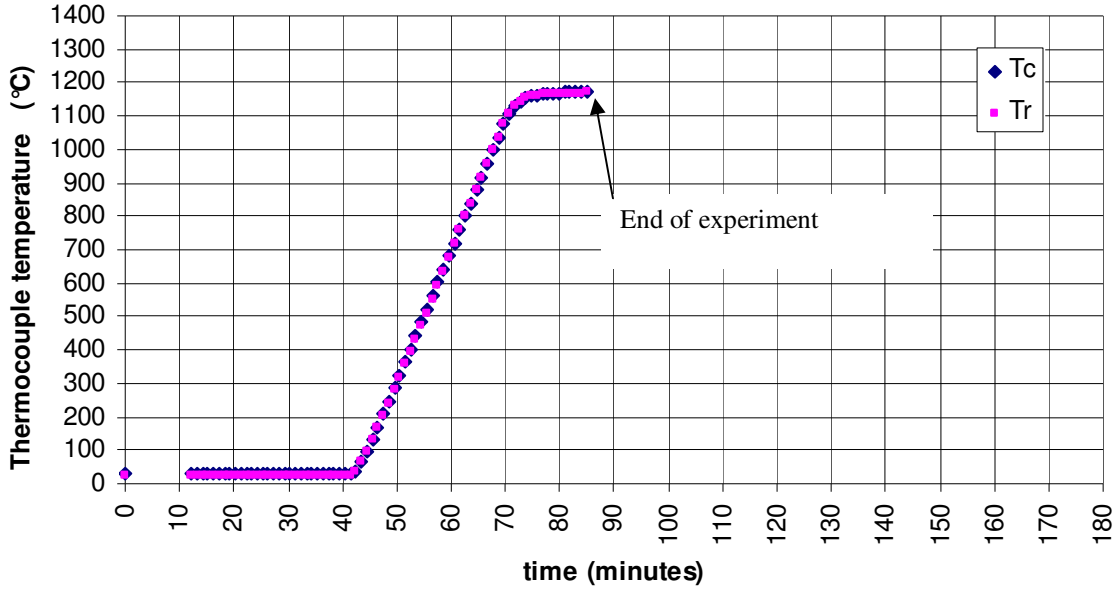

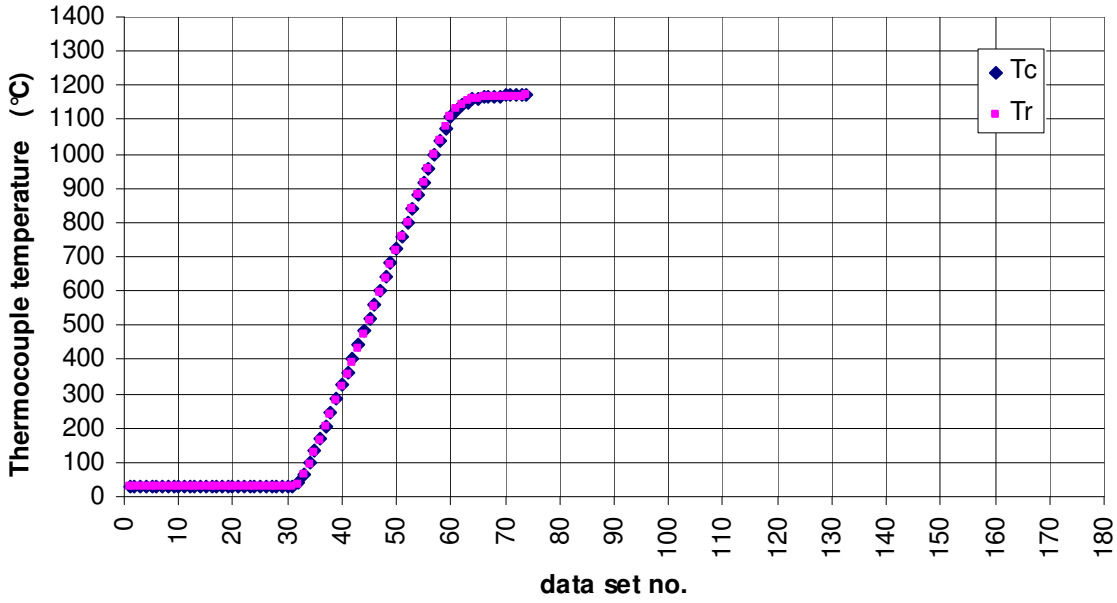

Appendix A - Figure 4: Thermocouple temperature history (vs. elapsed time and data set no.) collected via ATRANS for Sample 7 (N57923).

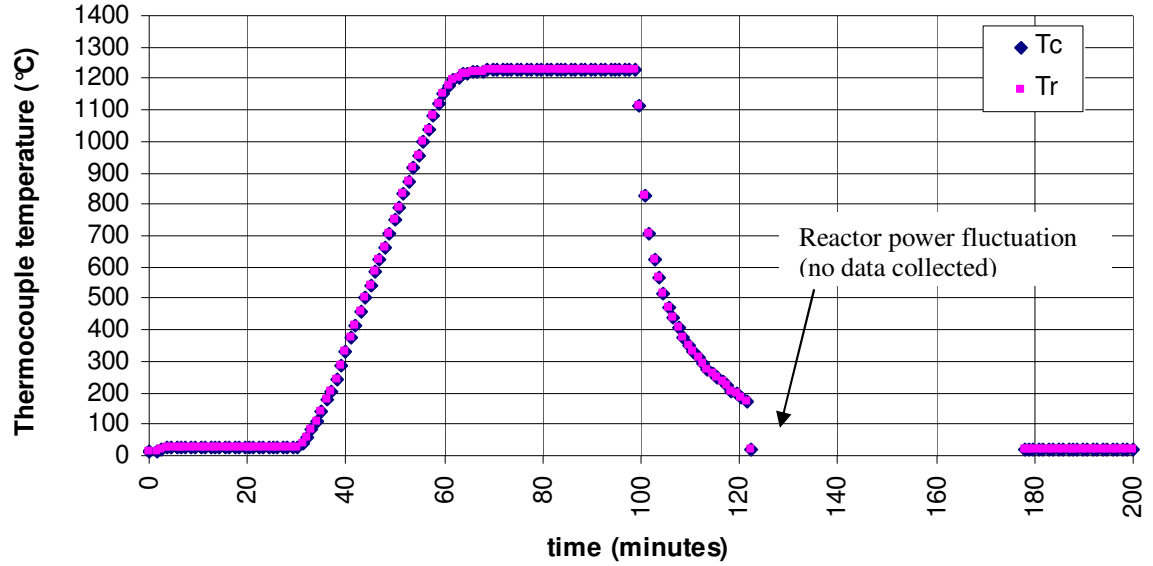

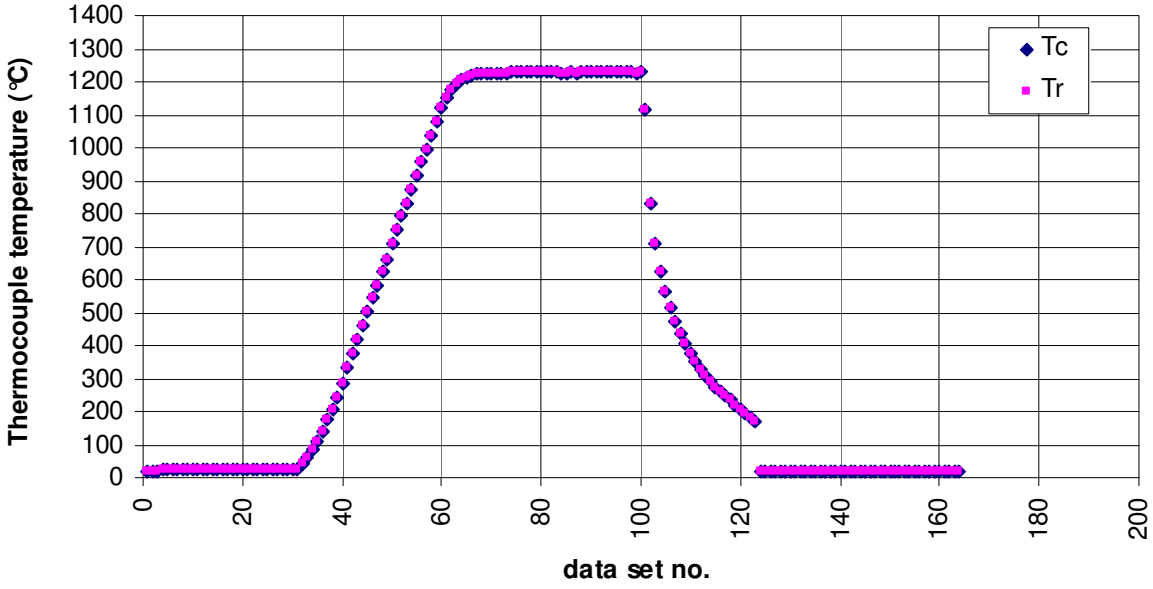

Appendix A - Figure 5: Thermocouple temperature history collected (vs. elapsed time and data set no.) via ATRANS for Sample 8 (N57919).

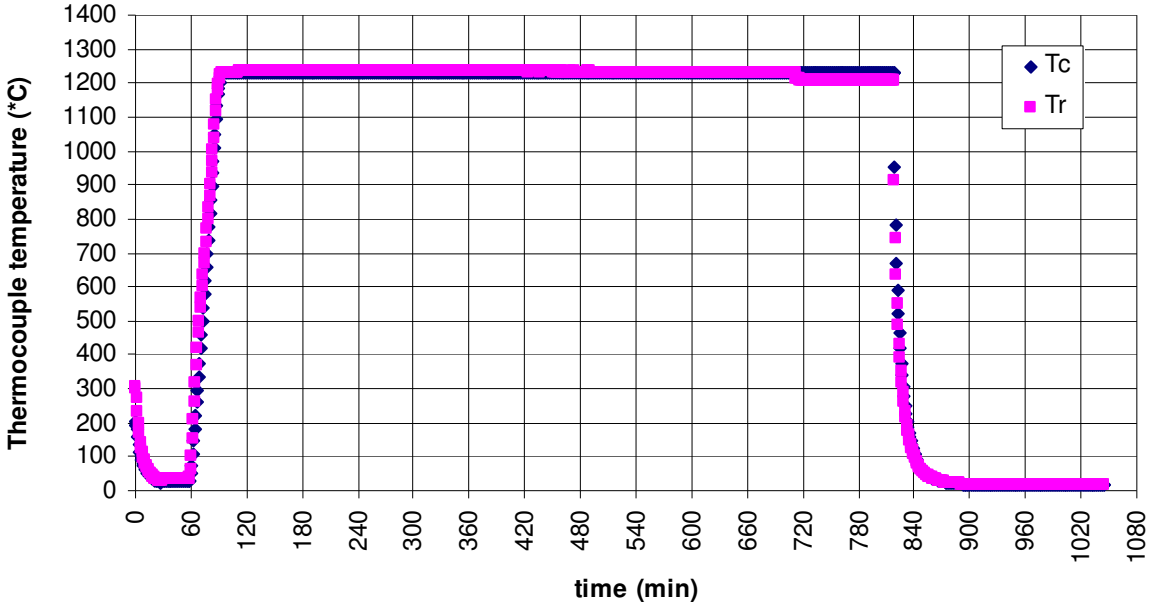

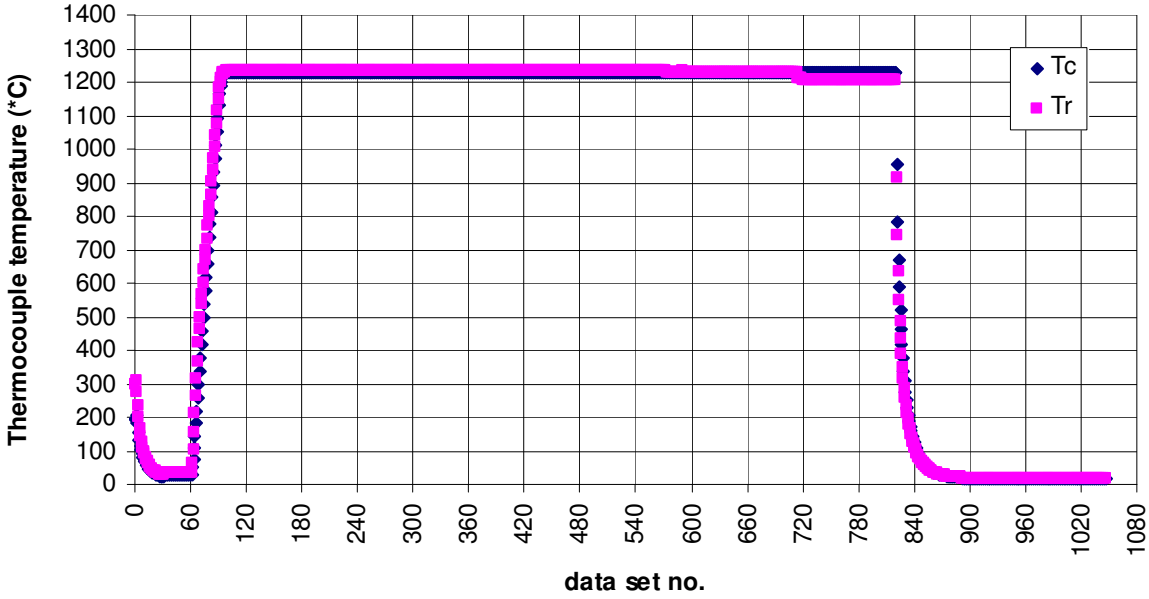

Appendix A - Figure 6: Thermocouple temperature history (vs. elapsed time and data set no.) collected via ATRANS for Sample 9 (N57920).

8. References

1. D.R. Askeland, *The Science and Engineering of Materials* – third S.I. Edition, Chapman & Hall, London, (1996).
2. R.M. German, *Sintering Theory and Practice*, Wiley-Interscience Publications, New York, (1996).
3. R.M. German, *Liquid Phase Sintering*, Plenum Press, New York, (1985).
4. A.P. Savitskii, *Liquid Phase Sintering of Systems with Interacting Components,*Tomsk, (1993).
5. F.J. Puckert, W.A. Kaysser, G. Petzow, Z. *Metallkde*, vol. 74 (11), pp. 737-743, (1983).
6. S. J. Yankee and B. J. Pletka" Journal of Materials Science, vol. 26, pp. 5067-5074, (1991).
7. G. Sethi, A. Upadhyaya, D. Agrawal, *Sience of Sintering,* vol. 35,pp. 49-65, (2003).
8. J. Pleva*, Rev. Environ. Health,* vol. 10 (1), pp. 1-27, (1994).
9. S. Srivastava and A. Upadhyaya, *Transactions of the Indian Institute of Metals*, vol. 58, 5, (2005).
10. X. Qiao, and S.F. Corbin, *Materials Science & Engineering*, vol. A283, pp. 38-45, (2000).
11. S.F. Corbin and D.J. McIsaac, *Materials Science & Engineering*, vol. A346, pp. 132-140, (2003).
12. S. F. Corbin, J. McIsaac, X. Qiao, *US Patent Application #No. 2002001260,* (2002).
13. S.F. Corbin and P. Lucier, *Metall. Mater. Trans. A,* vol. 32A, pp. 971-978, (2001).
14. S. F. Corbin, *Electronic Materials,* vol. 34(7), (2005).
15. D.M Turriff, S.F. Corbin, *Thermal and Metallographic Analysis of Transient Liquid Phase Sintered Cu-Ni Powders, Metall. Mater. Trans. A,* (accepted Jan. 2007).
16. D.M Turriff, S.F. Corbin, *Development of a Transient Liquid Phase Sintered Copper-Nickel Braze*, Proc. of the10th Int. Symp. of Processing and Fabrication of Advanced Materials, ASM International, eds. T.S. Srivatsan and R.A. Varin, (2002).
17. R. Ventkatraman, J.R. Wilcox and S.R. Cain, *Metall. Mater. Trans. A*, 28A, pp. 699-706, (1997).
18. P. Gandhi, C. Gallagher and G. Matijasevic, *J. Electronics Manufacturing,* 7, pp. 253-260, (1997).
19. M.A. Palmer, C.N. Alexander, and B. Nguyen, *J. Electronic Materials,* 28, pp. 912-915, (1999).
20. T. Studnitzky, and R. Schmid-Fetzer, *J. Electronic Materials,* vol. 32, pp. 70-80, 2003.
21. W.F. Gale and D.A. Butts, *Science and Technology of Welding & Joining*, vol. 9(4), pp. 283-300, (2004).
22. D.S. Duvall, W.A. Owczarski, and D.F. Paulonis, *Welding Journal*, vol. 53, pp. 203-214, (1974).
23. W.F. Gale, D.A. Butts, M. Di Ruscio and T. Zhou, *Metall. Mater. Trans. A*, vol. 33A(10), pp.3205-3214, (2002).
24. E. Lugscheider, T.H. Schittny and E. Halmoy, *Weld. J.*, vol. 68(1), pp. 9s-13s, (1989).
25. S.F. Corbin, *Metall. Mater. Trans. A*, vol. 33A, pp. 117-124, (2002).

26. R.N. Lumley, R.N. and G.B. Schaeffer, *Scripta Materialia*, vol. 35 (5) 589-595, (1996).

27. B. Reyburn, and S.F. Corbin, *Int. J. Powder Met.*, vol. 36(5), pp. 57-68, (2000).

28. J. McIsaac*, Effect of Powder Size on Transient Liquid Phase Sintering of Solders, MASc Thesis submitted to the University of Waterloo*, (August, 2001).

29. J.A. Schey, *Introduction to Manufacturing Processes*, 3rd edition, McGraw-Hill, Boston, (2000).

30. J.S. Reed, *Principles of Cermaics Processing*, 2nd ed., John Wiley & Sonds, Toronto, (1995).

31. D.A. Porter, K.E. Earterling, *Phase Transformations in Metals and Alloys*, 2nd ed., CRC Press., New York, (2001).

32. D.B. Butrymowicz, J.R. Manning, M.E. Read, *Diffusion Rate Data and Mass Transport Phenomena for Copper Systems,* INCRA Inc., National Bureasu of Standards, USA, (1977).

33. B. Kiebeck, K. Brand, W. Schatt., *Z"Densification and alloy formation during sintering of heterogeneous systems*, Powder Metallurgy World Congress (PM '94); Paris; France, vol. 2, pp. 1473-1476, (1994).

34. H. Riegger, J.A. pask, H.E. Exner, *Sintering Processes*, Plenum Press, New York (1980).

35. B.E. Magee, and J. Lund, *Z. Matallk.,* vol. 67, pp. 596-602, (1967).

36. A. Belhadjhamida, R.M. German, *" A Model Calculation of the Shrinkage Dependance on Rearrangement During Liquid-Phase Sinterinng." Advances in Powde Metallurgy and Particluate Materials,* vol. 3, A. Lawley, A. Swanson (eds.), Princeton NJ, pp. 85-96, (1993).

37. R.M. German and J.W. Dunlap, *Metall. Mater. Trans. A*, vol. 17A, pp. 205-213, (1986).

38 W.H. Baek, R.M. German, *Int. J. Powder Metall.,* vol. 22(4), pp. 235-244 (1986).

39. K. Brand, W. Schatt., *Z. Metallkde*, vol. 84 (12), pp. 893-898 (1993).

40. D.J. Lee, R.M. German, *Int. J. Powde Metall.,* vol. 21(1), pp. 9-21 (1985).

41. A. Lal, R. G. Iacocca, R. M. German, *J. Mater. Sci.*, vol. 35, pp. 4507-4518, (2000).

42. A. Lal, R. G. Iacocca, R. M. German, *Metall. Mater. Trans. A*, vol. 30A, pp. 2201-2208 (1999).

43. A. D. Smigelskas and E. O. Kirkendall, *Trans. AIME*, vol. 171, pp 130-142, (1947).

44. B. Fischer and P.S. Rudman, *Acta Metallurgica,* vol. 10, pp. 37-43. (1962).

45. F.J. Puckert, W.A. Kaysser, G. Petzow, *Sci. Sintering*, vol. 16, pp. 105-113 (1984).

46. R.A. Masumura, B.B. Rath, C.S. Pande, *Acta Mat.,* vol. 50, pp. 4535-4544, (2002)

47. J. Crank, *The Mathematics of Diffusion*, Oxford Press, London, (1956).

48. L.E. Larsson and B. Karlsson, *Mat. Sci. & Eng.*, 20, 155-160 (1975).

49. L.E. Larsson and B. Karlsson, *Mat. Sci. & Eng.*, 20, 161-170 (1975).

50. E. A. Brandes, *Smithells Metals Reference Book, 6th Ed.,* Butterworths, London (1983).

51. G.P. Grabovetskaya, I.V. Ratochka, Y.R. Kolobov, L.N. Puchkareva, The Physics of Met. and Metallography, vol. 83, No. 3, 310-313, (1997).

52. A Hassner, *Neue Hutte*, vol. 12, pp.161, (1967)

53. S.M. Schwarz, B.W. Kempshall, L.A. Gianuzzi, *Acta Materialia*, vol. 51(10), pp.2765-2776, (2003).

54. M.A. Krishtal, *Fiz. Metal. Metalloved.* Vol. 29(2), pp. 305-307, (1970).

55. T. Zhou and W.F. Gale, *Mat. Sci. & Tech.,* vol. 19(8), pp. 1084-1090, (2003).

56. I. Manna, S.K, Pabi, W. Gust, *Int. Mat. Rev*., vol. 46(2), pp. 53-91 (2001).

57. F.J.A. den Broader and S. Nakahara, *Scripta Metallurgica*, vol. 17, pp. 399-404 (1982).

58. Y. Yamamoto, S. Uemura, M. Kajihara, *Mat. Sci & Eng. A332*, pp. 176-181, (2001).

59. Y. Yamamoto, S. Uemura, K. Yoshida, M. Kajihara, *Mat. Sci & Eng.,* Vol. A333, pp. 262-269, (2002).

60. M. Moriyama and M. Kajihara, *ISIJ International*, vol. 38(1), pp. 86-92 (1998).

61. C.Y. Ma, E. Rabkin, W. Gust, S.E. Hsu, *Acta Metall. Mater.*, vol. 43(8), pp. 3113-3124 (1995).

62. M. Moriyama and M. Kajihara, *ISIJ International*, vol. 38(5), pp. 489-494 (1998)

63. J.K. Kim and D.Y. Yoon, A*cta Metall. Mater.,* vol. 42(3), pp. 913-919 (1994).

64. A. Wittebrood, C.J. Kooij, K. Vieregge, *Materials Science Forum, v*ols. 331-337, pp. 1743-1750 (2000).

65. M. Nylén, U. Gustavsson, B. Butchinson, A, Larlsson, *Science Forum,* vols. 331-337, pp. 1737-1742 (2000).

66. V.L. Acoff and R.G. Thompson, *Metall. Mater. Trans. A*, vol. 27A, pp. 2692-2703 (1996).

67. D.Y. Yoon, *Int. Mat. Rev., v*ol 40(4), pp. 149-179 (1995)

68. M.E. Brown, *Introduction to Thermal Analysis*, Chapman and Hall, New York (1988).

69. D.M Turriff, S.F. Corbin, *Thermal and Metallographic Analysis of Transient Liquid Phase Sintered Cu-Ni Powders, Metallurgical & Materials Transactions A*, (accepted Jan. 2007).

70. C.J. Howard and S.J. Kennedy, *Materials Forum*, vol. 15, pp. 155-176, (1994).

71. R.E. Smallman, R.J. Bishop, Modern Physical Metallurgy & Materials Engineering, sixth edition, Butterworth & Heinmann. (1999).

72. C. Surayanarayana and M. G. Norton, *X-ray Diffraction – a practical approach*, Plenum Press, New York, New York USA, (1998).

73. B.D. Cullity, *Elements of X-ray Diffraction*, second edition, Addison-Wesley Publishing Co., (1978).

74. G.L. Squires*, Introduction to the Theroy of Thermal Neutron Scattering*, Dover Publications, NewYork (1996).

75. CNBC website http://neutron.nrc-cnrc.gc.ca/specs_e.html, accessed March 14, 2007 (11/2002)

76. G.E. Bacon, *Neutron Diffraction, Second Edition*, Oxford. (1962)

77. J.S. Kennedy, A*dv. X-ray Anal.,* vol. 38, pp. 35-46 (1995).

78. J.S.O. Evans and I. Radosaviljevic, *Chem. Soc. Rev.,* vol. 33, pp. 539-547 (2004).

79. J.S.O. Evans , J.D. Jorgensen, S. Short, W.I.F. David, R.M. Ibberson, A.W. Sleight, *Phys. Rev. B.*, vol. 60 (21), pp. 14643-14648 (1991).

80. I. Bull, P. Lightfoot, L.A. Villaescusa, L.M. Bull, R.K.B. Goverm J.S.O. Evans, R.E. Morris, *J. Am. Chem. Soc.,* vol. 125, pp 4342-4349 (2003).

81. Y.S. Touloukian, R.K. Kirby, P.E. Taylor, *Thermophysical Properties of Matter - the TPRC Data Series. Volume 12. Thermal Expansion Metallic Elements and Alloys*, IFI/Plenum, New York (1979).

82. Y.S. Touloukian, R.K. Kirby, P.E. Taylor, T.Y.R. Lee, *Thermophysical Properties of Matter - the TPRC Data Series. Volume 13. Thermal Expansion - Nonmetallic Solids*, IFI/Plenum, New York (1977).

83. C.S. Barrett, *Structure of Metals – Crystallographic Methods, Principle, and Data,* McGraw-Hill, New York, (1952).

84. B. Fischer and P.S. Rudman, *J. Applied Physics,* vol. 32 (8), pp. 1604-1612. (1961).

85. P.S. Rudman, A*cta Cryst.,* vol. 13, pp. 905-909. (1960).

86. R. Delhez, E.J. Mittemeijer, E.A. van den Bergen, *J. Mater. Sci.,* vol. 13, pp. 1671-1679 (1978).

87. D.P. Riley, C.P. oliver, E.H.Kisi, *Intermetallics*, vol. 14, pp. 33-38 (2006).

88. E. Wu and E.H.Kisi, *J. Am. Ceram. Soc.,*vol. 84 (19), pp. 2281-2288 (2001).

89. E. Wu and E.H.Kisi, *J. Am. Ceram. Soc.,*vol. 89 (2), pp. 710-713 (2006).

90. R.A. Young, *The Rietveld Method,* Oxford University Press, Oxford, (2002).

91. A.C. Larson and R.B. von Dreele, GSAS – General Structure Analysis System, Los Alamos National Laboratory, Los Alamos, NM, USA (1985).

92. A.C. Larson and R.B. von Dreele, GSAS Manual, , Los Alamos National Laboratory, Los Alamos, NM, USA (2000).

93. H.B.Cary, *Modern Welding Technology* – fourth edition, Prentice Hall, Columbus, Ohio, (1998).

94. *Brazing Handbook* – fourth edition, American Welding Society, Miami, Florida, (1991).

95. S.D. Brandi *et al*, *Brazeability and Solderability of Engineering Materials*: ASM Handbook vol. 6, ASM Inernational, (1993).

96. M.L. Kuntz, S.F. Corbin, Y. Zhou, *Acta Mater.,* vol. 53(10) , 3071-3082 (2005).

97. T.B. Massalski, ed. *Ni-Cu binary alloy phase diagram. In: Binary Alloy Phase Diagrams,* vol. 1., Metals Park (OH): American Society for Metals (1986).

98. D. Antonsen and J. Tundermann, "*Production of Nickel and Nickel Alloy Powders*", Metals Handbook 9th Edition, vol. 7, compiled by E. Klar, American Society for Metals, Metal Park,OH, pp. 135-143. (1984).

99. Netzsch DSC 404c-Pegasus: *Instrument manual: Operating Instructions for DSC Apparatus* (1998).

100. M.L. Kuntz, *Quantifying Isothermal Solidification Kinetics during Transient Liquid Phase Bonding using Differential Scanning Calorimetry*, Ph.D. thesis, University of Waterloo (2006).

101. D.M Turriff, S.F. Corbin, *Reasearch Proposal #N579 submitted to the Canadian Neutron Beam Centre* (2005).

102. NIST Standar Reference Material certificate for pure Si powder (640c) https://srmors.nist.gov/view_cert.cfm?srm=640c

103. L. Lutterotti and P Scardiÿ, J. Appl. Crystallogr..vol. 23, pp. 246-252 (1990). Updated in Inorganic Crystal Structure Database (ICSD Collection Code 68591) (1997).

104. Personal Communication, I. Swanson, Canadian Neutron Beam Centre, National Research Council Canada, Chalk River Laboratories, Chalk River ON, Canada (March 23, 2007)

105. V. E. Sears, *Neutron scattering length and cross sections,* Neutron News, Vol . 3(3), (1992).

106. Personal Communication, M. Watson, Canadian Neutron Beam Centre, National Research Council Canada, Chalk River Laboratories, Chalk River ON, Canada (March 21, 2007).

107. Personal Communication, L. Cranswick, Canadian Neutron Beam Centre, National Research Council Canada, Chalk River Laboratories, Chalk River ON, Canada (July 18, 2005).

108. B. Hinrichsen, R. E. Dinnebier, M. Jansen, Powder 3D: a program for evaluation and presentation of multiple powder patterns in dependence of an independant variable, (2004).

109. B. Hinrichsen, R. E. Dinnebier, M. Jansen, *Powder3D: An easy to use program for data reduction and graphical presentationof large numbers of powder diffraction patterns,* Proc. Of European Powder Diffraction Conference, Sept. 2-5 (2004).

110. D.A. Porter, K.E. Earterling, *Phase Transformations in Metals and Alloys*, Van Nostrand Reinhold Co., New York, (1981).

111. R. Srinavasa and T.R. AnantharamanL, *Current Science* vol. 32, pp. 262-263 (1963). Updated in Inorganic Crystal Structure Database (ICSD Collection Code 53246) (1982).

112. H.E. Swanson and E. Tatge, *National Bureau of Standards (U.S.)*, (359) pp. 1-95 (1953). Updated in Inorganic Crystal Structure Database (ICSD Collection Code 53246) (1967).

113. Personal Communication, L. Cranswick, Canadian Neutron Beam Centre, National Research Council Canada, Chalk River Laboratories, Chalk River ON, Canada (April 19, 2007).

114. National Institute of Standards and Technology (NIST) Centre for Neutron Research website: http://www.ncnr.nist.gov/resources/n-lengths/, accessed July 14, 2007 (1999).